Doctoral Dissertation
Doctoral Program in Material Science and Technology (36^{th}cycle)

Hybrid Power-Energy Electrodes

By

Roberto Colombo

******

Supervisor(s):
Prof. C. Francia, Supervisor
Prof. S.Bodoardo, Co-Supervisor
Prof. J. Amici, Co-Supervisor

Doctoral Examination Committee:
David Peralta , Referee, Commissariat à l'énergie atomique et aux énergies alternatives (CEA).
Prof. Annukka Santasalo-Aarnio, Referee, Aalto University School of Engineering

Politecnico di Torino
2024

Declaration

I hereby declare that, the contents and organization of this dissertation constitute my own original work and does not compromise in any way the rights of third parties, including those relating to the security of personal data.

Roberto Colombo
2024

* This dissertation is presented in partial fulfillment of the requirements for **Ph.D. degree** in the Graduate School of Politecnico di Torino (ScuDo).

I would like to dedicate this thesis to my loving parents.

"Every day you may make progress. Every step may be fruitful. Yet there will stretch out before you an ever-lengthening, ever-ascending, ever-improving path. You know you will never get to the end of the journey. But this, so far from discouraging, only adds to the joy and glory of the climb."

Sir Winston Churchill

Acknowledgements

Many people have contributed to the realization of this doctoral work, and it would be impossible to thank them all in a few words, but I will do my best.

First of all, I would like to thank my supervisor, Carlotta Francia, and my co-supervisors Silvia Bodoardo and Julia Amici for the support they have shown me during my research activities, which would not have been possible without them.

A special thanks goes to two people who have greatly contributed to my journey (whether in terms of growth or not is up to them to say) over these years, Nadia Garino and Daniele Versaci, who have tried to teach me everything they knew (synthesis and data interpretation) without hesitation, also supporting me in fairly delicate moments.

I would then like to thank Professor David Peralta and Jeremie Fondard, who warmly welcomed me at CEA in Grenoble, where I had an enriching experience both from a human and scientific point of view. I greatly appreciated our meetings, David, and your work determination, Jeremie.

I would also like to thank all my office mates with whom I shared many of my hours spent at the Polytechnic (besides bad smells and good music): a sincere thanks to Andrea, Davide, Piera, and Daniele, without whom everything would have been much more difficult. Thanks also to all the other people I collaborated with in the laboratories of the Polytechnic and beyond.

A heartfelt thanks to the Hydra team, with whom I shared two years of teamwork. With this experience, I learned how important and enriching it can be to work with other people.

Infinite thanks also to my swimming and climbing mates, Roberto, Andrea, Alessandro, Davide, and the Escape team. With you, I shared fun moments that made everything lighter.

Thanks to my longtime friends Giorgio and Luke, the Galferini group, and other friends like Davide, Alessandro, Matteo, and many others.

Finally, I would like to dedicate this thesis work to the people who have supported me the most from a personal point of view over these years, motivating me even in moments of uncertainty: thanks to my parents, my sisters, Serena, and Lucy, who have always made me feel their affection and have accompanied me step by step on this journey. I am glad to have you by my side, and I hope you feel the same.

Abstract

Nowadays, lithium-ion batteries (Li-ion) represent the dominant technology in the field of energy storage, where they are used in various areas such as portable electronics, electric vehicles, and storage for renewable energy applications. This ever-increasing demand has brought the improvement of this technology and the development of alternative chemistries that can provide superior (or at least equivalent) performance and better environmental and economic sustainability into the focus of researchers.

In this context, one of the most promising technologies is lithium-sulfur (Li-S) batteries, as they offer high energy density (about 2600 Wh kg^{-1}) and low environmental impact costs. However, some intrinsic problems of Li-S batteries still need to be fully resolved to allow the commercialization of this type of battery. The main issues include the shuttle effect (the migration of long-chain polysulfides from the cathode to the anode and their reaction with metallic Li) and the significant volume change that sulfur undergoes from S_8 to Li_2S.

From this perspective, the research here presented has explored two innovative materials designed for the cathodes of Li-S batteries: high entropy oxides (HEO) and a composite of reduced graphene oxide (rGO) with zinc sulfide nanoparticles. Various physicochemical techniques (XPS, XRD, TGA, SEM) have been applied to characterize the materials, which were then electrochemically tested in coin cells.

Regarding Li-ion batteries, one of the most interesting approaches to increase energy density involves raising the operational potential of the cell by using alternative cathodic materials to the already commercialized NMC and LFP, which operate at about 4 and 3 V, respectively. From this perspective, spinel materials such as LNMO, which operates at about 4.8 V, are particularly interesting. Moreover, LNMO is also more sustainable compared to NMC due to the lack of Co in its composition. Consequently, the electrochemical behavior of LNMO and two different formulations of a physical blend of LNMO and LFP ($2\%_{wt}$ and $10\%_{wt}$ of LFP) obtained

through the technique of Resonant Acoustic Mixing (RAM) have been investigated. This technique is capable of reducing mixing times and increasing the homogeneity of LFP dispersion on LNMO particles. In this work, a thorough electrochemical characterization was conducted to investigate the effect of LFP on the performance of the cathode. This work was carried out as part of the European HYDRA project, which involved several partners (CEA, SINTEF, Johnson Matthey, ICSI).
Finally, during my research period abroad, specifically at the Commissariat à l'énergie Atomique (CEA) in Grenoble, another cathodic material with a spinel structure, lithium copper manganese oxide (LCMO), was synthesized. This material features copper as a substitutive element for Ni, which results in a decrease in theoretical capacity (from 147 to 95 mAh g^{-1}), but an increase in operational potential (from 4.7 to about 4.95 V). This material was also chemically over-lithiated, obtaining a lithium-rich cathode (LRCMO). Both materials were characterized from a physicochemical perspective, and a deep electrochemical characterization was performed both in half cells (also in an extended potential window from 1.6-5.1 V, still unexplored in the literature) and for the first time in full cells.

Contents

List of Figures

List of Tables

Chapter 1

Introduction

1.1 European and Global energy transition

Undoubtedly, the most significant challenges humanity must face in the coming years are climate change and global warming. These challenges are very complex as they require a radical change of our entire socio-economic model: it is not just a matter of changing how we produce energy but also how it is distributed and used by network users. From a practical point of view, this means passing from a traditional grid to one defined as "smart," (see Figure 1.1) which has numerous advantages: the assembly set-up is based on microprocessors and digital electronics (vs. relays, switches, meters, etc.); production and distribution are decentralized; the excess energy can be re-entered into the grid and the consumers themselves can contribute to the production; the introduction of numerous sensors makes it easy to identify any damage/faults and to monitor the distribution of energy; any failure in the infrastructure can be rerouted to go around the problem area, finally smart grid involves microprocessor based digital technology which allows the data communication between the devices of the system and makes the remote control possible.
However, the objectives to be pursued to carry out this energy transition are very ambitious: according to the latest IPCC report[1], to respect the Paris Agreement (maximum temperature increase of 1.5°C compared to pre-industrial levels), it is

[1]Available online: https://www.irena.org/

necessary to cut 37 gigatonnes (Gt) of CO_2 emissions from 2022 levels, while the annual deployment of some 1 000 GW of renewable power is needed.

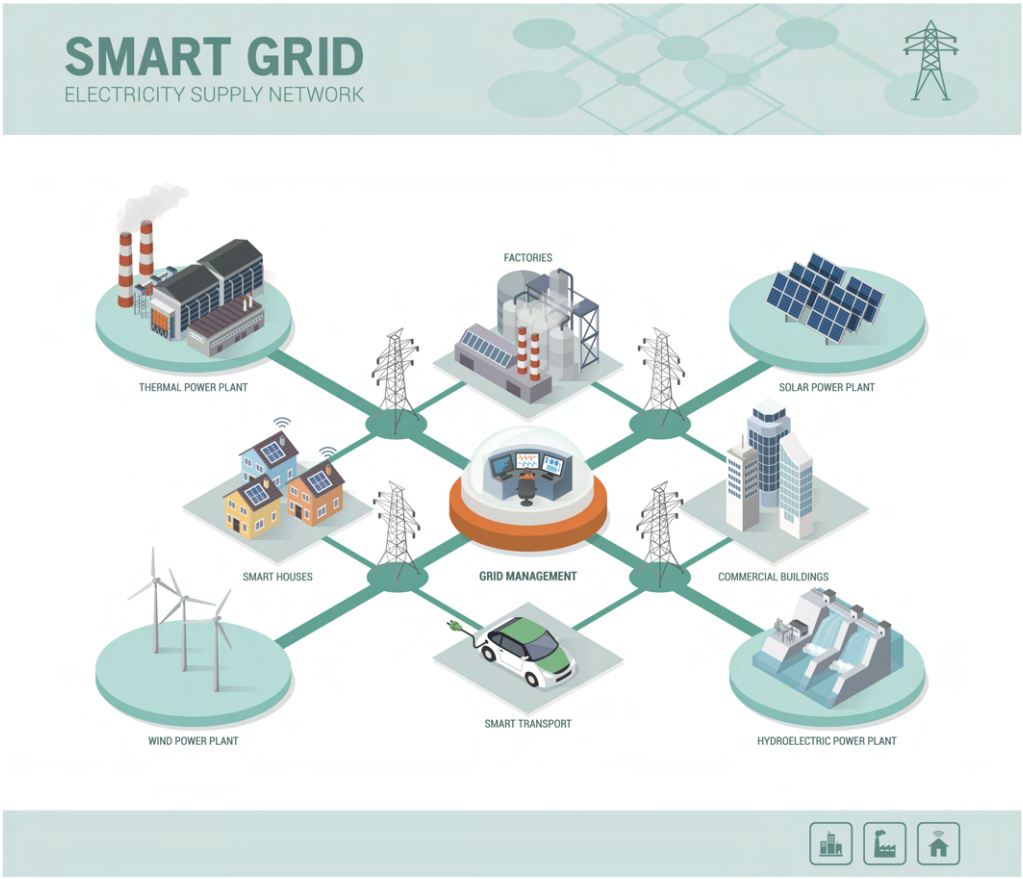

Fig. 1.1 An example of a smart grid, where all the components are integrated with each other to increase the efficiency of the system. Source: https://www.unicusano.it/blog/didattica/master/smart-grid/

In this sense, a significant acceleration, is needed across energy sectors and technologies, from deeper end-use electrification of transport and heat to direct renewable use, energy efficiency, and infrastructure additions. The 1.5°C scenario envisions electricity as the primary energy carrier, accounting for over half of the total final energy consumption (TFEC) (see Figure 1.2). Renewable energy deployment, energy efficiency advances, and electrification of end-use sectors all contribute to this trend. Furthermore, modern biomass and hydrogen are expected to play more significant roles, accounting for 16% and 14% of TFEC by 2050.

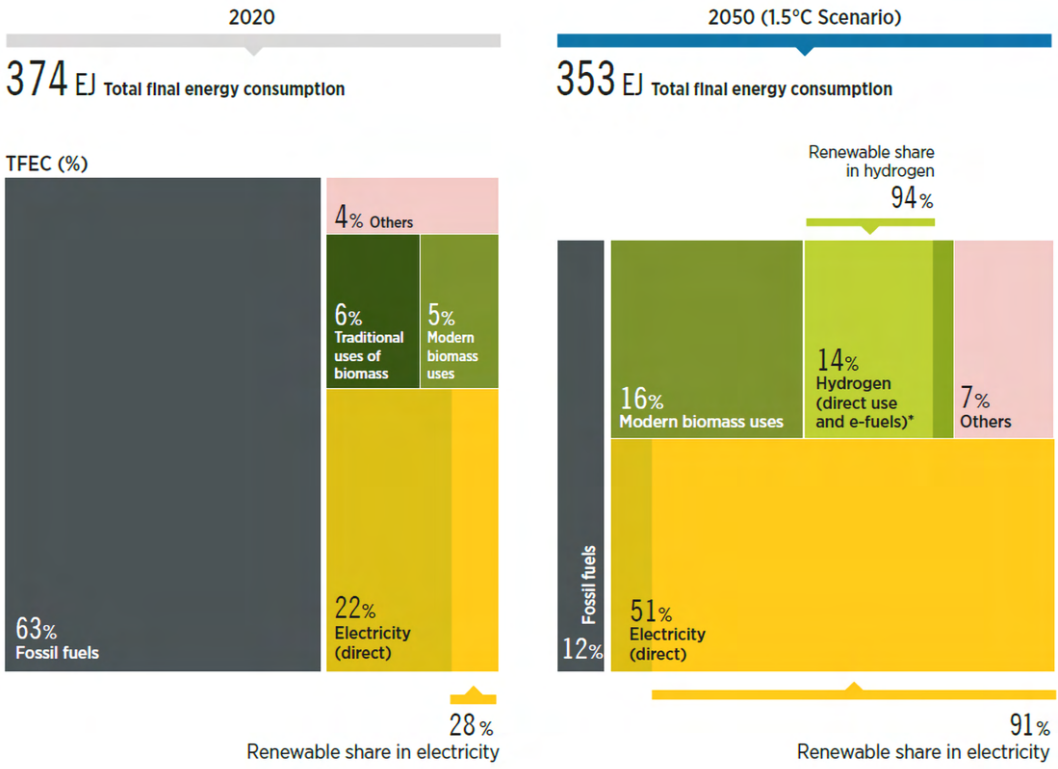

Fig. 1.2 The figures above include only energy consumption, excluding non-energy uses. For electricity use, 28% in 2020 and 91% in 2050 are from renewable sources; for district heating, the shares are 7% and 84% respectively; for hydrogen (direct use and e-fuels), the renewable energy share (i.e. green hydrogen) would reach 94% by 2050. Hydrogen (direct use and e-fuels) accounts for total hydrogen consumption (green and blue) and other e-fuels (e-ammonia and e-methanol). Electricity (direct) includes the consumption of electricity that is provided by all sources of generation: renewable, nuclear and fossil fuel-based. Traditional uses of biomass refer to the residential TFEC of solid biofuels in non-OECD countries. Modern bioenergy uses include solid biomass, biogas and biomethane used in buildings and industry; and liquid biofuels used mainly in transport, but also in buildings, industry and other final consumption. Remaining fossil fuels in 2050 correspond to natural gas (mainly used in industry and transport, and to a lesser extent in buildings), oil (mainly in industry and transport, and to a lesser extent in buildings) and coal (corresponds to uses in industry - cement, chemicals, iron and steel). Others include district heat and other renewables consumption. EJ = exajoule; OECD = Organisation for Economic Co-operation and Development; TFEC = total final energy consumption. Source: International Renewable Energy Agency (IRENA).

Another field in which it is necessary to work hard is the reduction and capture of CO_2. In fact, in this sense, the effort is enormous since it is needed to go from about 35 $GtCO_2$ (gigatonne of CO_2) in 2022, to zero emissions (net zero scenario, in

which the CO_2 produced is equal to that capable of being reabsorbed by the planet) in 2050. In this sense, the most effective measures, according to IRENA (International Renewable Energy Agency), are the replacement of fossil fuels with renewable energies (25% reduction of CO_2 emissions), the increase in energy conservation and efficiency (25%), and electrification in the end use sectors (19%), with only 8% of emissions reduction due to direct carbon capture and storage.
In this global context, Europe is moving with numerous new regulations and policies, such as the "European Green Deal," a document that sets the green transition ambitions in stone, including the climate targets towards net zero by 2050. Alongside with the REPowerEU plan (which is focused on the move away from fossil fuels) and the Circular Economy Action Plan, the Green Deal sets the framework for the trasformation of EU's industry for the net zero age. From a financial point of view, Europe has already mobilized considerable resources (around 250 billion with the Recovery and Resilience Facility, RRF) for green measures, including investments supporting the decarbonization of industry. At the same time, in the rest of the world, the leading economic powers are investing a lot of resources to implement the zero net scenario (the United States Inflation Reduction Act will mobilize over USD 360 billion by 2032, while Japan's green transformation plans aim to raise to EUR 140 billion).
In this context, Europe has activated five Important Projects of Common European Interest (IPCEI), large development projects undertaken by several Member States to fund new technologies in strategic areas: one in microelectronics, two in batteries, and two in hydrogen, with more projects in preparation. The public investment envisaged for these projects amounts to approximately 18 billion.
It follows from the above that developing adequate technological devices in energy storage, such as batteries, is crucial for implementing the ecological transition in the next thirty years. In particular, because of their importance in developing zero-emission mobility and storing intermittent renewable energy, batteries are critical to the EU's transition to a climate-neutral economy. Batteries are also crucial in powering the booming digital economy and the ever-increasing quantity of portable devices. Global battery demand is predicted to rise 14 times by 2030, driven by the electrification of transportation and the deployment of batteries in electrical grids. According to the "New EU regulatory framework for batteries"[2] the EU could provide 17% of that demand.

[2]Available online: www.europarl.europa.eu

In particular, a sector in which batteries are proving to be crucial is transport: automotive Li-ion battery demand increased by approximately 65% to 550 GWh in 2022, from around 330 GWh in 2021 (see Figure 1.3, mainly owing to the growth of electric passenger vehicle sales, with new registrations rising by 55% in 2022 compared to 2021[3] .

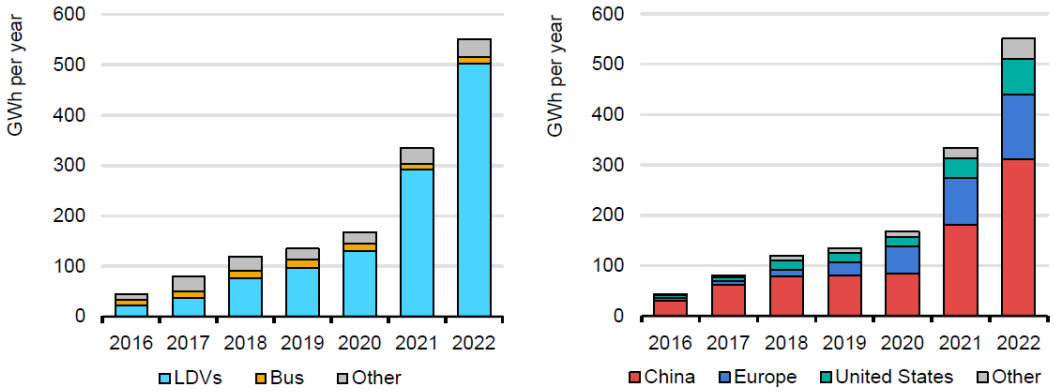

Fig. 1.3 In the left chart is represented the battery demand (for the automitive Li-ion market) by typology of vehicles, where LDVs stands for Light-duty-Vehicles, while on the right charte is shown the battery demand for the automotive sector by region. Source: IEA. International Energy Agency, Global EV Outlook 2023.

The demand for crucial raw materials has increased as a direct result of the massive growth in demand for batteries. Despite a 180% increase in production since 2017, lithium demand surpassed supply in 2022 (as it did in 2021). As Figure 1.4 shows, in 2022, EV batteries represented around 60% of lithium, 30% of cobalt, and 10% of nickel demand. Only five years ago, in 2017, these percentages were about 15%, 10%, and 2%, respectively.

[3]Available online: www.iea.org

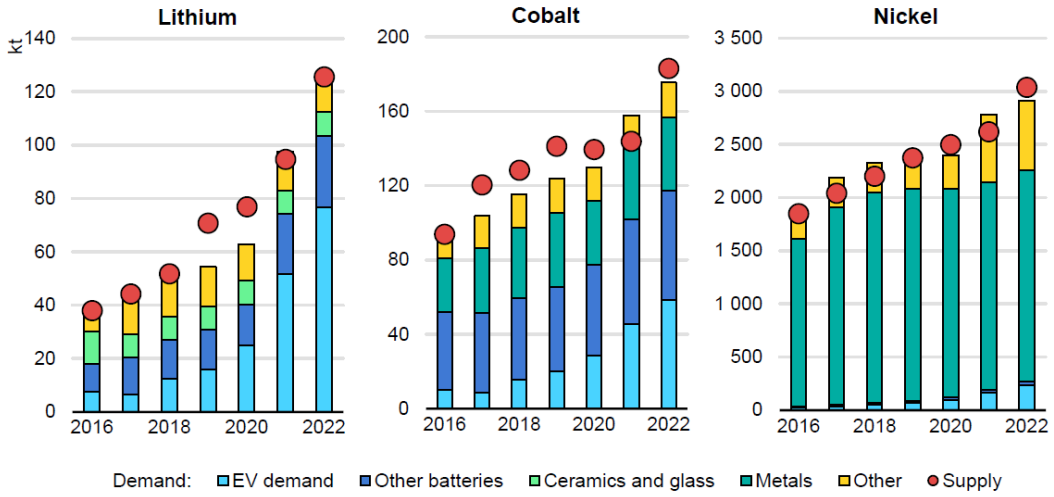

Fig. 1.4 Overall supply and demand of battery metals by sector in the time frame between 2016 and 2022. Note: The metals category includes alloying applications. Supply refers to refinery output and not mining output. Source: IEA. International Energy Agency, Global EV Outlook 2023.

In this global scenario, one can understand how important it is to invest economic and human resources in scientific research to support as much as possible the energy transition, which is increasingly urgent.

1.2 Goal of the dissertation

Under the scenario presented in the previous paragraph, it is clear that the need for better-performing and more sustainable batteries from an environmental point of view will increase considerably in the coming years. In particular, the scientific community is focusing its efforts on the following topics: [1]

- Substitution of critical raw materials (CRM) in the cathode with more sustainable and abundant ones. This is accomplished by the development of low Co-containing NMC (nickel-manganese-cobalt oxide) materials [2], as well as the study of innovative Co-free cathode materials with high capacities, such as Li-Ni-Mn-oxide (LNMO) systems or battery cathodes based on Li-iron phosphate (LFP) [3]

- The development of different anode technologies, where the Li^+ charge carrier is substituted by others ions such as Na^+, Mg^{2+}, Al^{3+}, or Zn^{2+}. [4]
- The development of conversion-based systems such as the Li-sulfur [5] and Li-O_2 [6], which are very promising alternative to Li-ion batteries, since they have very high theoretical capacities and they rely on abundant and unproblematic raw materials.
- The development of all-solid-state batteries (ASSB) could allow for greater storage capacity and safety by replacing the current liquid electrolyte in batteries with a solid ion conductor. With a solid-based system, the usage of lithium metal would be far more accessible, thus increasing the battery's energy density. [7]

Based on the considerations made in the previous paragraphs, the work carried out during my Ph.D. was mainly focused on two aspects of the four just listed above: (I) the synthesis and characterization of high-energy hybrid cathode materials for Li-S batteries and (II) the development of high-voltage cobalt-free cathodes for Li-ion batteries; Figure 1.5 helps to graphically visualize where the work done in these three years fits into the general picture of the various generations of batteries and materials used in the cathodes and anodes of batteries.

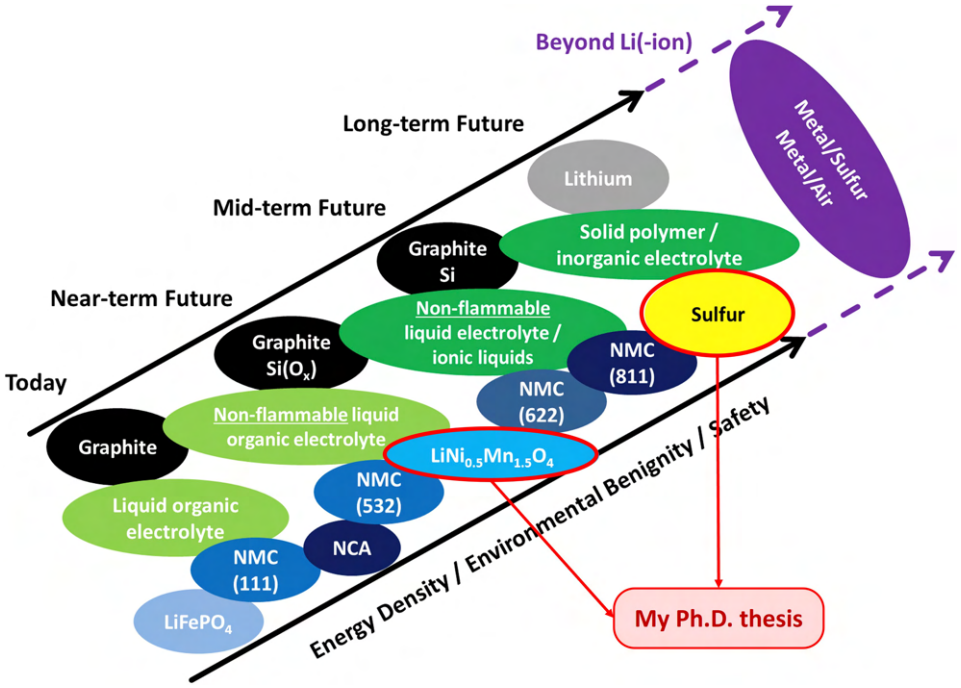

Fig. 1.5 Schematic representation of the technologies and materials currently used in the field of batteries, together with those that will likely be used in the future and those studied during my PhD. Modified from [8]

Chapter 2 provides a comprehensive overview of Li-ion batteries, explaining their operating principles and detailing the main parameters of Li-ion batteries. The chapter also delves into the various materials which are used inside these batteries, with a specific emphasis on the cathode materials.
Chapter 3 delves into Li-S batteries, exploring their operating principles and the significant challenges associated with this technology, as well as the advantages it may provide over traditional Li-ion batteries. Additionally, this chapter emphasizes the development of cathode materials, highlighting their importance in advancing Li-S battery technology.
Chapter 4 is centered on High Entropy Oxides (HEO), starting with a general introduction of the material and its applications in Li-S batteries. The second part of the chapter discusses the synthesis method of the material and its chemical-physical characterization, followed by the preparation of sulfur based electrodes and electrochemical testing.
Chapter 5 discusses a composite material consisting of reduced Graphene Oxide and Zinc Sulfide nanoparticles, which was developed to be used in Li-S batter-

ies. After an initial introduction to the material, the chapter outlines the synthesis method.The chapter continues with a description of the synthesis process, followed by the chemical-physical and electrochemical characterization of the cathodes produced by infiltrating sulfur into the rGO-ZnS.
Chapter 6 marks a departure from the previous ones as it focuses on two cathode materials for Li-ion batteries, LNMO and LFP. These two materials are described in detail from both a structural and electrochemical point of view. The chapter continues with the production of a cathode based on the blending of these two materials through physical mixing. The chapter concludes with the complete chemical-physical and electrochemical characterization of full-cells based on this cathode. The work presented in this chapter is the result of collaboration with several partners (ICSI ENERGY Department, Johnson Matthey, SINTEF) in the context of the European project HYDRA.
The final chapter details the work conducted on the synthesis and investigation of the chemical-physical and electrochemical properties of a high-voltage cathode material for Li-ion batteries, lithium copper manganese oxide (LCMO). The material underwent a chemical over-lithiation process to produce a Li-rich material, which was tested in both half-cell and full-cell configurations. This research was carried out in collaboration with the Commissariat à l'énergie atomique (CEA), where I spent a total of six months during the second year of my doctoral studies.
Finally, a brief chapter summarizes the conclusions and future perspectives in the field of Li-ion and Li-S batteries, providing a summary of the work accomplished and the potential for further research.

Chapter 2

Li-ion batteries

2.1 General overview of batteries

The beginning of the history of the energy storage sector can be fixed in the 18^{th} century (see Figure 2.1 when Alessandro Volta invented his "pila" consisting of alternating layers of zinc and copper (the electrodes), separated by a layer of cardboard soaked in salt water (electrolyte). One could be surprised to discover that the operating principle of the Volta battery is the same that is still found today in every modern battery. At this point, it may be helpful to give a definition of battery: it can be defined as an electrochemical storage device in which energy is stored in chemical bonds [9]. The advantage of batteries lies in the conversion mechanism of the chemical energy: it can be transformed into other types of energy (mechanical, electrical) with minimal heat dispersion, i.e., with high efficiency. Depending on whether or not a battery can be recharged, it is defined as primary (non-rechargeable and converts chemical energy into work only once) or secondary (rechargeable and capable of converting chemical energy into work and vice versa with a quasi-reversible mechanism). Following the significant development of electrical applications in the 19^{th} and 20^{th} centuries, progress was also made in the field of energy storage: in 1854 Gaston Plantè created the lead-acid battery (the first of the secondary type), while in 1899 Jungner developed the Nickel Cadmium (NiCd) battery, which was then improved almost a century later by replacing cadmium (due to its toxicity) with a hydrogen-absorbing alloy, thus also obtaining a higher energy density. However, in

the last 50 years, technological progress and the development of electronic devices have had a boost never seen before.

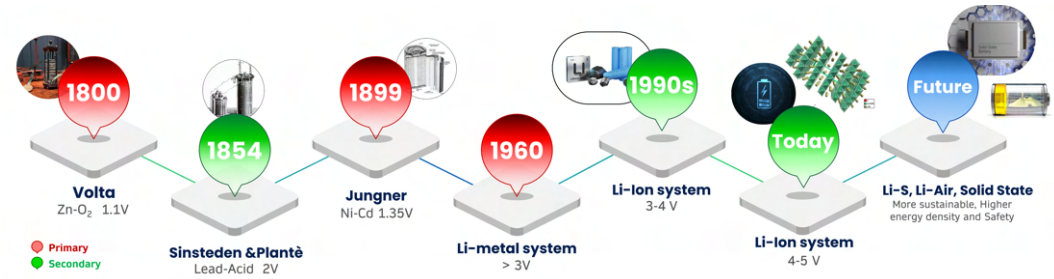

Fig. 2.1 Timeline of the hisory of batteries, from the first prototype developed by Volta to the latest generation of Li-ion devices.

Consequently, the demand for ever more performing batteries has prompted researchers to develop new battery designs and materials.The turning point in the world of batteries is represented by the development of electrochemical devices in which lithium ions are used as internal energy carriers. This step took place for the first time in 1960 when metallic lithium was used as an anode. [10, 11] The primary reason why lithium-based technology is very advantageous is that lithium is the most electropositive element (-3.04 V vs. Standard Hydrogen Electrode). Consequently, using lithium allows for producing batteries with high voltage differences at their terminals. [12] However, due to lithium metal's strong instability and reactivity, this battery design was shelved, and graphite was used as anode material instead, with this transition that took place between the 1980 and 1990. In particular, the first Li-ion battery put on the market was proposed by SONY in 1990, and since then, this type of technology has been continuously studied and improved in all its aspects. On the anodic side, new high-energy conversion materials are being developed, such as silicon. [13] Simultaneously, the cathode materials have evolved from the use of $LiCoO_2$ [14] to more sustainable and higher voltage alternatives such as NMC811 [15] and LNMO."[16] At the same time, an enormous effort is also required in the development of new electrolytes capable of withstanding the high voltages of the new cathodes and guaranteeing a good level of safety (in this sense, ionic liquids [17] and polymeric electrolytes [18] seem to represent the future. However, this work of optimization of Li-ion batteries can never exceed the intrinsic theoretical capacity of the materials that can be used in the electrodes; therefore, it is logical to invest resources in other types of systems, such as batteries based on conversion mechanism or on different types of internal energy carriers. In the first case, the reference is to

Li-S and lithium-air batteries, which, although presenting intrinsic problems that hinder their commercialization, are very promising in terms of energy density (2600 Wh/kg for Li-S and Up to 11140 Wh/kg, including oxygen from the air, for the Li-Air) and environmental sustainability, since Li-S batteries utilize sulfur as the cathode material, which is abundant, inexpensive, and has a lower environmental impact compared to the cobalt and nickel used in Li-ion batteries. Li-air batteries, on the other hand, employ oxygen from the air as a reactant, significantly reducing the need for mined materials and thus minimizing the environmental footprint associated with material extraction and processing. In the second case, systems such as aqueous rechargeable metal batteries, based on using Na^{+}, Mg^{2+}, Al^{3+}, or Zn^{2+} ions and water as an electrolyte, can guarantee better safety and lower costs. However, this type of battery also needs further studies and research to be developed and marketed.

2.2 Battery parameters and terminology

Batteries are characterized by various parameters regarding their electrochemical performance, the materials used or economic data. Consequently, it may be useful to provide a list of definitions of parameters and terms used in the thesis work.

Open-circuit voltage (OCV): The voltage between the positive and negative electrodes when no external current flows (i.e. when there is no load). The chemical potentials of the electrodes are compared to compute it. To get the highest possible value, the chemical potential of the positive electrode should be greater than that of the negative electrode.
Overpotential: During the discharge phase, the overpotential (η) is defined as the difference between the OCV and the cell potential, whereas during the charge phase, it is defined as the difference between the cell potential and its OCV.
Cell capacity: Defined as Q, it is the total energy available in a battery or total charge stored in a battery, measured in ampere-hours (Ah), with 1Ah = 3600 C. It is essentially the amount of current that the battery can supply over a certain time period. As a result, the higher the current, the more power may be discharged. The capacity stored/released in a battery between two instants t1 and t2 is defined by Equation 2.1:

$$Q = \int_{t1}^{t2} I(t)dt \tag{2.2.1}$$

Equation 2.2 can be used to calculate the theoretical capacity Qt, which is equal to the maximum electric charge from the cell, depending on the quantity of active material present inside the cell:

$$Q = x \cdot n \cdot F \tag{2.2.2}$$

Where n represents the number of equivalent electrons involved in electrochemical reactions, F is the Faraday constant and x is the mole of active material in the electrode. The specific capacity of a battery is defined as the amount of charge that a battery can accumulate/deliver per unit of mass (Ah g^{-1}).

C-Rate: The C-rate is a measure of how quickly a battery gets charged (or discharged) in comparison to its maximum capacity. This feature is related to the time necessary for the cell to fully charge/discharge. A charge at C/5 and 2C, for example, means that the charging current is such that the time required to fully charge the cell is 5 and 0.5 hours, respectively.

Coulombic efficiency: The coulombic efficiency, Y, is the ratio between the capacity supplied by the cell during the discharge ($Q_{discharge}$)step and the capacity stored in the same cell (Q_{charge}) during the charge phase:

$$Y = \frac{Q_{discharge}}{Q_{charge}} \tag{2.2.3}$$

Energy: The energy (E) that an electrochemical power source can provide, given in Joule (J) or, more typically, Watt hour (Wh), is linked to capacity and voltage by the equation:

$$E = Q \cdot V \tag{2.2.4}$$

State of charge (SOC): A measure of how much capacity or power is left in a battery. In particular, the SOC measures how much is left after a specified period of time for a particular application. Namely: The ratio of stored energy in a storage system (kWh) to its usable capacity (kWh).

Depth of discharge (DOD): The ratio of discharged energy (kWh) to usable capacity (kWh) **Cut-off voltage**: The final voltage between two electrodes during the complete charge or discharge process.

Cycle life: The number of (equivalent) full cycles that can be delivered by a storage system until its end of life, under given conditions where the Equivalent full cycle: The ratio of overall energy throughput (kWh) to the usable capacity (kWh).
Self-discharge: Self-discharge is the loss of a battery's capacity under open-circuit circumstances caused by internal chemical processes and/or short-circuits.

2.3 Li-ion battery fundamentals

Nowadays, Li-ion batteries represent the state-of-the-art of the electrochemical storage devices. Thanks to their high efficiency, gravimetric energy density, high operating voltage and relatively simple design, they are widely used in numerous applications, such as electric cars and electronic devices. The term battery derives from the fact that it is made up of several fundamental power elements (cells, see Figure 2.2 for a schematic representation of a Li-ion cell) assembled together in various possible designs.

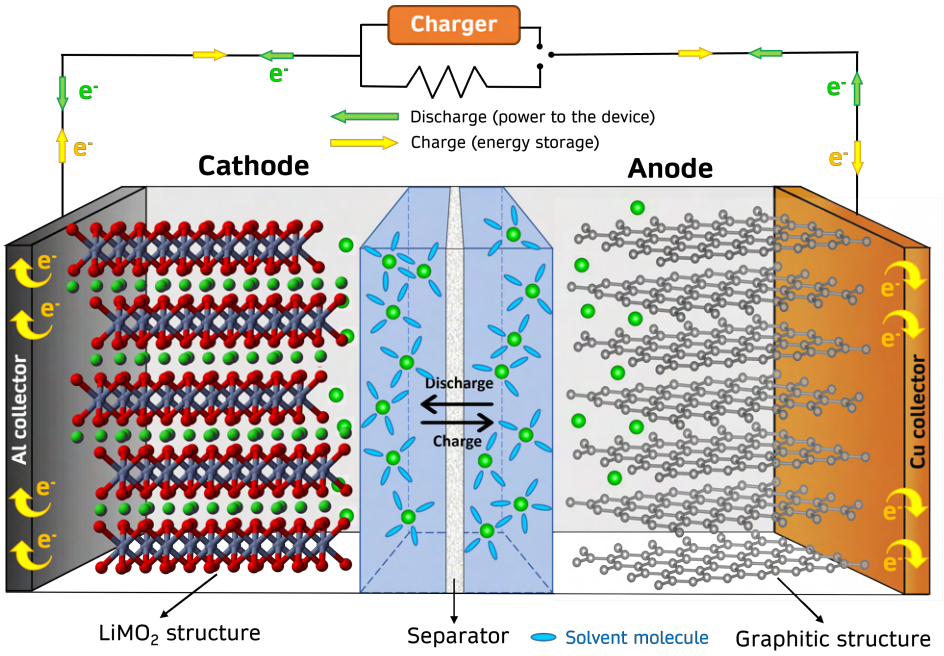

Fig. 2.2 A schematic representation of the structure of a typical Li-ion cell.

The fundamental components of any rechargeable battery (and consequently this also applies to Li-ion) are four: [19]

- **Cathode (Positive Electrode)**: Generally composed of lithium metal oxide; it is the electrode at which the reduction reaction occurs and electrons are captured. During the charge process, Li^+ ions flow from the cathode to the anode via the electrolyte, and electrons flow via the external circuit. During discharging, electrons go from the anode to the cathode via the external circuit, while Li^+ ions migrate back to the cathode via the electrolyte. Therefore, the cathode undergoes reduction during discharging and oxidation during charging, depending on the operating conditions.
- **Anode (Negative Electrode)**: Generally made up of carbon; it is the electrode at which the oxidation reaction occurs and electrons are released. During the charge process, the anode receives Li^+ ions from the cathode via the electrolyte and releases electrons via the external circuit. During discharging, the anode releases Li^+ ions back to the cathode and provides electrons to the external circuit. Hence, the anode undergoes oxidation during discharging and reduction during charging, depending on the operating conditions.
- **Electrolyte**: Usually a lithium salt in an organic solvent; the primary role of the electrolyte is to guarantee the mobility of the Li^+ ions, so that they can migrate, through the separator, between the anode and the cathode.
- **Separator**: Composed of an electronically insulating material (typically, glass fiber or polyethylene), in order to avoid short-circuiting the cell, but which allows the passage of ions.

The energy storage mechanism of Li-ion batteries is quite straightforward. As a result of the ease with which lithium ions and electrons may be transported back into the negative electrode, LIBs are rechargeable. [20] These movements of the lithium ions are also sometimes referred to as the “rocking chair” effect or as “shuttling” of lithium ions due to the back-and-forth nature of the reactions.
It is important to underline that the reduction reaction always takes place at the cathode (positive electrode) and the oxidation reaction always takes place at the anode (negative electrode). This means that during charging, the cathodic (reduction)

reaction occurs at what is referred to as the anode since it oxidizes and releases electrons. In contrast, the anodic (oxidation) reaction takes place at the cathode since it reduces and gains electrons. When the cells switch to discharging, the cathodic reaction takes place at what we would consider the cathode, as it is here that the electrons are gained as they follow the circuit from the anode side, where an anodic oxidation reaction occurs to release these electrons. In conclusion, both electrodes cover the roles of anode and cathode depending on the operating conditions (charge/discharge) of the cell.

These movements of the lithium ions are also sometimes referred to as the "rocking chair" effect or as "shuttling" of lithium ions due to the back and forth nature of the reactions.

The first lithium ion battery, which employed $LiCoO_2$ as the cathode and graphite (C) as the anode, was invented by SONY in 1991, thanks to the joint efforts of research carried out in previous years by John Goodenough, Stanley Whittingam, and Akira Yoshino, who received the Nobel prize for chemistry in 2019. In particular, Whittingam discovered the titanium disulfide (TiS_2), an exceptionally energy-rich compound that was utilized to build new intercalation cathodes in lithium-metal batteries [21]; Goodenough concentrated on the study of layered oxides (general formula $LiMO_2$, with M = Co, Ni or Mn) as cathode materials, while Yoshino studied in depth the anodic part of the cell, discovering the great suitability as anode material of several carbonaceous materials. [22]

The cell based on $LiCoO_2$ and graphite was able to provide high energy density (180 Wh kg^{-1}), high discharge potential (3.7 V) and long cycle life. Furthermore, due to the fact that lithium was already incorporated into the structure of the cathode material, the safety level was also increased compared to cells based on lithium metal as anode.

The reaction mechanism occuring in the $LiCoO_2$/C cell is described by the following equations:

$$\textbf{Cathode side: } Li_{(1-x)}CO_2 + xLi^+ + xe^- \rightleftharpoons LiCO_2 \tag{2.3.1}$$

$$\textbf{Anode side: } Li_xC_6 \rightleftharpoons 6C + xLi^+ + xe^- \tag{2.3.2}$$

$$\textbf{Overall reaction: } Li_xC_6 + 2Li_{(1-x)}CO_2 \rightleftharpoons 6C + 2LiCO_2 \tag{2.3.3}$$

To move electrons from the anode to the cathode, some form of energy potential must promote this process. The major driving factor for LIBs is the gradient of the electrochemical potential of Li between the anode and cathode. In particular, Li^+

ions reversibly move between two electrodes in a 'rocking chair' mechanism without significant structural change for the hosting materials. The concentration of lithium ions in the electrolyte remains constant regardless of the degree of charge or discharge. However, it fluctuates with charge and discharge states in the cathode and anode. The driving force that pushes the alkali ion and electrons from one electrode to the other is the battery voltage (E). In particular, according to the second law of thermodynamics and Nernst equation, the voltage is proportional to the Gibbs free energy.

$$\Delta G = -nFE \tag{2.3.4}$$

Where Δ G is the variation in Gibbs free energy due to the reaction during the discharge/charge process, n is the number of electron transferred and F is the Faraday's constant (96485.3 C mol^{-1}). Considering the definition of free energy,

$$\Delta G = \Delta H - T\Delta S \tag{2.3.5}$$

And comparing both equations,

$$V = \frac{\Delta H - T\Delta S}{nF} \tag{2.3.6}$$

Introducing the change in internal energy, ΔU_{int}, the pressure P and the variation in volume change ΔV, we obtain,

$$\Delta G = \Delta U_{int} - P\Delta V - T\Delta S \tag{2.3.7}$$

Thus, at low temperatures, the variation of internal energy U_{int} is considerably higher compared to the other thermodynamic parameters, that can be consequently neglected. Therefore,

$$\Delta G = \Delta U_{int} \tag{2.3.8}$$

Thus, the voltage of a battery can be estimated in terms of a change in Gibbs free energy owing to the Li^+ intercalation process depending on the concentration of the intercalated ion (x), and is represented as:

$$\Delta V(x) = \frac{\Delta G(x)}{\Delta x} = \frac{\Delta U_{int}(x)}{\Delta x} \tag{2.3.9}$$

Where Δx is the variation of Li^+ concentration during the de/intercalation process. Considering equation 2.8, the equilibrium potential of a battery is given by:

$$V(x) = -\frac{\Delta G(x)}{nF} \tag{2.3.10}$$

Considering a particular state of charge where the lithium concentration is x (relative to the initial value x_0), the Gibbs free energy for a battery results from the combination of the free energy of the cathode (G_C) and the anode (G_A).

$$\Delta G(x) = [G_C(x) - G_C(x_0)] - [G_A(x) - G_A(x_0)] \tag{2.3.11}$$

The total number of electrons (n) is determined by the valence of the working ion (z), where F is Faraday's constant.

$$n = zF(x - x_0) \tag{2.3.12}$$

Consequently, the voltage of the battery con be expressed as follow

$$V(x) = -\frac{[G_C(x) - G_C(x_0)] - [G_A(x) - G_A(x_0)]}{z(x - x_0)F} \tag{2.3.13}$$

By introducing the definition of chemical potential ($\mu = \delta G/\delta x$) in equation 2.17, we obtain:

$$V(x) = -\frac{\mu_C(x) - \mu_A(x)}{zF} \tag{2.3.14}$$

Consequently, the theoretical potential of the cell at equilibrium is directly proportional to the difference between the chemical potentials of lithium at the cathode and anode. This potential, also known as V_{oc} or OCV (open circuit potential, i.e. when no current is passing through the external circuit) is a fundamental parameter of a battery, since the higher it is, the higher the energy stored inside of the battery. [23] [24] However, the considerations just made are valid on a theoretical level. Still, on a practical level, the reaction mechanisms inside a battery are often complicated, deviating behavior from the ideal one. For example, in this discussion, the electrolyte has been considered a passive component that plays the sole role of Li-ion carrier, with only the electrodes involved in redox reactions. In reality, there are often parasitic reactions involving the electrolyte. Furthermore, although it is desirable to increase the cell working voltage as predicted by equation 2.18, the electrolyte's electrochemical stability voltage window must be considered. In particular, the relative electron ener-

gies in the electrodes and electrolyte of a thermodynamically stable battery cell with an aqueous electrolyte are displayed schematically in Figure 2.3. The cathode plays the role of the oxidant, and is characterized by an electrochemical potential μ_C, the anode is the reductant (with an electrochemical potential μ_A) and the "electrolyte's window" is the energy separation Eg of the lowest unoccupied molecular orbital (LUMO) and the highest occupied molecular orbital (HOMO). In general, a cathode with a μ_C below the HOMO oxidizes the electrolyte unless a passivation layer blocks electron transfer from the electrolyte to the cathode; similarly, and anode with a μ_A above the LUMO reduces the electrolyte (unless a passivation layer on the surface of the anode material is formed). Therefore, the operating voltage of the battery must lie within the electrolyte's window stability; otherwise, a continuous parasitic reaction will occur between the electrodes and the electrolyte, with consequent consumption of active material. [25]

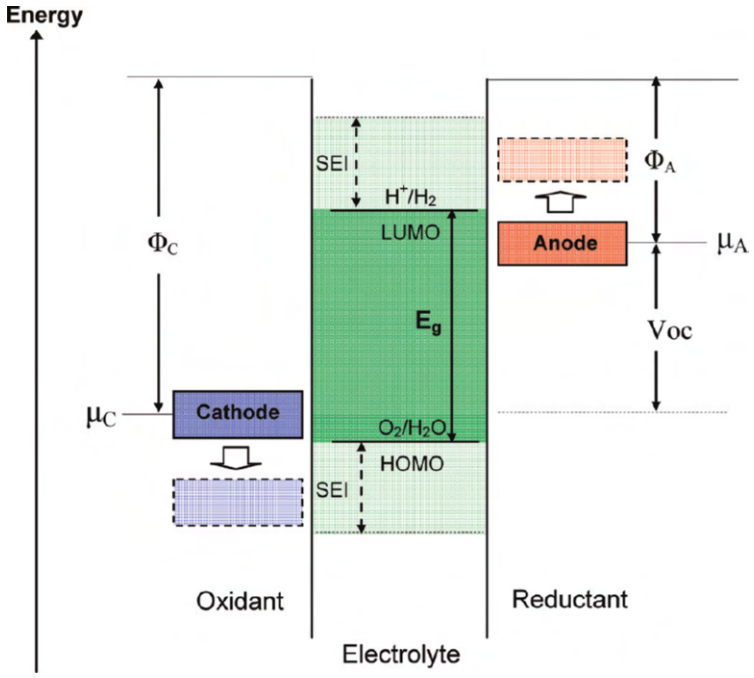

Fig. 2.3 Schematic open-circuit energy diagram of an aqueous electrolyte. ϕ_A and ϕ_C are the anode and cathode work functions. E_g is the window of the electrolyte for thermodynamic stability. A system with $\mu_A >$ LUMO and/or $\mu_C <$ HOMO can be thermodinamically stable only if passivation layer (Solid Electrolyte Inteface, SEI) that separates the electrodes and the electrolyte is formed. Reproduced from [25]

When an electric charge is delivered across battery terminals, the voltage response evolves with a non linear behavior due to complicated electrochemical events such

as polarization-diffusion, and double layer formation. Notably, an equivalent cicuit model as the one depicted in 2.4, known ad Thevenin model, can be used to represent a battery. By including resistors, voltage sources and capacitors, this model helps to understand the mechanisms and phenomena that occur inside the cell. In particular, the Thevenin model implements an ideal voltage source (Voc) to define the battery open-circuit voltage, R_o represents the ohmic internal resistance of the battery, R_p is used to describe the polarized internal resistance, C_p is the polarized capacitance used to describe the transient response during charging and discharging and V_t is the terminal voltage of the battery. [26, 27]

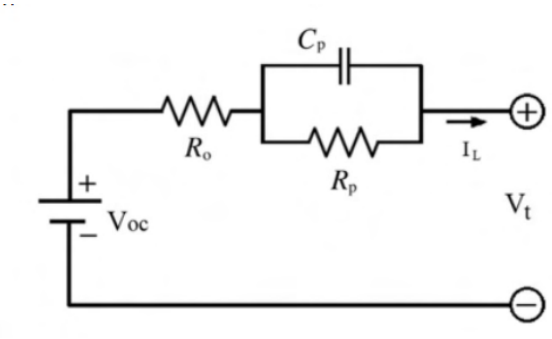

Fig. 2.4 The equivalent circuit based on Thevenin model, used to interpret the phenomena occuring in the battery through electrical components. [26]

Once the external circuit is closed and the current starts to flow, the V_{oc} is lowered by polarization effects, and the terminal voltage results to be:

$$V_t = V_{oc} - I \cdot R_0 - V_p \tag{2.3.15}$$

Where V_p is the voltage across the R_p element. Equation 2.3.15 is meaningful because it highlights that the polarization of the electrodes lowers the cell potential in operating conditions. Consequently, the chemical energy stored in the cell is not totally converted into electrical energy, but a part of it is dispersed as heat. In more detail, there are three main forms of polarization in a cell (see Figure 2.5:

- **Activation polarization:** The term refers to the several retarding variables inherent in the kinetics of an electrochemical process, such as the work function that ions must overcome at the electrode-electrolyte interface.
- **Ohmic polarization:** this terms is caused by the internal resistance of all components in the lithium battery. It is proportional to the current that flows

in the battery and is affected by the loss of contact between the components of the battery and the electrolyte resistence.

- **Concentration polarization:** This factor takes into account the resistance faced by the mass transfer (e.g. diffusion) process by which ions are transported across the electrolyte from one electrode to another.

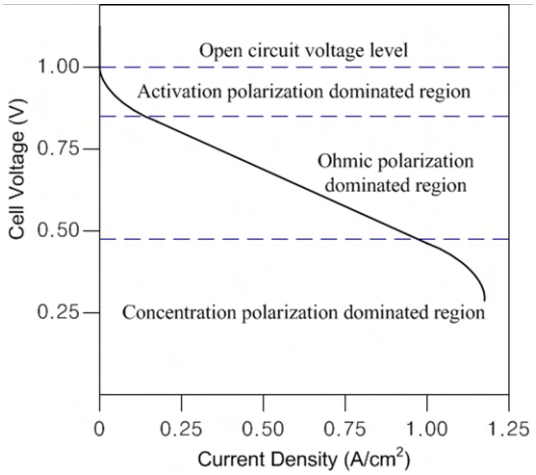

Fig. 2.5 Schematic representation of the three different polarization which typically affect an operating cell during the discharge process. Reproduced from [28]

All three forms of polarization govern the impact of the current rate on the cell voltage in practical batteries, and a range of experimental approaches are employed to analyze internal electrochemical processes. For example, one of the most common and useful is the analysis of the characteristic current vs voltage profile of the charge/discharge curve, which allows to evaluate the specific capacity of the cell and the value of polarization in unction of the applied current (C-rate) or temperature. At this point it can be pointed out that the performance of a battery are mainly related to the chemistry of the system (for example the valence of the ion carrier or the specific capacity of the active materials directly affect the available energy of the cell), but also other features such as the cell design, the type of electrolyte employed and its conductivity, the electrodes manufacturing, greatly influence the efficiency of the whole device.

2.4 Materials for LIBs and limitations

Active materials are the fundamental components of the cell, as they are primarily responsible for the energy storage and conversion mechanisms on which batteries are based. There are different types of materials [29], both cathodic and anodic, which are characterized by peculiar characteristics (such as, for example, the voltage at which they operate, their specific capacity, the reaction mechanism with which they can be lithiated and de-lithiated), and which consequently make them preferable or not for specific applications. However, other materials are also present in a cell, which, although not directly involved in the redox reactions, play fundamental roles in ensuring the correct functioning of the battery. In particular, they are the conductive carbons as additives, the binder (generally polymeric), and obviously the electrolyte. In the following subsections, each of these categories will be explored in depth.

2.4.1 Anode materials

The anode material of a Li-ion cell represents the "host" structure for the lithium ions when they are forced to leave the cathode material during the discharge process. The anode is composed of active particles mixed with small quantities of polymeric binder, ensuring contact with the current collector, which is most often copper. In simpler terms, the anode is usually identified with the negative side of the battery. The first requirement is that it can intercalate and de-intercalate large quantities of lithium ions in a reversible way without the material's structure being considerably damaged. Secondly, the material must have high electronic and ionic conductivity to ensure good kinetics of the redox reactions at the electrolyte interface. Thirdly, its redox potential with respect to Li/Li^+ must be as low as possible to maximize the operational potential of the cell and, consequently, the energy that can be stored in it. Fourth, the optimal anode must have a high specific capacity, both gravimetric (mAh/g) and volumetric (mAh/cm^3). Fifth, it must be thermally and chemically stable so it does not dissolve in the electrolyte. Finally, the anodic material should be as abundant as possible in nature, non-toxic, and easily available. [30]. Ideally, the gold standard for anode materials is represented by metallic lithium since it has a high specific capacity (3860 mAh/g) and energy density (11425 Wh/kg), a value very close to that of gasoline, 11860 Wh/kg. Furthermore, lithium exhibits the lowest

standard electrode potential (-3.045 V vs. SHE) and high electronic conductivity. However, despite these exceptional properties, lithium still has substantial drawbacks that require further research to ensure its use in commercial batteries. One of the most significant drawbacks of lithium metal is that it is prone to generate lithium dendrites, which can pierce the separator or solid electrolyte and cause an internal short circuit, as shown in Figure 2.6. Aside from the short circuit threat, lithium plating affects cell capacity and cycle life because producing these dendrites consumes lithium that would otherwise take part in redox processes. Furthermore, it is possible that the dendrites detach from the main lithium electrode, thus losing electrical contact and being passivated by the reaction with the electrolyte. This mechanism leads to the formation of the so-called "dead lithium". Another issue with lithium metal is its high reactivity, which can be dangerous because the organic solvents commonly employed in electrolyte composition are not particularly stable in the presence of strong lithium activity. [31]

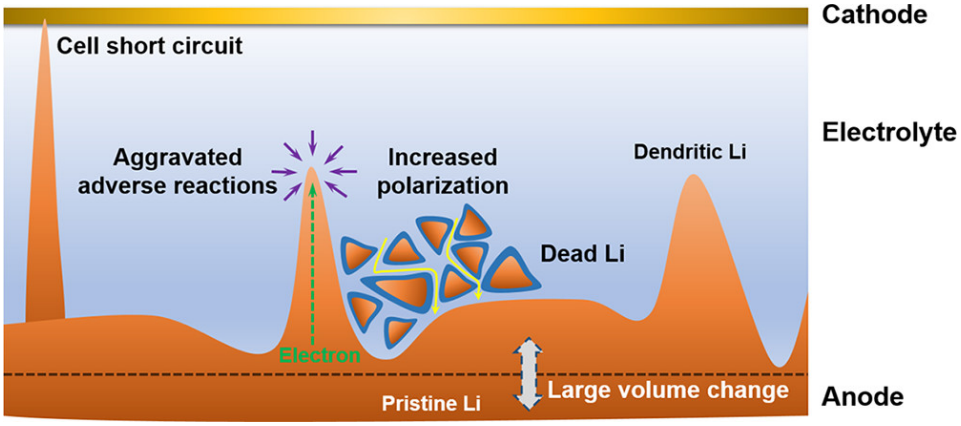

Fig. 2.6 Schematic representation of the dendrite mechanism formation on lithium metal anode. Reprinted from [32]

However, researchers are investing increasing efforts and resources to solve these problems related to lithium metal anode, for example, by developing solid electrolytes (polymeric or ceramic, generally), which significantly reduce the possibilities of short circuit and thermal runaway.
A part from metallic Li, several distinct types of anode materials have been discovered and improved after decades of research. So far, LIB anode materials can be classified into three groups based on their reaction mechanisms: intercalation, conversion and alloying anode materials. In Figure 2.7a the main anode materials

and their related structures (Figure 2.7b) are shown and classified into these three categories: the intercalation type materials exploit the "rocking-chair" mechanism already mentioned and include carbonaceous materials (e.g., graphite) and transition metal oxide (e.g., Ti-based oxides and Nb-based oxides); alloy-typed materials are mainly metallic (Sn, Sb and Bi, etc.) and semimetallic (Si, Ge and P) materials of the IVA and VA groups, which can react with numerous lithium ions (thus providing high specific capacities) to form metal alloys. [33]

Intercalation-type anodes:

Graphite is the most common and well-studied carbon-based anode material with a layered structure, thanks to its relatively low cost, good capacity and low operating voltage. In graphite, carbon atoms are hybridized sp^2 to produce a graphene layer with a layer spacing of 0.335 nm. Van der Waals forces and π interactions stack these graphene layers on top of one other to generate the typical 3D structure of graphite.

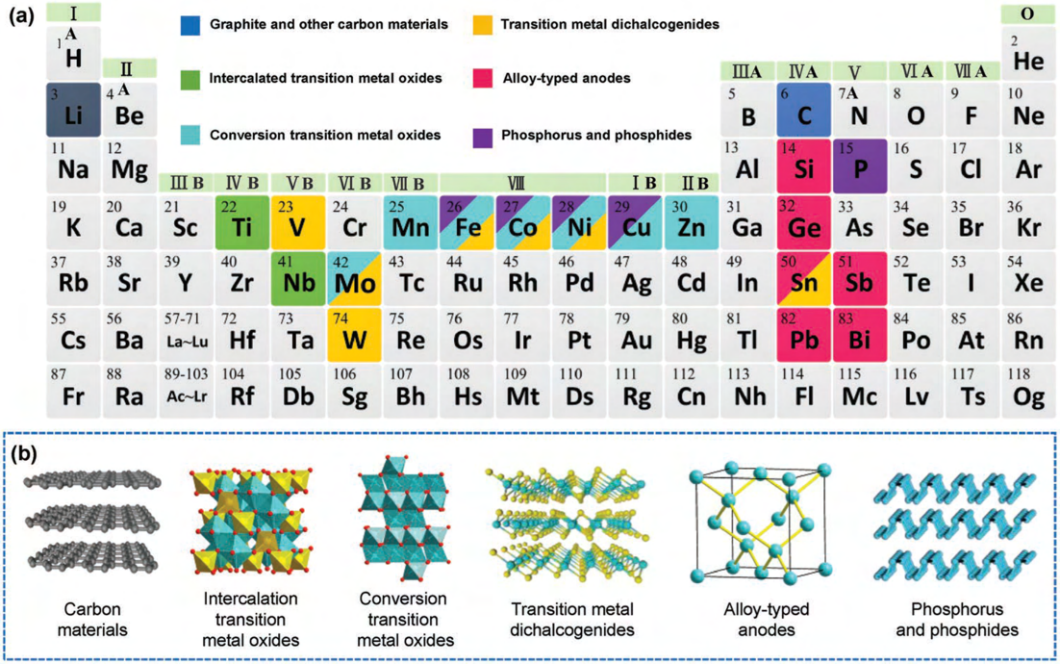

Fig. 2.7 (a) Elements that are mainly utilized to produce anodes in Li-ion batteries, (b) the inherent structures of the materials employed as anode materials. Reprinted from [34]

Graphite is markedly anisotropic, having much higher electrical and thermal conductivity on its basal plane than on its end faces (the plane that is perpendicular to the c-axis). The unique structure of graphite allows lithium ions to be embedded

and detached without severely damaging the two-dimensional reticular structure of graphite. [35] The lithium ion storage mechanism that occurs in graphite, which is reversible, can be described by:

$$Li_xC_n \rightleftharpoons xLi^+ + xe^- + C_n \tag{2.4.1}$$

During the charge step, Li^+ ions are incorporated in the graphite interlayer, leading to the formation of a lithium rich phase, LiC_x ($x \leq 6$) which is characterized by an increased layer spacing (from 0.335 nm to 0.370 nm) and volume (no more than 10%) [36]. It is often accepted that the maximum density of Li^+ in the graphitic structure is one ion for six carbon atoms, thus leading to a specific capacity of 372 mAh g^{-1}. However, graphite has some substantial issues: it has sluggish lithium intercalation kinetics and a low lithiation voltage (0.08 V versus Li/Li^+). Large polarization under high current circumstances (more than 1C) will drive the graphite potential to the lithium metal deposition threshold (0 V versus Li/Li^+), resulting in lithium plating on the graphite surface. The accumulated lithium metal can easily react with the electrolyte leading to the formation of dead lithium, thus increasing internal resistance and rapidly depleting battery capacity. In the recent past, several strategies have been adopted to modify the graphite to overcome its inherent problems. Cheng et al. [37] used KOH etching to achieve 3D diffusion of Li^+ in the graphite structure, which exhibited increased electrochemical performances. Another way to increase the mobility of Li^+ ions is to expand the layer spacing of the graphite. For example Kim et al. [38] modified natural graphite with a step of oxidation under mild condition, followed by a regraphitizing step through thermal reduction. As result, the layer spacing expanded from 0.3359 nm to 0.3390 nm and thus increasing the ion transport by reducing the kinetic barriers for Li^+ motion in the bulk graphite. Another approach is to modify the surface of the graphite to optimize the solid-electrolyte-interphase (SEI) structure, in order to get a SEI with higher ionic conductivity and better mechanical properties. In this sense, several materials have been used to produce coating on graphite, such as polymers [39] and ceramics.[40] Other interesting carbonaceous materials are the so-called hard carbons (which partially graphitize at high temperatures. These carbons are mostly amorphous, and the Li intercalation mechanism is different from graphite, as they have a "house of cards" structure with a short-range graphitized domain, numerous pores and voids, and edges rich in functional groups. The lithium ions can, therefore, be partly intercalated between the graphitic layers and partly adsorbed on the functionalized edges of the

material and in the pores. This particular structure gives hard carbons a higher gravimetric capacity than graphite; however, they also exhibit poor initial coulombic efficiency (ICE) and a high irreversible capacity loss. [41]
Another intercalation material widely investigated in the literature as an alternative to graphite is lithium titanate oxide ($Li_4Ti_5O_{12}$, LTO), which has a spinel structure. During the lithiation process, the Ti atoms are first reduced from Ti^{4+} to Ti^{3+} (at around 1.5V), thus forming a rock-salt structure of $Li_7Ti_5O_{12}$), which is further lithiated in a second step (which takes place at around 1 V vs Li/Li^+), forming $Li_9Ti_5O_{12}$. The reaction, described by equation 2.4.2, can deliver 175 mAh g^{-1}.

$$Li_4Ti_5O_{12} + 5e^- + 5Li^+ \rightleftharpoons Li_9Ti_5O_{12} \tag{2.4.2}$$

This material has the peculiarity of having an extremely stable structure during the lithiation processes and relative phase change, accompanied by a volume variation of only 0.77%. Furthermore, the working potential of LTO (1.5 V vs Li/Li^+) allows for avoiding the lithium plating phenomenon typical of graphite. However, the poor electrical conductivity (10^{-13} S cm^{-1}) resulting from its wide bandgap and slow Li^+ diffusion rate prevents its large-scale application, especially where fast charging is required.

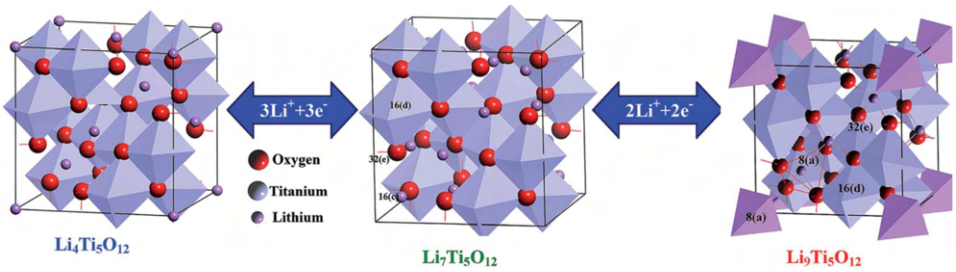

Fig. 2.8 Structure evolution of LTO during the lithiation process, reproduced from [42]

Alloy-typed anodes:

Alloy-typed anodes are made of metallic (Sn, Sb and Bi) and semimetallic (Si and Ge) materials of the IVA and VA groups, which can form alloys with numerous lithium ions, thus ensuring high specific capacities. Of all the alloy-typed materials, silicon is the most interesting and studied one. Consequently, it will be explicitly treated as a representative of this class of materials. Silicon has many characteristics that potentially make it the ideal candidate as an anodic material: it forms stable oxides, and more importantly, it is capable of storing four lithium ions for each

silicon atom (when, for example, in the case of graphite, the ratio was one ion for six carbon atoms). Consequently, the theoretical gravimetric energy density of about 4200 mAh g^{-1}, is about ten times that of graphite, while its volumetric energy density is about three times greater. Furthermore, silicon is abundant in nature and does not present critical environmental issues and its price per ton ($ 1284), according to the 2015 Minerals Yearbook, is competitive with that of graphite ($ 1360). However, pure silicon cannot be used as an anode material since, during the lithiation reaction (equation 2.4.3) it undergoes a volume increase of 320%, a value not compatible with any cell design.

$$Si + 4.4Li^{+} + 4.4e^{-} \rightleftharpoons Li_{4.4}Si \tag{2.4.3}$$

Consequently, to limit the effects of this high volumetric variation, it is often blended with graphite in percentages that typically range from 2% to 20%. The silicon expansion during cycling is not only a volumetric problem in the strict sense, but it causes a battery failure mechanism that drastically reduces its cycle life and capacity. In particular, as shown in Figure 2.9, when lithium reacts with Si, the volumetric expansion causes the Si particles to move away from each other and the current collector, thus causing the electrical contact to be lost. In subsequent contraction and expansion cycles, these particles undergo a microfracture process, as shown in Figure 2.9. This process damages the SEI, allowing fresh electrolyte to penetrate the cracks and come into contact with pure silicon, which reacts to form new SEI. The process is repeated at each charge/discharge cycle, resulting in a thickening of the SEI and a continuous consumption of electrolyte (and lithium). These, in turn, cause an increase in cell resistance and a decrease in electrochemical reactivity. Ultimately, this continuous cycle of contraction, breakdown of the SEI, and new expansion leads to the breakdown of the silicon into smaller and smaller particles, a process known as pulverization. When the particles are sufficiently small and surrounded by electrically insulating SEI, the material can be considered "dead," with a permanent loss of capacity and a consequent reduction in the cell's cycle life.

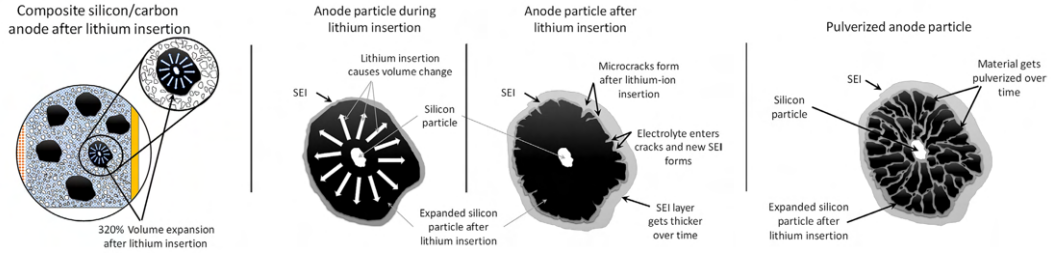

Fig. 2.9 Mechanism of degradation of the Si particles upon cycling, due to the expansion/contraction and the continuous fracture and thickening of the SEI, modified from [43]

Consequently, the studies carried out in recent years on silicon have primarily focused on how to alleviate this expansion problem. In particular, it has been shown that there is a critical particle size (150 nm) below which the microfracture of the particles is much less pronounced. [44] Furthermore, numerous porous materials, such as hollow tubular and mesoporous network structures, have been investigated to provide silicon with stable interfaces to mitigate its expansion during cycling. [45] Another interesting approach is using silicon oxide (SiO_x, with x < 2) instead of pure silicon due to its lower production cost and volumetric variation. In particular, lithium silicate (such as Li_4SiO_4 and $Li_2Si_2O_5$) and lithium oxide (Li_2O) may effectively reduce the volume change of SiO_x, especially during the early lithiation process, thus enhancing the cycling stability. [46]

Conversion-typed anodes:

The last class of anode materials is mainly composed of metal oxides, sulfides fluorides, selenides M_aX_b (where M=Mn, Fe, Co, Ni, Cu and X=O, S, F, Se) which, during the lithiation process, react with lithium ions through a redox reaction to form Li_nX and metals pristine elements. Li_nX and M can be reconverted to Li and M_aO_b again in the delithiation process: [47]

$$M_aX_b + (b \cdot n)Li^+ + (b \cdot n)e^- \rightleftharpoons bLi_nX + aM \tag{2.4.4}$$

Li_nX formation, as shown in Figure 2.10, is thermodynamically viable in this equation. On the contrary, the delithiation reaction (i.e. dissolution of Li_nX) is markedly less favored due to the electrochemical inactivity of the Li_nX species. For this reason, the presence of electroactive metal nanoparticles which favor the conversion reaction is crucial for the reversibility of the system. The reaction mechanism, is generally capable of providing high theoretical capacities (600-1000 mAh g^{-1}) depending on the transition metal present in the M_aX_b. Generally, these conversion materials are

easy to prepare and abundant in nature, although their environmental compatibility is undoubtedly lower than that of graphite or silicon.

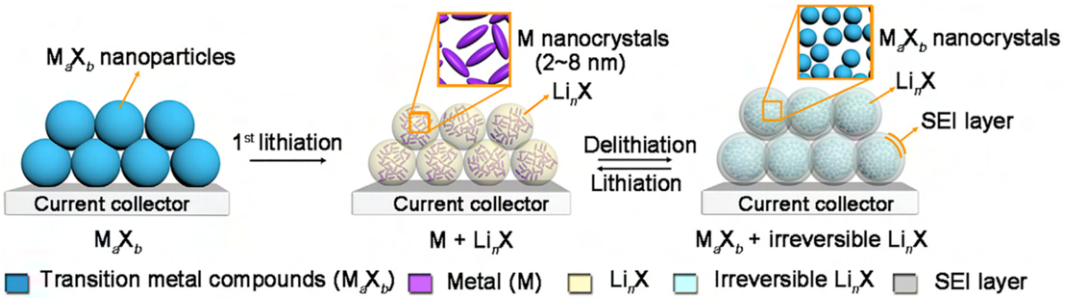

Fig. 2.10 Typical reaction conversion mechanism of anode metal oxides, reproduced from [48]

Most transition-metal compounds have reaction potentials regulated by the ionicities of M-X bonds that vary between 0.5 and 1.0 V against Li/Li^+ , making them good candidates as anodes. [49]In particular, the latter feature of these material is beneficial to avoid the nucleation and growth of the dendrites, a pivotal problem for a safe anode material. Nevertheless, conversion-type anode materials still face significant challenges because of intrinsically poor electronic and ionic conductivity, which translates into low rate capability performance. Moreover, these materials exhibit relatively large volume expansion (<200%), leading to pulverization issues and continuous electrolyte consumption; [50] finally, the electrolyte can undergo decomposition process due to the highly active M nanoparticles generated during the lithiation step. Over the last two decades, enormous efforts have been undertaken to cope with the mentioned problems of conversion-type materials. In particular, a strategy that has proven successful in this sense is nanoengineering. [51] In general, it has been shown that decreasing the size of the active material increases the reversibility of the conversion reaction because the metal nanoparticles formed during the lithiation step exhibit an enhanced electrochemical activity toward the decomposition of Li_nX. Furthermore, electrodes with nano-sized active materials exhibit a shorter diffusion length, a factor that helps take on the poor conductivity of these materials, thus ensuring better performance at high C-rates. In particular, Wu et al. [52] demonstrated that the introduction of 1D and 2D nanostructures significantly improved the electronic conductivity of the electrodes. At the same time, three-dimensional (3D) hierarchical porous structures and hollow structured nanomaterials can alleviate the problem of the volumetric expansion of the conversion-typed materials. [53]

2.4.2 Conclusions and future perspective for anode materials

To summarize, over the last twenty years, graphite has been developed and optimized as an anode for commercial LIBs, and its electrochemical performances are now close to the theoretical ones of the material, which, however, has intrinsic limitations such as the poor performance at C-rates above 1C and lithium plating. Consequently, as illustrated in the previous paragraphs, alternative materials have been developed in recent years. The radar plot reported in Figure 2.11 compare the main characteristics of the classes of materials discussed above. In particular, it can be noted that none of the families of materials can cover all the requirements of an ideal anode material: intercalation transition metal oxides (TMOs) lack high specific capacity, while TMOs that exploit the conversion mechanism perform well in every considered area of Figure 2.11, but they do not excell in any of them. Alloy-type materials, on the other hand, have a very high specific capacity, however, their cycle life must be significantly improved so that they can be used in commercial cells. [54]

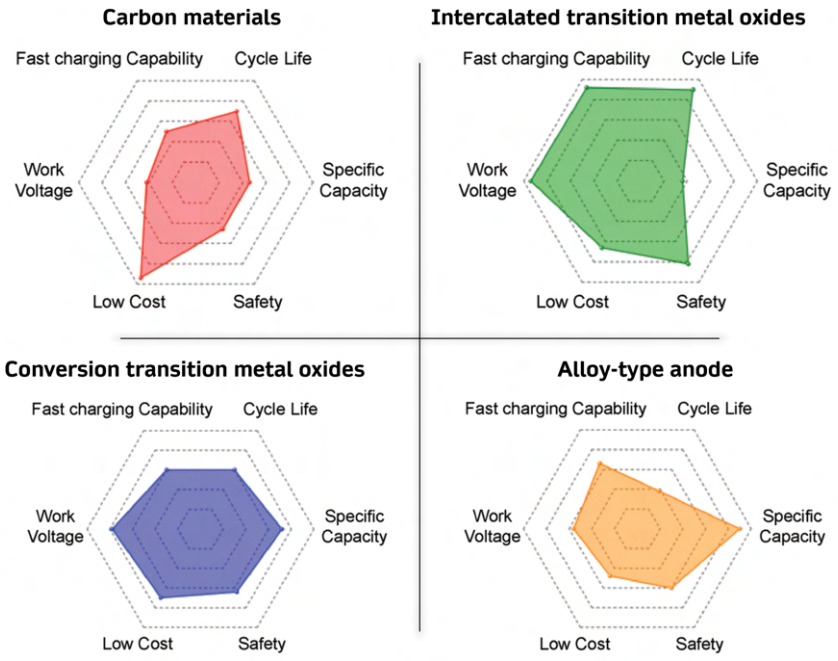

Fig. 2.11 Radar plot comparing the cycle life, specific capacity, safety, cost, work voltage and fast charging capability of the families of material discussed in the anode material's section. Modified by [55]

Consequently, while waiting for significant improvements in solid state technologies, which could make the use of metallic lithium possible, the idea of using an anode composed of different active materials appears to be very interesting for the next generation of batteries.

2.5 Cathode materials for LIB batteries

The cathode of a Li-ion battery is commonly referred to as the "positive side/electrode" of the cell and is generally made up of four main components: (I) the current collector (often aluminum), (II) a carbonaceous additive to ensure electronic conductivity in the electrode, (III) a binder and (IV) active material, which represents the focus of this section. To begin, the material must exhibit an elevated free energy reaction with lithium, resulting in a high voltage. Moreover, it must be capable of reversibly accommodating a large amount of lithium ions, which implies high energy density and rechargeability. This process, as in the case of anodes, should occur without severely altering and damaging the material's structure to provide a prolonged cycle life. The ability to intercalate lithium ions quickly, which implies having a high lithium ion diffusivity, is another essential aspect for a cathode material. Furthermore, the active material of the positive electrode should be a good electrical conductor and should also be stable towards the electrolyte, so as not to generate parasitic reactions harmful to both components of the cell. Finally, the material should be economical and non-toxic to ensure safety and health standards. Additionally, it should have a low environmental impact, meaning it should have a low carbon footprint, and be easily recyclable. The cathode materials found in current commercial LIBs are all based on the "rocking chair" de/intercalation mechanism and are derived from transition metal oxides, which are suitable materials for energy storage applications due to their incomplete outer energy shells, which enable the formation of cations when electrons are withdrawn. These materials can be classified based on their crystalline structure which can be layered, spinel or olivine. In the following sections each of these families will be described in detail. As with anode materials, also in the case of cathode materials some of them are not based on the rocking chair mechanism, but rather on the conversion one. In particular, among the conversion materials, metal fluorides are the most promising as a result of their relatively high theoretical potential (3.55V vs. Li/Li^+ for CuF_2) and gravimetric capacity (713

mAh g^{-1} for FeF_3). However, they are characterized by poor cycle behavior, low electronic conductivity and complex synthesis routes. [56] Conversion materials are fascinating in the long term perspective, provided these drawbacks will be overcome, but at the current state, they are still far from being used in commercial cells.

2.5.1 Layered materials

The materials defined as "layered" were the first cathode materials for Li-ion batteries to be successfully developed. These oxides, with the general formula A_xMO_2 (where A=alkali-metal ions, M=transition metal-ions) have a particular crystalline (layered) lattice, which significantly affects the material's electrochemical characteristics. In particular, Figure 2.12 shows all the possible structural variants of these materials. In general, in these materials, the oxygen atoms coordinate the transition metals (MO_6) octahedrically, forming (MO_2)n layers between which the A ions are arranged. Alkali ions can be coordinated in tetrahedral (T), octahedral (O), and prismatic (P) environments. In particular, it can be seen how the coordination of alkaline ions is determined by the oxygen stacking sequence in the various layers.

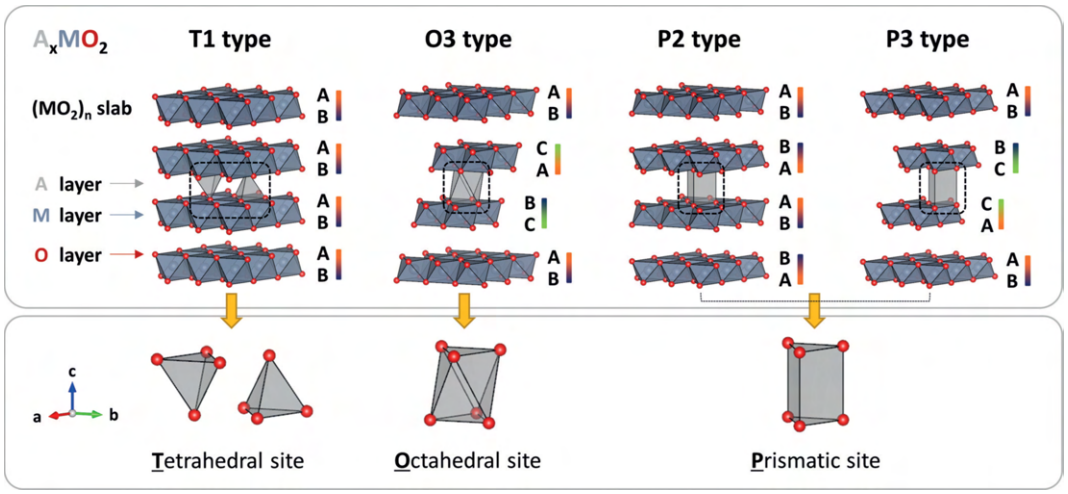

Fig. 2.12 Schematic representation of several A_xMO_2 layer oxides including T1, O3, P2, and P3 types. (A: Alkali metal ions, M: transition-metal ions). Reproduced by [57]

The "father" of this family of materials is considered lithium cobalt oxide, also known as $LiCoO_2$ (LCO), and was the first to be commercialized in 1991. It exhibits numerous interesting characteristics such as the nominal voltage (around 3.8V vs Li /Li^+), a high specific capacity (theoretical 274 mAh g^{-1}, practical 150 $mAhg^{-1}$

when cycling between 3 and 4.3V) and good stability during cycling. However, this material also presents numerous problems, including the high cost and toxicity of cobalt. Furthermore, at high temperatures, LCO is not remarkably stable and can experience the start of thermal runaway around 150°C and complete thermal runaway about 200°C. [58] For these reasons, other layered materials have been developed in the last twenty years. Undoubtedly, one of the most successful and the widely used materials in commercial Li-ion cells, is Lithium Nickel Manganese Cobalt Oxide, known as $LiNiMnCoO_2$ or NMC. The general chemical formula of NMC is reported as $LiNi_xMn_yCo_zO_2$ (x + y + z = 1), as it originated by partially replacing the Co in $LiCoO_2$ with Ni and Mn in order to simultaneously improve the electrochemical performance and reducing the cost of the active material. Usually, the most common investigated chemistries for NMC materials are the $LiNi_{1/3}Mn_{1/3}Co_{1/3}O_2$ (NMC333), $LiNi_{0.4}Mn_{0.4}Co_{0.2}O_2$ (NMC442), $LiNi_{0.5}Mn_{0.3}Co_{0.2}O_2$ (NMC532), $LiNi_{0.6}Mn_{0.2}Co_{0.2}O_2$ (NMC622), and $LiNi_{0.8}Mn_{0.1}Co_{0.1}O_2$ (NMC811). [59] These different stoichiometries were studied because, essentially, each transition metal provides specific properties, so it is possible to modify the composition of the material to meet particular requirements. For example, an NMC richer in Mn is more thermally stable and has a better cycle life, while a more significant presence of Ni translates into a higher specific capacity. Obviously, there are also disadvantages to replacing Co with Ni and Mn: an excess of Ni leads to faster degradation of the material's structure (due to the mixing between Ni and Li) over cycling. In contrast, a material rich in Mn will have limited capacity (due to the inactivity of Mn^{4+} ions in redox reaction with Li). Additionally, the Co content cannot be excessively low, as it is essential to have electronic conductivity and it also helps to give structural stability to the material. As a result, there is plenty of opportunity to adjust the composition of the ternary material NMC in order to achieve an optimal behavior in terms of cyclability, structural stability, rate capability and capacity. [60] A peculiar characteristic of layered materials is the diffusion kinetics of Li^+ ions within the crystalline lattice, which is described as a consecutive migration between a vacant octahedral site and another via two mechanisms: tetrahedral site hopping (TSH) and oxygen dum bell hopping (ODH), both shown in Figure 2.13, where the letter M indicates a transition metal ion. In the oxygen dumbbell hopping (ODH) process, the Li ion takes the shortest path to the neighboring unoccupied octahedral site through a bond of O atom. In order to accomplish this process, ionic connections must be formed with two transition metal ions (Mn^+ or Ni^+) on the opposite sides of the

oxygen structure. [61] The tetrahedral site hop (TSH) adds a further step to the process, since it is based on constant ionic bonding and debonding between each Li^+ and a neighboring transition metal as the ion moves through octahedral sites.

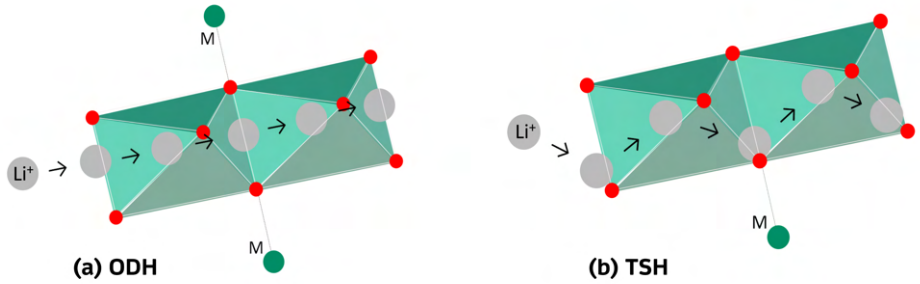

Fig. 2.13 (a) Oxygen dumbell hopping (ODH) and (b) tetrahedral site hopping (TSH) Li^+ ion diffusion mechanism in layered oxides. [61]

Both processes are only probable if energy activation barriers associated with Li-transition metal ionic bonds are overcome. Furthermore, because TSH demands Li divacancies, ODH prevails at the initial stage of charging. Considering ODH only takes place if both ionic bonds (one on each side) are broken, TSH is the most favored mechanism, assuming there are enough Li divacancies. Figure 2.14 shows the different properties of different chemistries of NMC materials depending on their composition. Several approaches have been tried to improve the electrochemical performance of this family, including synthesizing NMC particles with a Mn-rich outer shell and a Ni-rich core (to have stability with the electrolyte without capacity loss) [62], applying protective coatings on the surface of the NMC and doping the pristine materials. [63]

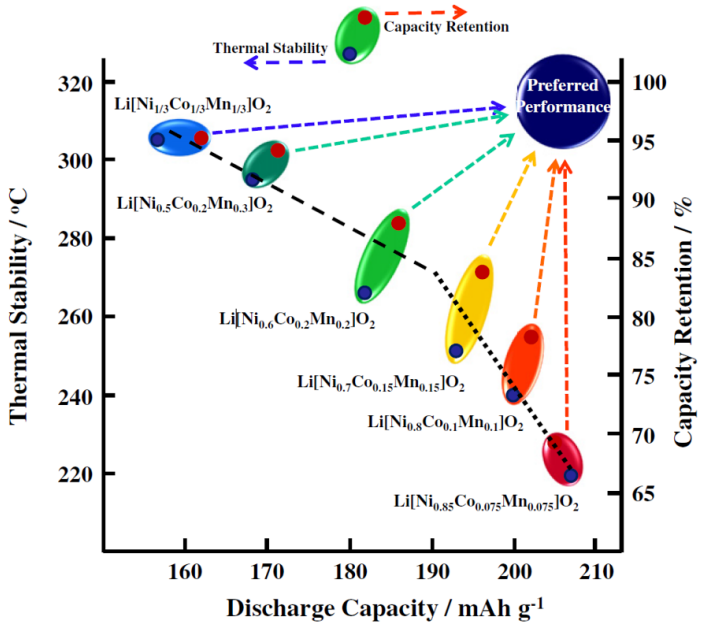

Fig. 2.14 A comparative graph of the capacity retention, thermal stability and specific discharge capacity of the different NMC chemistries. [64]

Another interesting layered material is Lithium Nickel Cobalt Aluminum Oxide, NCA. It is similar to NMC and is typically made of 80% nickel, 15% cobalt, and 5% aluminum ($LiNi_{0.8}Co_{0.15}Al_{0.05}O_2$). Aluminum doping is justified by introducing inactive Al^{3+} ions instead of Ni^{3+}, which reduces the risk of overcharging and, thus, thermally stabilizes the material. However, the problems of cost and toxicity of the material remain due to the presence of Co. [65]

Among the cathode materials that have aroused the most interest in recent years, there are certainly the Li-rich cathode materials with the chemical formula xLi_2MnO_3 $(1\text{-}x)LiMO_2$ ($0 < x < 1$,M = Ni, Mn, Co, etc.), which generally exhibit specific capacity up to 250 mAh g^{-1} and an operating voltage higher than 3.5V vs Li/Li^+ . Furthermore, they are less expensive and environmentally problematic than NMC. The high specific capacity is due to the particular arrangement of lithium in the material's structure, with Li atoms stored in the transition metal layers. However, this particular crystalline structure is subject to substantial changes during the charging process (as shown in Figure 2.15). In particular, in the first charge, the Li^+ ions are extracted from the structure of the material and evolution of oxygen, with the transition metals that can migrate into the neighboring Li slabs and consequent transition of the crystalline lattice into spinel or rock-salt structures. This phase

transition, repeated periodically during cycling, is spontaneous and detrimental to electrochemical performance since it involves decreased operational potential and specific capacity. Several approaches have been investigated to solve the problems of these materials, including cationic doping to stabilize the crystalline structure and alleviate the voltage reduction, or using a surface coating to prevent the phase transition. [66]

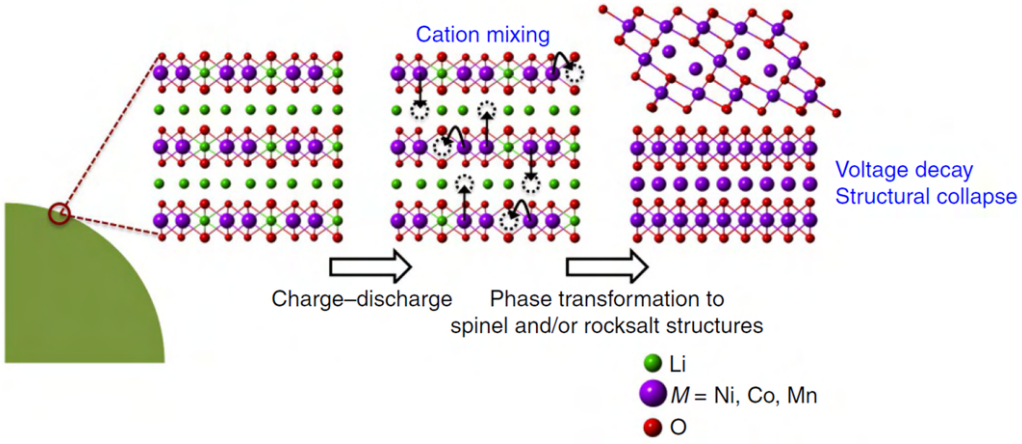

Fig. 2.15 The structure evolution of a Li-rich material upon cycling. [66]

2.5.2 Spinel and Polyanion-type materials

Since two materials (lithium nickel manganese oxide, LNMO and lithium iron phosphate, LFP) belonging to these two classes of materials were the object of study in this thesis, they are described more precisely in chapter 6 , while in this section only the general properties of these two families of materials are discussed. Olivine-type materials $LiMPO_4$ (M = Fe, Mn, Co, Ni) are cathode materials characterized by high thermal and chemical stability, good capacity (170 mAh g^{-1}), and good power performance. They present a well-defined charge/discharge curve at 3.4 V, however, this family of compounds suffers from poor electronic conductivity and sluggish Li^+ diffusion, it is very often necessary to apply a carbon coating on their surface. Spinel-type materials such as $LiMn_2O_4$ and LNMO are very attractive for the next generation of Li-ion batteries due to their low cost, high operating potential (> 4.5V for LNMO), good rate performance and absence of Co in their composition. The main limitations of these materials at the moment are the non-extraordinary specific

capacity (147 mAh g^{-1} for LNMO), the dissolution of Mn during cycling and, above all, the stability of the electrolytes at high voltages.

2.5.3 Conclusions and future perspectives for cathode materials

Table 2.1 summarizes the main characteristics of the cathode materials described in this section, together with their level of development.

Table 2.1 Comparison of different cathode materials for LIBs.

Material	Specific capacity [mAh g^{-1}]	Voltage plateau [V vs Li/Li^+]	Energy Density [Wh L^{-1}]	Status
$LiCoO_2$	160	3.7	400-600	Commercialized
$LiMn_2O_4$	130	4.0	250-360	Commercialized
LNMO	140	4.7	500-650	Research
NMC	180	3.7	300-330	Commercialized
NCA	185	3.7	450-600	Commercialized
$LiFePO_4$	160-170	3.3	190-300	Commercialized

Nowadays, almost all commercial LIBs cells are based on NMC (811 or 622), NCA, or LFP as cathode material, depending on the application. However, as reported in figure 2.16, which depicts the different generations of batteries according to the standards of the European Commission, these materials will have to be integrated in the immediate future (2025) by Li-rich NMC and high voltage spinels (LNMO), and then move on to other more promising systems (such as Li-S batteries) on the medium-long term. Consequently, in recent years, many scientific research efforts in the field of batteries have been directed towards the development of high voltage cathodes (LNMO) and conversion cathodes, with metallic lithium as the anode (Li-S batteries), and my doctoral thesis fits into this context since both of these areas were investigated during the three years of study.

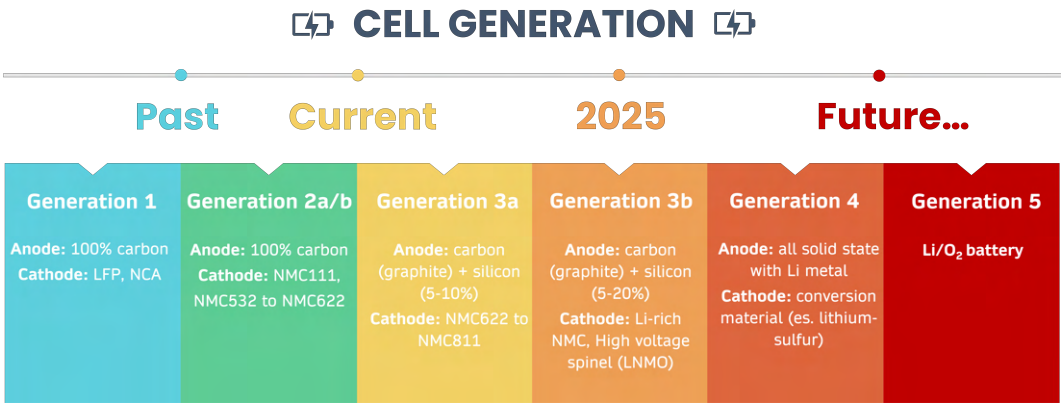

Fig. 2.16 Classification of the generation of batteries.

2.5.4 Inactive materials

In addition to the active materials present at the cathode and anode, a typical Li-ion cell (but in general, this is valid for any secondary cell) is composed of other elements, called "inactive," but decisive in the overall good functioning of the cell. These elements are the current collectors (made of aluminum for the cathodic side, copper for the anodic side), the separator (generally made of glass fiber or thermoplastic material), carbonaceous additives (useful for guaranteeing electronic conductivity inside the electrode), the binder and the electrolyte. In this section, the last two elements will be explored in depth since they are certainly the most interesting from the research point of view.

Electrolyte: A liquid electrolyte for Li-ion batteries is generally made up of organic solvents, lithium salt, and very often additives, and each of these components performs specific functions. Depending on the materials used, the working potential range of the cell, and the application, the composition of the electrolyte can vary considerably. In general, the necessary requirements of an electrolyte are several: it must have a high ionic conductivity, a wide electrochemical stability window (ESW), be electrochemically inert towards the cell components, thermally stable and non-toxic. [67] Solvents represent approximately 80% of the weight of a liquid electrolyte, so they are crucial in determining its final properties. In particular, they must meet the following requirements: 1) solvate the dissolved lithium salt, ability directly proportional to the dielectric constant 2) low viscosity to favor the diffusion of Li^+. This is in contrast to the first point because usually solvents with high dielectric constant

have high viscosity 3) broad ESW 4) provide adequate interfacial properties, helping to form a stable SEI 5) be chemically inert towards cell components. In current commercial cells, a mix of two aliphatic carbonate solvents is generally used: cyclic carbonates (e.g., ethylene carbonate EC, which have a high dielectric constant), and linear carbonates (e.g., dimethyl carbonate, DMC or diethyl carbonate DEC), which have a low viscosity. These two classes of solvents are different from the point of view of interfacial, chemical, and thermal properties. [68] Considerable efforts have been made to replace, at least partially, organic carbonates in order to increase the ESW and improve the thermal stability of the electrolyte. One approach integrates more electronegative components, such as fluorine, cyano, or sulfone groups, into commonly utilized organic solvent molecules. These components exhibit reduced HOMO/LUMO levels compared to classical carbonates; consequently, their addition into the electrolyte shifts the ESW towards higher potentials. In particular, one of the most recently studied compounds as a co-solvent is fluorinated ethylene carbonate (FEC), which has proven to be a beneficial element in the overall composition of a high-performance electrolyte. In particular, it has been demonstrated that its introduction into the electrode helps to reduce the irreversibility of the first cycle (allowing the formation of the anodic SEI at potentials higher than the pristine EC) and to increase thermal stability. Furthermore, Hu et al. [69] studied a FEC-based electrolyte for high voltage $LiNi_{0.5}Mn_{1.5}O_4$/graphite couple, which proved to be remarkably stable even during temperature cycling, while Suo et al. proved the beneficial effect of FEC towards the formation of a stable F rich SEI layer on the lithium metal anode. [70] Another successful approach to obtain stable electrolytes up to 5.4 V was to combine FEC and Lithium Bis(fluorosulfonyl)imide (LiFSI) with non-polar solvents. [71] Furthermore, the introduction of linear fluorinated carbonates such as (e.g., ethyl(1-fluoroethyl)carbonate) can be decisive for improving the safety of the electrolyte since their use allows the replacement of $LiPF_6$ with lithium bis(trifluoromethanesulfonyl)imide (LiTFSI), whose advantages will be described in the following lines. [72] The importance of the lithium salt is pivotal in Li-ion batteries. Obviously, the introduction of salt complicates the system, but it is necessary to ensure adequate ionic transport. The lithium salt must meet specific requirements to be suitable for use: 1) it must dissociate completely in the electrolyte. Typically, lithium salts for this function are composed of complex, Lewis acid stabilized anions 2) be stable in the window of potential use 3) be chemically inert towards the components of the cell, although in reality, sometimes, the decomposition is

"controlled" and can be a benefit as in the case of $LiPF_6$ which can form a passivating layer on the Al collector 4) be thermally stable 5) be non-toxic and benign from an environmental point of view. The most widespread salt in previous generations of LIB was certainly $LiPF_6$ given that it shows a broad ESW, chemical inertia, and excellent ionic conductivity. However, it is also affected by safety problems since its degradation occurs at relatively low temperatures (100 °C) or in the presence of a few ppm of H_2O. Consequently, different types of alternative salts have been studied in recent years. Imide-based lithium salts are among the most interesting substitutes, with LiTFSI being this family's most widely used compound. They generally have superior electrochemical, thermal, and chemical stability compared to $LIPF_6$, thus guaranteeing superior electrochemical performance and safety. However, imide-based lithium salts cannot passivate the Al collector, which degrades at voltages above 3.8V. Consequently, as with solvents, good performance can also be achieved for lithium salts using a mix of different salts. For example Xu et. al. proved that a mixture of LiTFSI, $Li(CF_3SO_2)_2$ and Lithium bis(oxalato)borate (LiBOB) in nitrile groups-based solvents could exhibit a wide voltage window of 6.0 V vs. Li/Li^+ . [73] The main lithium salts currently used and studied are shown in Table 4.2, with their relative advantages and disadvantages.

Table 2.2 Comparison of different lithium salts for LIBs, with their advantages and disadvantages.

Lithium salt	Advantages	Disadvantage
$LiPF_6$	High solubility and ionic conductiviy; it forms a stable passivation layer on Al	Easy to decompose (T and water)
$LiBF_4$	Thermal stability, enhance the film formation capability of electrolyte to electrodes, inhibiting aluminum foil corrosion	Low ion conductivity
$LiAsF_6$	Excellent conductiviy, stability and C-rate performance	Toxicity
LiBOB	High electrical conductiviy, large ESW, good thermal stability passivation of Al collector	Low solubility
LiTFSI	High solubility and conductivity, excellent thermal stability 300-330 °C, not easy to hydrolyze	Corrosion of Al foil when > 3.7V
$LiPF_2O_2$	High performance at low T, reduce battery impedance	Low solubility
LTBP	Improved cycling stability and coulombic efficiency	Low conductivity, high molecular weight and viscosity

Another approach that has been investigated is to significantly increase the salt concentration (>3M) to prevent corrosion of the Al collector and extend the ESW above 4.5V; however this method also has disadvantages such as high cost and low conductivity. [74, 75] Finally, in recent years, an enormous amount of research has been devoted to the development of gel-polymer electrolytes (GPE), solid-polymer electrolytes (SPE) [76], ionic liquids (ILs) [77] and solid-state electrolyte. All these

systems are fascinating because they significantly increase the safety of the cell compared to the liquid electrolytes based on organic solvents currently in use. However, their development is still at an experimental research stage, so it will take a few years before these technologies can appear on the LIBs market.

Binder: The binder is an essential component in the overall composition of the electrode, in fact its main function is to provide adequate adhesion and interaction between the active material particles and the current collector during cycling. Furthermore it must provide a mechanical network inside the electrode and have the ability to accommodate the volume variations of the active materials without breaking, as well as being electrochemically inactive in contact with the battery components. Other fundamental aspects of the binder are its compatibility with the electrode manufacturing process (typically tape casting), cost and toxicity. At the moment, the most used binder in LIBs is Polyvinylidene fluoride (PVDF), which ensures cohesion between the particles of active material and adhesion with the current collector, combined with a carbonaceous additive which ensures adequate conducibility to the entire electrode. However, this type of system presents drawbacks that must be overcome. First of all, the apolar structure of PVDF can form only weak intermolecular interactions with the active material and the current collector, so during the charge and discharge cycles , the original structure of the electrode is considerably damaged due to volumetric changes, resulting in delamination and loss of capacity. Secondly, the toxicity issues associated with the solvent N-Methyl-2-pyrrolidone (NMP), which is utilized in the tape casting process of PVDF electrodes, must be considered. [78] Developing new binders is essential because new conversion materials such as silicon or sulfur exhibit high volume variations compared to graphite or typical cathode materials. In this sense, polymers with a high concentration of carboxyl groups, such as carboxymethyl cellulose (CMC), which is usually combined with styrene-butadiene rubber (SBR) [79], poly(acrylic acid) (PAA) [80], and alginate [81], have recently been much studied. These polymers can establish more robust bonds with the active material particles, help form a more stable SEI, and provide a high elastic modulus capable of accommodating volume variations. However, even with this type of binders, the use of conductive carbon additives is still necessary. In this regard, conductive polymers like polyaniline (PANI) or Polypyrrole (PPy) are an intriguing option since they combine the ability to operate as conductive additives and adhesive elements in a single component. [82]

Separator: The separator is another important component in a battery since its task

is to prevent physical contact between the anode and cathode and therefore electrical short circuit; at the same time it must allow the passage of Li^+ ions. A separator must therefore possess the following characteristics: electrically insulating, mechanically robust and chemically inert in the internal environment of the battery and possess good wettability in the liquid electrolyte used. The most common separators are microporous polymers such as polyethylene (PE) and polypropylene (PP) or based on glass fiber. [83] Also in this case the development of new materials in the field of polymeric and ceramic electrolytes will be of great importance in replacing the current separators. Ceramic electrolytes (such as NASICON) are completely inorganic and have great thermal stability, minimal flammability, and a broad electrochemical window; however, they suffer from poor interfacial contact and flexibility.

Chapter 3

Lithium-sulfur batteries

Lithium-sulfur batteries (LSBs) have recently emerged as a promising alternative to other electrochemical devices, as these batteries provide a high theoretical specific capacity (1675 mAh g^{-1}) and energy density (2600 Wh kg^{-1}, a value that is around 2-3 times higher than a typical LIB, see figure 3.1) while maintaining a relatively low production cost and environmental benignity. However, the practical energy density of Li-S batteries lies between 350-500 Wh kg^{-1} [84], a value still considerably higher than those provided by LIBs (200-250 Wh kg^{-1}). Because of the great benefits of Li-S batteries, the scientific community has concentrated on developing this technology, with an exponential growth in the number of research publications and citations reported from 2011 to present. [84]

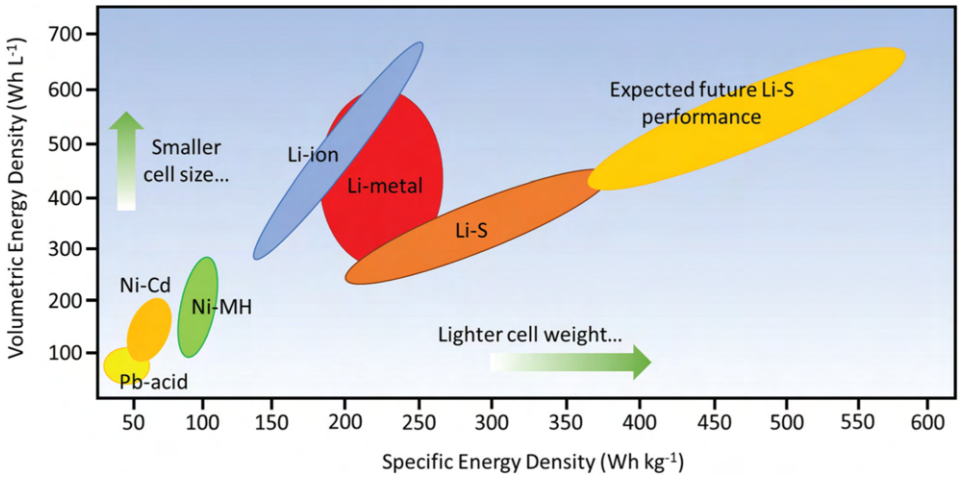

Fig. 3.1 Volumetric energy density vs Specific Energy density of various energy storage devices based on different technologies. [85]

However, various drawbacks of this technology prevent it from being fully technologically transferred to commercial applications. Significant progress has been achieved in recent years, but there are still numerous obstacles to overcome before this technology can be widely adopted. The next sections describe the fundamental operation and shortcomings of Li-S batteries.

3.1 Operational mechanism of Li-S batteries

Lithium–sulfur cells utilize a very similar architecture as today's Li ion cells, since they are essentially constituted by a lithium metal anode, a separator, an organic electrolyte and a cathode. The latter is made up of a combination of highly porous carbon, which offers electronic conductivity as well as an electrochemically active surface; sulfur, which is the active material in this electrode; and binder, which binds the structure together. The combination of a high energy safe and abundant material like sulfur and the most electropositive metal is the key of the interesting properties of this technology. [86] The operating potential of a Li-S cell is determined by the difference between the potential of lithium metal (E° = -3.040 V) and sulfur cathode (E° = - 0.445 V) and is normally around 2.4 - 2.5V. The general process that occurs in a Li-S cell during discharge is the progressive formation of dissolved polysulfides (Li_2S_x. $4 < x < 8$) by breaking the S-S covalent bonds of solid cyclo octasulfur (S_8); then these lithium polysulfides (LiPSs) are further reduced into solid Li_2S through multistep reactions. During the charge process Li^+ ions diffuse through the electrolyte towards lithium metal, with Li_2S being converted back to LiPSs and S_8, as reported in equation:[87]

$$S_8 + 16Li^+ 16e^- \rightleftharpoons 8Li_2S \tag{3.1.1}$$

Consequently, the reaction mechanism of a Li-S cell is very different from the rocking chair one typical of LIBSs, in fact in the case of the former, there is the continuous formation and breaking of chemical bonds during the reactions, so the Li-S is based on an active materials conversion mechanism. As can be guessed from the general reaction, each sulfur atom is able to accept 2e-, which is why the specific capacity is so high (1675 mAh g^{-1}). [88] In general, the complete reaction mechanism of a Li-S cell is much more complex than that described by equation

3.1.1, which can, in fact, be broken down into different reaction steps listed below:

$$S_8 + 2Li^+ + 2e^- \rightarrow Li_2S_8 \qquad (2.39\,V\ vs\ Li/Li^+) \tag{3.1.2}$$

$$3Li_2S_8 + 2Li^+ + 2e^- \rightarrow 4Li_2S_6 \qquad (2.37\,V\ vs\ Li/Li^+) \tag{3.1.3}$$

$$2Li_2S_6 + 2Li^+ + 2e^- \rightarrow 3Li_2S_4 \qquad (2.24\,V\ vs\ Li/Li^+) \tag{3.1.4}$$

In particular, the equations (3.1.2), (3.1.3) and (3.1.4) describe the opening of the solid-state sulphur (αS_8) and the subsequent reduction in long chain LiPSs (Li_2S_x. 4 < x < 8). During this stage of the discharge some reaction of disproportionation and chain growth are possible, so multiple species of LiPSs can be formed, even though the most probable products are Li_2S_6 and Li_2S_4. In a typical Li-S discharge curve these reaction deliver around 419 mAh g^{-1} and they occur in correspondance of the plateau at 2.4V. [89]. The reaction path continues as follow:

$$Li_2S_4 + 2Li^+ + 2e^- \rightarrow 2Li_2S_2 \qquad (2.2\,V\ vs\ Li/Li^+) \tag{3.1.5}$$

$$Li_2S_2 + 2Li^+ + 2e^- \rightarrow 2Li_2S \qquad (2.15\,V\ vs\ Li/Li^+) \tag{3.1.6}$$

The second part of the discharge profile is described by the equations (3.1.5) and (3.1.6), where long-chain LiPSs are further reduced to low-order polysulfides; this process is assigned a theoretical capacity of 1256 mAh g^{-1} at a voltage between 2.15 and 2.1 V. Finally, the discharge process ends with the deposition of Li_2S_2 and Li_2S on the cathode surface. The presence in the system of numerous chemically diverse species results in a complex voltage-time profile during discharging, which may be separated into four zones for the sake of description, as illustrated in Figure 3.2. The first region (I) is associated with the reduction of (0.25 e^- for S atom) S_8 to Li_2S_8 which is generally soluble in the electrolyte and results in a minor decrease in potential (from 2.4 to 2.2 V against Li/Li^+). In the second region (II) the reduction continues with 0.25 e^- per S atom and there is a progressive decrease in the length of the LiPSs chains from eight to four sulfur atoms (Li_2S_8). In this region the potential decays quickly to about 2.1 V. It should be mentioned that the viscosity of the electrolyte rises throughout these two phases due to an increase in the concentration of long-chain polysulfides. Between regions (II) and (III) there is usually a minimum point in the voltage curve, which is associated with an overpotential required for the nucleation of a solid phase (and in particular, it is thought that at this point, there is a supersaturation of Li_2S, which then begins to precipitate as a solid).

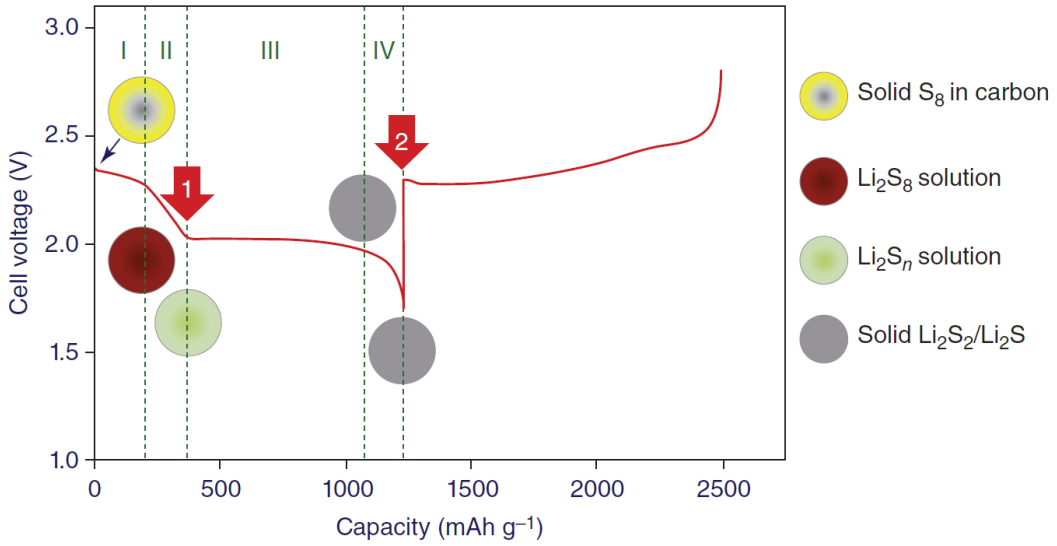

Fig. 3.2 Typical discharge/charge curve of a lithium sulfur battery. Reproduced from [90]

Region (III) is characterized by a relatively stable plateau (2.1 V vs Li/Li^+), during which tetrasulfide is reduced to Li_2S_2 and the latter to Li_2S. Finally, in the last region (IV) fully reduced sulfide is formed. Unlike long polysulfides, both Li_2S_2 and Li_2S are insoluble in most electrolytes.

In a nutshell, the charging process (see Figure 3.3) involves the conversion of insoluble Li_2S and Li_2S_2 to soluble long polysulfides, which are in turn oxidized to elemental sulfur. The charging process is as complex as the discharging one, and it is generally recognized that it is not exactly the inverse of the latter, in fact between the two charging/discharging voltage curves, shown in Figure 3.3, one can note the presence of a significant hysteresis. [91] This hysteresis is explained by taking into account the relative ease with which the different reactions associated with the two processes can take place: the reduction of elemental sulfur, which is indeed an insulating species (10 - 30 S cm^{-1}), but is also very soluble in aprotic solvents, occurs with little difficulty. In contrast, the oxidation of Li_2S is a much more hindered process due to its insulating nature and insolubility. Consequently, an overpotential (also known as "activation kick") is usually present at the beginning of the charge; the more consistent this kick is, the more difficult the Li_2S oxidation process is. Furthermore, the difference between the charging and discharging pathways can also be noticed by observing the formation (discharging) and consumption (charging) of Li_2S, as reported by Walus et al. [91] In particular, it can be seen how

the formation of Li_2S during the discharge is initially relatively fast, and it is the only product of the reaction, while in a second step the formation of Li_2S_2 becomes dominant over that of Li_2S. Charging process can also be divided into two steps: in the first part, there is the oxidation of approximately 75% of Li_2S formed during the discharge into Li_2S_4, while in the second part, the formation of Li_2S is slower than the reduction of Li_2S_4 in long polysulfides. The reasons for this difference in reaction pathways can be attributed to the different properties of the species involved such as their insoluble/soluble nature. Moreover, the dynamic balances that regulate the concentration of different LiPSs species are very complicated, and as consequence, the reactions that are energetically and kinetically favored during the charging and discharging process they are not the same. [91]

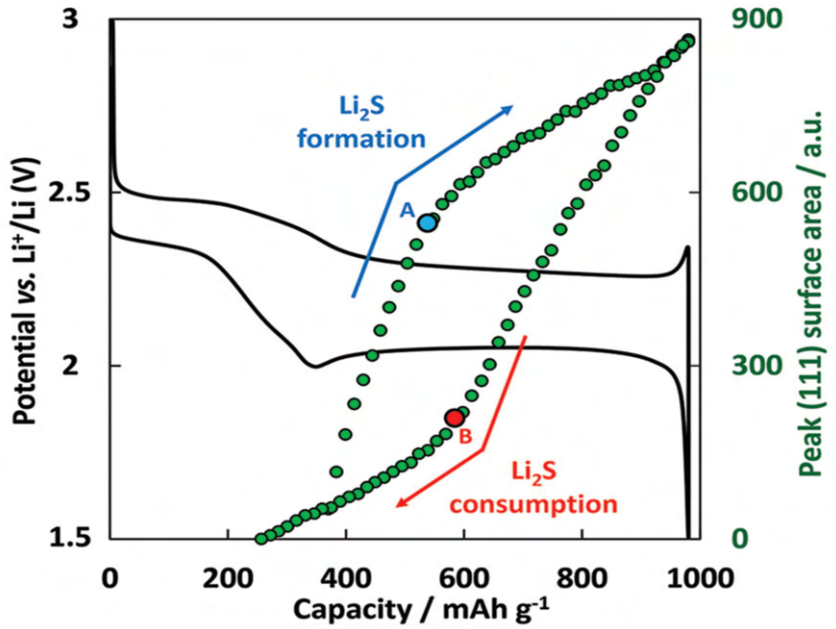

Fig. 3.3 Discharge/charge profiles of a Li-S cell along with the evolution of the area of the peak (111) of Li_2S during cycling. The blue arrow refers to the discharge process, where the Li_2S is formed and the area of (111) increases, while the red arrow refers to the charge process where Li_2S is converted into LiPSs. Reproduced from [91]

3.2 The Fundamental Challenges of Li–S Batteries

Despite the great advantages that Li-S technology offers, it still presents several key problems (see Figure 3.4) that must be addressed to allow its commercialization.

- **"Shuttle effect":** it is a parasitic phenomenon typical of the Li-S system that occurs during the charging process. In particular, it occurs when the charge state of the cell becomes deeper and the oxidation of Li_2S and Li_2S_2 in long LIPSs considerably increases the concentration of the latter on the cathode side of the cell. [92] At this point the long LiPSs begin to diffuse towards the anode side, where they react with the metallic lithium via disproportionation reaction. A certain amount of the reaction products are short/medium polysulfides that return towards the cathode side, while the rest of the polysulfides react directly on the lithium surface, forming insoluble Li_2S and Li_2S_2, thus causing its passivation, loss of capacity and low coulombic efficiency (because in this way the charging process is lengthened and in extreme cases can lead to the cell never reaching the cycling cut-off value). [93, 94]

- **Volumetric expansion:** Due to the considerable density difference between elemental sulfur and Li_2S (1.66 vs 2.07 g cm^{-3}), there is significant expansion (about 75%) [95] during the cell discharge process, which can result in pulverization and delamination of the cathode.

- **The conductivity of S and Li_2S:** Both discharge/charge products are electronic insulators, and their Li^+ ion transport properties are also poor, thus making the related formation reactions of these species difficult, leading to poor use of the active material. Additionally, during cycling, the precipitation of Li_2S as a passive coating on both the anode and cathode surfaces causes a rise in overpotential and reduced discharge capacity output.

- **Growth of lithium dendrites:** Dendrites are potentially capable of penetrating the SEI, leading to continued electrolyte consumption and the formation of dead lithium, thus reducing the useful life of the cell. Furthermore, the dendrites can, in extreme cases, lead to a short circuit of the cell by penetrating the separator. [96]

- **Side reaction:** Due to the high activity of lithium metal, it is possible for side reactions to occur when it is brought into contact with the electrolyte, resulting

in potential gas development, a clearly dangerous factor when it comes to sealed systems such as batteries. [95]

- **Self discharge**: during a possible resting of the cell, the sulfur reacts directly with the lithium ions present in the electrolyte generating lithium polysulfides, resulting in self-discharge of the cell. [97]

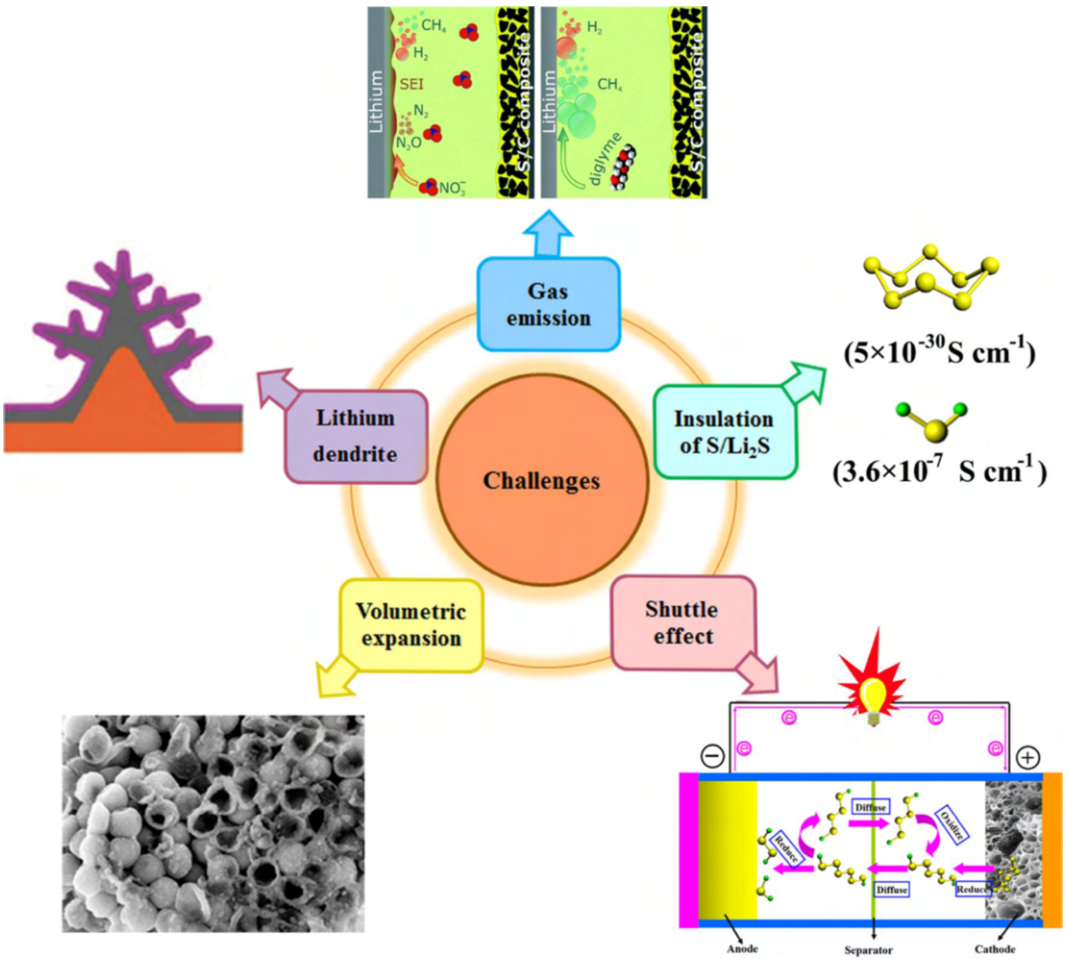

Fig. 3.4 The main challenges that must be overcome to make the Li-S suitable for future commercial application. Reproduced from [98]

3.3 Approaches to improve the Li-S technology

The typical problems of LSBs described in the previous section are very general and concern different components of the cell; furthermore, it must be taken into

consideration that LSBs are not standardized like LIBs, consequently the problems encountered in a particular cell design can also vary considerably depending on the materials and electrolytes used. In the same way, therefore, the strategies applicable to solving these problems are multiple and may concern more specifically the cathode, the electrolyte or the anode. Since the PhD research over the past three years has been focused on cathode materials for Li-S batteries, more space will be dedicated to this topic in the subsequent sections.

3.3.1 Cathode development

Over the past few years, several strategies have been explored to improve the performance of cathode materials used in LSBs, where sulfur is typically incorporated into electrically and ionically conductive matrices. In particular, the two most used approaches are based (I) on the physical confinement of the polysulfides (II) on a strong chemical interaction between the cathodic active material and the LiPSs. The figure summarizes the development of the cathode materials used in LSBs, underlining the methods that have been used in this thesis work.

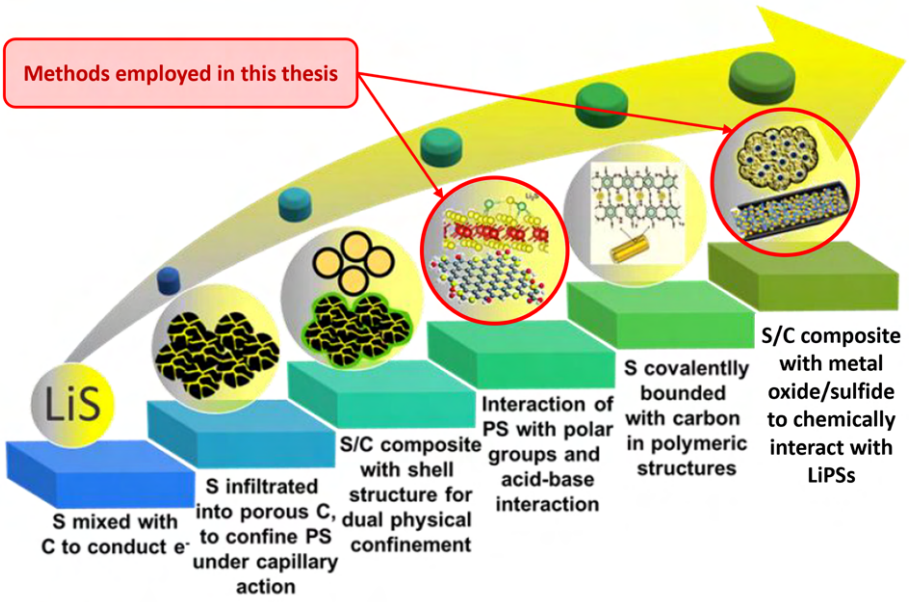

Fig. 3.5 The developement of cathode engineering for LSBs over the last years, Reproduced from [99]

Carbon based cathodes:

Carbonaceous materials are currently the most used to provide adequate conductive and flexible structures capable of hosting sulfur and ensuring its electrochemical activity. In particular, these materials are very versatile because their porosity, morphology, degree of functionalization, and level of graphitization can be modified during the synthesis phase. An important aspect is certainly the porosity of these materials: as shown in the figure, mesoporous carbons (2-50 nm) have a high specific area and an adequate pore size to physically confine the LiPSs and ensure good sulfur loading, while microporous materials (<2 nm) can encapsulate only the shorter LiPSs; consequently they can effectively mitigate the shuttle effect by reducing the amount of dissolved LiPSs, but this also results in poor sulfur loading and utilization.

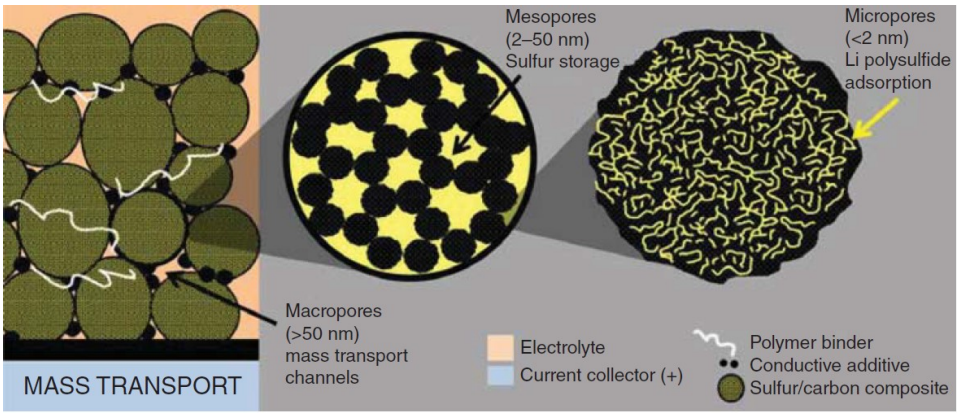

Fig. 3.6 Schematic representation of the microscopic and macroscopic structures of a typical cathode composed of carbonaceous material and sulfur, reproduced from [86]

In the past years, one-dimensional (1D) carbon nanotubes (CNT) and nanofiber [100], two-dimensional (2D) graphene [101], or three-dimensional (3D) carbon aerogels and sponge structures [102] have all been used to develop sulphur cathodes. In particular, the 2D structures deriving from graphene have excellent conductive and mechanical properties, which are fundamental to have a good utilization of sulfur and structural stability of the cathode upon cycling; furthermore, the functional groups present on the so-called rGO (reduced graphene oxide, obtained through the chemical or thermal reduction of graphene oxide, GO) can chemically interact with the LiPSs, reducing their dissolution in the electrolyte. [103] Moreover, heteroatom-doped rGO shows good electrochemical performance, since the presence of charged sites increases the conductivity and adsorption capability of the graphitic structure. [104] The most used synthesis methods to obtain a composite S/C are all based on

incorporating sulfur into the carbon structure. In the melt or vapor phase infiltration, the composite is heated in such a way as to reach the lowest possible viscosity of the sulfur, which is included in the carbon structure. In solution infiltration, a solvent is used to solubilize the sulfur, which can then permeate into the carbonaceous material; the solvent is then evaporated. With chemical reaction deposition, sulfur is deposited starting from different precursors such as Na_2S. Finally, the mechanical intrusion involves a ball milling step to reduce the size of the sulfur and increase its contact area with the carbon; however in this case, the adhesion between S and C is relatively weak. [105]

Metal Oxides and Sulfides as trapping agent for LiPSs:

Carbonaceous materials are extremely attractive for use in Li-S battery cathodes; however, the conjugate non-polar carbon planes have limited sites to firmly anchor polar molecules (e.g., lithium polysulfides and (di)sulfides). The insertion of polar sites onto carbon planes via doping by heteroatoms (N, O, P) or surface functionalization (-OH, -O- groups) has been proposed to provide anchoring sites for chemically attaching the polysulfide intermediates. It has been shown that nanostructured oxides and sulfides are efficient conductive polar host materials that effectively adsorb polysulfides during discharge and prevent the detachment of lithium (di)sulfides into the electrolyte. Additionally, these inorganic host materials can speed up converting lithium polysulfides to lithium (di)sulfides or the opposite process due to their superior reactivity and abundant surface sites (see Figure 3.7 for a schematic representation of the proposed conversion mechanism in presence of metal oxides and sulfides). [106] All these features of polar inorganics endow Li–S batteries with improved reversibility, better stability, and longer lifetimes.

In metal oxides where the oxygen anion is in the O^{2-} oxidation state, a strongly polar surface is usually present. However, due to metal oxides poor electronic conductivity, they must be coupled with carbonaceous matrices. One of the most studied oxides is certainly TiO_2, which was introduced into a Li-S cell for the first time by the Nazar group. [107] In particular, nanostructured TiO_2 with different morphologies have then been investigated as cathode host materials in Li–S batteries, such as mesoporous hollow TiO_2 spheres,[108] TiO_2 nanofibers,[109] nanoparticles,[110] and nanotubes. [111] A sulfur–amorphous-TiO_2 yolk–shell structure for the sulfur cathode of Li–S batteries was reported by Cui et al. [112] Furthermore, to overcome the problem of the intrinsic poor electronic conductivity of TiO_2, Nazar et al.

introduced a high-surface-area Magnéli phase oxide Ti_4O_7 with a theoretical bulk conductivity of 2×10^3 S cm^{-1} at 298 K (about three fold greater than graphite) as a metallic and polar host for Li–S batteries. [113, 114]

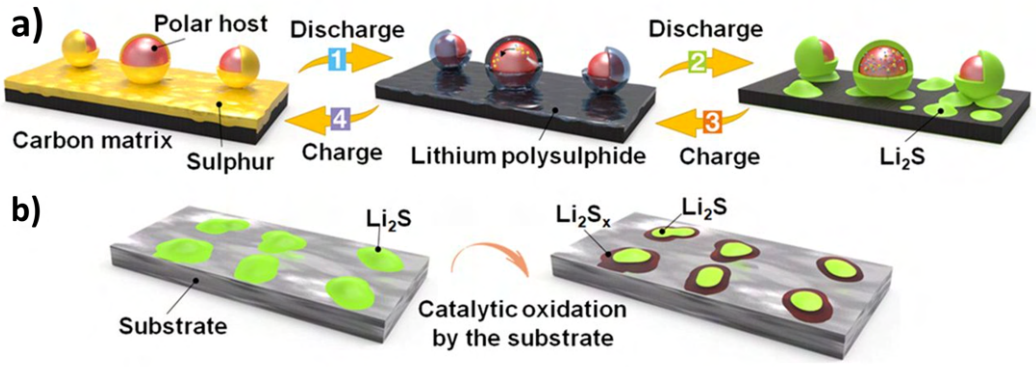

Fig. 3.7 Schematic representation of the Li_2S catalytic oxidation on the substrate surface and the sulfur conversion process. (a) Sulfur binds to the surfaces of carbon and a polar host to generate Li_2S_x, which is poorly adsorbed by nonpolar carbon and strongly bound to the polar host (step 1). In the second step, Li_2S_x converts into Li_2S, which is primarily absorbed by the polar host. Isolated islands of Li_2S are then deposited on the carbon surface. (b) The substrate promotes the oxidation of Li_2S to Li_2S_x near the substrate surface and, ultimately, to sulfur (steps 3 and 4 in A). [115]

Using MnO_2 as a polar host material for polysulfides was first proposed by Liang et al. [116] and by Zubair et al. [117] Ultrathin monoclinic birnessitis λ-MnO_2 nanosheets were synthesized by reducing graphene oxide with $KMnO_4$. The material obtained proved to be able to interact strongly with LiPSs, providing excellent performance (it displayed an initial capacity of 1300 mAh g^{-1} at C/20, 1120 mAh g^{-1} at C/5, and 950 mAh g^{-1} at 1C). Additionally, numerous additional polar metal oxide composites, such as Fe_3O_4, CeO_2, $NiFe_2O_4$, Si/SiO_2, Co_3O_4, V_2O_5, and MoO_2, have been employed as sulfur hosts to anchor the polysulfides, which considerably enhances the electrochemical performance of the Li-S batteries. [118–120] It should be mentioned that most oxide nanostructures are coupled with conductive polymers or carbon materials to enhance the overall conductivity of the cathode rather than relying on the intrinsic low conductivity to achieve the best service performances in the Li–S batteries. Metal sulfides are another class of typical polar inorganics that can accommodate sulfur and anchor polysulfides in Li–S batteries; in particular they have several intrinsic benefits in: (I) the strong sulfiphilic property to sulfur containing species and (II) low lithiation voltages vs Li/Li$^+$, which can avoid over-

lap in the working voltage window of Li–S batteries. For example, one of the first materials of this family to be used in LSBs was the pyrite-type CoS_2, which exhibits a conductivity of 6.7 x 10^{-3} S cm^{-1} at 25 °C. [121] Furthermore, DFT calculations showed good binding energy between CoS_2 and Li_2S_4, and the interfaces between CoS_2 and the electrolyte also provide strong adsorption and activation sites for polar polysulfides, accelerating their redox reactions. Another type of polar metal sulfide is Co_9S_8, which has a high conductivity of 290 S cm^{-1} at ambient temperature. Chen et al. created unique Co_9S_8 inlaid carbon hollow nano polyhedra and employed them as an efficient sulfur host for Li-S batteries. [122] TiS_2 has also been studied in Li–S batteries due to its high electronic conductivity and the polar nature of its surface. Cui and co-workers proposed a $Li_2S@TiS_2$ core–shell nanostructure synthesized by an in-situ reaction method as a cathode for Li–S batteries. [123] Various other metal sulfides, such as MoS_2 [124, 125], SnS_2 [126], NiS_2 [127], WS_2 [128], ZnS [129] and CuS [130], have also been investigated as polar hosts in Li–S batteries. Although the conductivity of metal sulfides is substantially higher than metal oxides, carbon-based compounds are still used to reduce internal resistance and improve the effective use of the active material.

3.3.2 Electrolyte formulations for Li-S batteries

The electrolyte is an essential component in Li-S batteries. In addition to the properties usually required in a typical Li-ion battery, in the case of LSBs the presence of polysulphides (PS) must also be considered. Generally, the electrolytes used are based on two groups of solvents: (I) organic carbonates, such as ethylene carbonate (EC) propylene carbonate (PC); (II) ethers, such as 1,3-dioxolane (DOL), 1,2-dimethoxyethane (DME). Most of the time, they can be coupled in the same electrolytic solution to optimize as many parameters as possible (volatility, viscosity, conductivity, etc.). The use of carbonates has decreased significantly lately since their tendency to react with polysulfides has been demonstrated (in particular, partially negatively charged sulfur atoms tend to attack carbonates) [86]. On the other hand, ethers are more stable in contact with PS, especially in the presence of anion S_n^- radicals. Furthermore, they have a lower viscosity, which favors the diffusion of Li^+ ions between the cathode and anode and a better impregnation of the cathode. The most used are cyclic ethers, such as DOL, and linear ethers such as DME. Alternative

solvents commonly used in electrolyte formulation are: tetraethylene glycol dimethyl ether (TEGDME), polyethylene glycol dimethyl ether (PEGDME), tetrahydrofuran (THF) and ionic liquids. [131] From the point of view of the lithium salts used in LSBs, the most common ones also used for LIBs ($LiPF_6$, LiBOB, $LiBF_6$, etc.) are generally unsuitable due to their reactivity with lithium polysulfides and their tendency to initiate DOL polymerization; consequently one of the most used salts in this type of battery is lithium bistrifluoromethanesulfone imide (LiTFSI). [132, 133] Another challenge in Li-S is establishing the correct ratio of electrolyte to sulfur because a low E:S ratio limits the production of polysulfides and thus alleviates the shuttle effect, but on the other hand, leads to a high viscosity, which inhibits the mass transfer and increases the internal resistance of the cell, resulting in a loss of capacity. A high E:S ratio, however, guarantees better ionic conductivity, allowing the electrochemical reactions to occur faster and with fewer overvoltages. However, at the same time, precisely because it favors a higher utilization of sulfur (Figure 1.19) during the first cycles, it involves a more consistent formation of insulating lithium sulfide on the cathode, so the performance (capacity loss) of the cell drops more markedly as cycling proceeds, compared to what happens with lower E:S ratios. This ratio generally varies between 5-30 μl of electrolyte per mg of S.

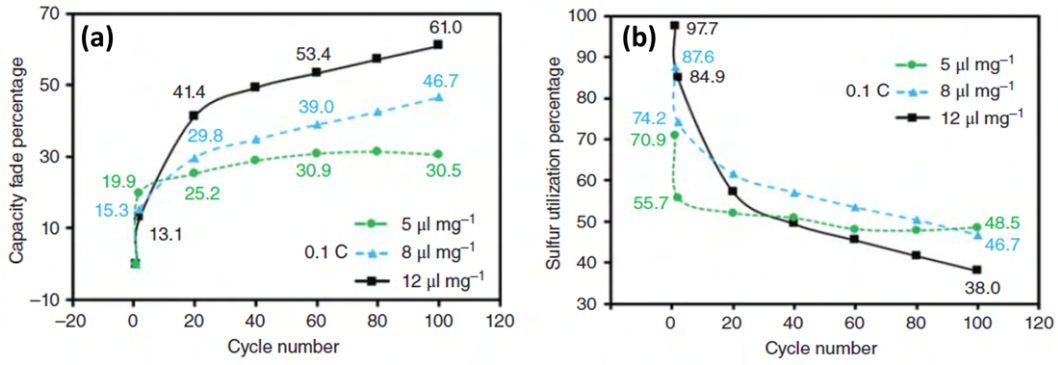

Fig. 3.8 a) Percentage drop in capacity of a Li-S cell as a function of the number of cycles and the E:S ratio, b) percentage of sulfur utilization as a function of the number of cycles and the E:S ratio, reproduced with modifications from [86]

Various additives have been studied to increase the stability of the interface between lithium metal and electrolyte. Among these, one of the most interesting is lithium nitrate $LiNO_3$, which effectively modifies the composition of the SEI and counteracts the shuttle effect. In particular, it was observed that the addition of $LiNO_3$ in an equimolar solution of DME and DOL is able to lead to the formation of

a SEI which inhibits the parasitic reaction between the polysulfides and the anodic lithium, significantly reducing the shuttle effect. The analysis of the SEI formed on lithium metal from an electrolyte solution of DME and DOL with addition of $LiNO_3$ shows that the upper layer consists of inorganic species such as LiN_xO_y and organic species such as ROLi and $ROCO_2Li$. Below the surface layer, a second layer is formed whose composition includes $ROCO_2Li$, LiN_xO_y, Li_2O and Li_3N; these insulating species prevent the continuous transfer of electrons from lithium metal towards the electrolyte solution, thus inhibiting parasitic reactions. [134] However, as in Li-ion batteries, liquid electrolytes suffer from high PSs solubility, flammability, and high volatility, leading to short cycle life, poor safety, and marked self-discharge. For these reasons, solid-state electrolytes (SSEs) have been much studied in recent years since they can avoid the dissolution of LiPSs, prevent lithium degradation, and act as separators simultaneously. These types of electrolytes can be classified into four types: solid polymerd electrolyte (SPE), gel electrolyte, and ceramic electrolyte. SPEs consist of a polymer matrix (e.g. PAN, PMMA, PEO) containing lithium salts. Gel polymer electrolytes (GPE) are obtained by adding plasticizers into the SPEs to increase ionic mobility and mechanical stability towards the dendrites. Despite these very attractive characteristics, solid electrolytes cannot provide the same ionic conductivities as liquid electrolytes, so further research is still needed to make them competitive.

3.3.3 Shuttle effect inibition

From a scientific point of view, the most studied problem of LSBs in recent years has certainly been the shuttle effect, described in section 3.2 of this chapter. It derives from the inevitable presence of polysulfides in the electrolytic solution; they are present in two forms in balance with each other: the singly charged radical monoanion (S_n^-) and the dianion (S_n^{2-}). PSs have strong chemical reactivity and sensitivity to oxygen and moisture, and their state and behavior depend highly on solvent choice, so it is extremely difficult to isolate and characterize a single specie of LiPSs. Despite these drawbacks linked to the presence of LiPSs, they are still an integral part of the system since their dissolution in the electrolyte near the cathode favors the kinetics of the conversion reaction and reduces the resistance to charge and ionic transfer. The approach that has proven to be most effective to alleviate the shuttle effect is to retain the LiPSs on the cathode side of the cell. This method is

generally based on the retention of LiPSs via physical and chemical adsorption on the cathode, which can be achieved in different ways:

- Polarization treatment of carbon matrix in cathode: In this case, the carbon matrix is doped with heteroatoms (N, O and S) so that the polysulfides are adsorbed via a coordination bond-like mode between doping atoms and lithium atoms. For example, Huang et al. designed a porous 3D nitrogen-doped graphene (3D-NG) as a sulfur host for Li-S batteries [135].

- Introducing functional inorganic materials in cathode: Inorganic materials with nanosized structures and unique properties, such as inorganic oxide [136], metal sulfide [137], 2D metal carbides/nitrides [138, 139], and metal organic framework (MOF) [140], have been shown to have significant benefits as polysulfide trapping agents in Li-S batteries. (see section 3.3.1)

- Introducing functional organic molecules in cathode: The functional groups of organic compounds and polymers are capable of creating electrostatic attraction or chemical binding interactions with polysulfide. Chen et al. [141] discovered that the keto groups of anthraquinone (AQ) can not only stick to the surface of graphene by π-π stacking, but also create a strong Lewis acid-based chemical bond with polysulfide.

- Using functional binders in cathode: the goal in this situation is to replace the inert PVDF towards LiPSs with functional binders. For example, Xiong et al. created a hyperbranched binder called PPA by crosslinking poly (ethylene glycol) diglycidyl ether (PEGDGE) and polyethylenimine (PEI). PPA was proven to have strong confinement capabilities of LiPSs. [142]

- Functionalization of the separators: this approach is usually based on the modification of commercial separators on the cathode side in order to block the LiPSs: The separators can be modified by introducing physical/chemical barrier materials such as graphene, MOF, Mxene and metal oxide/sulfide.[143]

- Introduction of functionalized interlayer: This case differs from the modified separator in that the interlayer is self-standing [144]; the inserted interlayer can adsorb the polysulfide before it passes through the separator and offer additional reaction sites for further electrochemical reaction. Generally, these interlayers are made of conductive polymers (polyaniline, PANI; polypyrrole

PPy), or they are based on carbon nanotube (CNT), carbon fiber and their composite with inorganic materials.

In conclusion, several strategies have been proposed to address the problems related to Li-S batteries, and research in this sense is proceeding rapidly since the number of publications regarding LSBs has increased significantly in recent years. In the case of this thesis dissertation, two different approaches to mitigate the shuttle effect and produce cathodes for Li-S batteries based on innovative materials (High entropy oxides, HEO, and heteroatomic doped reduced graphene oxide embedded with ZnS nanoparticles, SN-rGO/ZnS) have been investigated. Consequently, in the next two chapters, the synthesis methods of these two materials, their chemical-physical characterization, as well as the production of cathodes for Li-S based on them, and the electrochemical results obtained will be discussed.

Chapter 4

High entropy oxides (HEOs)

4.1 Entropy stabilization and HEOs properties

The concept of high entropy material is relatively recent; the first publications relating to this topic date back to 2004 [145], [146], and was initially applied to metallic materials in order to investigate the possibility of obtaining new alloys characterized by a very varied composition. The definition of high entropy alloy (High Entropy Alloy, HEA) was not immediately unambiguous: initially, HEAs were defined based on the complexity of their composition ("alloys made up of at least five metallic elements, each of which with a molar concentration between 5 and 35%"); to date, to define an alloy, but more generally any material, as "highly entropic", it must be characterized by a threshold value of configurational entropy [147] The configurational entropy is given by the Boltzmann equation:

$$\Delta S_{conf} = -k_b \ln W \tag{4.1.1}$$

Where k_b is the Boltzmann constant ($1.381 \cdot 10^{-23}$ J$\cdot$ K^{-1}) and W denotes the number of ways in which the sample's atoms or molecules can be organized while retaining their total energy unchanged (in other words, W represents the number of isoenergetic microstates that the system can adopt).
For a solid solution consisting of n-components, in which the i-th component is

characterized by a mole fraction Xi, its ideal configurational entropy is given by:

$$\Delta S_{conf} = -R\sum_{i=1}^{n} X_i \ln X_i \tag{4.1.2}$$

Where R is the constant gas 8.314 J $\cdot$ mol^{-1}K$-$1. Considering a solid solution of an equi-atomic metal alloy consisting of n components, its configurational entropy is given by:

$$\Delta S_{conf} = -k_b \ln W = -R\left(\frac{1}{n}\ln\frac{1}{n} + \frac{1}{n}\ln\frac{1}{n} + ... + \frac{1}{n}\ln\frac{1}{n}\right) = -R\ln\frac{1}{n} = R\ln n \tag{4.1.3}$$

As shown in the Table 4.1, the configurational entropy of an alloy strongly depends on n:

Table 4.1 Values of ΔS_{conf} in function of n

n	1	2	3	4	5	6	7	8	9
ΔS_{conf}	0	0.69	1.10	1.39	1.61	1.79	1.95	2.08	2.20

According to the most recent definition of HEAs, a high entropy alloy (but more generally a material) must satisfy the following condition (at 25°C):

$$\Delta S_{conf} \geq 1.5R \tag{4.1.4}$$

In the case of an alloy that is generated by the mixing of different elemental components, the formation of a phase is thermodynamically controlled by the Gibbs free energy, G, which is linked to the enthalpy, H, and the entropy through the following equation:

$$\Delta G_{mix} = \Delta H_{mix} - T\Delta S_{mix} \tag{4.1.5}$$

The temperature T is the temperature at which the different elements are mixed. The term ΔH_{mix} includes various contributions (configurational, vibrational, electronic and magnetic), but the most important one, which makes the others negligible, at least as far as this discussion is concerned, is the configurational one. [147] From equation 4.1.5 it can be understood that it is the competition between the factors ΔH_{mix} and -TΔS_{mix} that determines the formation of solid phases following the mixing of the elemental components. A markedly negative ΔH_{mix} value favors

the formation of intermetallic compounds and bulk metallic glasses (BGMs). On the other hand, the entropic contribution pushes towards systems made up of solid solutions characterized by a highly heterogeneous structure in the case of HEAs. Therefore, At high temperatures, ΔS_{mix} can significantly lower the free energy and favor the generation of solid solutions. The ΔH_{mix} is given by the following equation:

$$\Delta H_{mix} = \sum_{i=1, i\neq j}^{N} 4\Delta H_{AB}^{mix} x_i x_j \tag{4.1.6}$$

Where N is the number of elements present in the alloy (usually no more than six) and x_i and x_j are the atomic percentages of the i-th and j-th elements in the alloy, and is the enthalpy of mixture of the equiatomic AB alloy. Just as in binary alloys, also in HEAs the difference in atomic radius δ affects the formation of solid solutions; for a high entropy alloy, δ is defined as:

$$\delta = \sqrt{\sum_{i=1}^{N} x_i \left(\frac{1 - d_i}{\sum_{i=j}^{N} x_j d_j} \right)^2} \tag{4.1.7}$$

Where d_i and d_j are the atomic radii of the i and j-th species. From Figure 4.1 it can be seen that there are ranges of combinations of the three aforementioned parameters that lead to the stabilization of solid solutions, intermetallic compounds or bulk metallic glasses. In particular, HEAs made up of solid solutions have a ΔS_{mix} within a range of 12-17.5 J/(molK) and low values of δ, intermetallic compounds prevail if the ΔS_{mix} range varies from 11 to 16 J/(molK) and for higher δ, while BMGs are favored for low ΔS_{mix}, high δ values and negative ΔH_{mix}.

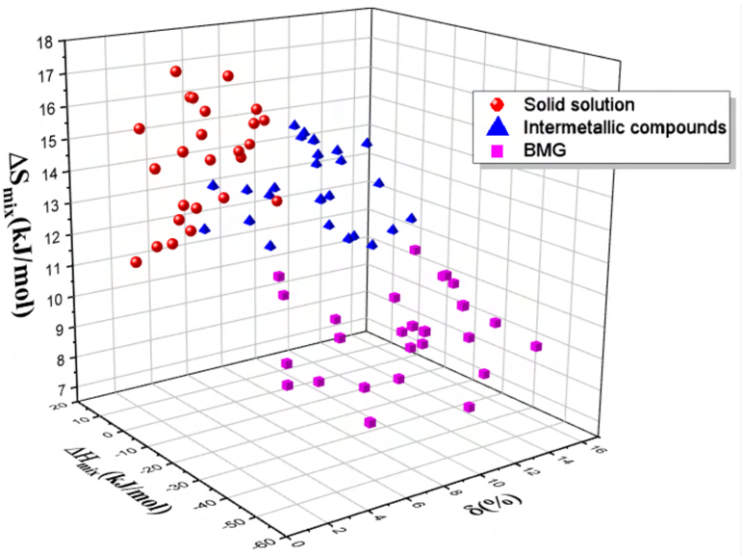

Fig. 4.1 Effect of the ΔS_{mix} and ΔH_{mix} on the formation of high entropy alloys, intermetallic compounds and BMGs.

The first high entropy oxides were synthesized by Rost and others in 2015 [148] starting from an equi-molar mixture of MgO, ZnO, CoO, CuO, NiO. The selection of the starting binary oxides was made following these guidelines:

- Crystal structure diversity for at least two components
- The presence of at least one pair of oxides that do not have extensive and mutual solubility.
- The metals of the oxides must be isovalent in order to guarantee electroneutrality even when the cation ratios are varied.

The material obtained by Rost's group through sintering at 1000°C exhibited a chaotic multiphase to single rock salt phase transition around 850-900°C. In order to verify the role of pushing force played by entropy in this transformation, it is useful to refer to figure 4.2 (a), which reports the value of configurational entropy in a solid solution of N components as a function (I) of the number of oxides/components (N) present in the material and (II) their concentration Mol%, X_N. In particular, it can be seen how, as the number of species present in the composition of the material increases, the entropy increases and how, with the same N, the maximum entropy value is reached in correspondence with the condition of equimolar composition. As

a consequence, as shown in Figure 4.2 (b-f), the temperature at which the system becomes monophasic has a minimum when all N components are present in an equimolar ratio, confirming the key role of configurational entropy in stabilizing the structure of the single phase material.

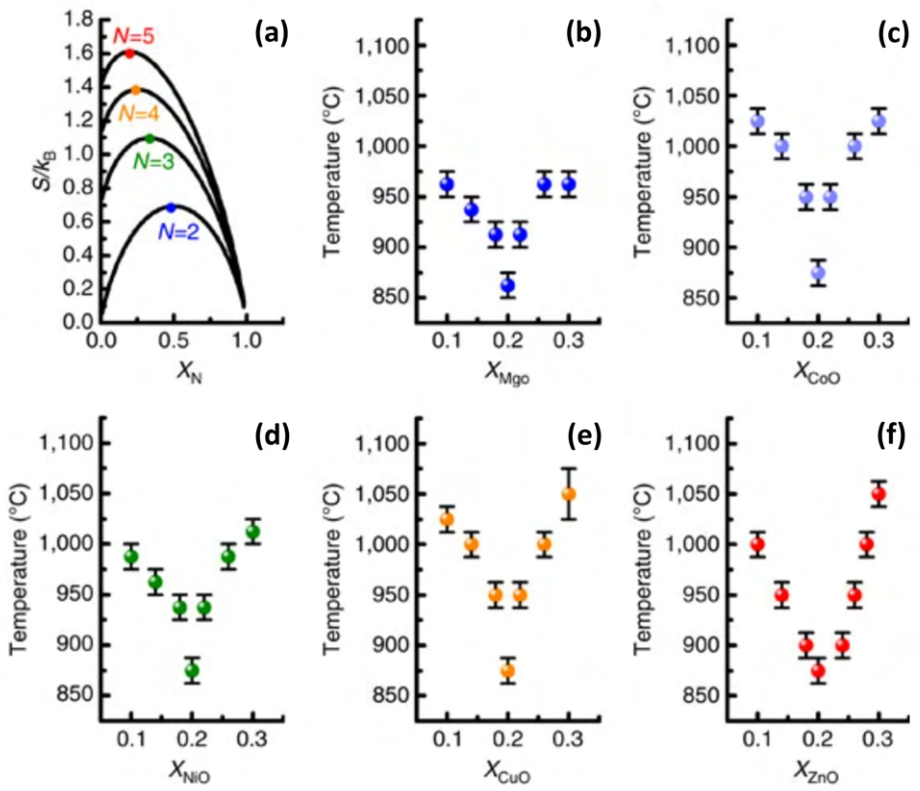

Fig. 4.2 a) Value of configurational entropy in a solid solution of N components as a function (I) of the number of oxides/components, N, present in the material and (II) their concentration Mol%, X_N. (b-f) Partial phase diagrams show how the single-phase transition temperature varies as a function of composition. It can be noticed that for each component, the transition temperature is minimal in correspondence with the equimolar composition. Reproduced from [148]

4.2 HEOs in Lithium-sulfur batteries

Since HEOs are relatively recent materials, their fields of application still need to be explored in depth. In the context of LSBs, it has already been mentioned (section 3.3.1) that metal oxides are materials widely used to produce cathodes capable of

alleviating the shuttling of LiPSs. Catalytic activity is mainly related to metal cation centers, and recently, multicomponent metal oxides have been shown to be an efficient regulator of soluble LiPSs due to the synergistic effect of several metal cations. For example, materials such as the spinel $NiFe_2O_4$ and $NiCo_2O_4$ demonstrated to have enhanced chemical adsorption of LiPSs when compared to the single metal oxides. [149] In this sense, HEOs are very interesting materials for applications in LSBs since they possess a highly polar surface capable of offering active sites for chemically anchoring and catalyzing the conversion of LiPSs. The first to verify the effective interaction between HEOs and LiPSs were Zheng et al. [150], who performed theoretical density functional theory (DFT) calculations to evaluate the binding energy and bond distance between the (100) plane of HEOs with Li_2S_6. The results showed great potential for interaction between the two materials. The theoretical results were confirmed by x-ray photoelectron spectroscopy (XPS) carried out on the pristine HEOs powders and on the same materials after interacting with a LiPSs solution. The Ultra Violet-Visible Spectroscopy (UV-VIS) technique was also used to evaluate the presence of LiPSs in the supernatant of a solution that interacted with HEOs, and even in this case, the result highlighted a good interaction HEOs/LiPSs. Similarly, Tian et al. [151] synthesized HEOs nanofibers and carried out the same chemical-physical tests, obtaining similar results to Zheng ones.

Consequently, it was decided to investigate the possibility of using these high-entropy materials in the context of Li-S batteries, using the "double-layer" approach which aimed to mitigate the shuttle effect by restraining the LiPSs on the cathodic side. The outcomes of the synthesis, characterization, and application of these materials within a Li-S cell are discussed in subsequent sections of this chapter.

4.2.1 HEOs synthesis and chemical-physical characterization

Typically, HEOs are synthesized by mixing the precursors via ball milling followed by a solid-state reaction at high temperatures. However, this approach is both energy and time-consuming. In this work, the synthesis that was used was similar to the hydrothermal one, but significantly faster and energy-saving. [152, 153] A hydrothermal synthesis usually consists of two steps: a first in which the precursor solution is heated to around 150-180 °C for a long time (5h to 2 days) and a second

calcination step at high temperatures. In the case of this synthesis, although the second calcination step is still necessary, the first step is significantly reduced in terms of time (1h) and temperature (130 °C) thanks to the use of a microwave oven (see Figure 4.3 for a schematic representation of the synthesis route). In particular, Nickel sulfate hexahydrate ($NiSO_4.6H_2O$; Merck), copper sulfate pentahydrate ($CuSO_4.5H_2O$; Merck), magnesium sulfate heptahydrate ($MgSO_4.7H_2O$; Merck), cobalt sulfate heptahydrate ($CoSO_4.7H_2O$; Merck) and zinc sulfate heptahydrate ($ZnSO_4.7H_2O$; Merck) were used as nickel, copper, magnesium, cobalt and zinc precursors, respectively. Equimolar amounts of the metal salts were separately dissolved in deionized water to obtain 0.02 M solutions. Then, 40 mL of the aqueous salt solution (0.1 M) was added to 10 mL sodium hydroxide NaOH solution (1.2 M) and was magnetically stirred for 15 min. Subsequently, the solution was placed in the microwave oven (Milestone flexiWAVE) and exposed to microwave irradiation at 130 °C for 1 h, with a heating time of 5 min (21 °C/min). The solution was then centrifuged at 7000 rpm (by Thermo Scientific SL16 centrifuge, Thermo Fisher) to separate the precipitated powder from the solution. The powder was washed several times with deionized water and ethanol (Aldrich). After drying, the powder was treated at 930 °C, in air, for 5 h.

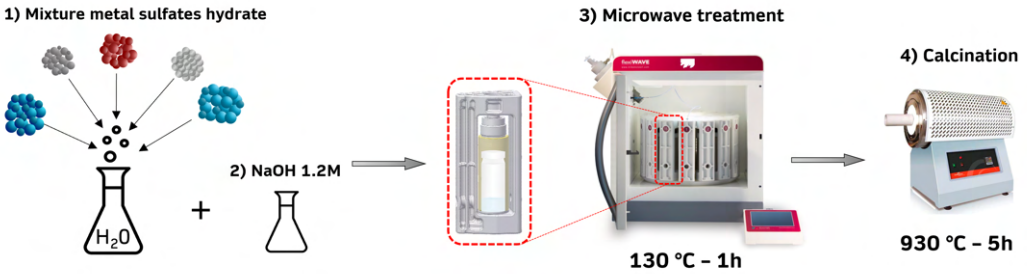

Fig. 4.3 Microwave synthesis route of HEOs materials. (1) preparation of the equimolar acqueous solution 0.1M (2) addition of the NaOH solution 1.2M (3) microwave heating (4) calcination step in air.

The percentage yield of the reaction, after the necessary washing steps and high temperature heat treatment, is in the range 23-25%.

Microwave effects: At this point, it may be helpful to delve deeper into the particularities that distinguish the synthesis approach via microwave heating. In a microwave treatment, heating occurs due to two major mechanisms: dipolar polarization and ionic conduction. Microwaves commonly heat any material having mobile electric

charges, such as polar molecules or conducting ions in a liquid or solid. During microwave heating, polar molecules such as water molecules attempt to orient with the fast changing alternating electric field; hence, heat is generated by the rotation, friction, and collision of molecules (dipolar polarization mechanism). In the case of ions, any ions present in solution will move within the solution based on the orientation of the electric field, and because this is constantly changing, the ion will proceed continually shifting directions through the solution, causing a local temperature rise due to friction and collision, as depicted in Figure 4.4 (a). [154] Figure 4.4 depicts a comparison of temperature profiles produced by (b) microwave heating and (c) oil bath heating. Microwave technology, as a result of these principles, can enable quick volumetric heating with shorter response times and higher reaction rate, selectivity, and yield when compared to conventional heating methods. Conversely, traditional heating often includes the use of an electric furnace or an oil bath to heat the reactor walls and subsequently the reactants by convection or conduction. The reactor serves as a medium for thermal energy to be transferred from the external heat source to the solvent, and then to the reactants. The sample's core takes substantially longer to reach the desired temperature.

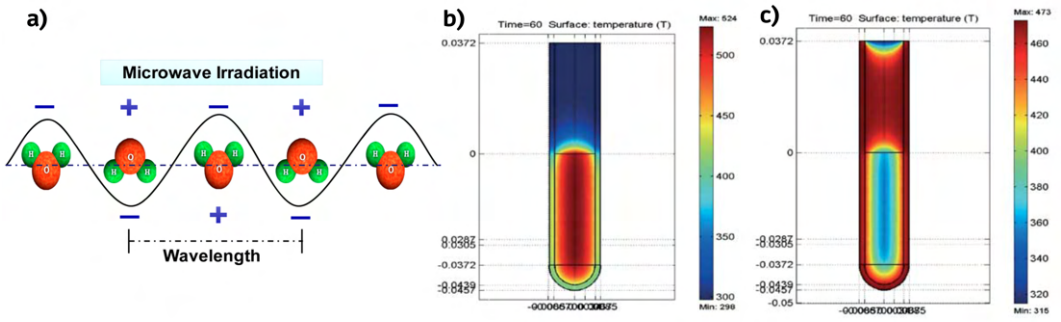

Fig. 4.4 (a) dipole polarization of water molecules in an electric field, (b) temperature profile of a vessel under microwave heating and (c) in the case of an oil bath.

This type of route often results in heat gradients across the bulk media, as well as inefficient and nonuniform reactions, which can cause major problems in scale-up production. Microwave heating, on the other hand, can heat specific materials without heating the entire furnace or oil bath, saving time and energy. It has been proven by numerous experiments that microwave heating is capable of increasing the speed of chemical reactions by several orders of magnitude. However, despite

numerous efforts to determine precisely the mechanism by which the reaction is accelerated, a single answer has yet to be identified. In particular, today's debate is focused on whether there are the "specific microwave effects" or "non-thermal microwave effects". [155, 156] Examples of "specific microwave effects" consist of superheating, selective heating of polar species in a microwave transparent (or at least less absorbing) medium, the formation of "molecular radiators" by direct coupling of microwave energy to specific reagents in homogeneous solution, and the elimination of vessel wall effects caused by inverted temperature gradients. Microwave heated liquids can have boiling points that are 10-20 °C higher than the usual boiling point at atmospheric pressure, making comparison of reaction rates under conventional and microwave heating problematic. Variations in activation energy, higher collision efficiency due to mutual orientation of polar molecules, and probable excitation of rotational or vibrational transitions are among the reported "nonthermal microwave effects". Perreux et al. postulated that microwave irradiation boosts the pre-exponential factor A in the Arrhenius law $k = A \exp(-\Delta G/RT)$, which represents the probability of effective molecular impacts. The mutual orientation of polar molecules participating in the process can significantly influence collision efficiency. Other studies [157, 158] report the fact that in most cases the increase in the speed and efficiency of the reaction is simply due to thermal effects deriving from the reaction temperatures that can be rapidly reached with this heating method. Conner and Tompsett [159] argued that the major effect of microwave irradiations on chemical processes is that they can change the reaction profile (or relative temperatures) instantly and/or periodically. These variations are caused by large disparities in microwave absorption by molecular species, particularly at interfaces. Microwave irradiation can thus greatly boost reaction rates by periodically supplying a more favorable reaction coordinate. In conclusion, it can be said that the scientific debate on how microwave radiation influences the speed with which reactions occur is still open and requires further clarification. However, all the cited studies still observed the beneficial effect of the efficiency of this type of heating compared to the traditional one.

Physical-chemical characterization - Results

The physicochemical techniques used to characterize the HEO materials and the electrochemical techniques used to study the Li-S cells based on double layered cathodes with HEO materials are reported in Appendix B.1.

Figure 4.5 shows the XRD patterns of the powders produced by microwave synthe-

sis before and after calcination. The visible presence of distinct peaks suggested that at least a portion of the microwave-irradiated powder was crystalline even before the thermal treatment at high temperature. $Co(OH)_2$ (card no. 98-002-6763, hexagonal, marked as ♦) and ZnO (card no. 98-002-6170, marked as •) crystalline phases can be identified in the sample; however, the presence of brucite $Mg(OH)_2$ and $Ni(OH)_2$ phases cannot be ruled out because their XRD reflexes are partially overlapped with those associated with the identified phases. The XRD distinctive peaks of the hydroxide vanished after calcination at 900 °C, but the pattern remained multiphasic (evident presence of ZnO phase). The diffraction peaks at 2θ values of 36.8, 42.7, 62.0, 74.1, and 78.2 are characteristic of (111), (200), (220), (311) and (222) planes of the rocksalt crystal structure (CoCuMgNiZn)O HEO (peaks designated as ♣, space group Fm-3 m) [160] respectively, but tiny peaks due to hexagonal ZnO are also seen. However, by raising the temperature to 930 °C, it can be noted that the material becomes monophasic, with the disappearance of the peaks associated with the ZnO phase and leaving only those relating to the rocksalt structure.

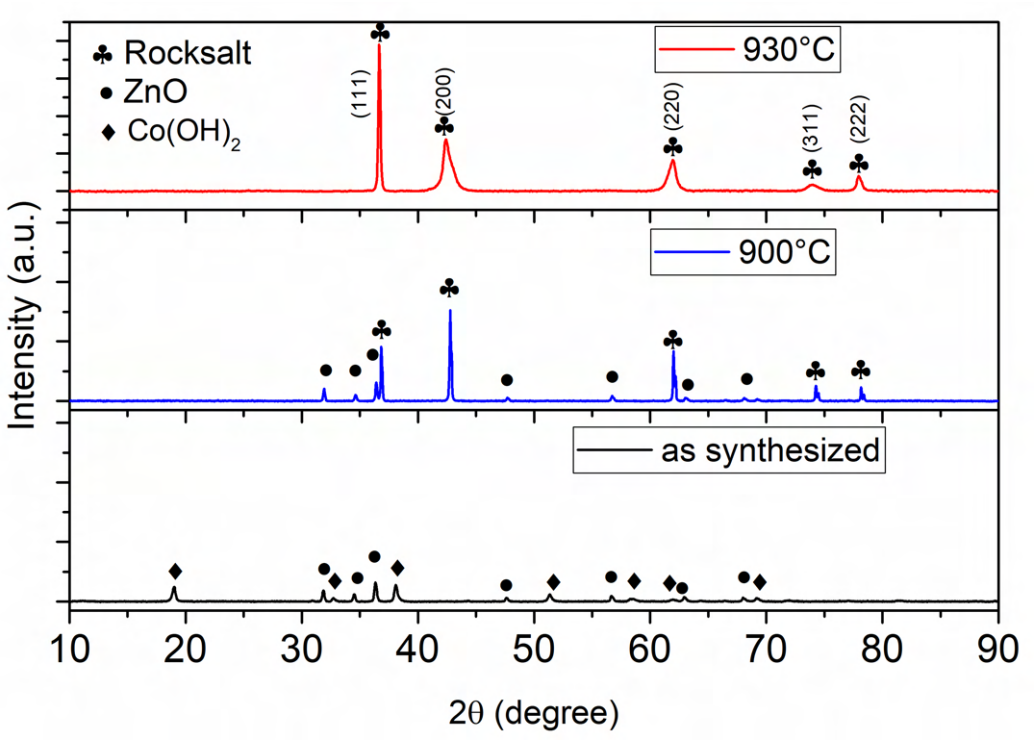

Fig. 4.5 (a) XRD of the materials as extracted and washed from the MW vessel (black line), after the calcination step at 900 °C (blue) and after the calcination step at 930 °C. the measurements were performed with Cu K_α radiation.

Furthermore, the relative intensity of the major peaks, (111) and (200), in the experimental spectra shown in Figure 4.5 is reversed compared to the theoretical one of the rocksalt structure: The peak connected with the (200) plane is usually more prominent than the one associated with the (111) plane. In addition, the XRD pattern displays a noticeable peak broadening of the (200), (220), and (311) reflections, but not the (111) and (222) reflections. This could be due to anisotropy in crystallite size or anisotropic lattice disorder, which occurs frequently in HEO materials as a result of cation/oxygen displacements in the lattice with respect to their theoretical position. The divergence from the ideal rocksalt structure, as reported by Berardan et al. [161], is mostly determined by the sample's thermal history, and the broadening along the (200), (220), and (311) reflections can be attributed to greater cationic site density along these crystallographic planes [162]. The N_2 adsorption/desorption study of HEO reveals a type IV isotherm [163] (see Figure 4.6 a), with pore size distribution showing the presence of mesopores (Figure 4.6 b), and a cumulative pore volume of 0.0847 cm^3/g. The BET SSA is 32.29 m^2/g, which is similar with HEO BET values obtained using mechanical ball milling [164]. The SSA may be an additional factor in cell capacity stabilization via surface adsorption of LiPSs, but it plays a limited impact in this case compared to the chemical interaction [165] because the value is fairly low.

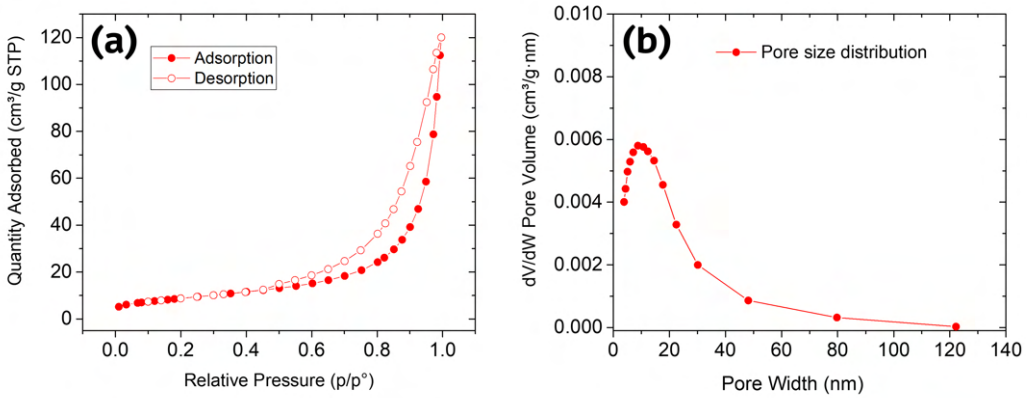

Fig. 4.6 (a) N_2 adsorption-desorption isotherms of HEO and (b) pore-size distribution curve of the same sample.

In order to investigate the morphology of HEOs, FESEM analysis was conducted on the powders obtained with the calcination treatment at 930°C, the results of which are shown in Figure 4.7, where FESEM micrographs at different magnification are

reported. As can be seen, HEOs are made up of grains of agglomerated particles with a fairly irregular shape whose dimensions are within the nano-micrometric scale and with well distributed small pores located at the grain boundaries (Figure 4.7) and similar in morphology and size to those obtained by hydrothermal synthesis. [166]

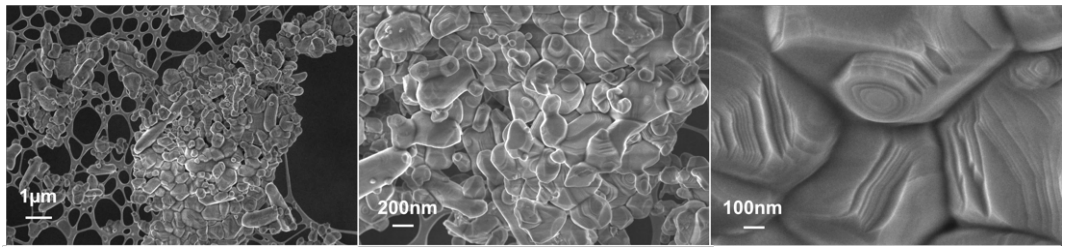

Fig. 4.7 FESEM micrograph of the HEO powders at different magnification, which highlights the typical morphology of the synthesized materials.

Energy-dispersive X-ray spectroscopy (EDX) also allowed mapping of the examined samples to verify their homogeneity from a compositional point of view. The results of the EDX signals for the K_α emission energies (4.8) of Mg, Ni, Zn, Co and Cu confirm the chemical and microstructural homogeneity of the sample since their distribution is highly uniform throughout the entire analyzed area at the micrometer level. Furthermore, the compositional analysis performed at the punctual level (right side of Figure 4.8) allowed to estimate the average atomic composition of O, Mg, Co, Ni, Cu, and Zn in HEO to be around 49.43%, 9.43%, 9.80%, 9.19%, 9.45%, and 12.7%, respectively, which is nearly equiatomic among the metals, excluding the possibility of a particular element segregating on the sample surface.

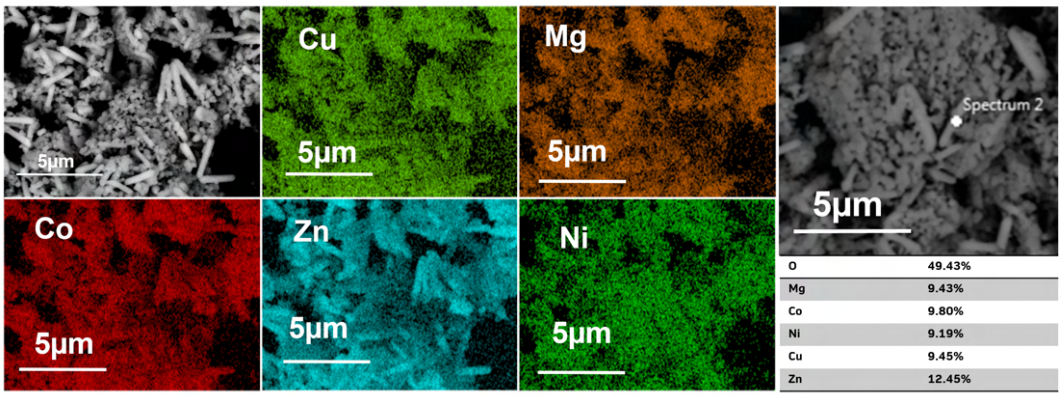

Fig. 4.8 EDX micrographs of the HEO powder which highlights the uniform distribution of the different metals in the sample. In the right part of the figure is reported a punctual EDX analysis and the calculated atomic percentages.

The Transmission electron microscopy (TEM) technique then highlighted (see Figure 4.9) the presence of lattice fringes, whose average distances between adjacent lattice planes were identified and calculated using the instrument software in two different areas. The values obtained, 0.241 nm and 0.21 nm can be associated with the (111) (Figure 4.9 a) and (200) (Figure 4.9 b) crystalline planes of the material, respectively, in agreement with the X-ray diffraction data.

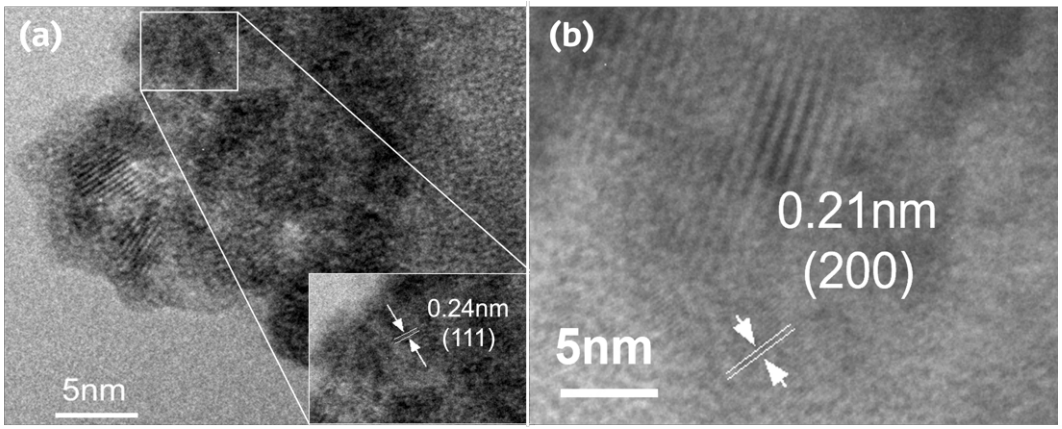

Fig. 4.9 TEM micrograph of two different area of the HEO sample, from whose it was possible to estimate the distances between adjacent lattice planes. (a) Fringes of (111) planes and (b) of the (200) planes.

In order to evaluate the polysulfide adsorption capability of HEOs material, a visual adsorption test under argon atmosphere was performed. More precisely, a solution 0.1 M of Li_2S_6 was prepared, directly reacting Li_2S and S_8 (ratio 1:5 in weight) into a mixture of DME and DIOX (1:1 by volume) for 72 h at 70 °C, under continuous stirring in an argon atmosphere. The resulting brownish-red Li_2S_6 solution was then diluted to 1 mM solution for the polysulfide adsorption test. Afterward, 50 mg of HEOs powders were added to 4 ml of the prepared 1 mM solution, which was stirred and allowed to stand for 12h.
As can be seen from Figure 4.10 a, which shows the pristine 1 mM Li_2S_6 solution used as a reference on the left and the one that interacted with the HEOs on the right, the latter became almost transparent after 12 h. Afterward, the solid product (HEO-Li_2S_6) was filtered and dried in glove box in such a way as to subject it to XPS analysis, while the pristine Li_2S_6 solution and the supernatant of the solution that had interacted with the HEOs were loaded into quartz cuvette sample holders inside the argon-filled glove box, then sealed and placed in closed vials. The vials were

brought out of the glove box to the Jenway 6850 double beam spectrophotometer to perform the UV–vis analysis, the results of which are shown in Figure 4.10 b. The pristine Li_2S_6 solution's UV-vis adsorption spectra exhibits three UV absorption bands between the 310-350 nm, 400-450 nm, and 550-650 nm regions. S_6^{2-} absorbs strongly at roughly 310 nm [167], with weaker bands observed around 420 nm (S_4^{2-}) and 610 nm S_3^{2-} [168]. When the solution is exposed to HEO powder, the typical bands of Li_2S_6 disappear; only a faint peak in the region from 300 to 400 nm arises from the interaction between HEO and Li_2S_6, revealing HEO's ability to adsorb LiPSs [169].

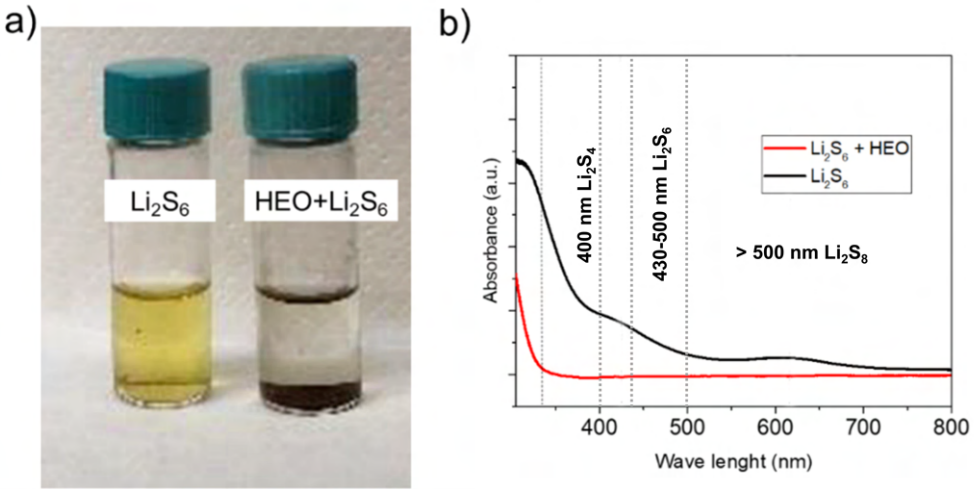

Fig. 4.10 (a) Picture of a Li_2S_6 adsorption test result using HEO powder; b) UV-vis absorption spectra of the pristine Li_2S_6 solution and the supernatant of the solution after having interacted with HEO powder.

Moreover, further confirmation of the chemical interaction between HEO and Li_2S_6 is offered through XPS analysis of HEO powder both before and after the Li_2S_6 adsorption test, as depicted in Figure 4.11. The more evident interactions are observed in the high-resolution spectra of Ni2p, Mg1s, and Zn2p [150]. In the case of Ni2p, Figure 4.11 (a), the spectra can be fitted with two spin-orbit doublets and two shake-up satellites. The symmetric shape of the primary Ni2p peaks and the presence of a prominent satellite peak at a higher binding energy point to the coexistence of Ni^{2+} and Ni^{3+} states in the HEO material [170]. All peaks exhibit a shift of approximately 0.40 eV towards higher binding energies after the Li_2S_6 adsorption test. This shift is symptomatic of the alteration of the chemical surroundings of the surface of the Ni atoms, providing evidence of a chemical interaction between nickel

and Li_2S_6 [150]. Additionally, the high-resolution spectra of Mg1s and Zn2p exhibit similar, shifts, with increases of 0.3 eV and 0.1 eV in binding energy, respectively (Figure 4.11 c and d). These results are attributed to the electropositive nature of magnesium and zinc, which induces electron displacement away from the metal core in the presence of LiPSs, resulting in increased binding energy [171]. Figure 4.11 (b) presents high-resolution O1s spectra, which can be deconvoluted into three distinct peaks [172]. The peak at 529.3 eV corresponds to lattice oxygen and originates from the ionic metal-oxygen bond. At 531.3 eV, there is a peak attributed to adsorbed oxygen species, while the peak at 532.6 eV is linked to -OH groups from adsorbed moisture in HEO. Following contact with Li_2S_6, all of these peaks shift by 0.3 eV towards higher binding energies. In this context, Zheng et al. [150] proposed through DFT calculations that an interaction occurs between oxygen species in HEO and lithium within LiPSs due to the interfacial compatibility between HEO and LiPSs. It is worth noting that the 0.3 eV binding energy shift in the O1s spectra of Figure 4.11 is relatively small, and the peak intensities remain largely unchanged from pristine HEO. Consequently, the formation of a chemical bond between lithium polysulfides and oxygen appears unlikely. In summary, XPS analysis indicates that the primary factor contributing to the absorption of Li_2S_6 is the multi-cation system within the HEO material.

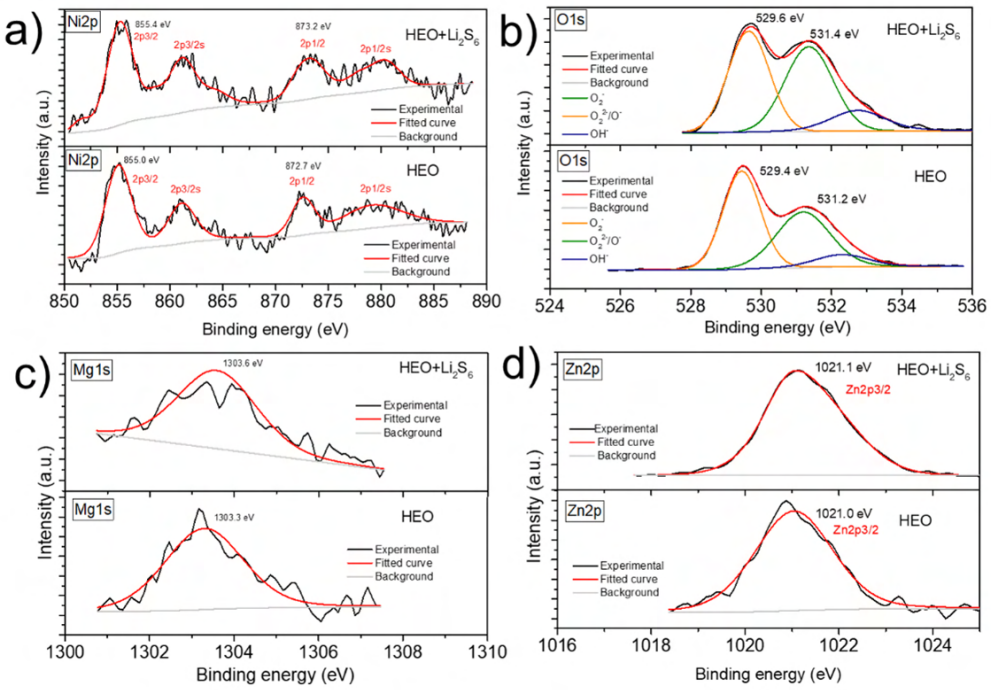

Fig. 4.11 High resolution XPS analysis of HEO powders before and after the absorption test in Li_2S_6 solution of a) Ni 2p, (b) Mg 1s, (c) O1s and (d) Zn2p (to better visualize the shift, only the $Zn2p_{3/2}$ peak is shown).

4.2.2 Preparation of double layered HEO based cathodes and Electrochemical characterization

In order to investigate the electrochemical behavior of HEO in a Li-S cell, I adopted the "double-layer" approach, in which a second layer of HEO covers a defined "standard" sulfur cathode. In this way, the HEOs, which are not particularly electronically conductive nor capable of hosting sulfur in their porosities, are not mixed directly in contact with the sulfur. The latter is in the first layer in close contact with the conductive carbon alone, in such a way as to facilitate electrochemical reactions. On the contrary, the second layer, rich in HEO, acts as a "barrier" for the migration of LiPSs towards the anode. The Figure 4.12 shows a scheme of the "double-layer" electrode configuration and the coin cell 2032 used to perform the electrochemical characterization of the cathodes. All the working electrodes were prepared by solvent tape casting method. The slurry for the “standard” S cathode (STD) was prepared

using sulfur, Ketjenblack carbon (KB, EC-300 J, AkzoNobel) and poly(vinylidene difluoride) (PVdF, Arkema) in Nmethyl-2-pyrrolidinone (Sigma-Aldrich).

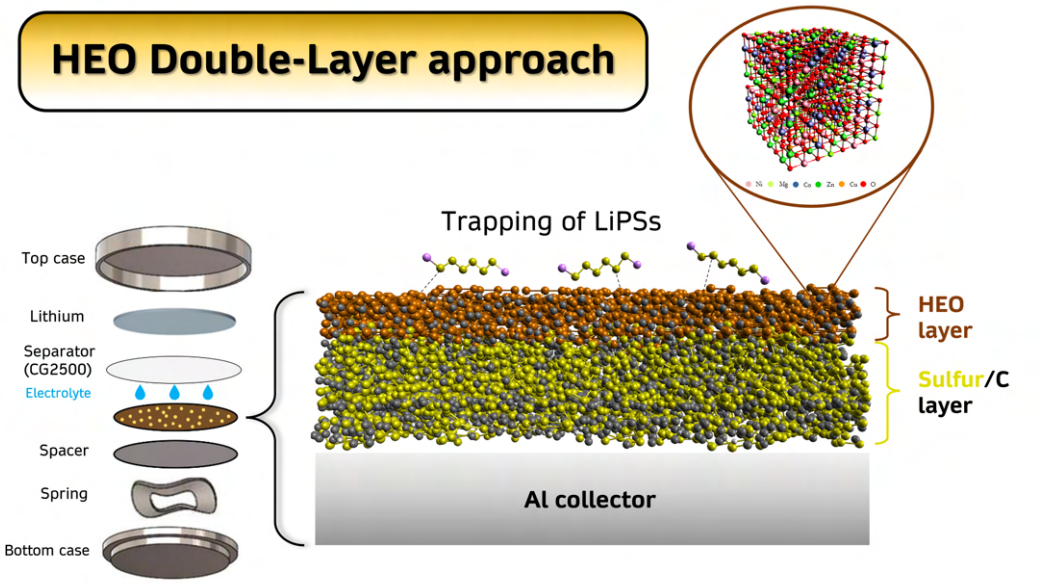

Fig. 4.12 Representative scheme of the approach of a double-layered cathode based on High Entropy Oxides (HEO) and the components that constitute a coin cell.

The composition of the "standard" electrode was established as 70% sulfur (S), 30% Ketjenblack (KjB), and 10% poly(vinylidenedifluoride) (PVdF) by weight for all the experiments in this section. This ratio was selected aiming to create a cathode with a substantial sulfur content. The intention was to achieve this using a straightforward mixing process while also considering the practical application of the electrodes and their scalability in an industrial context. The specific quantities of sulfur and Ketjenblack® were initially mixed by hand in an agate mortar. Afterward, this mixture was placed into a 2 mL Eppendorf tube. Then, an appropriate amount of PVdF solution (with a concentration of 10% in NMP) was added, along with an additional volume of NMP to achieve the desired ink viscosity. Finally, the Eppendorf tube was sealed and subjected to ball milling for a duration of 15 minutes at a frequency of 30 Hz. The final mixture was mechanically deposited on the aluminium current collector by Doctor Blade technique. The blade was adjusted for 200 μm deposition using an automatic film applicator (Sheen 1133N) with a speed of 50 mm s^{-1}. After the slurry deposition the coated aluminium foil dried at 50 °C in air. For the second layer coating, the selected ratio adopted between HEO, KB

and PVDF was: 90:0:10 and 80:10:10, respectively, named as STD+HEO90 and STD+HEO80. The blade was adjusted at 200 μm for the second layerdeposition . After solvent evaporation at 50 °C for 90 min, disks of 1.76 cm^2 were punched out, vacuum dried at 40 °C for 4 h (in Buchi Glass Oven B-585), and then transferred into an argon-filled dry glove box (MBraum Labstar, H_2O and O_2 content 1 ppm) for cell assembly. In the double-coated cathode, sulfur loading was 1.0 mg/cm^{-2}. The electrodes were assembled in 2032 coin-type cells with lithium disk (Chemetall Foote Corporation, ∅ 16 mm diameter) as counter electrode and Celgard 2500 separator, (25 μm thickness, ∅ 19 mm diameter). The electrolyte solution consisted of 1,2-dimethoxyethane (DME) and 1,3-dioxolane (DIOX) 1:1 *(v/v)* as electrolyte with 1.0 M lithium bis(trifluoromethanesulfonyl)imide ($CF_3SO_2NLiSO_2CF_3$, LiTFSI) and 0.25 M lithium nitrate ($LiNO_3$, 99.9%). The amount of electrolyte was calculated based on the sulfur content in each cathode, always maintaining a ratio of 10–11 μL of electrolyte per mg of sulfur.

Electrochemical results

The first electrochemical test that was carried out had the objective of evaluating the influence of HEOs on the redox reaction and conversion of LiPSs; in this sense, a very useful technique is cyclic voltammetry (CV), which was performed at the scan rate of 0.01 mV s^{-1} in the voltage range of 1.7–2.8 V vs Li/Li^+ . This type of analysis was carried out only on the standard sulfur sample and on the double coated cathode with the maximum amount of HEOs (90_{wt}%) since the aim of this characterization was to investigate the effect of HEOs on the reactions and kinetics of the Li-S cell. As a result, increasing the percentage of HEOs in the double layer permits emphasizing their role in this context.

As depicted in Figure 4.13 and Figure 4.14 (a) and (b), the CV profiles illustrate the characteristic occurrence of two pairs of redox peaks. These peaks are attributed to the cathodic reduction of sulfur (S) into long-chain lithium polysulfides at 2.27 V, followed by the conversion of the long-chain LiPSs into lower-order Li_2S_2 and Li_2S at 2.05 V. The two anodic oxidation peaks represent the process of oxidizing Li_2S into LiPSs and sulfur, occurring at 2.34 V and 2.38 V, respectively. Remarkably, when comparing the standard (STD) cathode (as seen in Figure 4.13 a and b) with the STD+HEO90 cathode, the former exhibits broader cathodic peaks with lower intensities. This observation corroborates the hypothesis of slower redox kinetics of LiPSs for both liquid/liquid and liquid/solid transformations for the STD electrode when compared with the double coated one. The CV curves shed to light the

significant influence of HEOs on the conversion of short-chain lithium polysulfides (Li_2S_x, $1 \leq x \leq 4$) into the ultimate Li_2S. This is evident as the reduction peak at 2.06 V and the oxidation peak at 2.35 V are more pronounced in the presence of the STD+HEO90 cathode compared to the STD cathode.

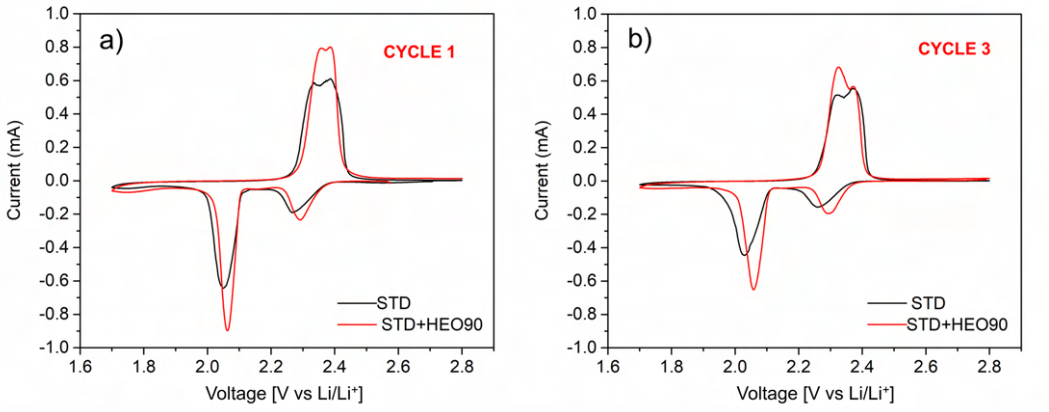

Fig. 4.13 (a) Comparison of the first cycle of the cyclic voltammetry performed at 0.01 mV s^{-1} for the STD sulfur electrode and the STD+HEO90 electrode and (b) comparison of the third cycle of the CV.

.

The onset potentials and peak potentials values can be found in Table 4.3; the onset potentials were determined using the method proposed by Yuan et al. [173], and the differential CV curves (dI/dQ) are presented in Figure 4.14(c) and (d). As indicated in Table 4.3, the inclusion of an HEO layer leads to a slight increase in the onset potentials for both the reduction of sulfur (S) and LiPSs. This increase can be attributed to the faster kinetics facilitated by HEO. In particular, for the STD cathode, a shift towards lower potentials in the reduction peaks is observed starting from the second cycle (as shown in Figure 4.13 and Figure 4.14 a). These differences between the first and subsequent cycles indicate a redistribution of active sulfur within the STD cathode towards a less stable state. Conversely, the overlapping peak positions in the CV of the STD+HEO90 cathode suggest a more reversible electrochemical reaction (as depicted in Figure 4.14 b).

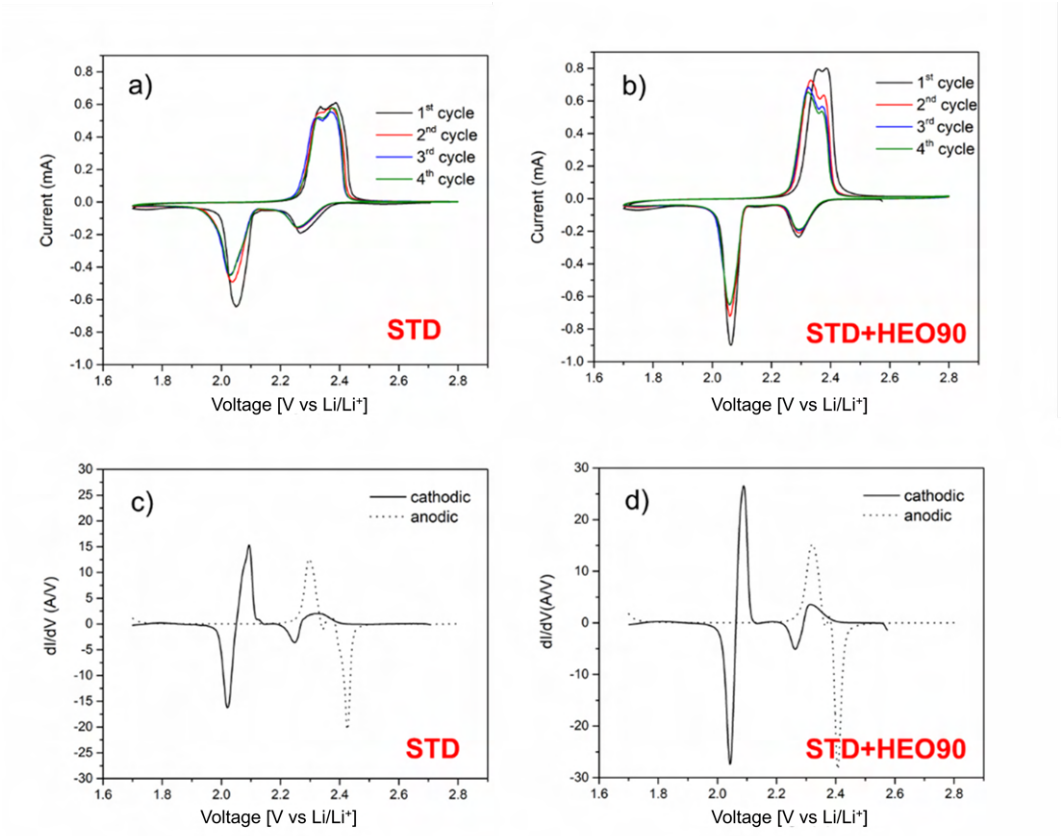

Fig. 4.14 Cyclic voltammetry measurements (four cycles) at 0.01 mV/s in the voltage range of 1.7-2.8 V vs Li/Li^+ of a) STD and b) STD+HEO90; c), d) corresponding derivative dI/dV, which helped to evaluate the onset of the electrochemical reactions.

Table 4.2 Comparison of different cathode materials for LIBs.

Onset potential [V]				
1^{st} cycle	I	II	III	IV
STD	2.37	2.12	2.22	
STD+HEO	2.39	2.11	2.24	
Peak Voltage [V]				
1^{st} cycle	I	II	III	IV
STD	2.27	2.05	2.33	2.38
STD+HEO	2.29	2.06	2.36	2.38
3^{rd} cycle	I	II	III	IV
STD	2.25	2.02	2.32	2.37
STD+HEO	2.29	2.06	2.35	2.37

To further explore the impact of utilizing a cathode double-coated with HEO on the redox kinetics of soluble intermediate LiPSs, cyclic voltammetry (CV) measurements were also conducted at different scan rates (from 0.1 mV s^{-1} to 0.5 s^{-1} mV. As illustrated in Figure 4.15, the linear correlation observed between the redox peak currents and the square root of the scan rate suggests that the rate-determining step in this process is the diffusion of LiPSs. The slopes of the curves in Figure 4.15 (panels c, d, and e) are directly associated with the respective Li^+ diffusion rates [174] through the Randles-Sevcik equation:

$$i_p = (2.687 \times 10^5) n^{\frac{3}{2}} A C_{Li^+} D^{\frac{1}{2}} \tag{4.2.1}$$

Where the constant term 2.687 $\times$ 10^5 has the unit of [C·mol^{-1}·V$^{\frac{1}{2}}$], n is the number of electrons transferred in a redox cycle, A is the electrode surface area [cm^2], C_{Li^+} is the concentration of Li^+ inside the cathodic material [mol·cm^{-3}] and D is the Li^+ diffusion coefficient [cm^2·s^{-1}]. Notably, the steeper slope observed for the STD + HEO electrode, in comparison to the STD electrode alone, indicates swifter Li^+ diffusion processes within the double-coated cathode. In particular, HEO amplifies the conversion of soluble Li_2S_4 into insoluble Li_2S (peak II). [175]
The activity of HEO materials in the Li-S cell is further investigated by galvanostatic charge/discharge testing at C/10 for the first three cycles, followed by a longer period of galvanostatic cycling at C/5 (250 cycles). These tests aim to assess the double-layer contribution and the impact of the layer composition on the performance of the Li-S cell. To delve deeper into this aspect, cathodes with two different HEO contents in the double layer, 80% and 90% by weight, were tested. This investigation aimed to determine which composition could maximize the advantages of HEO materials, as previously suggested by the results of cyclic voltammetry experiments, while also addressing their low electronic conductivity (10^{-8} S·cm^{-1}) [176]. All potentials are referenced against Li/Li^+ . It is important to underline that the mass loading of active material (sulfur) is very similar for all three samples (1 mg cm^{-2}), as is the quantity of electrolyte used in each cell (10 μL mg^{-1} of sulfur). Keeping these parameters unchanged, which can significantly influence the performance of a Li-S cell, allows for more accurate comparisons.

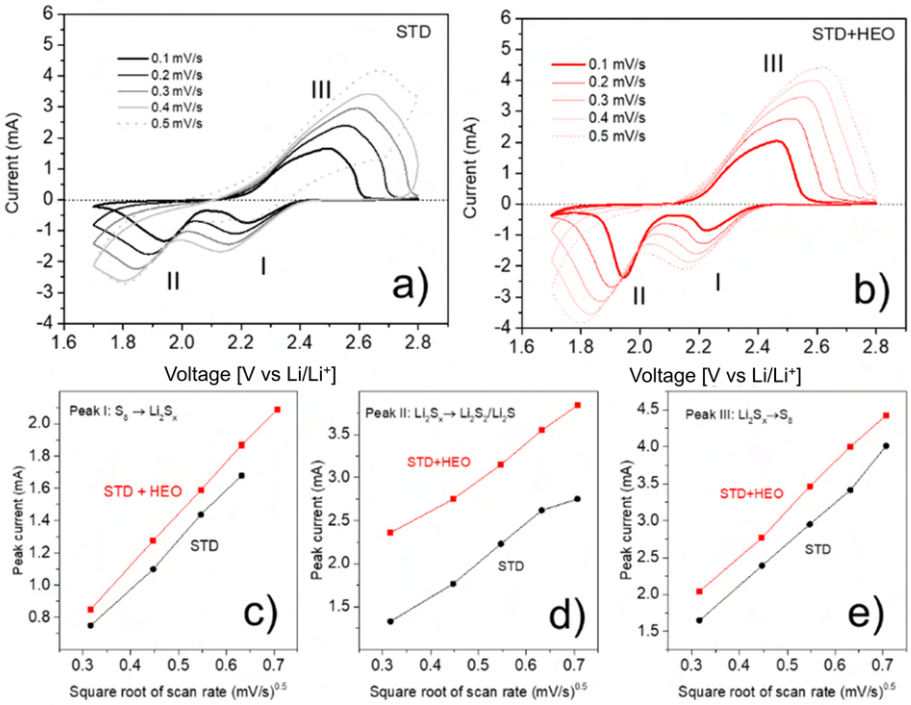

Fig. 4.15 Cyclic voltammetry measurements performed at different scan rates in the voltage range of 1.7-2.8 V vs. Li/Li^+ : (a) STD cathode, (b) double-coated cathode (STD+HEO90). The relationship between the peak current and the square root of the scan rate for the different reaction processes in STD and STD+HEO90 is associated to peak I (c), peak II (d), peak III (e).

As depicted in Figure 4.16, the standard (STD) cell exhibits an initial capacity of 778 mAh g^{-1} at C/10, whereas the STD+HEO90 and STD+HEO80 cells show initial capacities of 1173 mAh g^{-1} and 1175 mAh g^{-1}, respectively. It is evident that the inclusion of HEO in the double-layer leads to a higher specific capacity compared to the standard cell, resulting from more efficient sulfur utilization. A particularly interesting aspect observable from the discharge profiles of the cells is that the samples containing the double layer of HEO exhibit a more extended high potential plateau (2.3-2.1 V) compared to the STD sample. This demonstrates how the presence of HEO can increase the efficiency of sulfur conversion into long-chain polysulfides, as the plateau at around 2.2 V reflects the dissolution of S_8 in the electrolyte and its subsequent conversion to Li_2S_4. The higher capacity exhibited by the STD+HEO samples is therefore attributable to the confinement of LiPSs on the cathode side and the greater degree of conversion from S_8 to Li_2S_4.

It is worth to note that the addition of 10% carbon in the double layer (STD+HEO80) does not affect the capacity values at C/10, which remain the same in both STD+HEO80 and STD+HEO90 cells. Consequently, the capacity at low current regimes is solely attributed to the presence of HEO in the double-layer, excluding any significant contribution from the carbon additive. After 250 cycles at C/5, the specific capacity of STD+HEO90 and STD+HEO80 is 528 mAh g^{-1} and 650 mAh g^{-1}, respectively. The capacity retention for STD+HEO90 is 61%, and for STD+HEO80, it is 69%, considering the values at the initial cycle at C/5 and after 250 cycles at the same current regime. These differences in capacity retention between these cells are primarily due to the higher conductivity of the double layer in STD+HEO80, which includes an additional 10_{wt}% carbon. In fact, when we increase the C rate from C/10 to C/5 in the STD + HEO90 cell (as shown in Figure 4.16 c), we observe a 16% reduction in capacity. In contrast, the STD+HEO80 cell (Figure 4.16 d) only experiences a 7% capacity loss, indicating a more even distribution of non-conductive sulfur on the conductive carbon in the STD+HEO80 cathode. This improved distribution leads to enhanced performance at higher current rates. Therefore, adding 10_{wt}% of carbon in the double layer has the sole effect of improving the specific capacity after 250 cycles at C/5.

It is important to emphasize that, although the capacity retention of the two double layer samples after 250 cycles at C/5 was similar to that exhibited by the STD cathode (about 45%), the capacity in absolute terms was higher for both double layer cathodes (657 and 528 mAh g^{-1} for HEO80 and HEO90 vs 450 mAh g^{-1} for the STD cathode, with the same sulfur mass loading of the electrodes). These findings highlight the long-term stability of the STD+HEO80 and STD+HEO90 cells, and the coulombic efficiency remains relatively constant at 99.3% and 98.7% over 250 cycles at C/5 respectively, indicating limited side reactions in the double-layered cells.

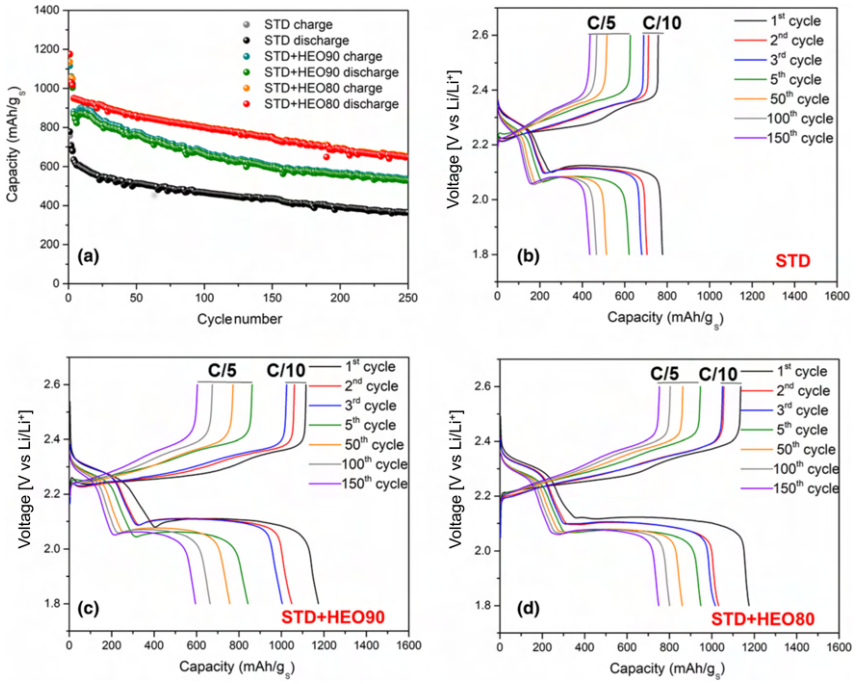

Fig. 4.16 Cycling performance of STD, STD+HEO90 and STD+HEO80 cells: the protocol consists of three formation cycles at C/10 followed by 250 cycles at C/5. The panels show the capacity versus voltage plots for: b STD cell, c STD+HEO90 cell, d STD+HEO80 cell. Sulfur loading: 1.0 mg cm^{-2}, electrolyte to sulfur ratio: 10 μl mg^{-1}

The dQ/dV (derivative of capacity with respect to voltage) profiles at different cycle numbers of the cells when operating at C/5 (as shown in Figure 4.17) demonstrate that STD + HEO90 and STD + HEO80 cathodes contribute more significantly to the reduction reaction at lower voltages. This is due to the conversion of short-chain LiPSs into the final product, Li_2S. Specifically, the peaks at 2.05 V (during reduction) and 2.25 V (during oxidation) exhibit greater intensity than those of the STD cathode. This consistency aligns with the observations from CV measurements. In general, the comparison of derivative-voltage profiles confirms enhanced process reversibility in the double-layer cathodes, attributed to the active role of HEO in the conversion of LiPSs.

To further analyze the capacity characteristics of the double layer in comparison to the STD cathode, we determined the capacity contributions from the upper plateau discharge capacity (Q_1) and the lower plateau discharge capacity (Q_2). The ratio (Q_2/Q_1) versus cycle number is presented in Figure 4.17 (d) for both STD and STD+HEO90 cells. Manthiram et al. [177] reported that the Q_2/Q_1 ratio should

be equal to 3, as the theoretical capacity attributed to Q_1 is 419 mAh g^{-1} and that of Q_2 is 1256 mAh g^{-1}. However, practical Li-S cells experience deviations from this theoretical ratio due to shuttle effects and/or inappropriate reactions, causing it to fall significantly below the theoretical value. As observed in Figure 4.17 d, the STD+HEO90 electrode demonstrates higher Q_2/Q_1 values, approximately 2.3 at C/10 and 2.1 at C/5 over 100 cycles, compared to the STD (which exhibits values of around 2.2 at C/10 and 1.8 at C/5). This indicates that the double layer containing HEO facilitates a more efficient conversion of LiPSs and improved sulfur utilization over 100 cycles at C/5.

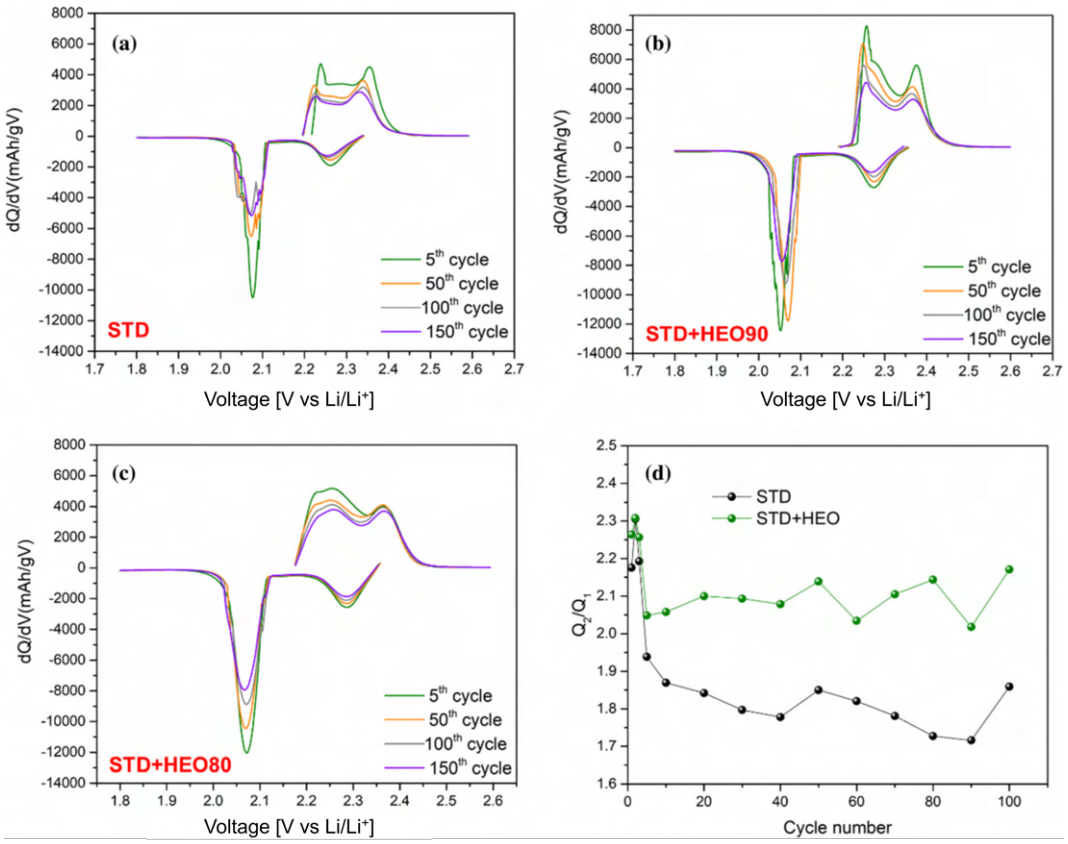

Fig. 4.17 dQ/dV curves obtained from the galvanostatic charge/discharge cycles shown in Figure 4.16 for: (a) STD electrode, (b) STD+HEO90, (c) STD+HEO80 and in panel (d) the ratio Q_2/Q_1 for STD and STD+HEO90 vs cycle number is reported.

Figure 4.18 displays the electrochemical impedance spectroscopy (EIS) responses for the pristine (uncycled) cathodes, and after eight CV cycles, the EIS results were analyzed using the equivalent circuit depicted in Figure 4.18 d. For all the samples,

a semicircular feature at high frequencies is evident, intersecting the real impedance (Z_{Re}) axis at the resistance (R_s), and then at R_s+R_{ct}. The diameter of this semicircle represents the charge transfer resistance (R_{ct}). For the three pristine electrodes, this value is approximately 36 ohms. However, after eight CV cycles, there is a slight increase in R_{ct} for the double-layer electrodes, while it remains relatively stable for the standard cathode, taking into account small experimental variations. This increase is more pronounced with a higher content of HEO in the double layer. After eight CV cycles, the change in R_{ct} is attributed to the formation of a more resistive cathode-electrolyte interface (CEI) on the HEO-modified electrodes. Notably, the greatest increase is observed in the STD+HEO90 cathode. At lower frequencies, a linear relationship is observed between Z_{Re} and -Z_{Im}, indicating processes with long, constant-time characteristics such as the diffusion of reactive and non-reactive ions that can accumulate within the electrode pores. This is fitted with a constant phase element (CPE), denoted as "W" in Figure 4.18 d. Comparing with the pristine cathodes, the responses of the STD+HEO80 and STD+HEO90 electrodes exhibit a more capacitive behavior as they have steeper slopes, while the STD cathode shows less capacitive behavior with a shallower slope. After eight CV cycles, the capacitive behavior diminishes, and the slope at low frequencies decreases. Furthermore, there are no significant differences between STD+HEO80 and STD+HEO90. In summary, the double-layer cathode exhibits an increase in R_{ct} after cycling, primarily due to a more resistive CEI, which is associated with the presence of the second layer.

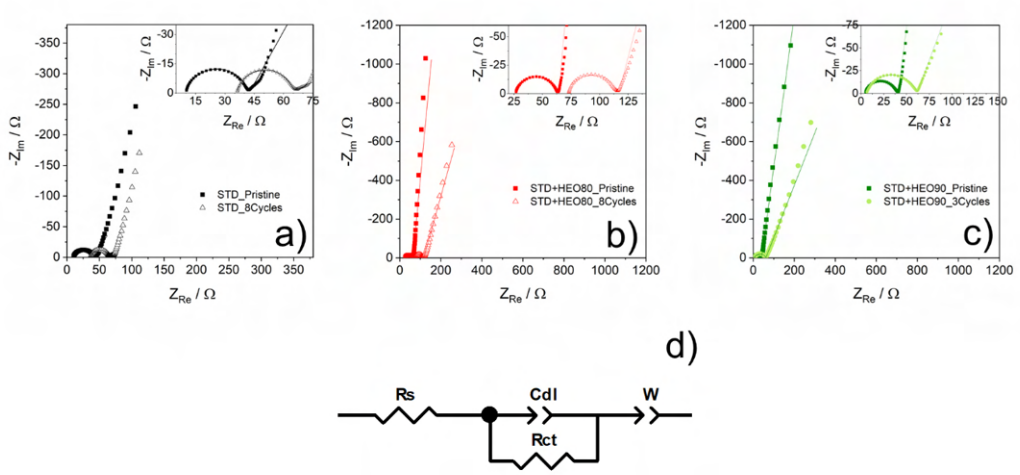

Fig. 4.18 Nyquist plots for STD (a), STD+HEO80 (b), STD+HEO90 (c) cathodes, before and after eight CV cycles. The fittings are represented by solid lines, while the experimental data by points. In panel (d) is shown the equivalent circuit used to fit the data.

Finally, the rate capability of the cathodes was assessed by applying an increasing current over 5 cycles, ranging from C/10 to 1C, as illustrated in Figure 4.19. In this testing conditions, it was observed that the STD+HEO80 cell exhibited the best performance. Starting with an initial capacity of approximately 1000 mAh g^{-1} at C/10, it delivered capacities of 930, 840, and 520 mAh g^{-1} at C/5, C/2, and 1C, respectively. The results from the rate capability tests emphasize that there are limited advantages in terms of high C rates for the STD+HEO90 cathode when compared to the standard one. In fact, there is a noticeable voltage hysteresis between the charge and discharge curves for the STD+HEO90 cell, especially at C/2 (as shown in Figure 4.19 (e). This is primarily due to the low conductivity of S (approximately 5×10^{-30} S cm^{-1} and HEO in the electrode. However, in contrast to the standard cell, when the C rate is reduced to C/10, the voltage hysteresis of the STD+HEO90 cell significantly diminishes (as indicated in Figure 4.19 (f)). Most of the reversible capacity, around 1065 mAh g^{-1}, is recovered, with very gradual capacity degradation of just 0.15% per cycle from the 45^{th} to the 100^{th} cycles. This underscores the synergistic affinity of the multi-element composition in HEO for lithium polysulfides, leading to stable cycling performance (as depicted in Figure 4.19 b).

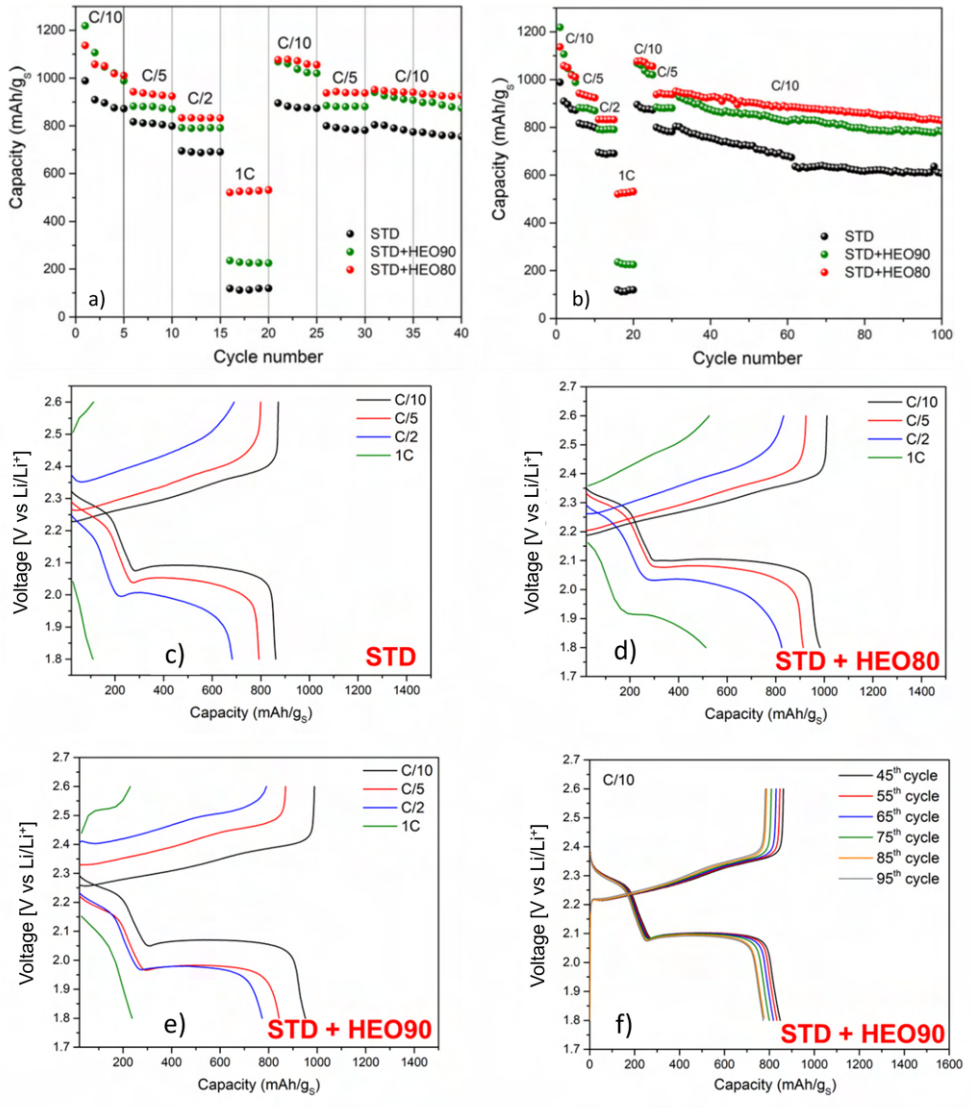

Fig. 4.19 Results of the rate capability test carried out on the three cathodes. (a) Enlargment of the cycles where the current was progressively increased (b) capacities of the cells over the entire test. In panels (c), (d) and (e) are reported the charge/discharge profiles of the three cathodes over the rate capability test, while panel (f) shows the profile curves of the STD+90HEO cathodes for the cycles performed at C/10 after the rate test.

Finally, Table 4.3 summarizes the works published so far in which HEOs have been used in the context of Li-S batteries, together with some information regarding the performance of the various materials/cathodes reported. The sulfur loading, electrolyte/sulfur ratio, C-rate, long cycling capacity, cycle number, and year of publication are summarized for various cathode materials. Notably, our work on the

$S@HEO_{DoubleLayer}$ shows a competitive performance with a long cycling capacity of 410 mAh g^{-1} at a C-rate of 0.2C and 500 cycles, demonstrating the potential of double-layer HEO structures in enhancing battery performance.
In summary, the data illustrates that while different configurations of HEO-based cathodes offer varying advantages in terms of capacity and cycle stability, there is a clear potential for optimizing these materials to achieve both high capacity and long cycle life in Li-S batteries.

Table 4.3 Table of comparison of the published work involving HEO in the Li-S batteries literature.

Cathode	Sulfur loading [mg cm^{-2}]	Electrolyte/S ratio [μl mg^{-1}]	C-rate	Long cycling capacity [mAh g^{-1}]	Cycle number	Year of publ.	Ref.
S@HEO/KB	1.2	-	0.5	479	600	2019	[150]
S@HEO$_{Nanofibers}$/CNT	1.4	20	1C	544	500	2023	[151]
S@HEO$_{Separator}$	-	-	0.5C	689	200	2023	[178]
S@HEO$_{DoubleLayer}$	1.0	10	0.2C	410	500	2022	our work [179]

Chapter 5

Reduced Graphene Oxide/Zinc Sulfide based cathode

In this case, the approach to obtain an innovative and good-performing cathode for Li-S batteries was quite different compared to that used in the double-layer of HEO. In particular, this work was inspired by the integration of carbon-based materials, such as hierarchically porous and microporous carbons [180, 181], N-doped carbon nanofibers [182], and graphene-based porous carbon [183], with inorganic materials such as Co and CoSe nanoparticles [184, 185], or metal oxides/sulfides. This approach aims to simultaneously exploit the excellent electrical conductivity of the former materials and the strong chemical affinity with polysulfides of the latter. Notably, metal sulfides have been explored as potential cathode materials for Li-S batteries due to their ease of preparation, high electrochemical activity, and redox chemistry [186, 187]. Additionally, it has recently been found that certain materials, such as VS_2, TiS_2, CoS_2, can act as catalysts in promoting the oxidation of Li_2S [188]. Consequently, utilizing sulfide-based cathodes presents a promising means to mitigate the shuttle effect, enhance sulfur utilization, and significantly improve the characteristics of Li–S batteries [189]. In this context, Zhang et al. [190] developed a composite cathode employing ZnS nanoparticles to facilitate the conversion of LiPSs, while Liu et al. [191] introduced an interlayer embedded with ZnS nanoparticles to trap LiPSs and reduce the shuttle effect. In our study, we developed an innovative composite material consisting of a graphene framework doped with nitrogen and sulfur on which zinc sulfide nanoparticles were directly formed by a one-step microwave synthesis. This combination of materials has proven successful in the

production of a cathode material that is well-suited for lithium-sulfur batteries. The graphitic network provides excellent electronic conductivity for sulfur conversion, and the doping with graphene, together with the presence of ZnS nanoparticles, provides robust interaction and catalytic activity towards LiPSs, effectively mitigating the shuttle effect.

5.1 SN-rGO and SN-rGO/ZnS synthesis and cathodes preparation

In order to evaluate the electrochemical effect of ZnS nanoparticles, two different samples were prepared: one named as sulfur-nitrogen doped rGO (SN-rGO) and a second one referred as sulfur-nitrogen doped rGO embedded with ZnS nanoparticles (SN-rGO/ZnS). Their synthesis was carried out according to the procedure described below. For the SN-rGO sample, 105 mg of graphene oxide (GO), purchased from Cheap Tubes Inc, Cambridgeport, VT, USA, was added to a 100 mL Teflon reactor equipped with pressure and temperature sensors (Milestone FlexyWave, Milestone Inc, Shelton, CT, USA). This GO was mixed with 50 mL of deionized (DI) water and subjected to 30 minutes of sonication using an Elmasonic P 30H sonicator. Subsequently, 71 mg of thiourea were added to the mixture and sonication was continued for an additional 30 minutes. The resulting uniform slurry was irradiated in a microwave at 200°C for 15 minutes, with a gradual heating ramp of 2 step minutes to reach the desired temperature. The maximum pressure reached during this process was 15 bar. The reactor was then allowed to cool to room temperature (RT) and the resulting suspension was collected in small containers, washed with DI water and subjected to freeze-dried using a Lio 5P freeze dryer (5Pascal, Trezzano sul Naviglio Milano, Italy) until all the water was removed. The synthesis of SN-rGO/ZnS followed a similar procedure: 105 mg of GO and 219 mg of zinc acetate were dispersed in 35 mL and 15 mL of DI water, respectively. After 30 minutes of sonication, the two solutions were combined and 142 mg of thiourea were added. The microwave synthesis parameters remained consistent with those used for the SN-rGO sample. In order to load the two samples SN-rGO and SN-rGO/ZnS with sulfur, a melt infusion procedure was carried out for both. Pure sulfur (99.5% Sigma Aldrich) and the SN-rGO (as well as SN-rGO/ZnS) powders were gently mixed in a 3:1 weight ratio using a mortar and pestle. The resulting mixture was then placed

in a furnace tube under a stream of argon, where it was heated to 155 °C with a gradual increase in temperature at a rate of 2.5 °C per minute to reach 155 °C(step 5 of the scheme shown in Figure 5.1). This heating process lasted 12 hours allowing for the sulfur to infiltrate the carbonaceous material. The microwave synthesis method employed in this study to produce SN-rGO and SN-rGO/ZnS is illustrated in Figure 5.1. Initially, an aqueous dispersion of graphene oxide (GO) underwent 30 minutes of sonication. This step aimed to increase the negative charges on the GO's surface, facilitating the attraction of Zn^{2+} ions through electrostatic interactions and generating defective sites [192, 193]. While the temperature increased, the thermal reduction of GO began, but it was not entirely completed. As the temperature reached 200°C, thiourea decomposed, yielding highly reactive N/S-rich species, including H_2S, NH_3, and CS_2. These reactive species readily reacted with the aforementioned defective sites generated by the removal of oxygen-containing groups on GO, thus completing the reduction and doping process [194, 195]. Simultaneously, ZnS nanoparticles nucleated and grew on the surface of rGO due to the coordination of S^{2-} ions, originating from CS_2, with Zn^{2+} ions.

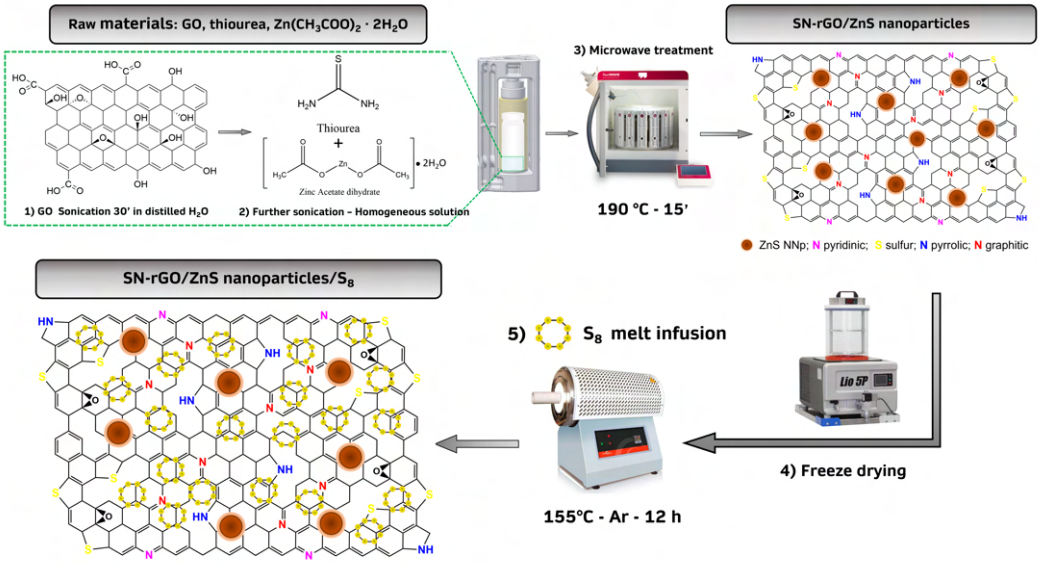

Fig. 5.1 Scheme of the microwave-assisted synthesis of the SN-rGO, SN-rGO/ZnS, and the following melt infusion step to produce the SN-rGO/S_8 and SN-rGO/ZnS/S_8 samples

It is important to highlight the optimization of the entire synthesis process in terms of time and steps required. Thiourea served both as a precursor for GO doping and as a sulfur source for the generation of ZnS nanoparticles. The yield of the

reactions was calculated to be 45.5% and 85.7% for the doped rGO/ZnS and doped rGO, respectively. Additionally, the microwave heating process was significantly faster compared to the traditional hydrothermal method.

The physicochemical techniques used to characterize the materials, the method of preparing the electrodes, and the electrochemical techniques used to characterize the Li-S cells based on rGO/ZnS and rGO materials are reported in Appendix B.2.

5.2 Physical-chemical characterization

The morphological investigation of the SN-rGO and SN-rGO/ZnS samples was carried out using the FESEM and TEM techniques, as reported in Figure 5.2. In particular, the micrograph of the former is shown in Figure 5.2 (a) while the one of the latter in 5.2 (b). Notably, both specimens showcase the characteristic exfoliated structure of reduced graphene oxide, along with the evident presence of evenly distributed nanoparticles on the carbonaceous surface in the sample synthesized in the presence of zinc acetate. The average size of these nanoparticles is around 80 nm, as it is shown in Figure 5.2 (c). The TEM analysis was exclusively performed on the SN-rGO/ZnS sample, in order to deeply investigate the morphology and cristallinity of the nanoparticles, and the results are shown in Figure 5.2 (d) (e) (f). Basically, this investigation brought to light the fact that the ZnS nanoparticles are made up of primary particles much smaller than 80 nm, as can be seen from Figure 5.2 (d); moreover, it was possible to evaluate the crystallinity of the ZnS nanoparticles by estimating the distance between the (111) planes to be around 3.07 Å, in conformity with the previous literature [196, 197].

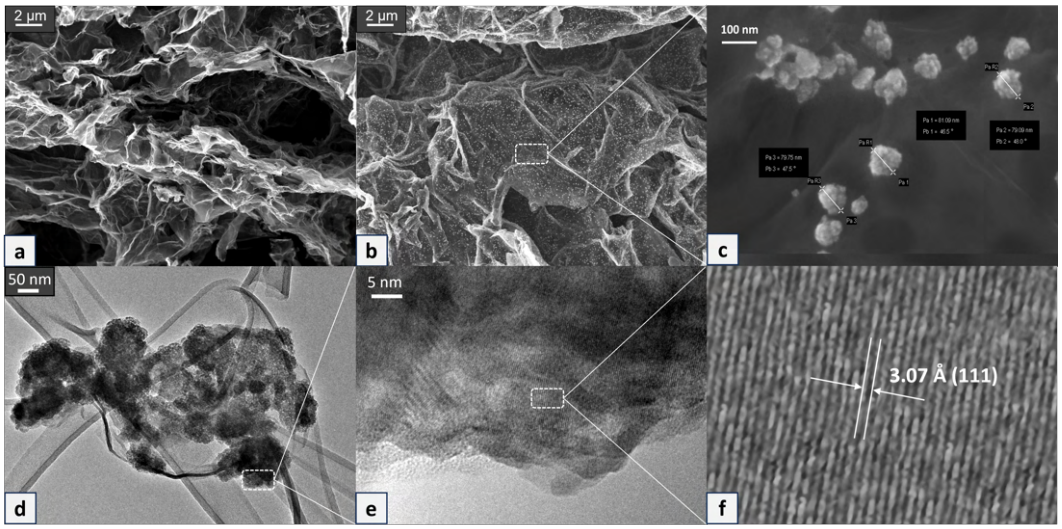

Fig. 5.2 FESEM micrographs of (a) SN-rGO sample (b) SN-rGO/ZnS sample (c) enlargement of the SN-rGO/ZnS sample, from which it was possible to estimate the nanoparticles size. TEM micrographs of the SN-rGO/ZnS sample, (d) a conglomerate of ZnS primary nanoparticles (e) enlargement of the previous micrograph from which some lattice fringes are visible (f) estimation of the interplanar distance between the (111) planes.

The superficial elemental distribution of the two samples was investigated with the EDS analysis (see Figure 5.3). For each sample, three different areas were analyzed to obtain reliable information about the average composition of the elements. As expected, zinc is present only in the sample called SN-rGO/ZnS, while all the other elements used in the synthesis phase were detected in both samples. In the case of ZnS nanoparticles (Figure 5.3 b) the weight and atomic percentages of sulfur and zinc are much higher than those observed on a larger area of the sample (Figure 5.3 a), however the other elements (C, N, O) are present in non-negligible quantities, probably due to the very nature of the type of analysis. Regarding the SN-rGO sample, the results align with what was expected since N and S are in significantly lower quantities than carbon. All weight and atomic percentage values of the EDX analysis are shown in Table 5.1.

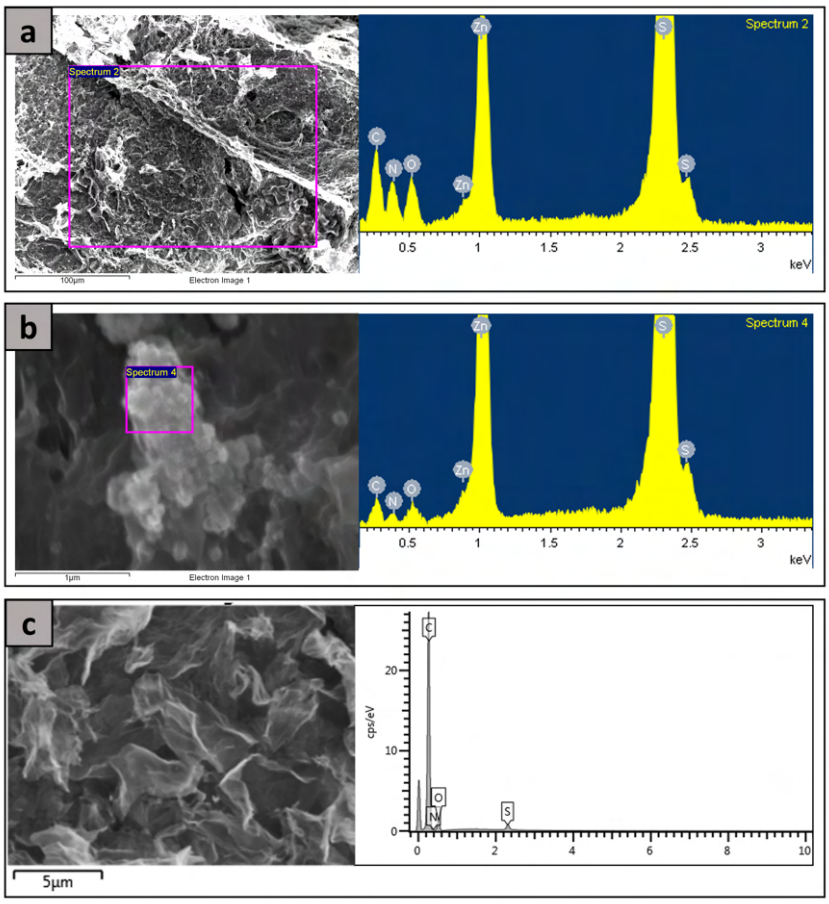

Fig. 5.3 EDX superficial analysis standard for (a) SN-rGO/ZnS wide area, (b) ZnS nanoparticles, (c) SN-rGO wide area.

Table 5.1 EDS element analysis reported values for the three samples reported in Figure 5.3

Element	(a) SN-rGO/ZnS		(b) ZnS nanoparticles		(c) SN-rGO	
	Wt%	Atomic%	Wt%	Atomic%	Wt%	Atomic%
C	25.64	40.27	16.99	36.15	81.59	85.50
N	21.29	28.66	7.19	13.12	4.28	3.84
O	9.04	10.65	3.32	5.31	12.98	10.20
S	25.74	15.14	42.05	33.52	1.15	0.45
Zn	18.29	5.28	30.45	11.91	-	-
Total	100	100	100	100	100	100

The investigation of the functional groups and surface chemical composition of SN-rGO and SNrGO/ZnS was conducted using X-ray photoelectron spectroscopy

(XPS). The survey spectra for both samples, depicted in Figure 5.4, reveal S2p, C1s, and N1s peaks at approximately 164, 284, and 400 eV, respectively. As expected, the Zn2p peak at around 1021.4 eV is exclusively detected in the SN-rGO/ZnS sample. Initial insights from the survey spectra include the confirmation of nitrogen and sulfur incorporation into the graphene networks, supporting the hypothesis of heteroatoms doping. Furthermore, the presence of thiourea appears to enhance the reduction degree of graphene oxide (GO), as indicated by the C/O ratio of 3.01 for SN-rGO and 4.62 for SN-rGO/ZnS, surpassing typical values for GO. The nitrogen content in SN-rGO and SN-rGO/ZnS is 8.9 at.% and 7.4 at.%, respectively, while sulfur doping is quantified as 7.25 at.% for the former and 6.5 at.% for the latter (Table 5.2).

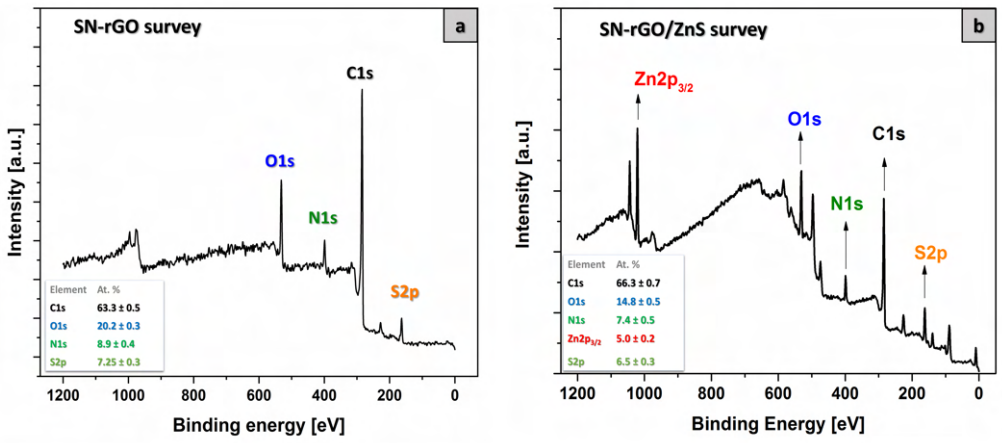

Fig. 5.4 XPS survey spectra for (a) SN-rGO and (b) SN-rGO/ZnS samples.

Table 5.2 Atomic percentages of the element detected in the XPS surveys of SN-rGO and SN-rGO/ZnS

Sample	C (at%)	O (at%)	N (at%)	S (at%)	Zn (at%)	C/O
SN-rGO	66.3 ±0.5	20.2 ±0.3	8.9 ±0.4	7.2 ±0.3	-	3.01
SN-rGO/ZnS	66.3 ±0.7	14.8 ±0.5	7.4 ±0.5	6.5 ±0.2	5.0 ± 0.3	4.62

Detailed examination of the chemical environment of C, N, S, and Zn atoms was performed through high-resolution C1s, N1s, S2p, and Zn2p spectra, presented in Figures 5.5 (a) (b) (c) for SN-rGO and Figure 5.5 (d) (e) (f) and Figure 5.6 for SN-rGO/ZnS. Deconvolution of the C1s spectrum (Figures 5.5 a and d) highlights

the reduction in the intensity of oxygen-containing functionalities of GO, such as C-O/C=O and O=C-OH, with the introduction of N and S into the carbon network for both SN-rGO and SN-rGO/ZnS. The high-resolution S2p peak for SN-rGO/ZnS exhibits peaks (Figure 5.5 e) associated with the Zn-S bond (160.8 eV), thiophenic -C-S-C- (162.4 eV), and conjugated -C=S- bond (163.6 eV), confirming the formation of ZnS nanoparticles. In contrast, the S2p spectrum of SN-rGO (Figure 5.5 b) shows a peak at 164.3 eV attributed to -C-S-C- and -C=S- bonds, without the Zn-S bond peak at 160.8 eV, indicating the absence of ZnS nanoparticles in the SN-rGO sample. Two additional peaks at 162 and 168.5 eV in the S2p spectrum of SN-rGO suggest the presence of sulfide and sulfate -SOx groups at the graphene edges. The N1s spectra for both SN-rGO and SN-rGO/ZnS were deconvoluted into three peaks (Figures 5.5 c and f), indicating the predominance of pyridinic and pyrrolic N in both samples, with a lower content of graphitic-like N. Notably, the amount of pyridinic N is almost double in SN-rGO/ZnS compared to SN-rGO, which is significant for applications where pyridinic N is a preferred adsorption site for lithium polysulfides (LiPSs) [198–200]. The Zn $2P_{3/2}$ spectrum (see Figure 5.6) was completely deconvoluted with a single peak corresponding to the Zn-S bond, thus confirming the presence in the sample of a compound with this composition. Quantitative XPS data for the two samples are provided in Table 5.3.

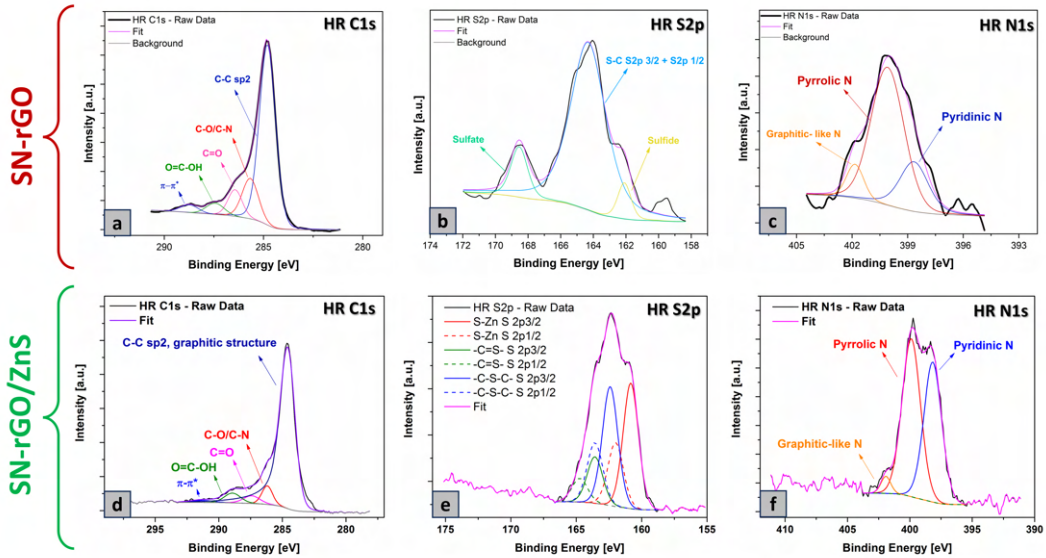

Fig. 5.5 XPS high resolution spectra of C1s, S2p and N1s of the SN-rGO sample (panels a, b and c) and SN-rGO/ZnS sample (panels d, e ,f)

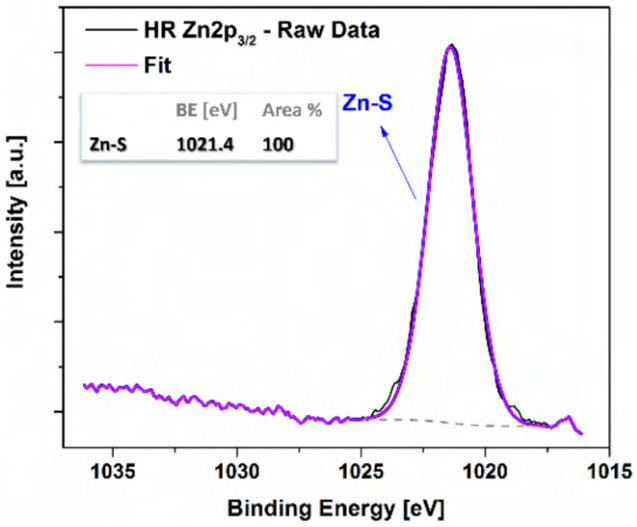

Fig. 5.6 High resolution spectra of Zn 2p for the SN-rGO/ZnS sample.

Table 5.3 : Position in term of binding energy [B.E.] and quantification [Area %] of the peaks used to deconvolute the XPS data of SN-rGO and SN-rGO/ZnS.

		Species	SN-rGO		SN-rGO/ZnS	
			B.E. [eV]	Area [%]	B.E. [eV]	Area [%]
High resolution spectra	C1S	C-C	284.80	68.17	284.50	84.40
		C-O/C-N	285.67	15.35	286.20	5.90
		C=O	286.43	8.80	287.40	3.70
		O=C-OH	287.43	4.48	288.90	4.70
		π-π^*	288.74	3.12	291.30	1.30
	S2P	S-Zn	-	-	160.80	42.80
		Sulfide	162.05	6.17	-	-
		-C-S-C	164.31	82.83	162.40	41.10
		-C=S-	-	-	163.60	16.10
		Sulfate	168.54	11.00	-	-
	N1S	Pyridinic N	398.66	23.14	398.20	52.20
		Pyrrolic N	400.09	68.10	399.90	44.90
		Graphitic-like N	401.84	8.76	401.90	2.90

The physical-chemical properties of the pristine SN-rGO and SN-rGO/ZnS were further investigated using XRD, BET, and TGA techniques. These analyses were also applied to examine the materials after the sulfur loading in the tubular oven, as depicted in Figure 5.1. The resulting samples after the infiltration step are denoted as SN-rGO/S_8 and SN-rGO/ZnS/S_8. The XRD spectra of SN-rGO and SN-rGO/ZnS, depicted in Figure 5.7, do not show any signal at 2θ = 10.6, associated with the (001) lattice plane and corresponding to a d-spacing of 0.83 nm in GO. This observation confirms the reduction of GO during microwave synthesis. In the SN-rGO sample, the removal of oxygen-containing groups results in a broad diffraction peak (002) between 21° and 30°, corresponding to a d-spacing of 0.38 nm [201]. In the SN-rGO/ZnS spectra, a crystalline phase is evident, identified by characteristic positions at 28.5°, 47.6°, and 56.3° representing the (111), (220), and (311) lattice planes of ZnS, respectively. The XRD spectra of the two rGO infiltrated with sulfur, shown in the upper part of Figure 5.7, exhibit similarities due to the prominent presence of sulfur patterns obscuring the peaks of the two pristine materials.

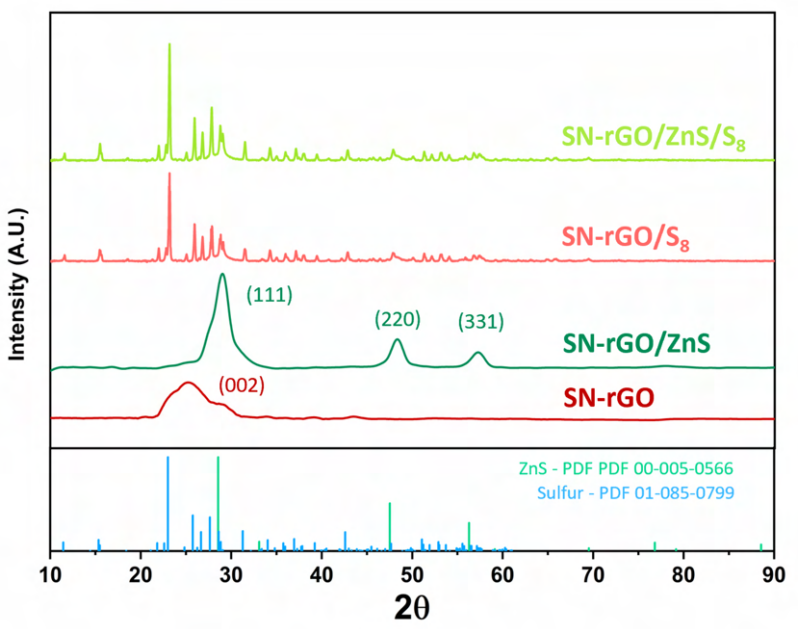

Fig. 5.7 XRD spectra of the pristine SN-rGO, SN-rGO/ZnS and their correspectives after the sulfur melt infusion, denoted as SN-rGO/S_8 (light red line) and SN-rGO/ZnS/S_8 (light green line).

The analysis of nitrogen adsorption-desorption for SN-rGO and SN-rGO/ZnS, depicted in Figure 5.8 (a) and (b), reveals notable distinctions for the two samples: the former displays a reversible Type II isotherm indicative of monolayer coverage and multilayer adsorption in non-porous adsorbents, while the latter exhibits a Type H3 hysteresis loop, likely attributed to slit-shaped pores formed by the overlap of multiple rGO layers separated by ZnS nanoparticles [202, 203]. These findings align with the morphological features observed in Figure 5.2 for the two samples. The isotherms of the two samples, following infiltration with sulfur (Figure 5.8 c and d), display a reversible Type II behavior without any discernible porosity, likely attributed to the insertion of S_8 into the cavities of the pristine materials. Using the Brunauer–Emmett–Teller (BET) model, the specific surface areas of SN-rGO, SN-rGO/ZnS, SN-rGO/S_8, and SN-rGO/ZnS/S_8 were determined to be 30.6 $m^2 \cdot g^{-1}$, 56.9 $m^2 \cdot g^{-1}$, 7.9 $m^2 \cdot g^{-1}$, and 8.8 $m^2 \cdot g^{-1}$, respectively. It is evident that the presence of ZnS nanoparticles enhances the surface area by almost twofold, a desirable feature for increasing available sites for LiPSs adsorption. Similarly, after sulfur infiltration for both composites, the surface-specific area is comparable, indicating that the pores induced by the presence of nanoparticles become blocked after sulfur loading.

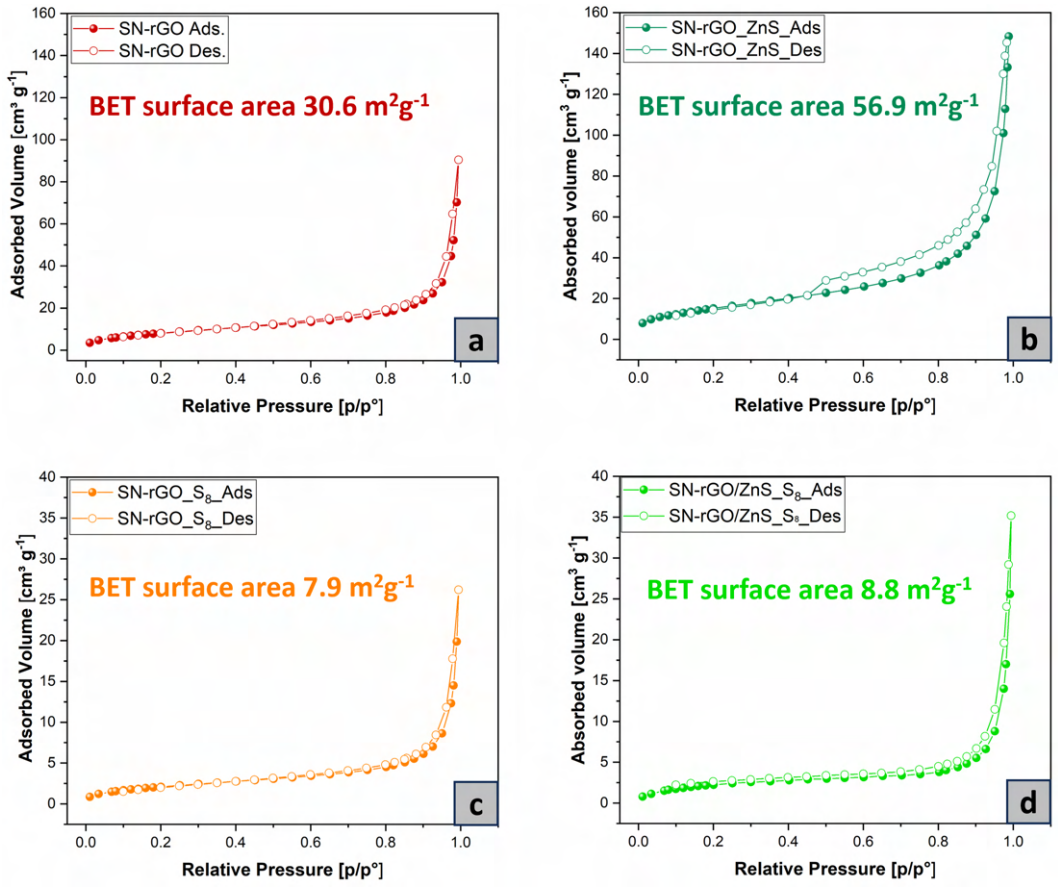

Fig. 5.8 (a) N_2 adsorption-desorption isotherms of SN-rGO (b) SN-rGO/ZnS (c) SN-rGO/S_8 and (d) SN-rGO/ZnS/S_8, with the calculated surface area based on BET model.

The thermogravimetric analysis (TGA) was conducted on all prepared samples to assess the weight percentage of ZnS nanoparticles in SN-rGO/ZnS and the sulfur loading in the infiltrated samples. Specifically, Figure 5.9 (a) presents the TGA results of SN-rGO and SN-rGO/ZnS, revealing a substantial residue (48.11%$_{wt}$) in the case of SN-rGO/ZnS. Based on this data, the estimated weight percentage of ZnS is approximately 57.6%$_{wt}$, considering the ratio between the molecular weight of ZnS and ZnO, as ZnS is oxidized into the latter at high temperatures [204]. The TGA curves of the composite materials after the melt infusion step, illustrated in Figure 5.9 (b), exhibit a similar trend over temperature. In particular, the SN-rGO and SN-rGO/ZnS samples can accommodate around 69%$_{wt}$ and 63%$_{wt}$ of sulfur within their structures, respectively. This discrepancy may be attributed to the distinct pore sizes of the two materials, as previously revealed by the nitrogen adsorption-desorption analysis.

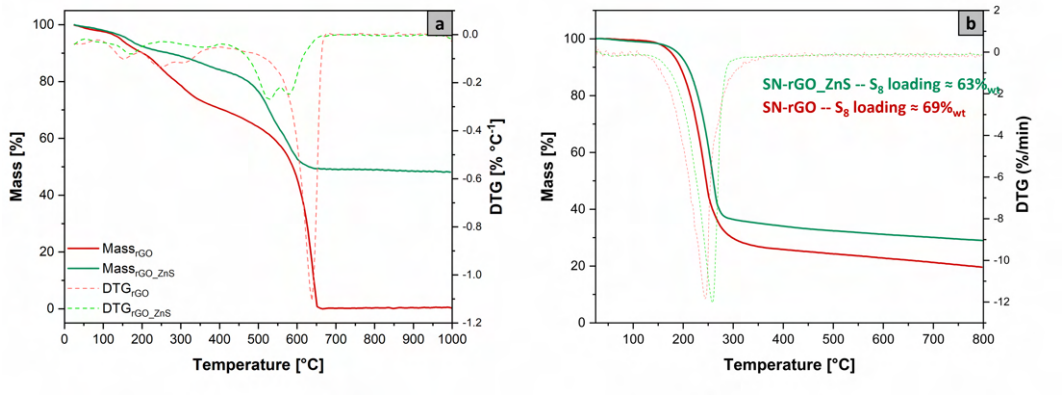

Fig. 5.9 (a) TGA of SN-rGO and SN-rGO/ZnS samples in air from 25 °C to 800 °C.(red and green line, respectively), (b) TGA curves of the SN-rGO/S_8 and SN-rGO/ZnS/S_8 samples, in the same conditions.

Given that one of the critical attributes of the cathode material in lithium-sulfur batteries is to exhibit a strong interaction and heightened catalytic activity to facilitate a quicker kinetic reaction in the conversion of LiPSs, minimizing the shuttle effect, the adsorption test was performed on the samples to investigate this aspect. Specifically, the adsorption capability of the materials (pure KjB, SN-rGO, SN-rGO/ZnS) towards LiPSs was assessed by immersing 30 mg of powders in a 4 mL DME:DIOX 1:1 mixture containing Li_2S_8 0.5 mM. The solution was stirred and left overnight. The various samples are illustrated in the upper right corner of Figure 5.10. Notably, the color of the solution remains almost unchanged in the case of KjB, underscoring its minimal adsorption capability. Conversely, the SN-rGO sample significantly lightens the solution, achieving complete transparency only in the case of the SN-rGO/ZnS sample.

Ultraviolet-visible absorption spectroscopy was performed to further assess these interactions, with results in Figure 5.10. A baseline was established using a pure DME:DIOX 1:1 mixture, while the pure 0.5 mM Li_2S_8 solution served as a reference to identify the typical peaks associated with different Li_2S_x species visible in the purple spectra of Figure 5.10 (b). Following the adsorption test, it is evident that the intensity of the LiPSs peaks markedly decreases in the case of SN-rGO and is nearly eliminated in the SN-rGO/ZnS spectrum. These findings confirm the ability of the rGO based samples to capture LiPSs, aligning with existing literature. The simultaneous introduction of nitrogen and sulfur into the graphene structure generates highly effective sites for LiPSs adsorption. Specifically, the presence of

pyrrolic or pyridinic N adjacent to thionic sulfur significantly increases the binding energy between graphene and LiPSs species, rendering SN-rGO an efficient material for trapping LiPSs [205]. Moreover, the inclusion of ZnS nanoparticles seems to enhance the interaction with LiPSs, as predicted by DFT calculations by Razaq [192] and Xu [206], where the adsorption energies on the (100),(110), and (111) facets of ZnS are notably higher than those on graphene.

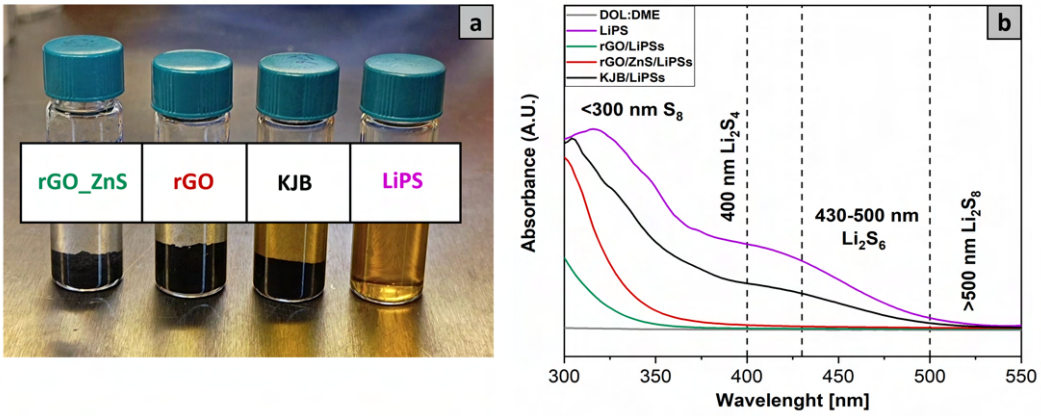

Fig. 5.10 (a) pristine 1:1 DOL:DME Li_2S_8 0.5 mM solution and the same solution after being in contact with SN-rGO, SN-rGO/ZnS and KjB (b) UV-VIS analysis of the supernatant of the previous solutions.

5.3 Electrochemichemical characterization - Results

The electrochemical methods used in this section are reported in appendix B.2.
To assess the impact of the doping process and the presence of ZnS nanoparticles on the kinetic reaction of LiPSs conversion, cyclic voltammetry (CV) tests were conducted within the voltage window of -1 to 1 V in symmetrical cells. These cells were filled with both a catholyte of Li_2S_8 0.125 M and a standard electrolyte, as depicted in Figure 5.12.
As expected, the CV of symmetrical cells devoid of Li_2S_8 (Figure 5.11 a) exhibited an almost flat voltammogram, indicative of capacitive current contribution, which is also relatively low in absolute current values (below 0.1 A g^{-1}). In contrast, when Li_2S_8 was introduced into the electrolyte formulation, both SN-rGO and SN-rGO/ZnS demonstrated a significantly enhanced current response. This improved response was governed by the characteristic conversion reactions of a Li-S battery,

overshadowing the contribution from double-layer capacitance. Notably, the SN-rGO/ZnS sample displayed good reversibility and facile polysulfide conversion, evident from distinct peaks at -0.092, 0.087, 0.342 V in reduction and 0.079, -0.086, -0.291 V in oxidation, as shown in Figure 5.11 (b) and further emphasized in the scan performed at 1 mVs^{-1} (Figure 5.11 c). The cathodic scan peaks indicated a stepwise reduction from the original Li_2S_8 to insoluble Li_2S on the working electrode. At the same time, oxidation of Li_2S_8 occurred on the counter electrode as referred into Table 5.4 with Equations 5.4.1 - 5.4.8 which describe the reaction path during the scan [207, 208]. Furthermore, the current response in the symmetrical CVs followed the order SN-rGO/ZnS > SN-rGO > KjB, supporting the hypothesis that the kinetics of polysulfide conversion are primarily enhanced by ZnS nanoparticles and, to some extent, by the heteroatomic doping process of graphene with N and S. Another interesting feature that can be observed from the symmetrical CVs is the difference in intensity between SN-rGO and SN-rGO/ZnS for peaks b and c in reduction compared to peaks b' and c' in oxidation, which are more prominent in the sample containing the nanoparticles, thus highlighting their greater contribution in the oxidation process.

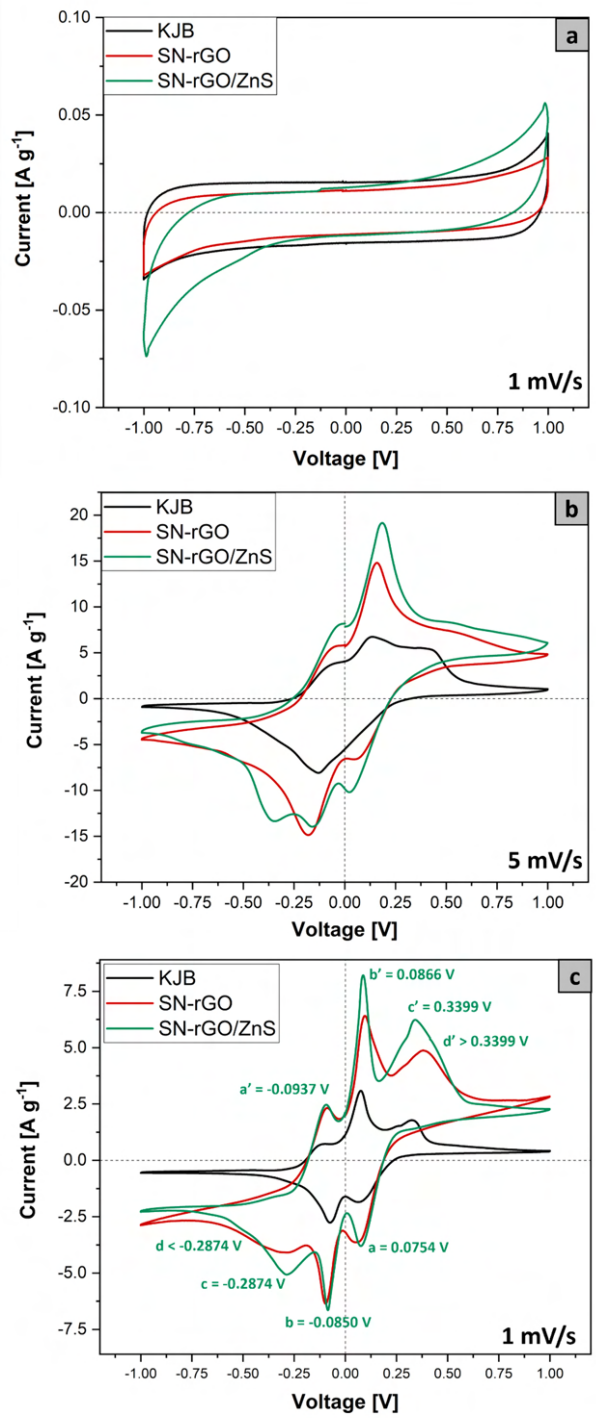

Fig. 5.11 (a) Cyclic voltammetry of free symmetrical cells using a solution of 1,2-dimethoxyethane (DME) and 1,3-dioxolane (DIOX) 1:1 (v/v) as electrolyte, performed in the $\pm$1V window at the scan rate of 1 mV s^{-1} (b) cyclic voltammetry of free symmetrical cells with STD electrolyte 0.125M using a solution of 1,2-dimethoxyethane (DME) and 1,3-dioxolane (DIOX) 1:1 (v/v) Li_2SS_8 0.125M, performed at 5 mVs^{-1} and (c) 1 mVs^{-1}.

Table 5.4 List of the reactions occurring at the working electrode (WE) and counter electrode (CE) in symmetric cells during cyclic voltammetry within the ± 1 V range. It is crucial to note that for peaks labeled a', b', c', and d', the reactions undergo reversal between the WE and CE. Even though peaks d and d' may not be clearly discernible in the voltammograms presented in Figure 5.11, their presence, evident as shoulders of peaks c and c', is justified by the widening of these peaks.

Peak	**Voltage [V]**	**Reaction**
a	0.0754	**WE:** $Li_2S_8 + \frac{2}{3}Li^+ + \frac{2}{3}e^- \rightarrow \frac{4}{3}Li^+ + Li_2S_6$
		CE: $8Li_2S - 8Li^+ - 8e^- \rightarrow 4Li_2S_8$
b	-0.0850	**WE:** $\frac{4}{3}Li_2S_6 + \frac{4}{3}Li^+ + \frac{4}{3}e^- \rightarrow 2Li_2S_4$
		CE: $4Li_2S_2 - 4Li^+ - 4e^- \rightarrow 2Li_2S_4$
c	-0.2874	**WE:** $2Li_2S_4 + 4Li^+ + 4e^- \rightarrow 2Li_2S_2$
		CE: $2Li_2S_4 - \frac{4}{3}Li^+ - \frac{4}{3}e^- \rightarrow \frac{4}{3}Li_2S_6$
d	$<$ -0.2874	**WE:** $4Li_2S_2 + 8Li^+ + 8e^- \rightarrow 8Li_2S$
		CE: $\frac{4}{3}Li_2S_6 - \frac{2}{3}Li^+ - \frac{2}{3}e^- \rightarrow Li_2S_8$

The redox dynamics of our specimens during the discharge and charge steps were explored through current exchange measurements utilizing linear sweep voltammetry (LSV) with a Li_2S_8 catholyte solution in a coin cell configuration. Specifically, Figure 5.12 illustrates the Tafel plot for KjB, SN-rGO, and SN-rGO/ZnS concerning the cathodic and anodic reactions. An evident deduction from this graph is the substantial reduction in lithiation and delithiation overpotentials of sulfur, achieved primarily through the SN doping process and even more prominently with the presence of ZnS particles on the graphene sheets [209]. Following Nazar's protocol [210], the exchange current densities, indicative of the electron transfer rate, were derived from the Tafel plot. The calculated values (0.51 μA cm^2 for KjB, 0.89 μA cm^2 for SN-rGO, and 1.31 μA cm^2 for SN-rGO/ZnS) underscore the accelerated charge transfer kinetics facilitated by the ZnS nanoparticles.

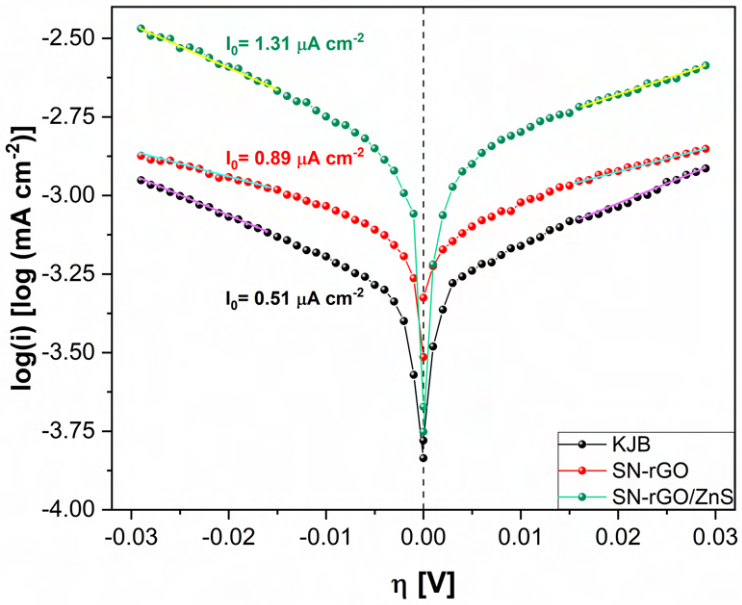

Fig. 5.12 Tafel plots of the Li_2S_8 solution redox on KjB, SN-rGO and SN-rGO/ZnS materials, derived from positive and negative LSV scans

Another crucial consideration in Li-S batteries pertains to the process of converting long polysulfides into Li_2S, transitioning from a liquid to a solid state. Particularly, given the insulating properties of Li_2S, achieving a highly controllable deposition of solid Li_2S is paramount. To examine the deposition process of lithium sulfide on various samples, we conducted an experiment wherein cells (refer to Section 5.3 for cell assembly details) were discharged at a current of 100 μA until reaching 2.15 V. Subsequently, a potentiostatic step at 2.02 V was applied until the recorded current reached zero. Figures 5.13 (a) and (b) depict the results of the Li_2S deposition test for the SN-rGO and SN-rGO/ZnS samples, respectively. In a qualitative assessment, the initial drop in current-time response is attributed to the formation of a non-faradaic double-layer and the reduction of long-chain polysulfides into mid-chain polysulfides [211]. The subsequent portion of the curve reflects a nucleation and growth process. Initially, during nucleation, the increasing current indicates a growth in the electroactive area due to either the proliferation of Li_2S nucleation centers or the enlargement of each nucleus precipitated on the electrode surface [212]. Subsequently, during the growth phase, the current decreases as a result of coalescence between neighboring nuclei centers and the overlap of the adjacent hemispherical diffusion developed by the sparsely distributed nuclei to an infinite linear concentration gradient [213]. Delving into more specifics, according

to Faraday's law, the Li_2S deposition capacities on SN-rGO and SN-rGO/ZnS are 242.2 and 258.5 mAh g^{-1}, respectively. This discrepancy implies that the presence of ZnS nanoparticles offers more active sites for the nucleation and growth of Li_2S.

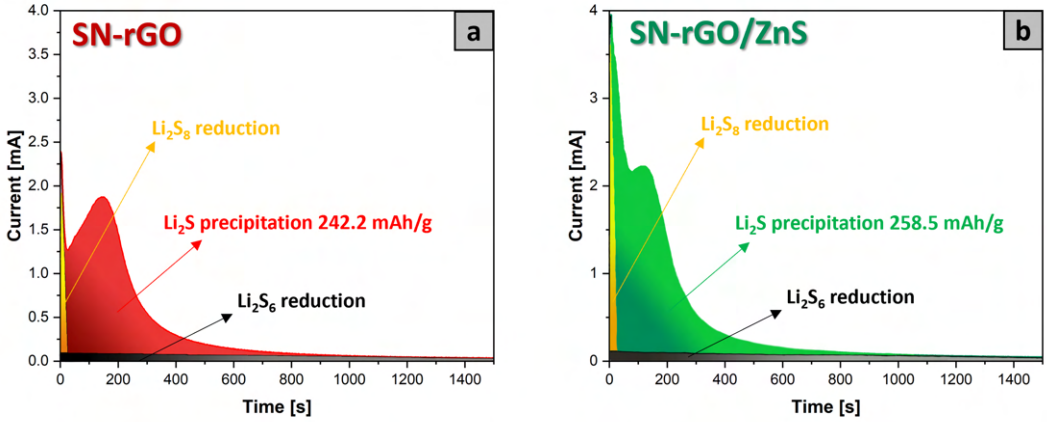

Fig. 5.13 (a) current transients obtained during the potentiostatic step of the Li_2S deposition test the for SN-rGO; and (b) for the SN-rGO/ZnS

To comprehensively explore the impact of both sample morphology and ZnS nanoparticles on the kinetics of Li_2S nucleation and deposition, dimensionless electrochemical deposition models based on current-time transient responses were utilized. These models are based on in the Scharifker-Hills and Beick-Fleischman equations, as detailed below:

- Instantaneous Nucleation (2DI):

$$\frac{j}{j_m} = \frac{t}{t_m}\left\{exp\left[\frac{t_m - t_m^2}{2t_m^2}\right]\right\} \tag{5.3.1}$$

- Progressive Nucleation (2DP):

$$\frac{j}{j_m} = \frac{t}{t_m}\left\{exp\left[\frac{-2(t^3 - t_m^3)}{3t_m^3}\right]\right\}^2 \tag{5.3.2}$$

- Instantaneous Nucleation (3DI):

$$\frac{j}{j_m} = \left(\frac{1.9542}{\frac{t}{t_m}}\right)^{0.5}\left\{1 - exp\left[1.2564\left(\frac{t}{t_m}\right)\right]\right\} \tag{5.3.3}$$

- Progressive Nucleation (3DP):

$$\frac{j}{j_m} = \left(\frac{1.2254}{\frac{t}{t_m}}\right)^{0.5} \left\{1 - exp\left[2.3367\left(\frac{t}{t_m}^2\right)\right]\right\} \tag{5.3.4}$$

The models, namely 2DI and 2DP, signify an instantaneous (I) or progressive (P) two-dimensional nucleation process with adatom lattice incorporation governing the Li_2S growth rate. On the other hand, 3DI and 3DP imply the nucleation of a 3D hemispherical nucleus with ion diffusion regulating the growth rate [214, 215]. These current-time transients are illustrated in Figure 5.14 (a) and (b) for SN-rGO and SN-rGO/ZnS, respectively.

The experimental curve of SN-rGO exhibits a resemblance to a 2D-type nucleation and growth model, although no clear distinction between the instantaneous or progressive process is evident. This observation leads to the hypothesis that a relatively large number of Li_2S nucleation centers form on the SN-rGO surface and subsequently grow laterally, completing the 2D structure of the deposited Li_2S. In contrast, the SN-rGO/ZnS curve shows a trend more akin to a 3DI model during the nucleation phase and the initial part of the growth. As the deposition reaction progresses, the curve gradually settles into a hybrid 3DP/2D model. This trend suggests that the interfacial sites provided by ZnS nanoparticles may guide radial Li_2S development, thereby balancing surface lateral atomic diffusion and mass transfer in the electrolyte, as ion diffusion primarily controls the growth rate in a 3D-type deposition process. Therefore, the 3D deposition process of Li_2S is attributed to selective nucleation and growth near ZnS-rGO heterointerfaces with high activity [211], thus preventing the complete 2D passivation of the substrate and enabling a higher deposition capacity.

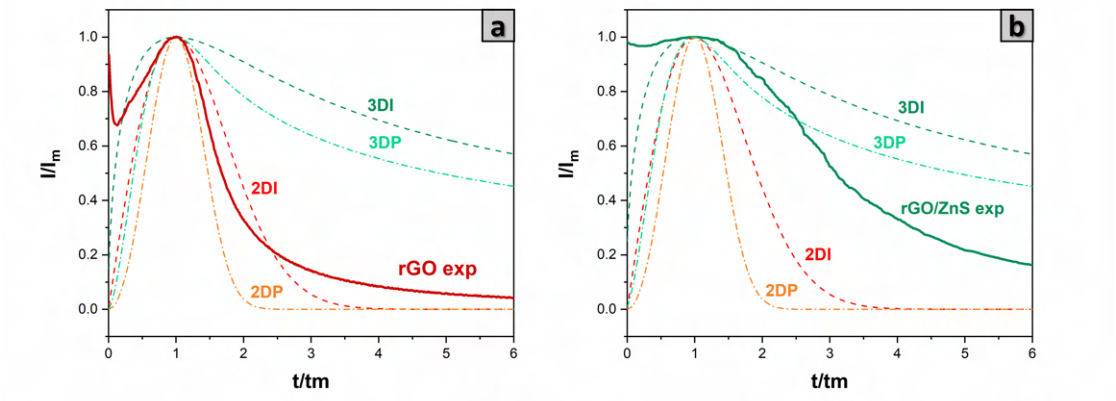

Fig. 5.14 (a) current transients obtained during the potentiostatic step of the Li_2S deposition test the for SN-rGO; and (b) for the SN-rGO/ZnS

In order to evaluate the electrochemical performance of Li–S cells based on SN-rGO and SN-rGO/ZnS, coin-cell batteries were assembled with a sulfur loading ranging from 1.1 to 1.3 mg cm^{-2} and subjected to electrochemical testing. Figures 5.15 (a) and (b) depict the cyclic voltammetry (CV) outcomes for Li-S batteries with sweeping rates escalating from 0.05 mV s^{-1} to 0.5 mV s^{-1} for SN-rGO and SN-rGO/ZnS, respectively. Both samples reveal two distinct peaks at 2.25 V ($P1_c$) and 2.05 V ($P2_c$) in the cathodic scan, corresponding to the reduction of S_8 to high-order soluble Li_2S_x ($4 \leq x \leq 8$) and the subsequent reduction to low-order insoluble Li_2S_2/Li_2S. In the anodic scan, a single prominent peak around 2.4 V (denoted as P_a) is observed, showing a shoulder at approximately 2.35 V for SN-rGO and a secondary shoulder at about 2.48 V for SN-rGO/ZnS. These sub-peaks indicate the gradual oxidation mechanism of Li_2S to polysulphides and eventually to S_8 [216–218]. Moreover, the positive catalytic activity exhibited by ZnS nanoparticles was assessed by changes in the onset potentials for the redox peaks during CV in both reduction and oxidation. The voltage values of the baseline currents right before the onset potential of the relative peaks in the voltammograms were defined thanks to the derivatives of the cyclic voltammetry (dI/dV) shown in Figure 5.16 (a) and Figure 5.17 (a); in particular, the baseline voltage and current density are defined as the last point where the variation on current density is the smallest, namely dI/dV= 0. Following a commonly used definition in electrocatalysis, the onset potential is identified when the current density surpasses 10 μA cm^{-2} relative to the baseline current density (specifically, 10 μA cm^{-2} more negative than the baseline current

density for cathodic peaks or 10 μA cm^{-2} more positive than the baseline current density for anodic peaks). The presence of ZnS reduces the onset potential of the anodic peak P_a while increasing those of the cathodic peaks compared to the pristine SN-rGO electrode (refer to Table 5.5 for onset values), indicating enhanced kinetics facilitated by the nanoparticles [217]. Additionally, the analysis of dI/dV derivative curves obtained from the CVs (Figure 5.18 for SN-rGO and Figure 5.19 for SN-rGO/ZnS) allowed the identification of potential values at which the peaks P_a, $P1_c$, and $P2_c$ occur (reported in Table 5.6). In this context, the trend observed in onset reaction potential is reaffirmed, with the SN-rGO/ZnS characterized by lower E P_a and higher E $P1_c$ and $P2_c$, suggesting reduced susceptibility to polarization in the SN-rGO/ZnS cell.

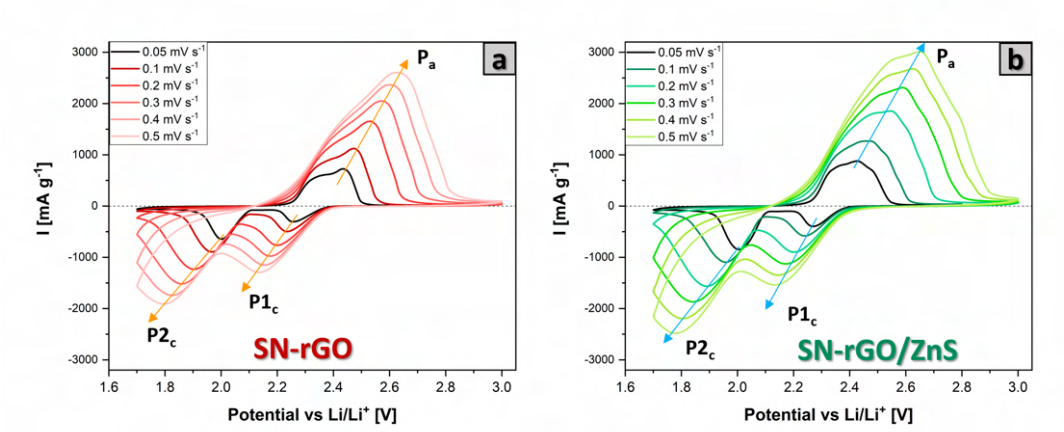

Fig. 5.15 (a) CVs of the SN-rGO/S_8-based cathode at various scan rates (b) CVs of the SNrGO/ZnS/S_8-based cathode at different scan rates.

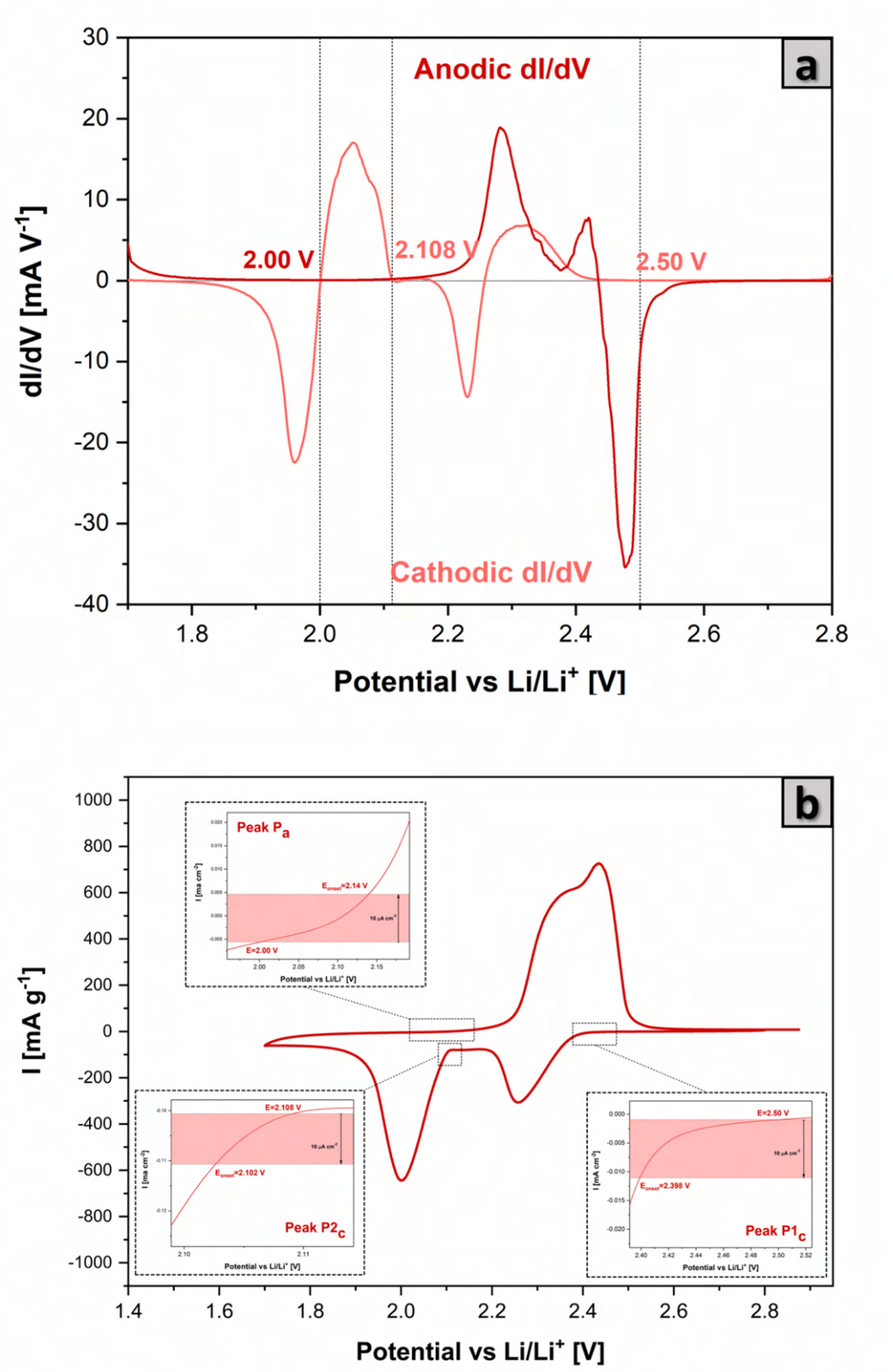

Fig. 5.16 (a) Differential CV curves for SN-rGO . The baseline voltage and current density are defined as the values where the variation in current density is minimal, i.e., $\frac{dI}{dV} = 0$. Dotted lines indicate baseline voltages, with corresponding values marked in pink for the cathodic scan and in red for the anodic scan. (b) CV of the SN-rGO sample at a sweeping rate of 0.05 mV s^{-1}, along with the determination of the onset potential for the anodic peak and two cathodic peaks (P_a, $P1_c$, $P2_c$)

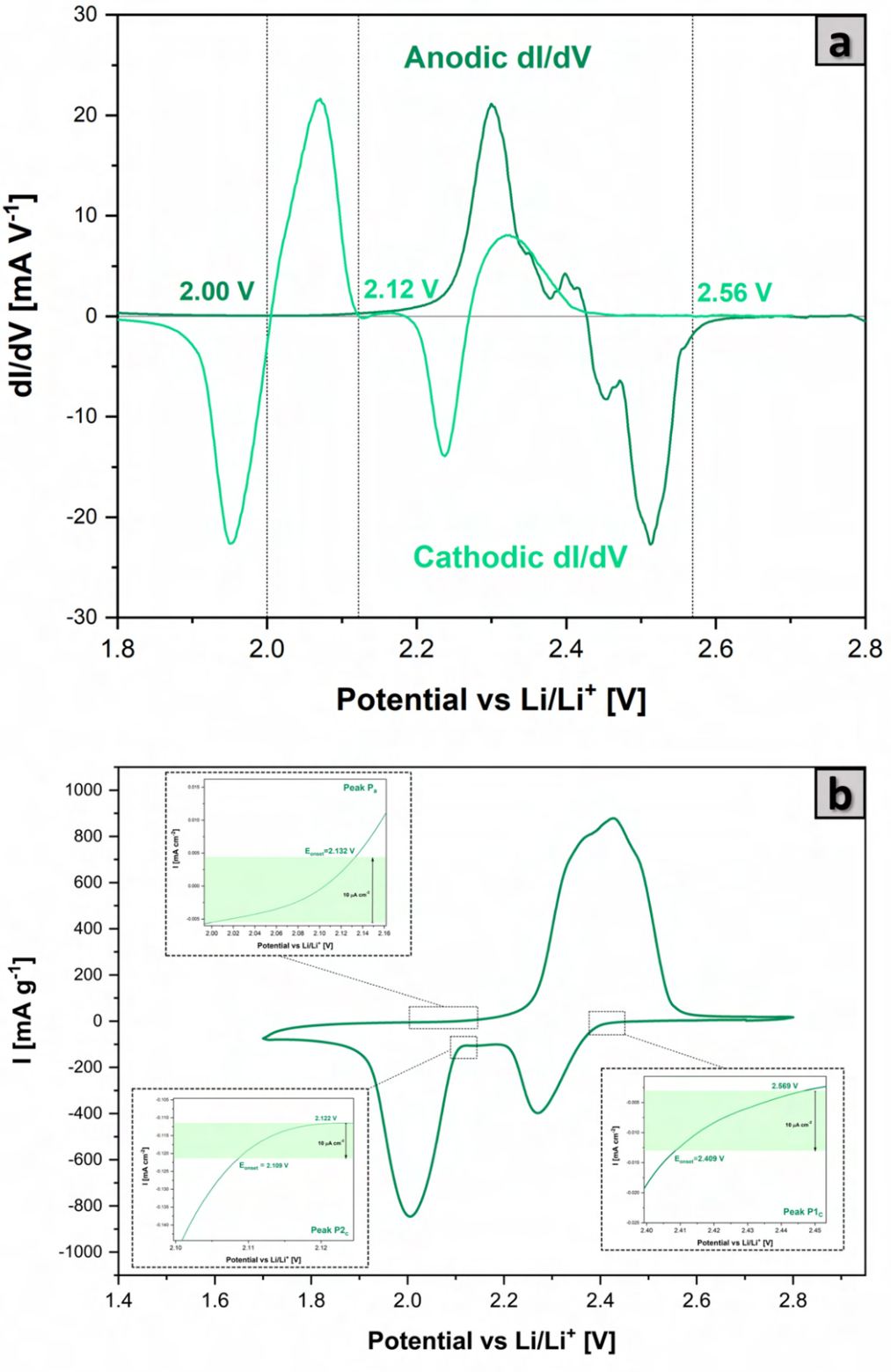

Fig. 5.17 (a) Differential CV curves for SN-rGO/ZnS. The baseline voltage and current density are defined in the same way as was done for the SN-rGO sample. (b) CV of the SN-rGO/ZnS sample at a sweeping rate of 0.05 mVs^{-1}, along with the determination of the onset potential for the anodic peak and two cathodic peaks (P_a, $P1_c$, $P2_c$)

Table 5.5 List of onset potentials for current peaks in cyclic voltammetry analysis for SN-rGO and SN-rGO/ZnS samples.

Sample	$\mathbf{E}_{onset}$ $\mathbf{P}_a$ **[V]**	$\mathbf{E}_{onset}$ $\mathbf{P1}_c$ **[V]**	$\mathbf{E}_{onset}$ $\mathbf{P2}_c$ **[V]**
SN-rGO	2.140	2.376	2.102
SN-rGO/ZnS	2.132	2.409	2.109

Table 5.6 : List of the voltages at which the current peaks (Pa, $P1_c$ and $P2_c$) occur in the cyclic voltammetry analysis for SN-rGO and SN-rGO/ZnS samples.

Sample	**E** $\mathbf{P}_a$ **[V]**	**E** $\mathbf{P1}_c$ **[V]**	**E** $\mathbf{P2}_c$ **[V]**
SN-rGO	2.437	2.253	2.000
SN-rGO/ZnS	2.421	2.270	2.005

Further information can be extracted from CV by increasing the scanning rate; in this way, an exploration of lithium diffusion into the electrodes was conducted using the Randles-Sevcik equation. According to this equation, the peak current (I_p) demonstrates a linear correlation with the square root of the scanning rate, and the slope is a factor determined by the lithium diffusion coefficient within the material [219]. Figure 5.20 displays the linear representation of peak current values against the square root of the scanning rate for the three peaks observed in the voltammograms. A higher slope indicates a greater diffusion coefficient. In Figure 5.20 (d), the computed values of Li^+ diffusion coefficients are graphed in relation to the fraction of converted Li^+ in the cathode [219]. The estimation of the latter was carried out by assuming that at the conclusion of the cathodic scan, all sulfur had transformed into Li_2S, signifying the fraction of lithium as maximum and conventionally equal to 1. The fraction of lithium within the cathode material was determined by dividing the area under the maximum current of the considered peak by the area under the entire reduction branch for the $P1_c$ and $P2_c$ peaks and the oxidation branch for the P_a peak. As depicted in 5.20 (d), the Li^+ diffusion coefficient is marginally higher in the case of SN-rGO/ZnS, thus affirming the advantageous role played by ZnS nanoparticles in the cathodic formulation.

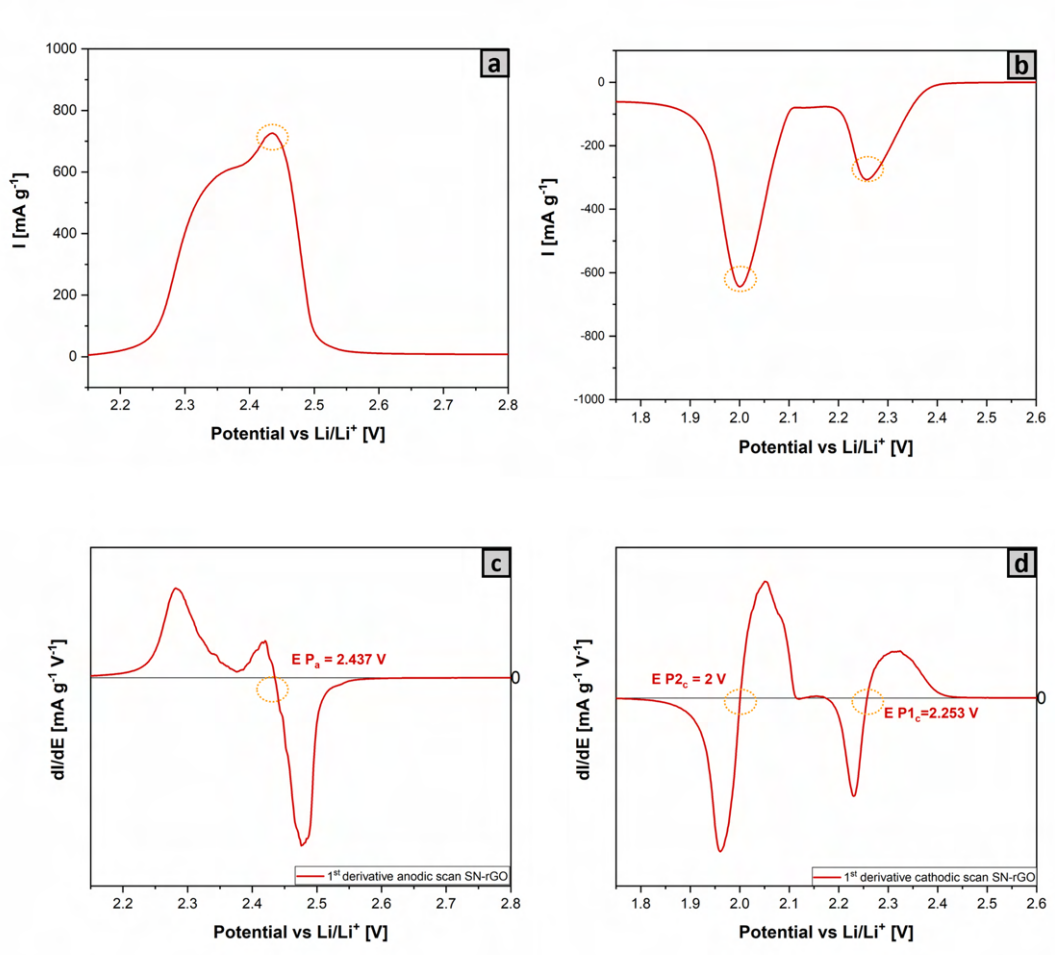

Fig. 5.18 Panels (a) and (b) report the magnification of the anodic and cathodic branch performed at 0.05 mVs^{-1} for the SN-rGO sample, while panels (c) and (d) show the potential values where the derivative $\frac{dI}{dV} = 0$ (associated with a sign variation), enabling the precise identification of the current peaks (yellow dotted circles) (P_a, $P1_c$, $P2_c$)

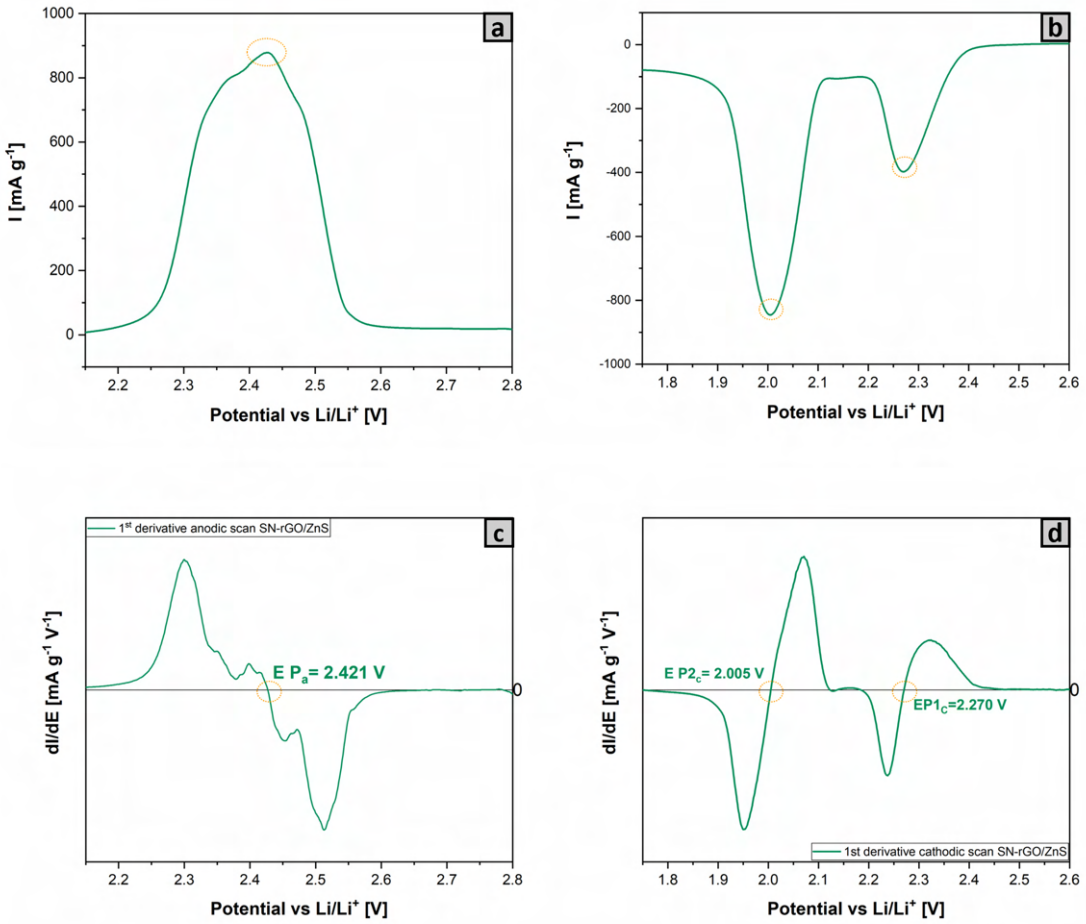

Fig. 5.19 Panels (a) and (b) report the magnification of the anodic and cathodic branch performed at 0.05 mVs^{-1} for the SN-rGO/ZnS sample, while panels (c) and (d) show the potential values where the derivative $\frac{dI}{dV} = 0$ (associated with a sign variation), enabling the precise identification of the current peaks (yellow dotted circles) (P_a, $P1_c$, $P2_c$)

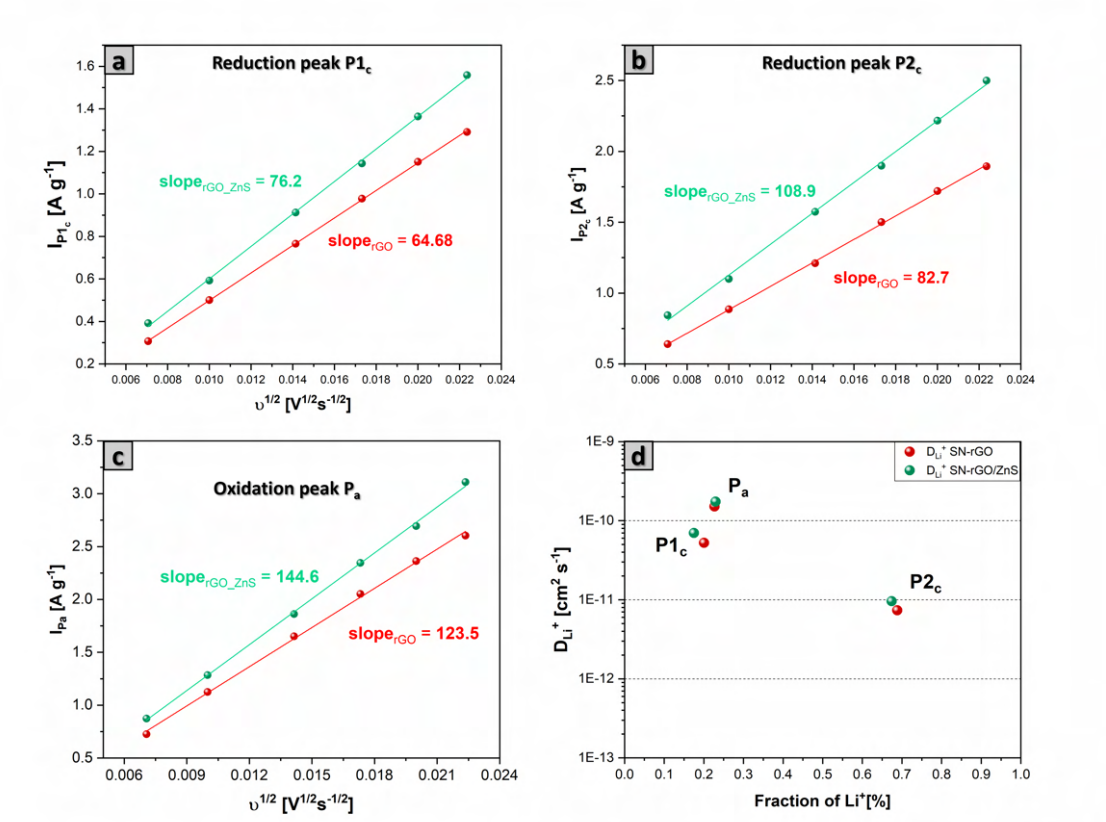

Fig. 5.20 (a) linear fitting of the reduction current peak $P1_c$ values (occurring at 2.0-2.1 V), (b) of the peak $P2_c$ (occurring at 1.8-2.0 V) and (c) of the peak P_a (occurring in the range 2.3-2.5 V) as a function of the square root of the applied scan rate for SN-rGO (red) and SN-rGO/ZnS (green) (d) comparison of the Li^+ diffusion coefficient within the cathode material as a function of the fraction of converted Li^+ for SN-rGO and SN-rGO/ZnS.

The electrochemical impedance spectra (EIS) were conducted on the untested cell and after each CV at various scan rates to gather additional insights into the reaction kinetics within our cells. As depicted in Figure 5.21, the Nyquist plots primarily featured a single semicircle at high and medium frequencies, representing the charge transfer resistance (R_{ct}), along with a straight line at lower frequencies indicative of lithium diffusion impedance (Z_w) in the cathode. The corresponding equivalent circuit employed for data fitting is illustrated in Figure 5.21 (h). Notably, the fresh SN-rGO/ZnS cell displayed an increased R_{ct} compared to SN-rGO, likely attributed to the lower electronic conductivity of ZnS nanoparticles in comparison to pure rGO. Conversely, a noteworthy reversal in trend was observed after the initial cycle at 0.05 mVs^{-1} [220], where the R_{ct} of SN-rGO became significantly

higher than that of SN-rGO/ZnS, as demonstrated in Figure 5.21 (i). This shift could be attributed to distinct deposition mechanisms of Li_2S on the two materials. ZnS nanoparticles seem to play a crucial role in alleviating the passivation of the cathode surface, resulting in lower resistance and increased activity towards lithium polysulfides (LiPSs).

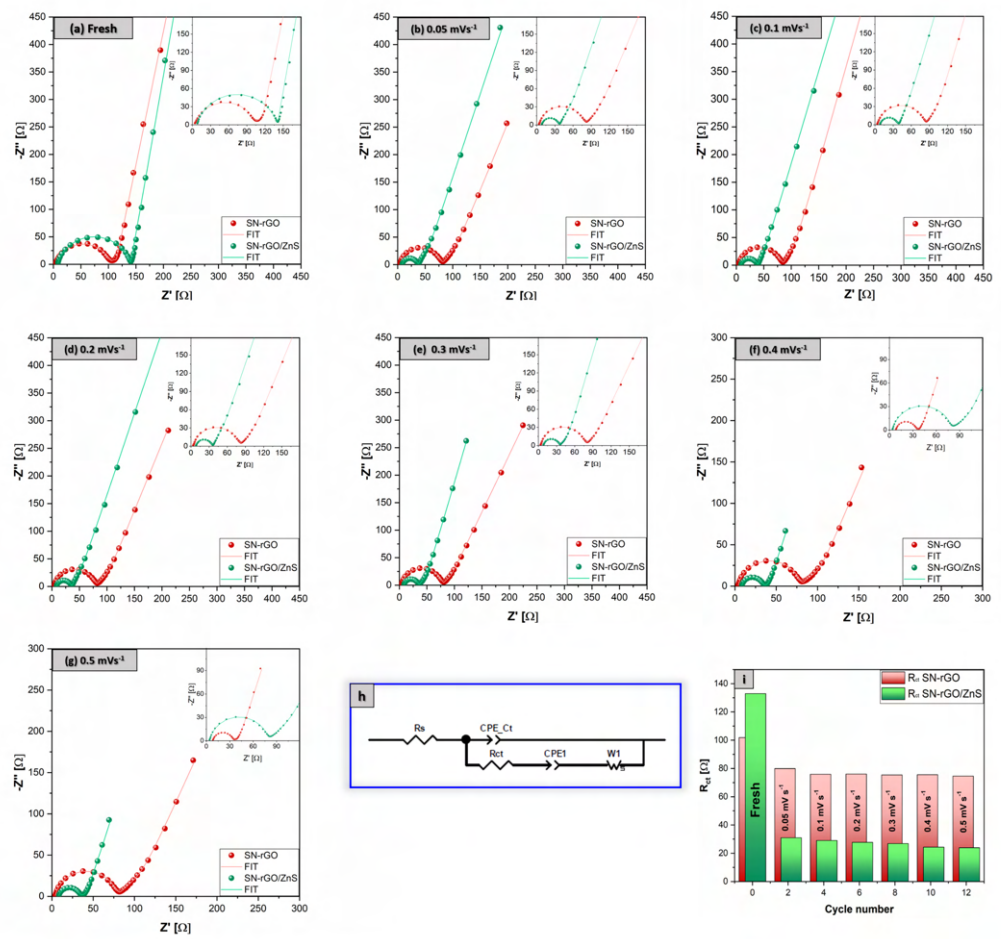

Fig. 5.21 Electrochemical impedance spectroscopy (EIS) conducted on the coin cell, where lithium metal served as the anode, and SN-rGO/S_8 and SN-rGO/ZnS/S_8 were utilized as cathodes. The impedance testing was carried out under various conditions, including (a) the initial state of the cell without being tested, (b) after cyclic voltammetry at 0.05 mVs^{-1} at 2.8 V, (c) following cyclic voltammetry at 0.1 mVs^{-1}, (d) post cyclic voltammetry at 0.2 mVs^{-1}, (e) subsequent to cyclic voltammetry at 0.3 mVs^{-1}, (f) after cyclic voltammetry at 0.4 mVs^{-1} and (g) after cyclic voltammetry at 0.5 mVs^{-1} while the panel (h) depicts the equivalent circuit employed for fitting the EIS data and panel (i) reports the comparison of the R_{ct} values for the two different materials recorded at 2.8 V after the second cycle of CV at each different scan rate.

To assess the electrochemical performance of our cathodes, we tested them with an extended galvanostatic cycling test within the potential range of 1.85–2.6 V vs. Li/Li^+ at a current density of 0.5 C for 750 cycles. Prior to the long cycling, three formation cycles were conducted at 0.1 C. The outcomes are illustrated in Figure

5.22, revealing that the SN-rGO/ZnS/S_8-based cathode outperforms the SN-rGO/S_8 sample over cycling. It exhibited an initial discharge specific capacity of 786 mAh g^{-1} during the first cycle at 0.5 C, which decreased to 379 mAh g^{-1} after 750 cycles (retaining 48.2% of its capacity). The fading decay rate was 0.07% per cycle, and the coulombic efficiency (CE) ranged between 99.0% and 96.0%. In contrast, the SN-rGO/S_8 displayed a higher initial discharge capacity (832 mAh g^{-1} during the first cycle at 0.5 C). However, its decay over cycling was more pronounced (0.09% per cycle with a final capacity retention of 32.5%), and it exhibited a lower CE (97.1% at the first cycle at 0.5 C and 95.0% at the 750th cycle). The charge-discharge voltage profiles at the third cycle at 0.1 C are depicted in Figure 5.23 (a), allowing the extraction of the polarization potential ΔE ($Q_{\frac{1}{2}}$) between the second discharge plateau and the charge plateau. The polarization values for both SN-rGO/ZnS and SN-rGO over the 750 cycles are presented in Figure 5.23 (b), indicating that at low C-rates, the ΔE ($Q_{\frac{1}{2}}$) is not particularly pronounced, while at 0.5 C, the polarization is consistently higher for the SN-rGO/S_8-based cathode. These findings align with the different onset potentials and peak potentials extracted from the CV measurements.

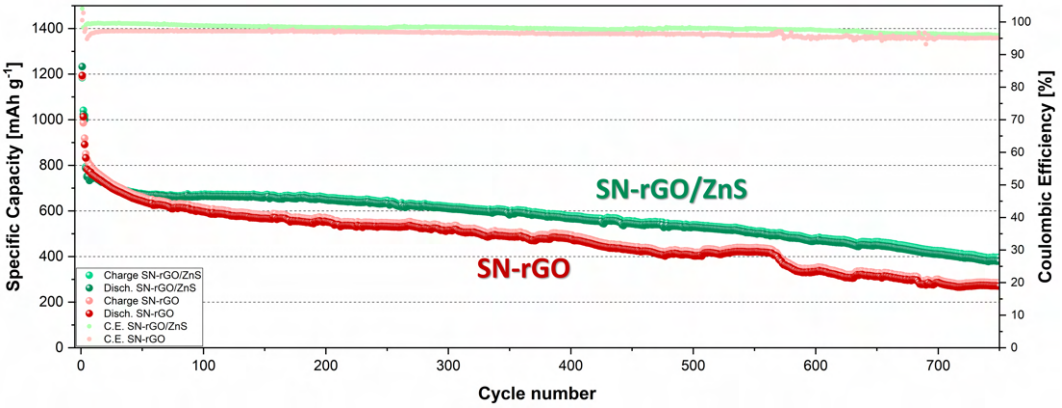

Fig. 5.22 Comparison of specific capacity over cycling at the current density of 0.5 C for 750 cycles of the SN-rGO/S_8- and SN-rGO/ZnS/S_8-based cathodes

Additionally, Figure 5.23 (c) provides a magnification of the initial charge step of the third cycle at 0.1 C, offering insights into the activation energy required to initiate the oxidation process of Li_2S. The potential jump exhibited by the SN-rGO/S_8-based cathode is significantly higher than that needed for the SN-rGO/ZnS/S_8 (20.7 mV vs. 4.9 mV), confirming the hypothesis of the 2D passivation of graphene sheets by Li_2S as previously proposed. Another crucial parameter extracted from the charge-

discharge profiles is the ratio between the capacities associated with the two distinct plateaus, denoted as Q_1 and Q_2 in Figure 5.23 (d). The Q_2/Q_1 ratio, indicative of the catalytic activity of the cathode material towards lithium polysulfides, is consistently higher for SN-rGO/ZnS over the 750 cycles, suggesting superior catalytic ability.

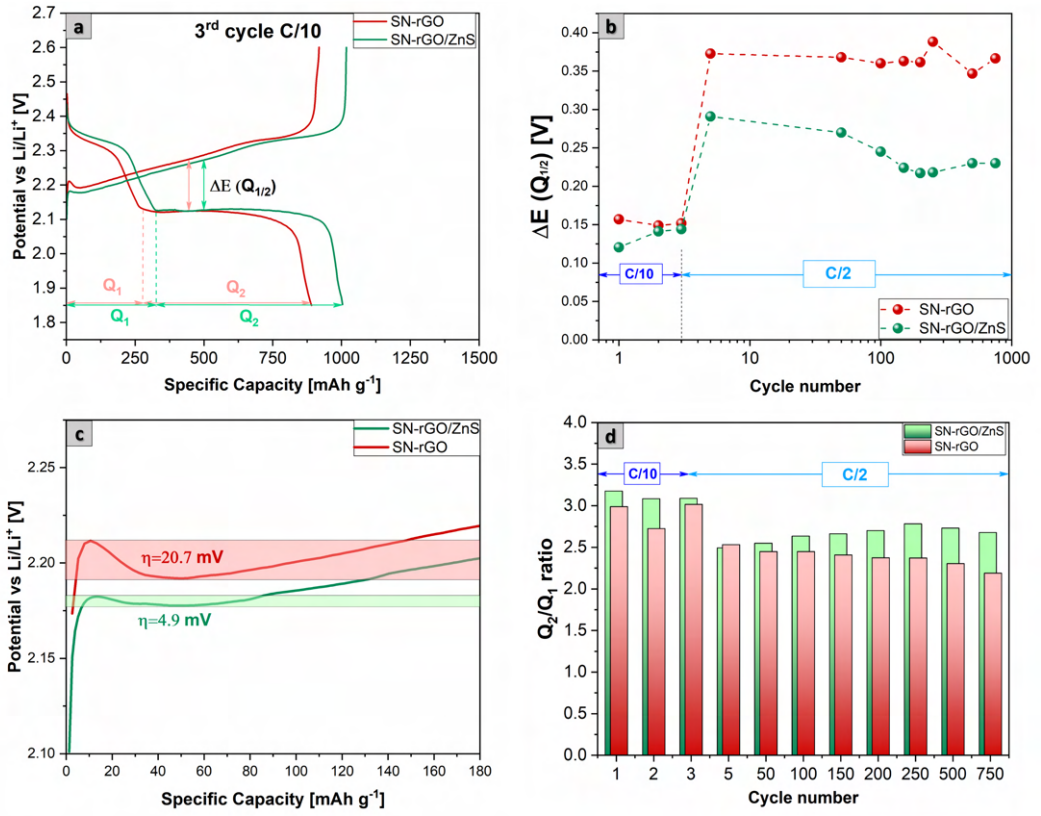

Fig. 5.23 (a) comparison of the charge-discharge voltage profiles of SN-rGO and SN-rGO/ZnS samples at the third cycle at 0.1 C (b) visualization of the values of overpotential ΔE ($Q_{\frac{1}{2}}$) between the lower discharge plateau and charge plateau over cycling; (c) magnification of the charge profile of the third cycle at 0.1C which highlights the lower overpotential needed to activate the Li_2S oxidation in the case of the SN-rGO/ZnS/S_8-based cathode (d) comparison of the Q_2/Q_1 ratio values over cycling for the SN-rGO/S_8 and SN-rGO/ZnS/S_8-based cathodes.

Finally, the rate performance at increasing current density was tested for the two distinct cathodic formulations, as illustrated in Figure 5.24. In this scenario as well, the SN-rGO/ZnS/S_8-based cathode demonstrated the capability to deliver significantly higher specific discharge capacities as the current density increased, as detailed in Table 5.7, which also provides the reversible capacity for each scan rate.

Furthermore, Figure 5.24 (b) reveals that the polarization between the low discharge plateau and the charge plateau gradually rises for both SN-rGO and SN-rGO/ZnS, albeit with the latter exhibiting a notably lower absolute value. This trend persists until reaching 1 C, suggesting a potential intrinsic limitation of the material in coping with the escalating current.

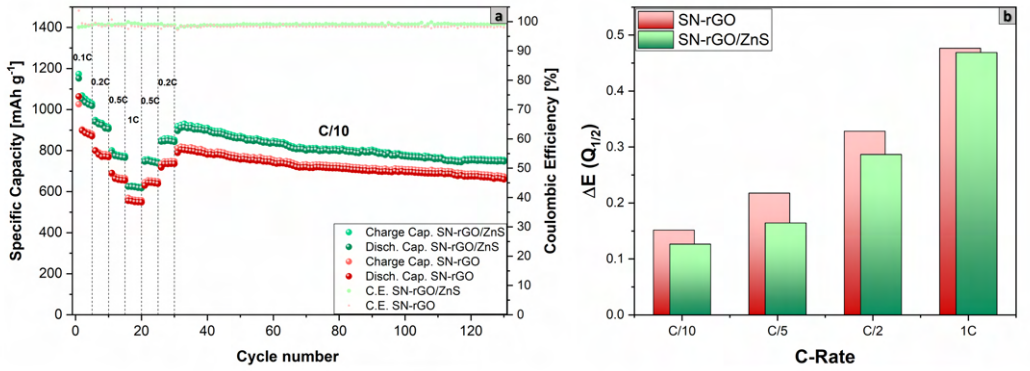

Fig. 5.24 (a) The rate capability performance at increasing C-rate was compared between the SN-rGO/S_8-based and SN-rGO/ZnS/S_8-based cathodes. (b) The polarization between the low discharge plateau and the charge plateau for the different cells was plotted against the applied C-rate.

Table 5.7 List of onset potentials for current peaks in cyclic voltammetry analysis for SN-rGO/S_8 and SN-rGO/ZnS/S_8 samples.

Sample	**0.1 C [mAh]**	**0.2 C [mAh]**	**0.5 C [mAh]**	**1 C [mAh]**	**Reversible capacity 0.2C [%]**	**Reversible capacity 0.5C [%]**	**Reversible capacity 1C [%]**
SN-rGO/S_8	872	769	653	547	96.1	93.1	90.0
SN-rGO/ZnS/S_8	1017	903	766	613	97.3	93.6	90.2

Chapter 6

LNMO-LFP blended cathodes for Li-ion batteries

In the contemporary landscape, Li-ion batteries find widespread use in powering mobile electronic devices, such as smart devices, laptops, and cameras. However, for Electric Vehicles (EVs), there is a pressing need for substantial advancements in energy density, cost efficiency, and safety features. [221]
As we approach the era of cathodes without cobalt, various potential alternatives (depicted in Figure 6.1) have been devised or are currently under development. Notably, $LiFePO_4$ and $LiMn_2O_4$, despite their commendable thermal stability and cost-effectiveness, may not stand out as the optimal choices. The primary drawback of $LiFePO_4$ lies in its inadequate electrical and low voltage plateau at 3.3 V, imposing constraints on its specific energy density. Moreover, the $LiFePO_4$ system has undergone extensive scrutiny, making further enhancements in this direction exceptionally challenging. [222] Turning to $LiMn_2O_4$ (LMO), the first cathode material synthesized in 1958, it faces challenges due to significant volumetric changes during cycling, attributed to the Jahn-Teller distortion associated with Mn^{3+}. Conversely, novel polyanion-type cathode materials like $LiMPO_4$ [223], $LiMBO_3$ [224], (where M represents Fe and Mn) have been thoroughly investigated. However, their adoption in industrial applications remains distant due to their relatively modest specific energy densities, low-temperature performance, and intricate synthesis procedures. Despite the potential of Li-rich oxides, Ni-rich layered oxides, and LNMO (spinel) as promising cathode materials with favorable performance and cost-effectiveness, practical implementation faces several challenges. In the case of high-voltage LNMO,

developed based on spinel lithium manganese, it demonstrates reversible capacities of approximately 146.7 mAh g^{-1} and a high working voltage of 4.7 V vs Li/Li^{+} . [225] Nonetheless, severe interfacial side reactions between LNMO and electrolyte at elevated voltage or temperature levels pose significant challenges. Additionally, the by-products of these side reactions, such as Mn^{2+} and Ni^{2+}, tend to migrate toward the anode, compromising the solid electrolyte interphase (SEI) and depleting active Li^{+}, ultimately leading to the degradation of overall cell performance. [226] In some instances, the relatively unstable Mn^{3+} ions in disordered LNMO (spinel) undergo disproportionation into Mn^{4+} and Mn^{2+} ions, further contributing to the deterioration of cycling performance in full cells.

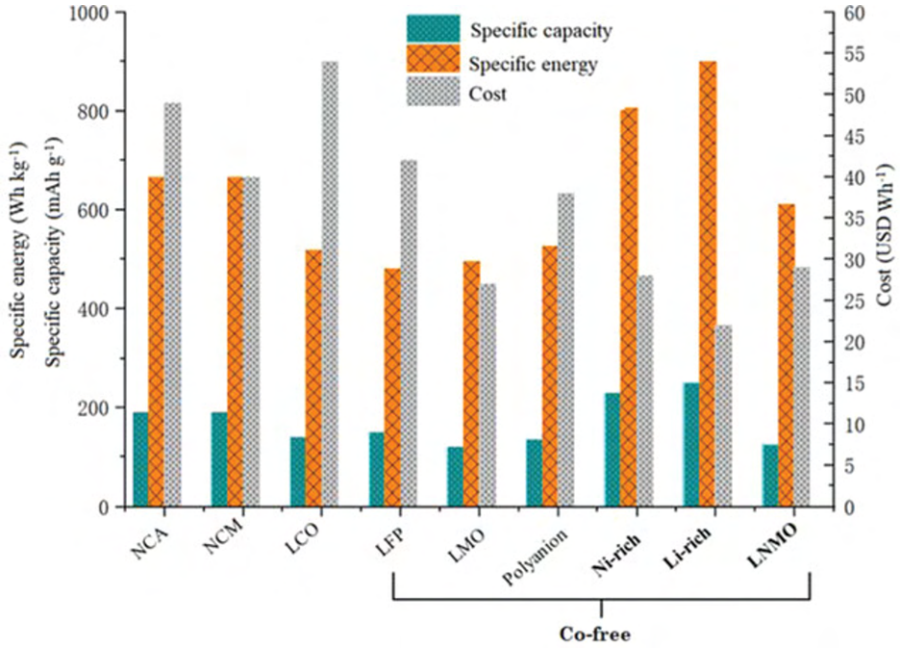

Fig. 6.1 Comparison of different cathode materials NCA: $Li[Ni_{0.8}Co_{0.15}Al_{0.05}]O_2$; NCM: $Li[Ni_{0.8}Co_{0.8}Mn_{0.1}]O_2$; LCO: $LiCoO_2$; LFP: $LiFePO_4$; LMO: $LiMn_2O_4$; Polyanion: $LiMnPO_4$; Ni-rich: $Li[Ni_{0.9}Mn_{0.1}]O_2$; Li-rich: $Li_{1.2}Ni_{0.2}Mn_{0.6}O_2$ and LNMO: $LiNi_{0.5}Mn_{1.5}O_4$. Reproduced from reference [227]

A promising approach to improve the features of a single cathodic material involves blending different lithium insertion materials to design advanced electrodes for future LIBs. The concept of a "blended cathode" entails a mixture of multiple lithium insertion compounds, aiming to combine the favorable properties of individual active materials and enhance energy or power density, cycling, and storage durability. An important aspect that should be underlined about this work is that it

was carried out within the framework of the European project HYDRA, on which I worked during all the years of the duration of the PhD and thanks to which I was able to come into contact with different realities and researchers from whom I learned a lot. Specifically, in this project, the blend consists of LNMO and LFP in two different formulations (LNMO+2%$_{wt}$ LFP and LNMO+10%$_{wt}$ LFP). In this context, the combination of diverse insertion materials may be seen as a delicate equilibrium seeking to enhance the strengths of each individual component (see Figure 6.2)

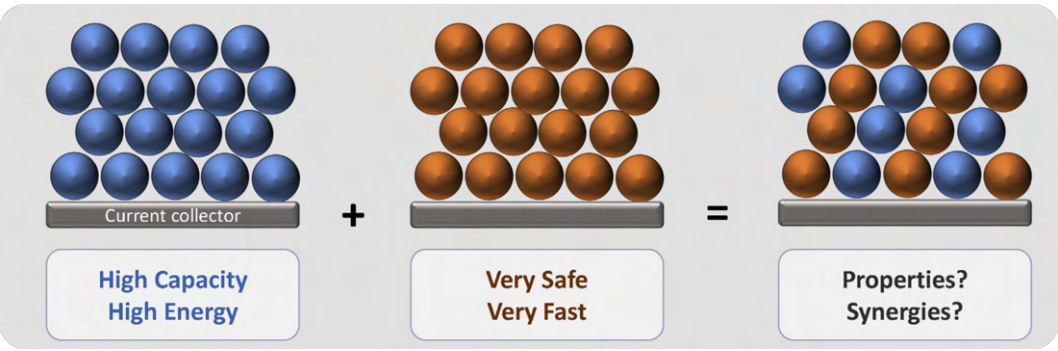

Fig. 6.2 Simple representation of the principle underlying mixing between two different active materials. Reproduce from [221]

However, recent findings in the literature also propose synergistic effects arising from blending, wherein the collective properties of the blend surpass those of each constituent material. It is worth mentioning that there are essentially two strategies for obtaining a blending of two different materials. In one case, defined as chemical blending, the two materials are directly synthesized in the same process or in different sequential steps, resulting in core-shell structures [228, 229] or different composites [230, 231]. This strategy is undoubtedly interesting due to the particular structures that can be obtained and the high degree of interaction between the two materials. In the second case, defined as physical blending, the two materials are previously and individually synthesized and are then mixed through physical processes. This type of approach is simpler than the first and it is also preferable from an industrial point of view. For example, layered-type materials exhibit high capacities and energy densities but face cost challenges, thermal stability, and rate capability. Olivine-structured cathode materials offer improved thermal stability but lower electrode potentials, reducing energy density. Spinel-type compounds exhibit higher operating voltages, lower cost, higher rate capability, and better thermal stability but suffer from low discharge capacity and poor cycle life.

Blending different insertion materials helps balance these advantages and disadvantages, improving overall cathode material performance. This strategy allows customization of Li-ion battery characteristics for specific applications, from small-scale devices to large-scale energy storage systems. Recent investigations have focused on blended cathodes using commonly employed active materials like NMC, LMO, LFMP, and LFP. However, understanding the beneficial effects of blending cathode materials remains challenging, requiring further efforts in the mixing procedure and electrode design. Recent emphasis has been put on environmentally friendly, cobalt-free, and cost-effective cathode materials like LNMO (spinel) and LFP (olivine). In particular, LNMO offers high voltage and specific capacity but faces challenges of cation leaching and electrolyte decomposition, compromising safety, while LFP stands out for safety and stability but has lower energy density. Consequently, blending LNMO and LFP presents an opportunity to balance high energy density and stable cycle life, making them a viable solution for the next generation of LIBs. Despite the existing context, the exploration of blended materials, specifically the combination of LNMO with LFP, has been given limited attention. At the time of writing this work, apart from a few studies involving the application of a layer of $FePO_4$ or LFP to LNMO particles, the physical mixing of these two materials has not been extensively investigated [232–234]. Therefore, the primary objective of the work reported in this chapter is to delve into the electrochemical properties of blended LNMO/LFP cathodes. More specifically, two different LNMO/LFP ratios were explored, meticulously examining the influence of each component on the electrochemical performance through various techniques. The results were systematically correlated with the morphological aspects of the electrodes.

6.1 Lithium Nickel Manganese Oxide (LNMO)

6.1.1 Structure and electrochemical performance of $LiNi_{0.5}Mn_{1.5}O_4$

The $LiMn_2O_4$ spinel is a commonly used cathode material valued for its cost-effectiveness, environmental friendliness, and safety attributes. The MnO_2 framework offers 3D pathways for Li^+ diffusion, ensuring high-rate capability. However,

$LiMn_2O_4$ faces significant challenges related to capacity fading, particularly when subjected to repeated cycles at elevated temperatures. The capacity decay arises from irreversible structural shifts from spinel to tetragonal structures due to the Jahn-Teller distortion of Mn^{3+}, and the dissolution of Mn ions in the electrolyte caused by H^+ corrosion. Furthermore, the energy density of $LiMn_2O_4$ is not competitive due to its standard electrode potential (4.0 V vs. Li/Li^+) and theoretical capacity (148 mAh g^{-1}). Fortunately, substituting Mn with other metal ions has proven effective in enhancing $LiMn_2O_4$ performance. Dopants are able to alleviate the Jahn-Teller distortion and improve structural stability, resulting in improved cyclic performance. Among the doped $LiMn_2O_4$ (LMO) materials, the LNMO cathode has garnered attention for its enhanced cycling behavior and discharge voltage (plateau at 4.7 V vs. Li/Li^+) compared to the undoped spinel. LNMO exhibits a higher energy density (650 Wh kg^{-1}) than $LiCoO_2$ (518 Whkg^{-1}), $LiMn_2O_4$ (400 Wh kg^{-1}), $LiFePO_4$ (495 Wh kg^{-1}), and $LiCo_{1/3}Ni_{1/3}Mn_{1/3}O_2$ (576 Wh kg^{-1}), making it promising for practical use. Despite its advantages, LNMO faces challenges, particularly a potential corrosion reaction between the cathode surface and electrolyte at the high voltage of 5 V, leading to poor rate stability, especially at elevated temperatures. [235]

LNMO is derived from an arrangement of oxygen atoms in a cubic close-packed structure, where transition metals (TMs) occupy half of the octahedral sites, forming a stable 3D framework of MO_6 octahedra that share edges. Lithium atoms are situated at 1/8 of the tetrahedral sites, and LiO_4 tetrahedra share their vertices with MO_6 octahedra and faces with vacant octahedral sites, facilitating the 3D mobility of Li^+ ions. The ordering of TMs in LNMO is influenced by synthesis parameters. In the disordered LNMO (structure reported in Figure 6.3 a) , Ni and Mn atoms are randomly distributed on specific sites, while Li atoms occupy 8a sites in the Fd-3m cubic unit cell. In the ordered LNMO (Figure 6.3 b), achieved at a higher synthesis temperature, Ni and Mn atoms order at 4b and 12d sites of the $P4_332$ cubic cell, respectively, and Li atoms are positioned at 8c sites. [236]

The disordered spinel-based materials may contain a Ni-rich rock-salt phase impurity, leading to the formation of Mn^{3+} in the Fd-3m spinel phase and affecting Mn redox activity, as well as introducing additional charge carriers. Several investigations have concentrated on comprehending the influence of diverse physicochemical characteristics, such as particle shape, size, exposed facets, oxygen, TM stoichiometry, and the degree of TM ordering on the electrochemical performance of LNMO. The

electrochemical performance of the disordered Fd-3m phase has been a subject of debate, with some studies claiming its superiority, while others have contested this perspective. During the charging process, Li^+ diffusion within the spinel structure occurs in three dimensions, with lithium ions migrating to adjacent octahedral positions. The established understanding is that the diffusion path of lithium in spinels forms a comprehensive three-dimensional network. In spinels like $LiMn_2O_4$, lithium undergoes migration from one tetrahedral site to the next through a vacant octahedral site. [237] In the case of the ordered $LiNi_{0.5}Mn_{1.5}O_4$, a distinct Ni site in 4b and a Mn site in the 12d position of the $P4_332$ space group are created. Correspondingly, vacant octahedral sites are categorized into 4a and 12d sites. The 4a site is surrounded by three Ni and three Mn atoms, while the 12d site is surrounded by one Ni and five Mn atoms. The migration of lithium between tetrahedral sites takes place through intermediate vacant octahedral sites. Given that each tetrahedral site is surrounded by one 4a and three 12d sites, two separate lithium diffusion paths emerge, as depicted in Figure 6.3 (c). Following the path I, three Ni atoms undergo a transition from 2^+ to 4^+, resulting in an escalation of electrostatic repulsion and activation barriers during the Li^+ delithiation process along this route. In contrast, the activation barriers in path II are noticeably lower than those in path I, both in the lithium-rich phase and the vacancy-rich phase. [238] In the case of the disordered Fd-3m structure of the LNMO, however, since it lacks a long-range cationic order, the diffusion mechanism of lithium ions does not follow preferential paths as in the case of the ordered structure but rather is very similar to the phenomenon that occurs in the original lithium manganese oxide.

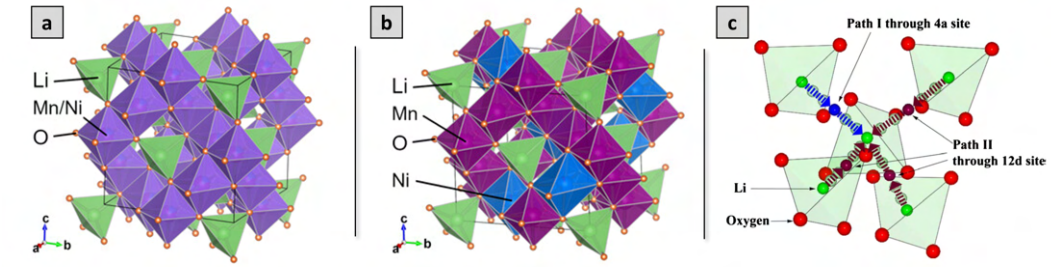

Fig. 6.3 (a) Crystal structure Fd-3m of the disordered LNMO (b) Crystal structure $P4_332$ of the ordered LNMO (c) Diagram depicting two separate routes for lithium migration within structured LNMO. Green spheres represent lithium ions, while red spheres represent oxygen ions. The first lithium diffusion route, labeled as Path I, is illustrated by blue arrows, with the blue sphere indicating the 4a site situated in the middle of Path I. The second lithium diffusion route, Path II, is highlighted by dark scarlet arrows, with dark scarlet spheres representing the 12d sites along Path II. Reproduced from [239] and [238].

Now suppose to consider the charging process of the LNMO (which occurs with consequent de-insertion of Li^+ ions), taking into account the electronic structure shown in Figure 6.4. The crystal field splits the 3d levels of Mn and Ni octahedrally coordinated with oxygen into e_g and t_{2g} levels. For Mn^{3+}, among the four $3d^4$ electrons with majority spin (↑) three electrons are on t_{2g}(↑) and one electron is on e_g(↑). The $3d^8$ electrons of Ni^{2+} have six electrons on the t_{2g}(↑↓) levels and two electrons on the eg(↑) level. When an electron is taken away from Mn^{3+} (and this is the case in which the LNMO appears in its disordered structure, Figure 6.4 (b)), it is removed from the Mn e_g (↑) state that has an electron binding energy at around 1.5–1.6 eV, and this explains the appearance of the plateau occurring at 4.1 V, which is present in the charge/discharge profiles shown in Figure 6.4 (c). When there are no more electrons left on Mn e_g (↑) (which means that all Mn are oxidized to Mn^{4+}, and this is instead the case of the LNMO with ordered structure), then electrons are removed from Ni e_g (↑) that has an electron binding energy of about 2.1 eV, and the voltage plateau moves up to 4.7 V vs Li/Li^+ because of the increased energy needed to extract electrons. Anyway, it is widely accepted that disordered LNMO has higher electronic conductivity than that of ordered LNMO in a low state of charge (SOC). But after full delithiation, the electronic conductivity of both is almost the same. [240]

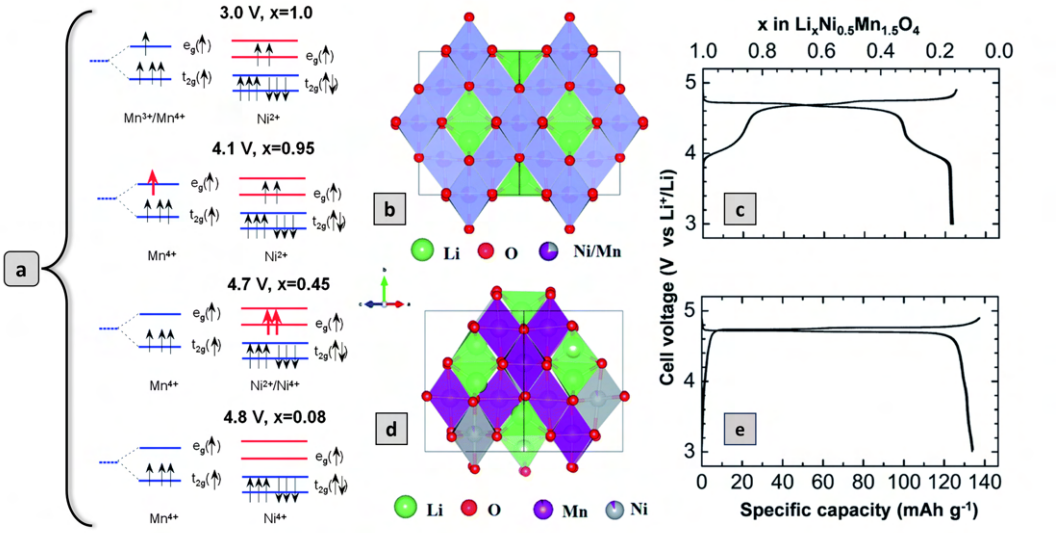

Fig. 6.4 (a) Diagram showing the electronic levels of Mn^{3+}, Mn^{4+}, Ni^{2+} and Ni^{4+} in LMNO material, reproduced from [241] (b) disordered structure of LNMO, (c) typical charge/discharge profile of the disordered LNMO cycled in the 3-4.9 V vs Li/Li^+ potential window, showing the 4.1 V plateau due to the presence of Mn^{3+} (d) ordered LNMO structure and (e) typical charge/discharge profile of the ordered LNMO cycled in the 3-4.9 V vs Li/Li^+ potential window, reproduced from [242]

6.1.2 LNMO limitations and possible approaches

At present, the capacity fade, the relatively short cycle life, and low coulombic efficiency are the main drawback of spinel LNMO, as a result of bulk structural and surface chemical instability, as well as a lack of suitable electrolyte for high-voltage operation, hindering the commercialization and further application of LNMO.

Structural and surface chemical instability: The surface stability of LNMO is certainly one of the aspects that can be improved in this material, since it contributes to rapid capacity decay, which usually involves the parasitic dissolution of transition metals, particularly Mn, into the electrolyte (especially if based on carbonate solvents and salt $LiPF_6$) during cycling. In particular, Mn dissolution in spinel $LiMn_2O_4$ has been explained by the surface disproportionation reaction:

$$2Mn^{3+} \rightarrow Mn^{2+} + Mn^{4+} \tag{6.1.1}$$

The average oxidation state of Mn in LMO is +3.5 (50% Mn^{3+} and 50% Mn^{4+}), and one of the most straightforward approaches to mitigate Mn dissolution in LMO is increasing the average oxidation state of Mn by partly substituting Mn with monovalent (Li^{+}) and/or divalent cations (such as the Ni^{2+} in LNMO). However, as already specified previously, depending on the synthesis conditions (in particular temperature is the most important parameter in this sense), the LNMO can present itself in its ordered structure (T < 700 °C), which contains a very low quantity of Mn^{3+}, or disordered (T > 700 °C) which is formed with a loss of oxygen in the structure and a consequent formation of Mn^{3+} to maintain electroneutrality. In particular, Pieczonka and others conducted an in-depth study on the dissolution mechanisms of Mn and Ni using an electrolyte of "standard" composition (1 M $LiPF_6$ in ethylene carbonate (EC)/diethyl carbonate (DEC) (1:2 volume ratio)), evaluating the effect of different parameters such as:

- **State of charge (SOC):** in this case, electrodes at different SOCs were immersed in fresh electrolyte and stored at 60 °C for 60 days. The amount of TM dissolved in the electrolyte was evaluated by X-ray fluorescence (XRD) and the results are shown in Figure 6.5 (a). It can be noted that the amount of TM dissolved in the electrolyte increases slightly when the SOC is around 50%, and then increases considerably when the cathode is completely de-lithiated (SOC > 75%). An interesting aspect is that not only is manganese affected by the dissolution mechanism, but also Ni has high concentration values at high SOC.

- **Storage temperature:** in this scenario, the observed pattern can be elucidated by the hydrolysis of $LiPF_6$ in the presence of limited amounts of water within the electrolyte composition, leading to the subsequent generation of HF, as depicted by the following equations [243, 244]:

$$LiPF_6 \rightleftharpoons LiF + PF_5 \tag{6.1.2}$$

$$PF_5 + H_2O \rightleftharpoons OPF_3 + 2HF \tag{6.1.3}$$

$$OPF_3 + 2xLi^{+} + 2xe^{-} \rightleftharpoons LixPF_{3-x}O + xLiF \tag{6.1.4}$$

$$OPF_3 + 3H_2O \rightleftharpoons PO_4H_3 + 3HF \tag{6.1.5}$$

According to findings from the differential scanning calorimetry (DSC) measurement, the mentioned hydrolysis reaction was noted to occur approximately at 60 °C, and the resultant HF is responsible for the additional dissolution of Mn, as reported in 6.4 (b); with the increase in temperature, both the hydrolysis reaction of $LiPF_6$ and the dissolution reaction of TM are accelerated.

- **Storage time:** In this case, the trend of the TM concentration in the electrolyte is more complicated: it increased significantly during the first 20 days of storage and then reached a plateau. The explanation for this behavior was attributed to the fact that the electrode immersed in the electrolyte was completely de-lithiated, so Pieczonka et al. [245] hypothesized that there was a re-lithiation phenomenon (or self-discharge of the LNMO) over time. This phenomenon was evaluated via XRD, evaluating the lattice parameter of the LNMO after storage at 60 °C, which was found to be very similar to that of the lithiated LNMO (SOC 0%). Consequently, since the $LiPF_6$ degradation and dissolution reactions are strongly influenced by the composition (at LNMO SOC=0% with the LMNO fully lithiated), one can understand why, after a long period of storage and consequent self-discharge of the electrode, the concentration of TM reaches a stationary value.

- **LNMO crystal structure:** about this feature, as illustrated in Figure 6.5 (d), the disparity in the dissolution of transition metals in the electrolyte appears to be minimally affected by the crystalline structure of the LNMO. However, this outcome may seem unexpected given that the disordered form contains a higher concentration of Mn^{3+}, which is prone to undergo a disproportionation reaction. Although Pieczonka and his group did not offer an exhaustive explanation for this trend, a possible explanation can be sought in studies published subsequently. Notably, Quiao et al. [246] observed through in situ soft X-ray spectroscopy (sXAS) studies that the presence of Mn^{2+} on the electrode surface is higher at high State of Charge (SOC) levels (when LNMO is fully delithiated, and theoretically, all Mn should be oxidized to Mn^{2+}). This trend was observed for both ordered and disordered LNMO. Consequently, it is suggested that the SOC exerts a significantly greater influence than the crystalline structure of LNMO on the dissolution of TMs. Furthermore, Sun et al. [247] delved into the impact of TM dissolution and LNMO crystal structure on the electrochemical performance of the cell. Their study involved sXAS analyses

on electrodes cycled for 200 cycles, examining ordered LNMO, disordered LNMO, and a blend of both. Interestingly, they noticed that the disordered LNMO sample was the one that presented the highest Mn^{2+} concentration values on the surface. Nonetheless, the electrochemical performances of the ordered sample were the poorest, while the blended sample exhibited superior performance, with the disordered LNMO in the middle. Consequently, they concluded that the phenomenon of TM dissolution should be comprehended within a broader context, emphasizing that lithium delithiation/lithiation behaviors are fundamentally holistic chemical processes within cathode materials, encompassing both surface and bulk structures. Thus it can be concluded that the degradation of LNMO capacity is closely linked to, but not restricted to, variations in surface or structural chemistry.

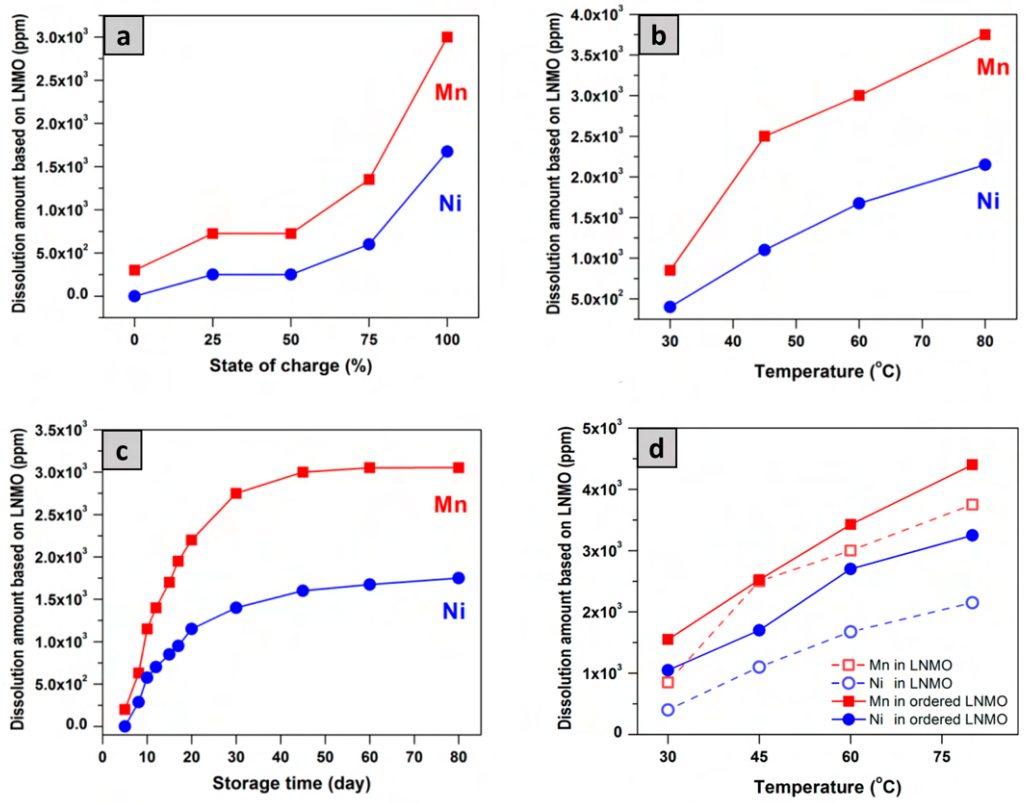

Fig. 6.5 Results of the TM dissolution tests from the stored LNMO electrodes under different conditions: (a) influence of different SOC of LNMO on TM dissolution after being stored at 60 °C for 60 days; (b) dissolution of TM in disorderd LNMO vs different temperature (electrode stored at 100% SOC for 60 days); (c) time dependence of TM dissolution for an electrode at 100% SOC. (d) Comparison of the amount of Mn and Ni dissolution in aged electrolyte samples from disordered LNMO and ordered LNMO electrodes at 100% SOC, after being stored at various temperatures for 60 days. Reproduced from [245])

In light of the aforementioned points, the surface instability of LNMO, irrespective of its ordered or disordered structure, proves challenging to be isolated within the broader environment that constitutes an electrochemical cell. For instance, the composition of the electrolyte stands out as a crucial parameter capable of profoundly altering the surface degradation mechanisms of the electrodes. Another significant factor is the nature of the anode; if made of graphite for example, the dissolution of Mn^{2+} in the electrolyte can trigger the subsequent reactions:

$$Mn^{2+} + 2LiC_6 \rightarrow Mn + 2Li^{+} + graphite \tag{6.1.6}$$

This reaction promotes the loss of active Li^+ through the formation of thick solid electrolyte interface (SEI) layers, leading to substantial capacity decay in full cells.

A plausible mechanism theorized by Choi et al. [248] and depicted in Figure 6.6 illustrates the involvement of $LiPF_6$, the most widely used salt in Li-ion batteries. As previously emphasized, the dissolution of TM and electrolyte degradation are interconnected phenomena. The mechanism in Figure 6.6 underscores how initial steps could involve either the thermal degradation of the salt to form PF_5 or its oxidation.
Delithiated LNMO, charged up to 4.9 V vs. Li/Li^+ , exhibits oxidative characteristics, readily accepting electrons from electron-rich PF_6^- anions in the electrolyte. This process forms $PF_6\cdot$ radicals through the oxidation of PF_6^- anions, which then generate phosphate-carbon complexes (P-O-C group) by reacting with carbonates. This sequence of events results in the reduction of Mn^{4+} to Mn^{3+}, where the presence of Mn^{3+} in disordered LNMO may not be the determining factor. Subsequently, trivalent manganese ions undergo a disproportionation reaction, releasing divalent manganese ions and yielding tetravalent ones. The divalent manganese ions dissolve into the electrolyte, while tetravalent manganese ions may form MnO_2 compounds on the cathode surface. At this stage, radicals and PF_5 can react with trace amounts of H_2O in the electrolyte, forming PFO_3 and HF, which can then combine with Mn^{2+} ions to precipitate as MnF_2, in accordance with the equation [249]:

$$4HF + 2LiNi_{0.5}Mn_{1.5}O_4 \rightarrow 3Ni_{0.25}Mn_{0.75}O_2 + 0.25NiF_2 + 0.75MnF_2 + 2LiF + 2H_2 \tag{6.1.7}$$

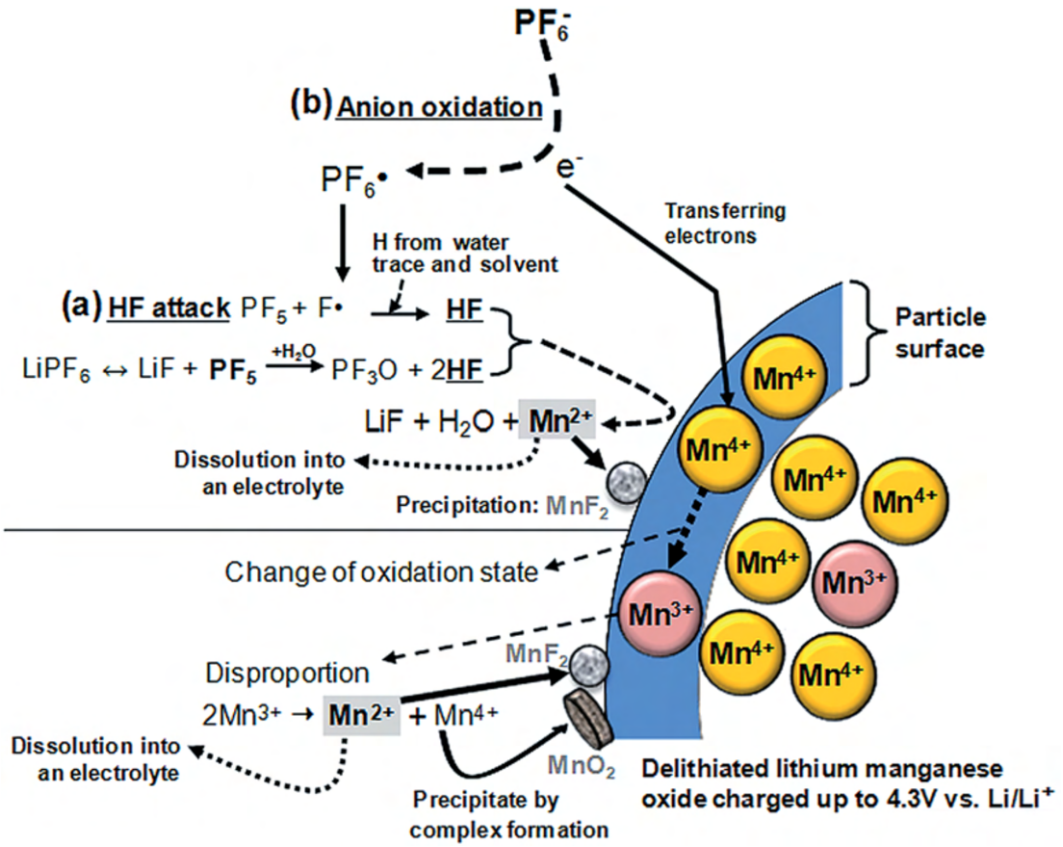

Fig. 6.6 Image showing the dissolution mechanism of Mn in a delithiated $LiMn_2O_4$ cathode via (a) attack by HF and (b) anion oxidation. Reproduced from [250]

Electrolyte instability and degradation: This issue, typical of high-voltage cathodes, is probably the most complex to address to allow its commercialization. It is closely correlated with the problems of surface and structural stability of cathode materials since the electrolyte constitutes the component of the cell in direct contact with the particles of active material, so it is essential to take into account the effects that the composition of the electrolyte could have both in terms of its stability in the working potential range of the cell, but also from the point of view of interfacial stability towards both the cathode and the anode.
Ideally, an electrolyte suitable for utilization with a high-voltage cathode like LNMO should possess the following characteristics:

- Elevated boiling point, high flash point, low melting point, and characteristics of low toxicity and flame retardancy: these attributes serve as prerequisites

for widespread practical applications in high-voltage cells featuring LNMO cathodes.

- High ionic conductivity (exceeding 10^{-4} S cm^{-1}) at room temperature to facilitate the lithium transfer: ionic conductivity stands out as the paramount parameter for electrolytes in LIBs.
- High dielectric constant and low viscosity: these features are crucial for dissolving more lithium salts and facilitating the easier transport of lithium ions.
- Inert chemical and thermal stability: these attributes confer electrolytes with reduced side and exothermic reactions, thereby enhancing overall safety for cells.
- Broad electrochemical stability window: electrolyte systems with high oxidation decomposition potentials (>5.2 V vs Li/Li^+) can be used in high-voltage LNMO-based LIBs without undergoing severe oxidative decomposition.

Nowadays the electrolytes currently used in commercial cells are essentially made up of a mix of organic solvents such as ethylene carbonate (EC) Dimethyl carbonate (DMC), a lithium salt such as Lithium hexafluorophosphate ($LiPF_6$), or Lithium bis(trifluoromethanesulfonyl)imide (LiTFSI) and various additives aimed at stabilizing the solid electrolyte interphase (SEI) on the negative electrode or cathode electrolyte interphase (CEI). However, this formulation is problematic when coupled to high-voltage cathodes due to its intrinsic instability at potentials of 5V. The oxidation processes occurring within a cell are complex, involving the participation of electrolyte salts, [251] [252] with solvents believed to be the primary component in commercial electrolytes responsible for catalytic decompositions on fully oxidized, delithiated cathode surfaces. Regarding the Solid Electrolyte Interphase (SEI) on the anode, both salts and solvents contribute to its formation. Recent investigations suggest that the EC solvent poses a dual impact in Li-ion batteries. On one hand, it demonstrates an excellent protective effect on graphite anodes, attributed to its proficient SEI-forming capability at the graphite/electrolyte interface. [253] On the other hand, being one of the carbonate solvents with the least resistance to oxidation, EC also has an adverse effect on the electrochemical properties of high-voltage cathodes. This is manifested through the formation of a less robust Cathode Electrolyte

Interface (CEI) layer.
Several carbonate degradation mechanisms have been proposed, such as nucleophilic attack, [254] electrophilic attack, [255] dehydrogenation reactions, and ring-opening reactions, [256] which lead to the cathode reconstruction and transition-metal dissolution at the high-voltage delithiated cathodes. In particular, the nucleophilic reactions between the oxygens on the surface of the delithiated cathodes and electrolytes lead to the decomposition of the electrolyte solvents and the formation of Li alkoxides and semicarbonates. In this sense, Martha et al. [257] have demonstrated that the nucleophilicity or basicity of the O atoms in the delithiated layered Li_xMO_2 is higher than that in the spinel $Li_xM_2O_4$ and olivine Li_xMPO_4 compounds, therefore, the Li_xMO_2 exhibits a more aggressive reactivity to the carbonate electrolytes than $Li_xM_2O_4$ and Li_xMPO_4 compounds. In the olivine compounds, the P atoms with the +5 valence could partially shield the nucleophilic nature of the O atoms. The dehydrogenation mechanism of organic solvents instead consists of the transfer of an electron from the solvent molecule towards the inert electrode with the consequent formation of a radical cation. In particular, recent computations showed that the EC-based electrolytes could be chemically dehydrogenated and oxidized on delithiated high-voltage cathode surface, especially with increasing Ni content. The increased reactivity of the cathode surface with a higher degree of delithiation promotes the accumulation of decomposition products such as the polymeric and salt-derived (PF_3O, $Li_xNiO_yF_z$, $Li_xPF_yO_z$) species in the CEI layer. [258] Regarding the ring-opening reaction mechanism, Musgrave et al. [259] revealed that the Lewis acid–base complexation between the EC molecule and either delithiated LCO or PF_5 weakens the C–O bonds of the EC ring and accordingly reduces the barrier of EC ring-opening reactions. This reaction catalyzed by the delithiated cathode surface and PF_5 Lewis acid leads to the formation of CEI layers composed of an organic and organofluorine film. This mechanism was applied to LCO and summarized by the following two equations,

$$Co^*(s) + EC + PF_6^- \rightarrow Co - OCOOCH_2CHF^- + PF_5 \tag{6.1.8}$$

$$2EC + PF_5 \rightarrow PF_5 - OCOOCH_2CH_2 - OC(OCCH_2)_2 \tag{6.1.9}$$

This mechanism was then taken up and investigated by Lutch and others [260] for the LNMO: they investigated the surface of the LNMO via FTIR and XPS and found that at potentials higher than 4.7V a poly(ethylenecarbonate) passivation film

was formed on the LNMO surface (process shown in Figure 6.7, indicating that the organic-based CEI cannot effectively block the continuously parasitic reactions between the delithiated cathode and the electrolytes at high voltages. The EC solvent is also susceptible to oxidative breakdown, leading to the formation of a radical cation (EC+), particularly at the high-voltage cathode, as is depicted in Figure 6.7 (b).

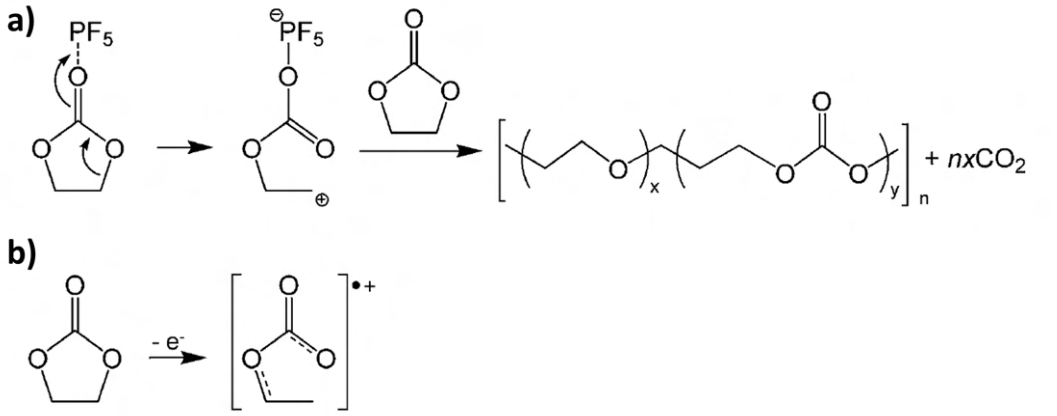

Fig. 6.7 Two possible mechanisms of EC decomposition: route (a) involves the PF_5 as a strong acid, leading to the formation of PEC, route (b) is the oxidative decomposition which is favored at high potentials.

It should be pointed out that these proposed EC degradation mechanisms are not isolated but intertwined to some extent, each of which highlights some aspects of decomposition reactions. Further strict experimental characterization and rigorous calculations are needed on the model cathodes to bridge the understanding of the formation of the CEI layers (Li_2CO_3, LiF, $Li_xPF_yO_z$, ROCOF, $ROCO_2Li$, RCOOR, polymeric species etc.) on the cathode surface and released gases (CO, CO_2 etc.), and evaluate the proposed reaction mechanisms. For example, He et al. [261] investigated the stability of typical alkyl-carbonate electrolytes during cycling of LNMO-based electrodes by performing in situ gas analysis. Their analyses were carried out using electrolytes based on the standard of 1 mol/L $LiPF_6$ in EC-DMC, but with various weight ratios of the EC-DMC co-solvents. In particular, they arrived at the following conclusions:

- H_2, CO, CO_2, and POF_3 are the predominantly formed volatile species during electrochemical cycling of LNMO in EC-DMC electrolytes (with $LiPF_6$ salt), with the detailed reaction routes reported by Moshkovich [262]

- Electrolyte Li salts participate directly or indirectly in the electrolyte decomposition processes. Electrolytes based on $LiClO_4$ salts display a higher extent of electrolyte decomposition (despite the absence of POF_3) compared with those based on $LiPF_6$.
- According to the equation reported below, the self-discharge of LNMO caused by the reactions between the fully delithiated LNMO and the electrolyte could explain the additional gas evolution around 5.0 V.

$$Ni_{0.5}Mn_{1.5}O_4 + xLi^+ + EC/DMC \rightarrow Li_xNi_{0.5}Mn_{1.5}O_4 + decomposition\,products + gas \quad (6.1.10)$$

- Elevated levels of DMC in the electrolytes under examination result in a notable increase in gas production. This phenomenon can be attributed to the facilitation of electrolyte decomposition by mass transport, a process that occurs due to the reduction in viscosity brought about by the presence of DMC.

Given these considerations, it is clear that current electrolytes consisting of carbonate solvents and lithium salts will need to be significantly improved or possibly even replaced to support the development of next-generation batteries. These batteries are characterized by their utilization of high-voltage cathodes (up to 5V) and anodes made of silicon or lithium metal. Specifically, the performance of Si microparticle (SiMP) anodes is notably limited in EC-based electrolytes. This limitation is due to the formation of an organic-inorganic SEI layer that cannot withstand the substantial volume changes occurring during lithiation and delithiation cycles, leading to its cracking. Similarly, metal anodes also exhibit rapid degradation and low cycling CE in EC-based electrolytes. To mitigate the distortion of the SEI layer, it is crucial that this layer exhibits minimal affinity towards the Si/Li anodes. This would allow the lithiated Si or the deposited Li to move at the interface during volume fluctuations without inflicting damage to the SEI layer.

Possible solutions for LNMO surface and structural instability: In an effort to enhance the structural and interfacial stability of LNMO, researchers have explored various strategies. One such strategy involves using nanostructured LNMO, like nanoparticles or nanofibers, which have been shown to provide shorter paths for Li^+ diffusion and exhibit improved electrochemical performance. [263] However, these nanostructures can increase the surface area, potentially leading to more unwanted

side reactions at the electrode-electrolyte interface. Consequently, the focus has shifted towards developing spinel materials in micrometer sizes. [264] In an integrated approach, Liu and colleagues combined LNMO microspheres with nanorods, which resulted in enhanced electrochemical performance. [265]

Additionally, optimizing the external surface orientation of LNMO has been identified as a possible approach to mitigate surface instability. The orientation significantly influences the dissolution of transition-metal ions, Li^+ transport kinetics, and electrode-electrolyte interface compatibility. For instance, Sun et al. [266] discovered that the (111) planes are superior due to higher Li^+ diffusion in this direction, and Hai et al. confirmed that Li^+ diffusion is considerably greater across the (111) faceted LNMO compared to (112) faceted plates. [267] Chemelewski et al. [268] found that the undesirable reactions at the electrode-electrolyte interface could be reduced at the (111) planes, especially at high voltages, attributing this to the planes low surface energy, dense ion arrangement, and reduced transition-metal dissolution.

Structural stabilization has also been achieved through doping LNMO with various elements, including Na^+, Mg^{2+}, Cu^{2+}, Zn^{2+}, Al^{3+}, Cr^{3+}, Co^{3+}, Fe^{3+}, and others. Transition metal elements with a +3 oxidation state in the 3d energy level can reduce Mn^{2+} dissolution from Mn^{3+} through the mitigation of Jahn–Teller distortion. [269] Doping with elements that have a stronger bond energy than Mn-O can help prevent structural collapse during cycling and suppress Jahn–Teller distortion, thereby improving cycling performance and reducing capacity fade. Additionally, Na and Mg substitution is reported to enhance the electronic conductivity of LNMO and decrease voltage polarization during cell operation. [270] However, it is important to note that single ion doping may not be sufficient to significantly improve the rate capacity or cycling stability of spinel LNMO, particularly at higher temperatures.

Research has extensively focused on the surface modification of LNMO to achieve three main objectives: stabilizing the LNMO/ electrolyte interface, minimizing side reactions between LNMO and the electrolyte, and curtailing the dissolution of transition metal ions. Surface engineering in this context is generally categorized into three types: chemically protective coatings, lithium-ion conductive coatings, and electrically conductive coatings.

For chemically protective coatings, metal oxide layers like TiO_2, SnO_2, and V_2O_5 have been found effective in shielding LNMO from HF attacks. However, metal fluoride coatings such as AlF_3 have shown even more promising results. The de-

velopment of lithium-ion conductive coatings is critical as high ionic conductivity at the electrode-electrolyte interface is vital for the optimal functioning of the cell. These materials typically include lithium-ion conductive ceramics such as Li_4SiO_4, Li_3PO_4, $Li_4P_2O_7$, and Li_2SiO_3. Besides providing excellent ionic conductivity, these coatings also need to offer substantial protection against electrolytes and prevent the dissolution of transition metals. Regarding electrically conductive coatings, this method aims to improve electrochemical reaction kinetics. This technique has been successfully applied to other cathode materials like phosphate materials, $LiCoO_2$, and $LiNiO_2$, yielding positive results. For instance, Yang et al. [271] have explored the impact of carbon coatings with varying contents on the physical and rate properties of LNMO.
It is important to note that these surface modification strategies for LNMO must be finely tuned. The coatings need to be effective ionic conductors without being overly thick, which could otherwise compromise the gravimetric capacity of the cathode. Additionally, achieving a high uniformity in the coating and considering cost-effectiveness are crucial factors. Therefore, combining element doping with surface coating might be a reasonable and effective approach to balance the enhancement of specific energy density and cycling stability.

Possible solutions for electrolyte degradation In this area, the research work carried out in recent years has been enormous and it would be impossible to enclose it in a section of this thesis, the aim of which is not to study this component of the cell, however, some of the approaches that have proven most interesting to be applied in high voltage cathodes are briefly discussed below.
Early investigations by scientists revealed the potential benefits of utilizing fluorinated solvents. The presence of C-F bonds in organic molecules significantly influences the HOMO and LUMO levels of these solvents, enhancing the interfacial chemistry for both Li-ion and Li-metal batteries. Notable examples include FEC and 3,3,3-trifluoropropylene carbonate (TFPC). [272] Compared to their non-fluorinated counterparts, fluorinated molecules exhibit several advantageous properties, such as markedly lower melting points, increased surface tension, and enhanced stability at elevated temperatures, making fluorinated electrolytes prime candidates for batteries operating across a broad range of temperatures and potential windows. Furthermore, the high capability of fluorinated electrolytes to form SEI layers renders them highly compatible with graphite and Li metal anodes. For instance, Dahn and [273] col-

leagues tested graphite NMC442 pouch cells at a high cut-off voltage of 4.5 V using a fluorinated electrolyte mixture (1 M LPF_6 FEC/TFEC + x% prop-1-ene-1,3-sultone (PES)). These cells, in comparison to those employing commercial carbonate or sulfolane-based electrolytes with added blends, demonstrated superior capacity retention, reduced polarization over extended cycling, and diminished voltage drops. This indicates that fluorinated electrolytes can create a more dense and compact SEI/CEI layer on the electrodes.

Another very interesting approach is to greatly increase the concentration of salt in the electrolyte (3M), in order to create a system called "solvent-in-salt". These high-concentrated electrolytes contain few free carbonates and as a consequence, the ion-transference mechanism of high-concentrated electrolytes is different from the one that occurs in free carbonate solvents. Specifically, with increasing concentration, there are fewer free solvent molecules and more ions in the electrolyte coordinating into multidimensional networks, in which ion transfer mainly depends on ion hopping along the network chains. [274] In addition, the solvent molecules coordinated with lithium ions exhibited improved oxidation-resistant properties owing to their lower HOMO energy levels than the free solvent molecules. These unique solution systems deliver superior electrochemical and thermal properties, and safety, such as high oxidative stability, superior antireductive abilities, Al anticorrosion, fast electrode reactions, high thermal stability, and low volatilities. [275, 276] However, solvent-in-salt electrolytes suffer poor wettability to the separators and the electrodes, increased viscosity, and decreased ion conductivity, all of which are adverse for the electrochemical devices. [277]

From a physicochemical perspective, ionic liquids (ILs) are essentially special salts that exist in a liquid state at ambient temperatures, attributed to the relatively weak electrostatic forces between their anions and cations. The primary benefits of using ILs in electrolytes include their potentially broader electrochemical windows, enhanced safety characteristics, high thermal resilience, and minimal volatility. [278] As a result, ILs dissolved in lithium-ion salts have been identified as a promising substitute for conventional carbonate-based electrolytes. Nonetheless, their path to industrial-scale adoption is hindered by several challenges, such as their high cost, significant viscosity, and low compatibility with electrodes. ILs featuring TFSI and FSI anions have garnered considerable attention in research due to the anions' electron-delocalizing structure within the sulfonyl imide groups. A notable strategy for augmenting the performance of these electrolytes involves blending different

ILs to harness synergistic effects. For instance, the work by Fox and colleagues [279] systematically explored the behavior of binary IL mixtures of $PY_{1x}TFSI$ (x = 1 through 5), revealing that for an IL-blended electrolyte to achieve high conductivity, the melting transition (T_m) between the two ILs should be minimal, their crystal structures distinct, and the cation sizes within each IL markedly different. Beyond these ILs, recent advancements have led to the development of novel ILs formulated with innovative cations and anions, like the FTFSI and FPSI anions, [280] aimed at further reducing viscosity, enhancing conductivity, and expanding the operational voltage range.

The most studied approach in recent years, however, has been the modification of the composition of carbonate solvent-based electrolytes with additives capable of improving their stability and electrochemical performance. Considering the ease of preparation and the low cost of additives, it is believed that in the near future, this type of solution will remain dominant. These electrolyte additives could be divided into several categories according to their functions, such as SEI/CEI forming improver, overcharge protectant, salt stabilizer and fire-retardant agent.

One of the most studied families of additives is that of unsaturated carbonate derivatives, which include vinylene carbonate (VC), vinyl ethylene carbonate (VEC), and vinylene trithiocarbonate (VTTC). In particular, VC undergoes polymerization at both the anode and cathode surfaces, creating protective poly(VC) layers. [281] Thus, VC can yield a positive effect on the electrochemical performance with a better CE, lower side reactions, and enhanced capacity retention. [282] Vinyl ethylene carbonate (VEC) was first proposed as a good film-forming additive for the graphite anodes, which could create a similar SEI as VC on the edges of the graphite. Moreover, VEC shows an evident oxidation potential at 4.4 V and generates an effective CEI film on the high-voltage cathodes, favoring the cells with a high working voltage of 4.5 V. [283] Fluorinated compounds constitute a distinct category of additives. While they have been acknowledged as potential alternatives to carbonate solvents, their substantial cost limits their use to concentrations below 10%, hence their classification as additives. These compounds are noted for their ability to form CEI/SEI layers consisting of fluorinated species/polymers. Such layers prevent potential side reactions between the core solvents of the electrolyte and the oxidized surface of the cathode. Notably, FEC and $LiPO_2F_2$ emerge as the most recognized among these fluorine-rich additives, having gained widespread adoption as commercial electrolyte additives. Their effectiveness extends across various anode materials including graphite, Li

metal, and Si-based alloys, as well as enhancing the performance of high-voltage cathodes through superior film formation capabilities. Unlike the sluggish CEI formation in EC-based electrolytes, FEC accelerates the creation of protective CEI films on high-voltage cathodes, resulting in a more effective protective layer compared to those derived from EC oxidation or those formed by VC or ES-derived CEI layers. Recent advancements have seen the exploration of novel fluorinated additives. For instance, Jimsol et al. [284] explored the stabilization effects of 5% wt methyl (2,2,2-trifluoroethyl) carbonate (FEMC) on NMC532 cathodes, while Kim et al. [285] introduced a dual-function additive, ethyl 4,4,4-trifluorobutyrate (ETFB), capable of passivating graphite anodes and simultaneously stabilizing Ni-rich NMC cathodes.

Boron-based additives represent another innovative class, attributed to the electron-deficient nature of boron, which enables complexation with anions to stabilize carbonate electrolytes. Initial studies on lithium tetrafluoroborate ($LiBF_4$), lithium bis(oxalate)borate (LiBOB), and lithium difluoro(oxalate)borate (LiDFOB) identified them as potential Li salts. Subsequent research indicated their preferential decomposition on delithiated cathodes, creating a borate-rich, durable interphase that boosts the electrochemical performance of high-voltage cathodes. Experiments with compounds like Trimethyl borate (TMB-1)[286] and Trimethylboroxine (TMB-2) [287] on various cathodes, including LNMO, showed that these are oxidized during the initial charging, forming a borate-based CEI layer that curbs electrolyte oxidation on the catalytic surface.

6.2 Lithium Iron Phosphate (LFP)

6.2.1 Structure and electrochemical performance of Lithium iron phosphate

Ever since Goodenough and his team first revealed the electrochemical potential of $LiFePO_4$ as a cathode material for Li-ion batteries in 1997, $LiFePO_4$ and its derivatives have garnered significant attention due to its abundance, eco-friendliness, and low cost. Also, $LiFePO_4$ is characterized by its high chemical and thermal stability, enhancing its safety and cyclability. Its charge-discharge profiles are notable

for a flat voltage plateau around 3.4 V versus Li/Li^+ , albeit with a modest theoretical capacity of about 170 mAh g^{-1}. Despite its low conductivity (around 10^{-9} S cm^{-1}), significant enhancements in electrochemical performance are achievable through various methods, including nanostructuring, carbon coating, and doping. Although its theoretical working potential and energy density (about 580 Wh/kg) are relatively modest compared to other cathode materials, its operational voltage range is beneficial in reducing cathode-electrolyte side reactions, particularly under the condition of high-rate charging. [288]

$LiFePO_4$ also presents intriguing aspects in terms of its electrochemical insertion mechanism, which operates through a biphasic mechanism that remains a topic of ongoing debate and research. Despite the biphasic mechanism between the end members $LiFePO_4$ and $FePO_4$ leading to a volume change of approximately 6.8% during the delithiation process, $LiFePO_4$ nanoparticles have the notable ability to be cycled at high current rates.

LFP is characterized by an olivine-type structure with orthorhombic symmetry, classified under the *Pnma* space group. It features a unique distorted hexagonal arrangement of anions. In this structure, Li and Fe occupy octahedral sites, while phosphorus atoms are placed in a tetrahedral configuration. As shown in Figure 6.8, the architecture of $LiFePO_4$ shows each FeO_6 octahedron linking to four others at the corners, forming a zigzag configuration along the (b, c) plane. The arrangement of these layers along the a-axis, by means of sharing an edge and two corners of PO_4 tetrahedra, results in the formation of a three-dimensional framework. This structure gives rise to one-dimensional channels that host the Li^+ ions. The original crystalline structure of LFP is largely maintained during delithiation, forming $FePO_4$, with a consequent volume reduction of approximately 6.8%, thus giving the material excellent stability and resistance to cycling.

The removal and insertion of Li^+ from and into the $LiFePO_4$ structure occurs via a dual-phase reaction:

$$LiFePO_4 \rightleftharpoons FePO_4 + Li^+ + e^- \tag{6.2.1}$$

Which results in a flat plateau of charge/discharge around 3.4 V versus Li/Li^+ /. Understanding and optimizing the performance of the cathode hinges significantly on the mechanism of lithium insertion and extraction, thus making the study of these processes in $LiFePO_4$ a subject of considerable interest. In particular, several models have been proposed that can describe how the intercalation and de-insertion phenomena of Li^+ ions proceed within the LFP particles. The first of these, pro-

posed by Goodenough et al, was called the "core-shell" model and envisaged that as de-lithiation proceeded, the $LiFePO_4$ was converted into $FePO_4$ forming a two-phase interface.

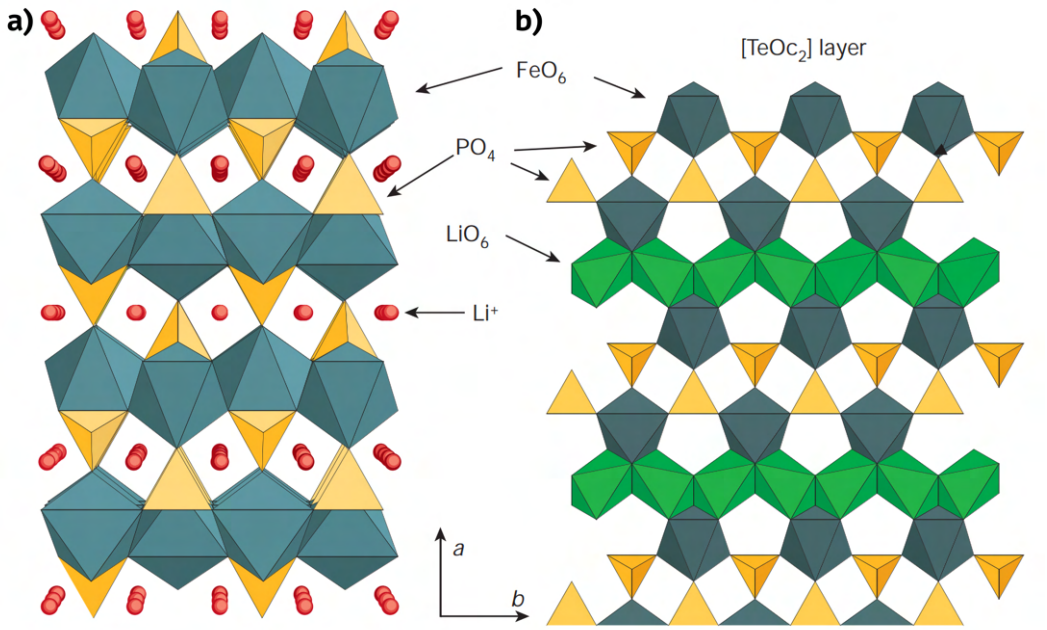

Fig. 6.8 (a) The olivine $LiFePO_4$ structure, viewed along [001], features FeO_6 and PO_4 tetrahedra building a framework with red Li ions, interconnected via corner-sharing in the (b, c) plane. (b) A different view of LFP structure shows Li, Fe, and P arranged among hexagonal close-packed oxygen-dense layers, with LiO_6 octahedra edge-sharing, allowing Li ion diffusion along [010] and [001]. Reproduced from [289]

Subsequently, the team led by Srinivasan introduced a "shrinking core" model to explain the lithiation process in $FePO_4$. According to this model, which is schematically shown in Figure 6.9, a single-phase region is created at the boundaries of the two-phase coexistence area. In this region, lithiation begins at the surface of the particle and pushes the two-phase boundary inward. During the charging phase, a $FePO_4$ shell is created, and the boundary between $FePO_4$ and $LiFePO_4$ moves further into the particle. The inefficient removal of lithium from $LiFePO_4$ located at the center of larger particles often results in a decrease in capacity. Moreover, this shrinking-core model effectively describes the behavior observed in the electrochemical charging and discharging cycles at different C-rates. However, this model is based on the hypothesis that the de-intercalation of Li^+ ions occurs isotropically

in the crystalline structure of the material, while several studies [290, 291] have demonstrated that lithium diffusivity in this material is very anisotropic. In particular, Ceder and colleagues [292] highlighted a significant disparity in ionic conductivity, noting it is substantially higher in the *b*-direction tunnels while being markedly lower in the other olivine structure directions. Consequently, the core-shell model may have been acceptable for describing how de-lithiation proceeds at the level of agglomerated particles, but not within the primary particles themselves. A model that could better explain this phenomenon was therefore provided by Laffont et al. [293], who applied high-resolution electron energy loss spectroscopy (HREELS) to study the mechanism of (de)intercalation in the LFP. Unlike the earlier shrinking core model, the findings indicate that the interface consists of both $FePO_4$ and $LiFePO_4$ without detecting any Li_xFePO_4 solid solution phase where x varies from 0 to 1. According to this new core model, Li^+ diffusion in the [010] direction is highly preferential, and the Li_xFePO4 particles always maintain the structure with the shell of $FePO_4$ and core of $LiFePO_4$. This model, called the "new core-shell model" was also supported by the results of Prosini [294] and Zhang. [295]

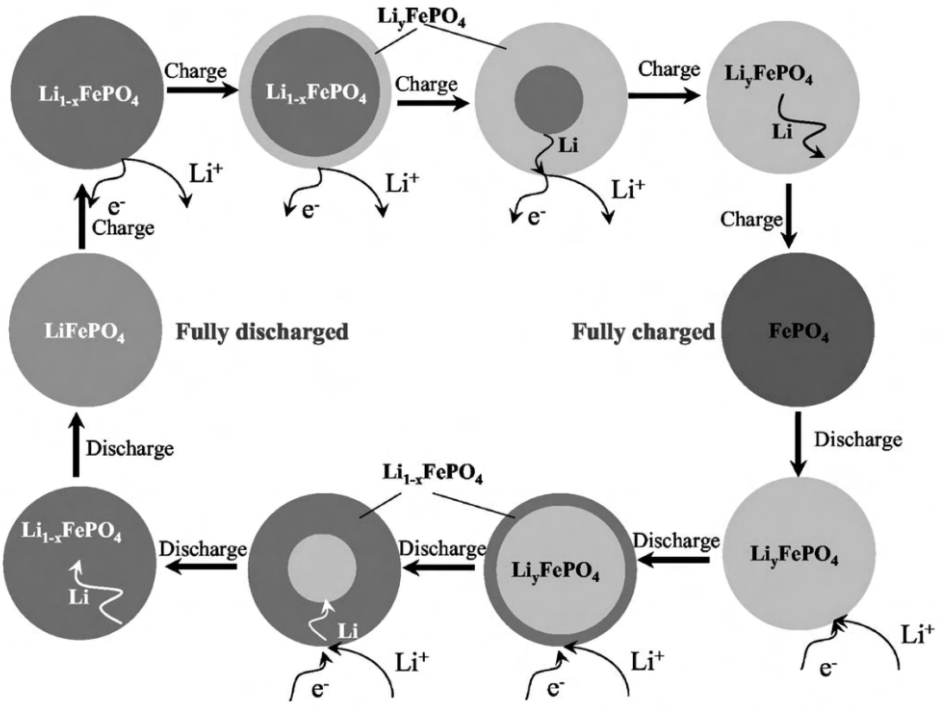

Fig. 6.9 Schematic representation of the shrinking-core model used to explain the de-lithiation and lithiation of LFP. Reproduced from [296]

The approach suggested by Laffont was later implemented by Delmas and colleagues [297]. In particular, by utilizing data from X-ray diffraction (XRD) and high-resolution transmission electron microscopy, they formulated a "domino-cascade" model to elucidate the phase transition process in $LiFePO_4$ nanoparticles. This model revealed that the expansion of the $FePO_4$ phase, at the cost of the $LiFePO_4$ phase, occurs significantly quicker than the formation of a new domain (based on the principle that the growth of a phase requires less energy than the nucleation of a new one). According to the "domino-cascade" model, lithiation/delithiation occurred completely and rapidly in some $LiFePO_4$ nanoparticles during the charge/discharge cycles.

The model is easier to understand with the help of Figure 6.10. In particular, the deintercalation process in the LFP occurs with a consequent constraint for the material's structure in the vicinity of the $LiFePO_4/FePO_4$ interface, as shown in Figure 6.10 (a). More specifically, when a boundary plane is generated, it propagates in the *a* direction across the crystal as lithium de-intercalates. The movement can be viewed as a wave propagating across the crystal with no energy barrier, allowing lithium intercalation/deintercalation to occur extremely fast. Figure 6.10 (b) illustrates the forward movement of the interface where intercalation/deintercalation and subsequent structural distortion takes place within a single crystallite. In contrast, the far right part of the figure showcases how the interface progresses within a particle, leading to a shell of $LiFePO_4$ and a core of $FePO_4$.

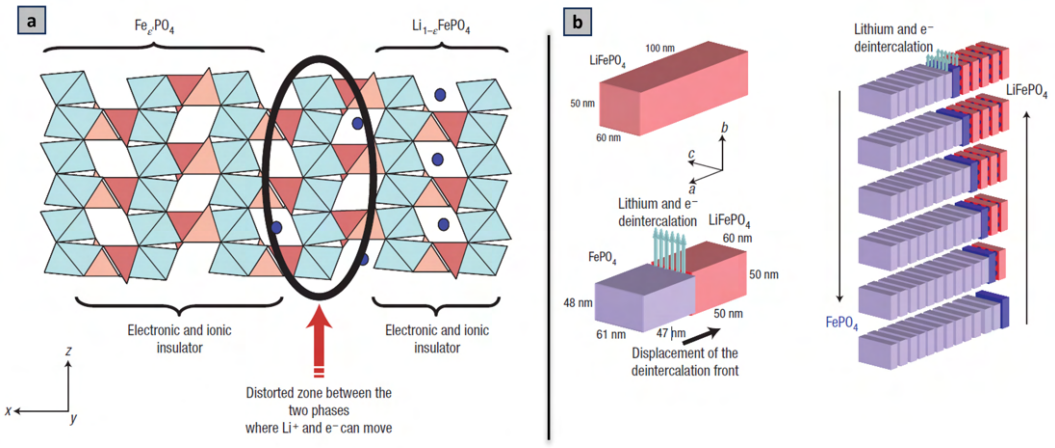

Fig. 6.10 (a) The oval region represents the distoted zone in the ac plane between the lithiated and de-lithiated phase in the LFP material during the Li^+ de-intercalation/intercalation process. (b) Illustration of the "domino-cascade" mechanism for used to describe the de-intercalation/intercalation in LFP. Reproduced from [297]

At this point in the discussion, it is worth underlining that the size of the LFP particles plays an important role in the LFP reaction mechanism; in fact, Kobayashi et al. [298] demonstrated that LFP nanoparticles exhibit a narrower miscibility gap compared to larger particles. This thesis was also supported by Gibot et al.[299], who, conducting in situ XRD, observed that particles of about 40 nm of LFP exhibited a continuous shift of the diffraction peaks, a typical characteristic of materials that undergo a single-phase reaction.

Consequently, the hypothesis took hold that (de)intercalation in the LFP could occur without the formation of an intermediate phase. In this sense, Bazant's group [300] proposed in 2011 a new electrochemical-phase field model, which envisaged a variable mechanism depending on the applied current: at low currents the phase separation occurs either via nucleation or spinodal decomposition, while above a critical current threshold, I_c, phase separation reaches its kinetic limit, leading to its suppression, and the system then operates similarly to a quasi-solid solution. Hence, this model could account for the LFP impressive electrochemical performance at high currents, since the absence of a phase transition involving structural rearrangements and significant volume variations (6.8% between $LiFePO_4$ and $FePO_4$) is generally recognized as a key factor in this sense.

The findings of Bazant's group were further validated by studies carried out by Grey et al. [301], who used the time-resolved in situ x-ray powder diffraction technique

to study the mechanism of (de)intercalation on LFP nanoparticles at high C-rates (up to at 20C). In particular, their results strengthened the thesis that the application of high currents favors, in the LFP, the formation of a metastable solid solution, which bypasses the classical nucleation process (see Figure 6.11) and allows a faster (de)intercalation of the Li ions.

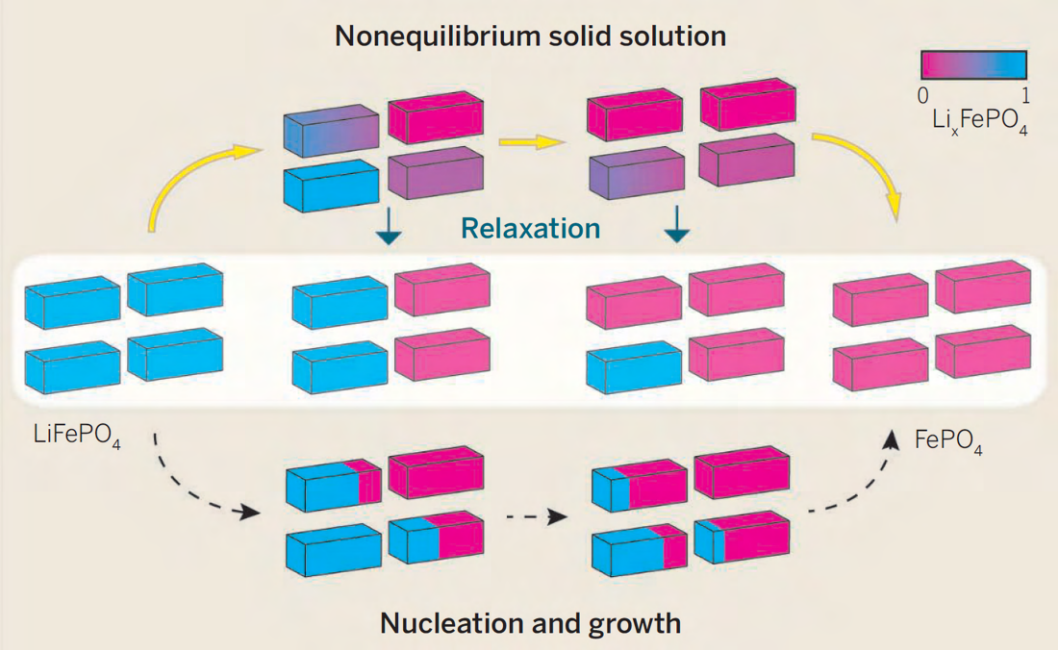

Fig. 6.11 In the upper part of the figure is reported the delithiation mechanism in LFP material proposed by Grey et al., which occurs with the formation of a metastable solid solution phase Li_xFePO_4, represented by intermediate purple color, in contrast with the classical proposed route (lower part of the figure), which instead is based on the nucleation and propagation of a new phase. During a relaxation step, the LFP particles turn back to their equilibrium condition of single phase $LiFePO_4$ or $FePO_4$. Reproduced from [301]

6.2.2 Challenges and solutions of lithium iron phosphate

Despite the many positive aspects of the LFP, it still obviously shows some drawbacks. For example, the limited volumetric energy density of the LFP derives from its low tap density, in fact, this property of the material does not only depend on its intrinsic density but is also affected by the particle size and morphology [302]. In this sense, it is challenging to find a compromise since it is well known that for the LFP the rate capability improves as the particle size decreases [303], while the tap density decreases. Another problem of the LFP is its intrinsic poor electronic

conductivity, which must necessarily be improved in order for it to perform well at high currents. In this sense, numerous studies and approaches have been investigated in recent years. In particular, one of the methods that has proven to be most effective is the application of carbon coating on the surface of the LFP particles, which is generally carried out by means of solid-state reactions at high temperatures starting from carbonaceous organic compounds precursors. [304] The resulting carbon layer, if well optimized, can significantly improve the cycling stability of the LFP and its conductivity, as well as being eco-friendly and inexpensive. An in-depth review on this topic was written by Sun et al . [305]
Another approach that has been attempted to improve the properties of LFP is to dope the material with other metal cations (for example Zr^{4+}, Mg^{2+}, Al^{3+}), however, this route has proven not to be particularly satisfactory, since the divalent and trivalent cations can replace Li^{+} ions in the structure, thus reducing diffusion pathways. In the case of Zr^{4+}, Nazar's group [306] found that the improvements in electronic conducibility were due to the presence of impurities such as Fe_2P or iron phosphocarbide.

6.3 Blending of LNMO and LFP and physical-chemical characterization

HYDRA project: As previously mentioned, this work was carried out within the framework of the European project HYDRA, funded by the European Union's Horizon 2020 innovation program under grant agreement number: 875527. This project involved many different partners across Europe such as the French Alternative Energies and Atomic Energy Commission (CEA), Johnson Matthey, ICSI, German Aerospace Center (DLR), Solvionic, SINTEF, Vianode, UCl Louvain, and Uppsala University and of cours, Politecnico di Torino (see Figure 6.12).

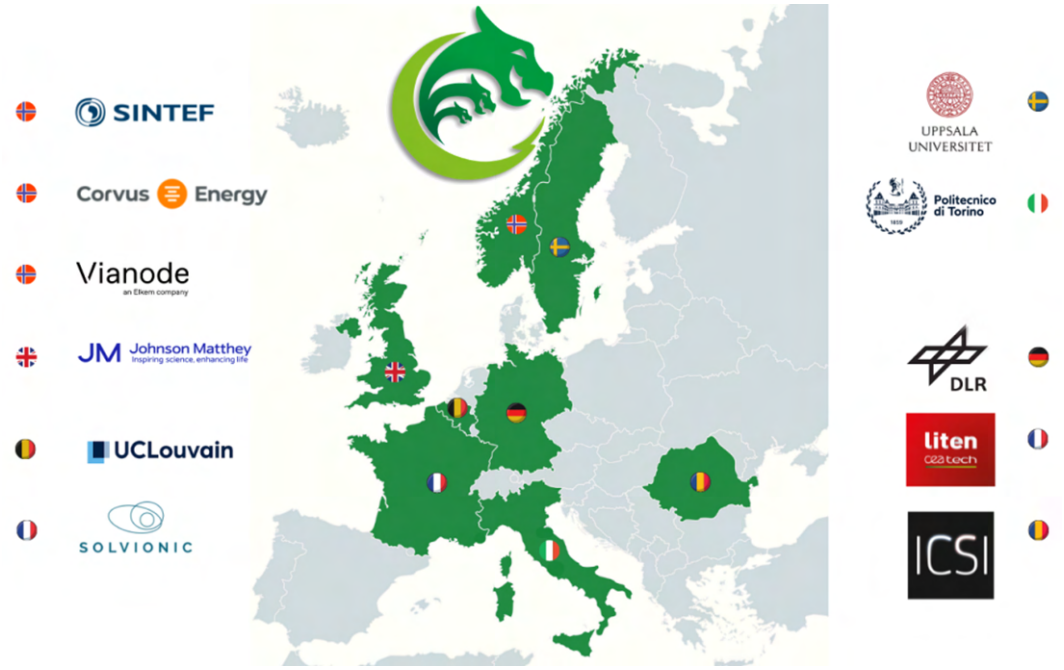

Fig. 6.12 Map of the european partners involved in the HYDRA project.

The goal of the project was to investigate the possibility of implementing state-of-the-art technology in the three main components of a Li-ion cell to develop and demonstrate, in a sustainable way, hybrid electrode-based batteries combining high power with high energy density. Specifically, from the perspective of the materials used at the cathode, the idea was to use a blend of LNMO and LFP, due to the characteristics already mentioned in the previous paragraphs (essentially, the high voltage of LNMO and the high power of LFP). Within the project, the pristine LNMO and LFP materials were supplied by Johnson Matthey. From the anode perspective, the focus was on developing a silicon-graphite blend, with partner Vianode being more involved in this aspect. The electrolyte was studied extensively by Uppsala University in collaboration with Solvionic, and in this regard, significant work was done in terms of additives (FEC, VC), salts (LiBOB), and ionic liquids.
The role of Politecnico di Torino, and therefore my PhD work, were mainly centered in the production of blended LNMO/LFP cathodes and their electrochemical characterization. In particular, the approach followed in this work was focused on using an innovative, effective, and scalable method such as Resonant Acoustic Mixing (RAM) to study the properties and possible synergistic effects between LNMO and LFP in

the cathodic composition, noth in half-cell and full-cell configuration.

Resonant Acoustic Mixing: The two cathode materials were mixed using a LabRAM I ResonantAcoustic® Mixer from Resodyn Acoustic Mixers. The instrument is able to automatically tune its resonant frequency between 60 and 61 Hz; the mixing was carried out for 5 minutes at an acceleration of 100 g. The RAM technique is a very efficient technology to blend powders and slurries, thanks to the fact that it can produce significant mixing energies by always functioning at the system's resonant frequency. Typically, machines of this kind have their own resonant frequency that oscillates between 58 and 62 Hz, which is constantly monitored and adjusted during operation. In this way, the RAM mixer is able to continuously and homogeneously apply forcing energy (up to 100g) to the processed powders/slurries and optimize the power consumption. The mixing process using RAM was carried out by one the partner (ICSI Energy Department) of the HYDRA project; the powders were then sent to the laboratories of the Polytechnic di Torino where they were physicochemically and electrochemically characterized.
In this study two different compositions of LFP and LNMO were investigated, one containing $2\%_{wt}$ of LFP (denoted as LNMO+2%LFP) and one $10\%_{wt}$ of LFP (denoted as LNMO+10%LFP). These percentages were selected to ensure good dispersion of LFP, as its primary nanometric particles tend to form micrometric aggregates (the aggregation increases with increasing LFP content), and to allow the LFP to serve as a lithium donor in the cathode, a role that will be explained in subsequent sections.
Physical-chemical characterization of blended LNMO/LFP: The Brunauer-Emmett-Teller (BET) specific surface area (SSA), the X-ray diffraction (XRD), and Field Emission Scanning Electron Microscopy (FE-SEM) analysis were carried out using the same equipment reported in the previous sections.
Figure 6.13 shows the FE-SEM micrographs of the pristine LNMO at different magnifications. In particular, most of the particles appear as regular octahedrons with dimensions laying between 1 and 100 μm.

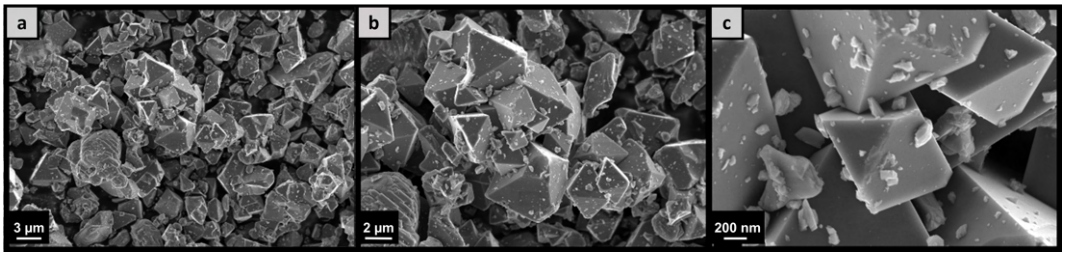

Fig. 6.13 FE-SEM micrograph of the pristine LNMO at (a) 2.5 kX, (b) 5kX, (c) 25 kX.

The results of the FE-SEM for the LNMO+2% LFP sample are presented in Figure 6.14, clearly showing the presence and homogeneous distribution of LFP nanoparticles, which are indicated with orange arrows. These nanoparticles exhibit morphology and dimensions that are markedly different from those of the LNMO.

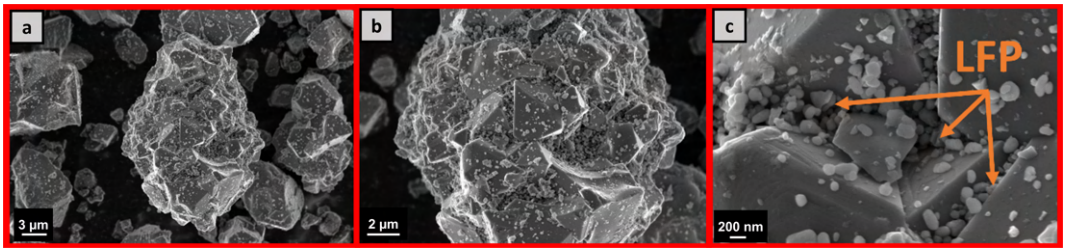

Fig. 6.14 FE-SEM micrograph of the blended LNMO+2%LFP at (a) 2.5 kX, (b) 5kX, (c) 25 kX.

Finally, Figure 6.15 reports the micrographs of the LNMO+10%LFP sample. It can be seen that in the case of blended samples, the LFP particles are dispersed in such a way as to partially cover the surface of the LNMO and the voids between the octahedral particles.

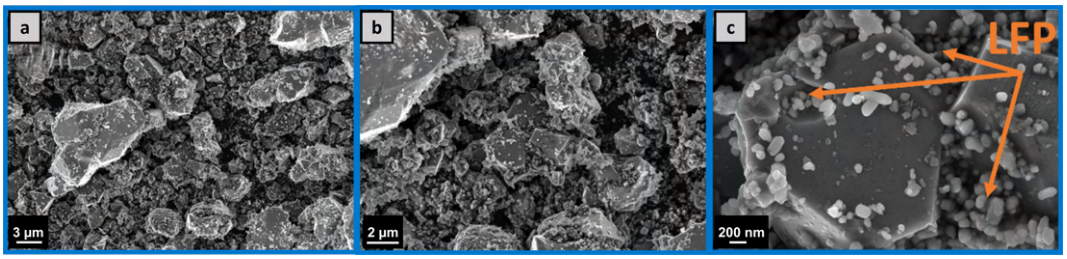

Fig. 6.15 FE-SEM micrograph of the blended LNMO+10%LFP at (a) 2.5 kX, (b) 5kX, (c) 25 kX.

The EDX analysis was carried out on the two blended samples to better investigate the effective dispersion of the LFP on the surface and between the LNMO particles after the RAM treatment. This analysis was conducted by the partner Johnson Matthey in their laboratories. As can be seen in Figure 6.16, despite the presence of some particle clusters, the LNMO+2%LFP sample presents a more homogeneous distribution of LFPs (which is identified by the purple color of the P element in the figure) compared to the LNMO+10 %LFP, which instead clearly shows less mixing between the two materials. It is important to underline that good dispersion of the LFP can result in a microstructural configuration of the electrode that improves the electronic and ionic transport between the two materials, with possible synergistic effects and improvements in electrochemical performance. [307]

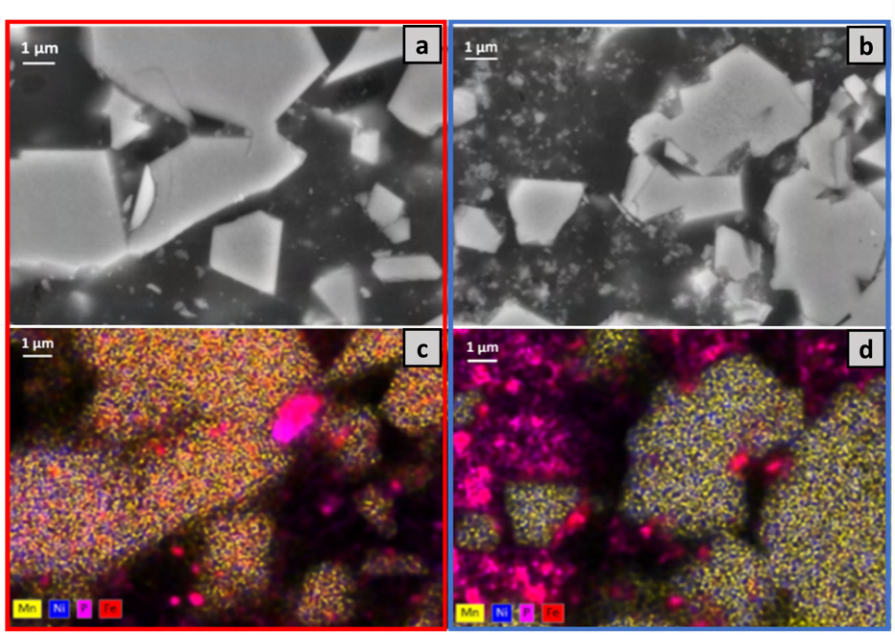

Fig. 6.16 Panels (a) and (c) report the EDX analysis on the LNMO+10%LFP sample, while in (b) and (d) the EDX analysis on the LNMO+2%LFP sample is shown. This analysis was conducted by the partner Johnson Matthey.

The XRD analysis of the blended electrodes shows that their crystalline structures match the expected patterns of each component, as illustrated in Figure 6.17 (a). In particular, for the LNMO+2%LFP sample, the peaks relating to the LFP are difficult to identify due to the low added percentage, while in the LNMO+10%LFP sample, it is possible to observe the diffraction peaks typical of the olivine structure of the LFP (see Figure 6.17 b). It is worth highlighting that the XRD analysis of the blends does

not show the presence of any new phases or impurities, indicating that the individual components maintain strong stability with each other, without any apparent chemical interactions or degradation of the samples taking place throughout the blending process.

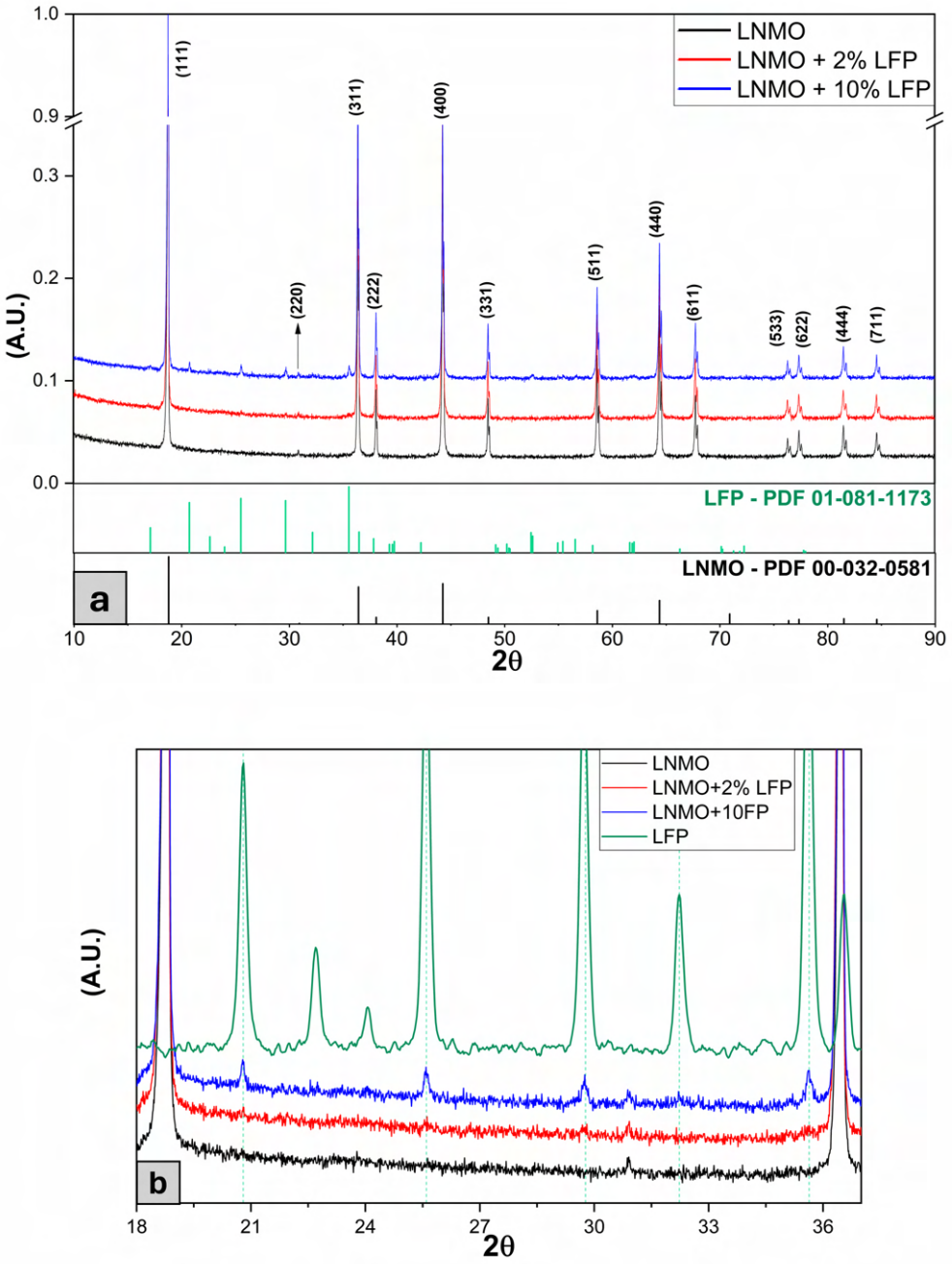

Fig. 6.17 (a) XRD spectra comparison of the pristine LNMO, the LNMO+2%LFP and LNMO+10%LFP samples (b) magnification of the range between 18 and 26.5 2θ, where the most intense peaks of the LFP fall. The spectrum of the pristine LFP has been added to facilitate the identification of its peaks.

In order to further investigate how the addition of different percentages of LFP modified the chemical-physical properties of pristine LNMO, the specific surface area of various samples was assessed using N_2 adsorption/desorption isotherms. As depicted in Figure 6.18, LFP shows a notably higher surface area (15.9 m^2g^{-1}), mainly due to its smaller particle size. On the other hand, pure LNMO has a much smaller surface area, around 1.0 m^2g^{-1}. For the mixed cathodes, adding LFP increases the surface area to 1.3 m^2g^{-1} for 2%LFP and to 3.7 m^2g^{-1} for 10%LFP. This is equivalent to a 30% enhancement in specific surface area for 2%LFP and an impressive 370% boost for 10%LFP in comparison to pure LNMO. These findings on surface area align well with what is observed in FE-SEM images, suggesting an LFP particle distribution within the electrode that could alter the contact surface between active materials and the electrolyte.

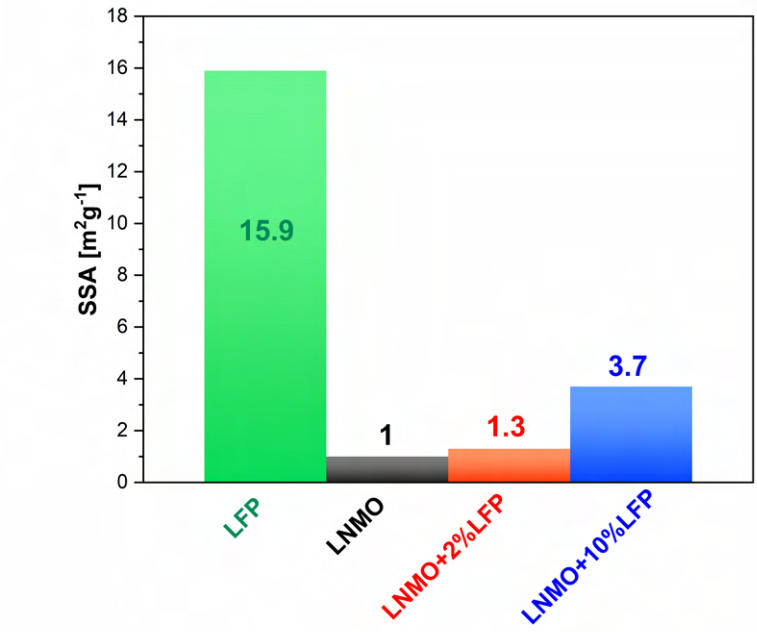

Fig. 6.18 The figure summarizes the specific surface area calculated by nitrogen adsorption/desorption isotherms of the pristine LNMO, LFP, and the two blended samples.

6.3.1 Electrochemical results

The elecrochemical methods used to characteriza the LNMO and the blended cathodes are reported in Appendix B.3.

In order to be able to evaluate the effect of the addition of LFP on the performance and electrochemical behavior compared to the pristine LNMO, the areal mass loading of the produced electrodes was standardized as much as possible and was kept in the range of 10.5-11.5 mg cm^{-2} of active material. In fact, this parameter is of non-negligible importance in evaluating the performance and electrochemical responses of a cathode. [308]
Another aspect that should be highlighted about the preparation of these electrodes is that they did not undergo any pressing or calendering treatments in order to maintain the electrode's natural porosity. This feature is designed to reduce potential issues related to the infiltration of the electrolyte into the pores, thereby enhancing the movement of lithium ions.
The electrochemical characterization of both pure and mixed electrodes was initially carried out through cyclic voltammetry (CV) tests using a three-electrodes cell setup. According to Figure 6.19, all samples showed clear peaks within the explored voltage spectrum between 3.0 and 4.9 V (against Li/Li^+). In particular, every sample exhibited a smaller peak at 4.1 V, which is linked to the manganese oxidation process (from Mn^{3+} to Mn^{4+}). Moreover, within the voltage range of 4.65 to 4.75 V, the voltammograms exhibit a doublet of peaks that is ascribed to the successive oxidation stages of nickel (from Ni^{2+} to Ni^{3+} and Ni^{3+} to Ni^{4+}, respectively). In the case of the blended cathodes, an extra redox peak was visible, corresponding to the iron oxidation (from Fe^{2+} to Fe^{3+}), showcasing that the electrochemical reaction of LFP within the mixed electrodes is consistent and reversible in both cases. Notably, the area related to the LFP reversible redox activity was fivefold larger in the electrode blend containing 10 wt.% LFP compared to the one with only 2 wt.% LFP, highlighting a direct relationship between the LFP capacity and the quantity of its mass incorporated through the physical blending process in the electrode composition.

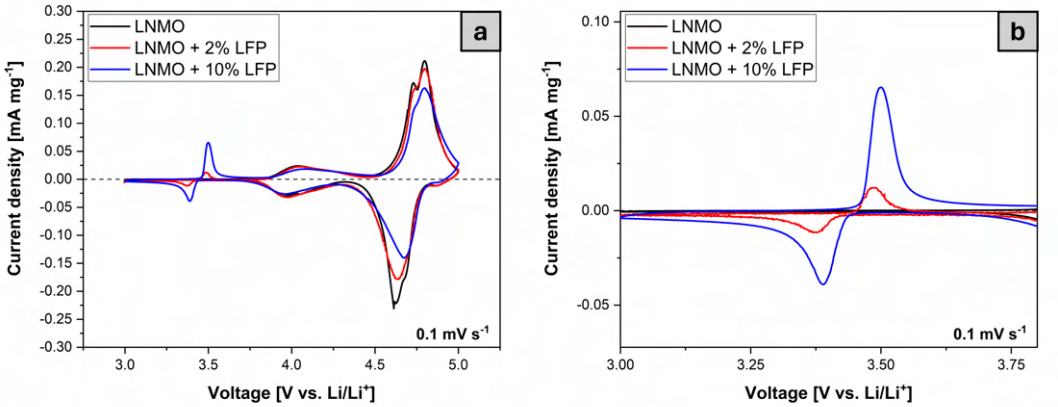

Fig. 6.19 Image (a) shows the voltammograms at the fifth cycle of the LNMO, LNMO+2%LFP and LNMO+10%LFP samples carried out at 0.1 mV s^{-1}, while in (b), the enlargement allows to better observe the current peak attributed to the LFP in the two blended samples.

Figure 6.20 (a), (b) and (c) show all five cycles performed at the scan rate of 0.1 mV s^{-1} for the three samples. A characteristic that seems to be common for all samples is the presence of a marked polarization between the cathodic and anodic branches during the first cycle, with a relative stabilization in subsequent cycles. In particular, the pristine LNMO sample appears to be the least capable of stabilizing the potential at which the oxidation and reduction peaks occur during the potential scan, while the LNMO+2%LFP sample exhibits perfectly overlapping voltammograms starting from the second one, lastly the LNMO+10%LFP sample presents an intermediate behavior, with a percentage of peak overlap higher than the LNMO, but lower than the LNMO+2%LFP. Overall, it can be concluded that the mixed cathodes exhibit remarkable stability within the examined potential window, showing no negative interactions between the materials or evidence of unexpected chemical reactions.

Cyclic voltammetry was performed also at various scan rates (0.1, 0.2, 0.3, 0.4 and 0.5 mV s^{-1}) in the same voltage window (3 - 4.9 V) using a three-electrodess setup to assess the kinetics of Li^+ insertion/extraction and calculate the apparent diffusion coefficient employing the Randles-Ševčík equation (Eq. 4.2.1, as previously discussed). The results are reported in Figure 6.20 (d), (e) and (f) for the pristine LNMO, the LNMO+2%LFP and LNMO+10%LFP.

As can be seen in the 6.20, as the scan rate increases the voltammograms exhibit less

defined and more prominent oxidation and reduction peaks due to a slower charge transfer in the material. By analyzing the disparity in the oxidation and reduction peak values, two pairs of peaks were identified for the calculation of the apparent Li^+ diffusion coefficient (D_{Li}): O1/R1 (attributed to the $Mn^{3+/4+}$ transition) and O2/R2 (attributed to the $Ni^{3+/4+}$ transition), as reported in 6.21 (a) and (b), respectively. The linear relationship between the peak current (I_p) and the square root of the scan rate ($\nu^{1/2}$), depicted in Figure 6.21, allowed for the determination of D_{Li} from the slope of the linear fit, with results summarized in Table 6.1. The table reveals a significant variation in D_{Li} across the O1/R1 and O2/R2 reactions, albeit the average diffusion coefficient is consistent with values found in the existing literature. [309, 310]
All three samples under investigation show diffusion coefficients that are closely matched across each distinct reaction observed. Nonetheless, it is significant to mention that the composite cathodes reveal a marginally increased lithium diffusion coefficient D_{Li} for both the O1 $Mn^{3+/4+}$and the R2 $Ni^{3+/4+}$ reactions. This implies that the inclusion of LFP in the cathodes might boost the kinetics of specific reactions, which occur at different states of charge/discharge of the cathode.

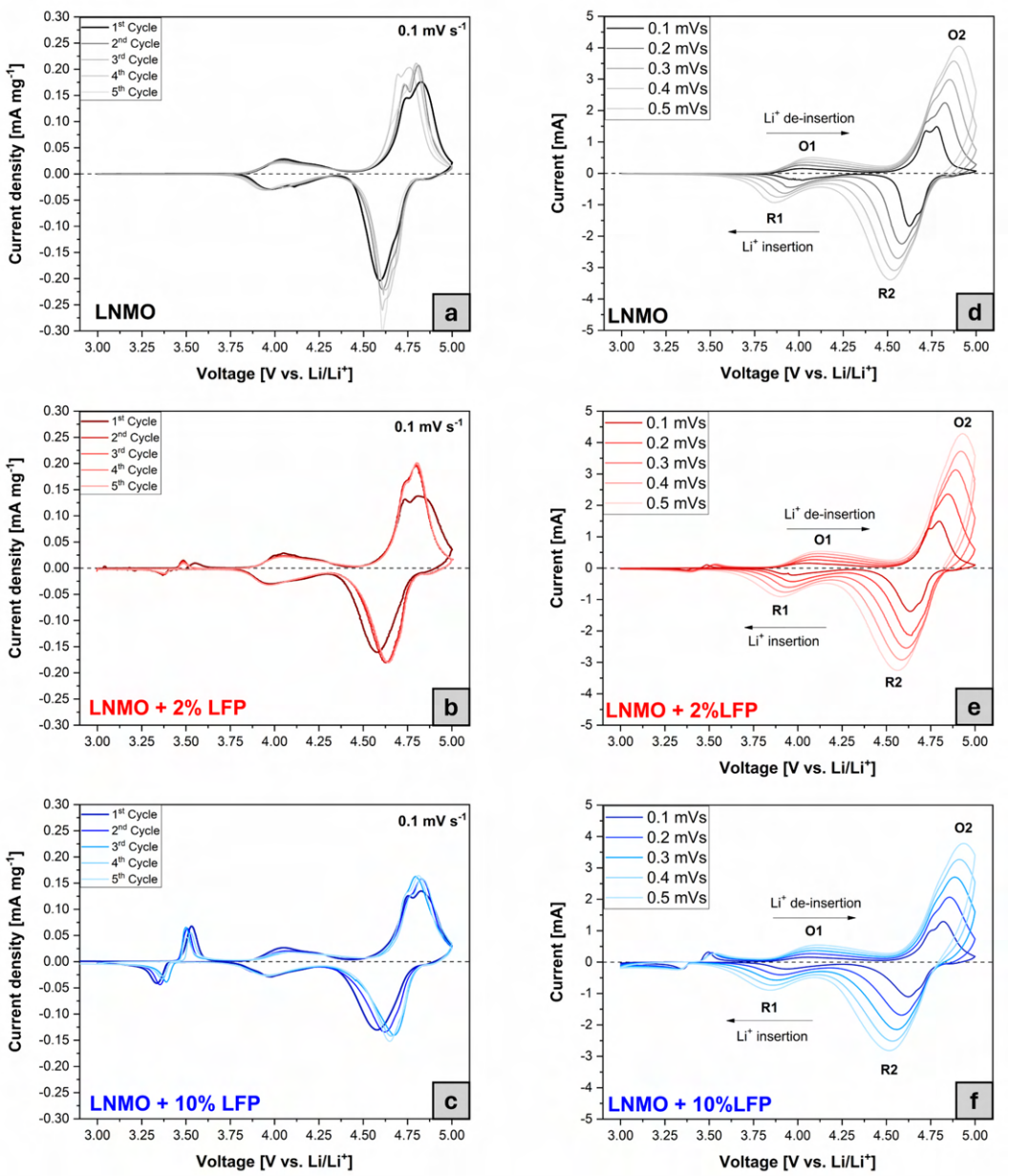

Fig. 6.20 Cyclic voltammetry profiles (scan rate 0.1 mV s^{-1} in the voltage range of 3–4.9 V) for pure LNMO (a), LNMO +2%LFP (b), LNMO +10%LFP (c). In panels (d), (e) and (f) are reported the cyclic voltammetry profiles at different scan rates (0.1, 0.2, 0.3, 0.4 and 0.5 mV s^{-1}): pure LNMO (a), LNMO +2%LFP (b), LNMO + 10%LFP (c).

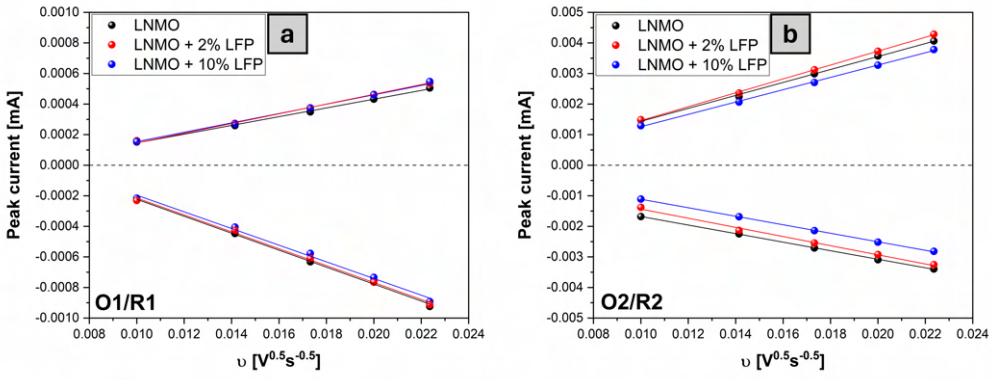

Fig. 6.21 (a) Linear plot of the peak current vs square root of the scan rate for the O1/R1 peaks, (b) Linear plot of the peak current vs square root of the scan rate for the O2/R2 peaks. The slope was used to determine the D_{Li} using the Randles-Ševčík equation.

Table 6.1 Values of the apparent lithium diffusion coefficients calculated from CV measurements for different O/R reaction peaks.

Sample	**Apparent diffusion coefficient D_{Li} [cm^2 s^{-1}]**			
	O1	**O2**	**R1**	**R2**
LNMO	$4.48{\cdot}10^{-12}$	$2.43{\cdot}10^{-9}$	$2.02{\cdot}10^{-11}$	$5.49{\cdot}10^{-10}$
LNMO+2%LFP	$5.19{\cdot}10^{-12}$	$2.29{\cdot}10^{-9}$	$1.76{\cdot}10^{-11}$	$7.00{\cdot}10^{-10}$
LNMO+10%LFP	$4.73{\cdot}10^{-12}$	$1.94{\cdot}10^{-9}$	$1.75{\cdot}10^{-11}$	$8.68{\cdot}10^{-10}$

To assess the impact of LFP incorporation on the cathodic reaction kinetics, cycling protocols focusing on the rate capability and capacity retention were conducted using half-cells (coin-cell 2032 configuration) with lithium metal serving as the counter electrode. These evaluations were carried out within a voltage window of 3.0 - 4.9 V vs. Li/Li$^+$ at room temperature, with the specific capacities of all tested electrodes normalized against the combined mass of the active materials (LNMO+LFP). The study initially sought to understand how LFP inclusion affects the performance of the cells concerning their rate capability. The reasoning behind this investigation arises from the hypothesis, which was supported by the FE-SEM analysis, that blending two materials of differing particle sizes and morphology might improve the interface contacts among the constituents of the cell, such as the current collector, carbon black, and notably, the cathode materials themselves.

For these rate capability experiments, the cells underwent charging and discharging

at a constant rate of ∼C/10 during the first three formation cycles, followed by a sequence of cycles at varying C-rates (from C/10 up to 5C) for discharging, while maintaining a constant 1C rate for charging. The discharge profiles at the different current regimes of the three samples taken into consideration are shown in Figure 6.22(a), (b) and (c) for LNMO, LNMO +2%LFP and LNMO +10%LFP, respectively. It can be seen that for the blended samples (very small in the case of LNMO +2%LFP, more accentuated in the case of LNMO +10%LFP) there is an additional discharge plateau at around 3.3V, corresponding to the electrochemical activity of the LFP. This result is in agreement with cyclic voltammetry previously shown. The discharge capacity at different C-rates of each sample was assessed through a rate capability test (see Figure 6.23) and the results are summarized in Table 6.2. As can be seen, the performances of the three different cathodes are very similar at low C-rates, while as the current increases it seems that the pristine LNMO is able to maintain a slightly higher discharge capacity compared to blended cathodes.

However, further considerations can be made on the results of the rate-capability tests; for instance, Liebmann et al. [311] highlighted an important observation regarding the effective C-rate experienced by materials in blended cathode formulations. Specifically, the effective C-rate on a given material escalates markedly as its proportion within the cathode blend diminishes. This implies that with the low percentages of LFP used in this study, the current intensity impacting the LFP is substantially high. For example, in the hypothesis of applying a positive charging current of 0.1C calculated on the total capacity of the cathode (thus based on the weight fraction of LNMO and LFP and their specific capacity), this current would initially affect only the LFP particles within the cathode. It would then impact the LNMO at a later stage, owing to the distinct potential windows in which these materials operate. As a result, this hypothetical current of 0.1C would effectively become an actual current of around 4C for the $2\%_{wt}$LFP and 0.8C for the $10\%_{wt}$LFP. Additionally, the rate capability is further affected by several other variables such as the electrode homogeneity, porosity, as well as the quantity and dispersion of carbon black and binder [311]. This suggests that not all LFP is actively involved in the lithiation and de-lithiation processes, thereby not fully contributing to the reversible capacity, especially at higher C-rates (like 2C and 5C) where the LFP capacity contribution is barely noticeable.

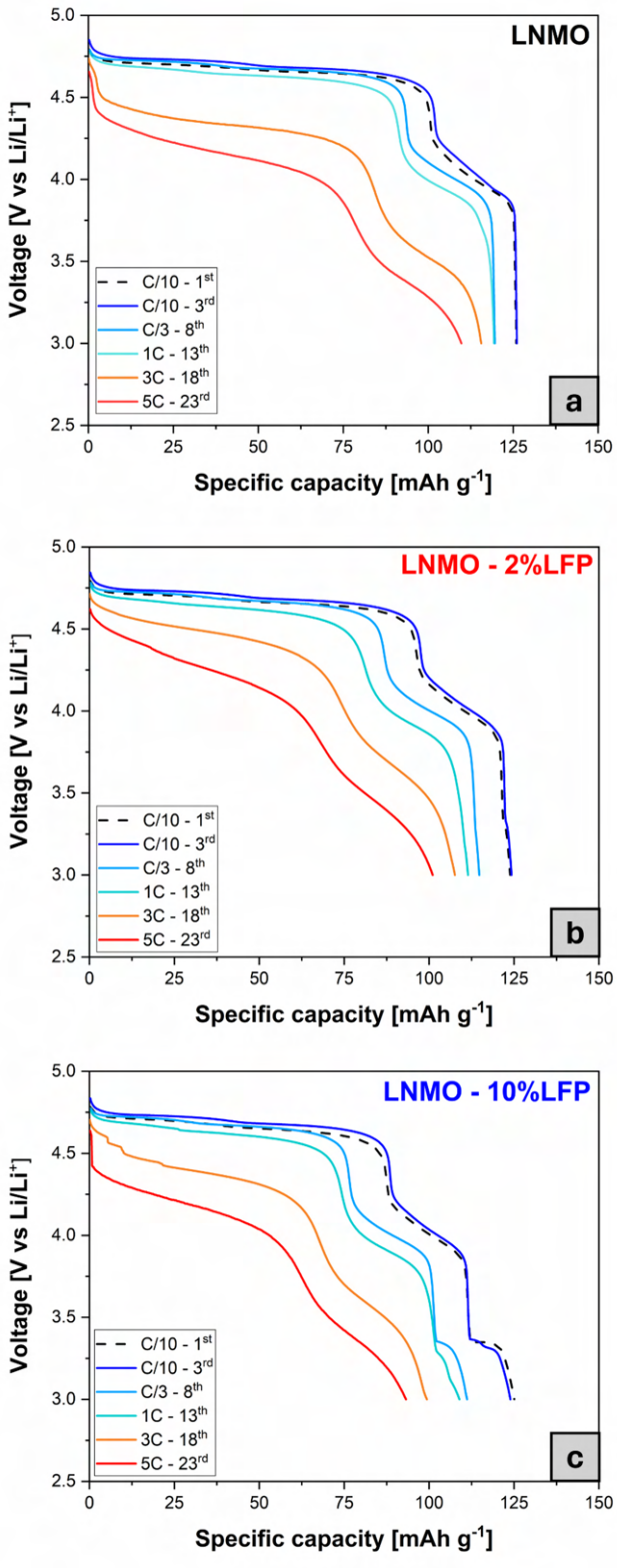

Fig. 6.22 Discharge profiles of the LNMO (a), LNMO +2%LFP (b), LNMO +10%LFP (c) at different C-rate.

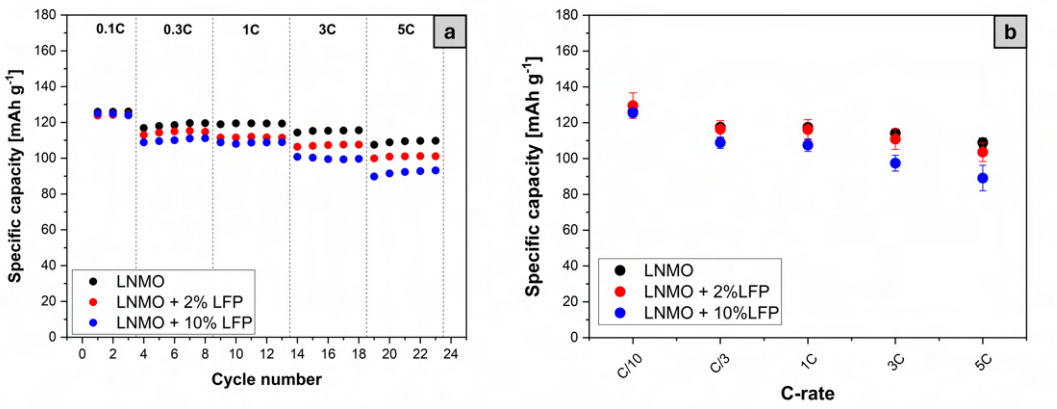

Fig. 6.23 Rate capability performance in discharge; panel (a) shows the comparison of all the discharge capacities over the test for three representative cells, while (b) is the comparison of the mean discharge capacity for each sample at different C-rate.

Table 6.2 The table summarizes the discharge capacity values obtained for the three samples in half-cell configuration during the rate capability test.

C-rate	**Average discharge capacity, [mAh g^{-1}]**		
	LNMO	**LNMO+2%LFP**	**LNMO+10%LFP**
C-10	126.11	129.56	125.55
C/3	117.53	116.34	108.90
1C	117.39	116.12	107.49
3C	114.14	110.83	97.43
5C	108.91	103.56	89.12

However, the results of the rate capability test also show that the LFP is indeed electrochemically active in its potential window (below 3.9 V vs Li/Li$^+$) up to currents of around 1C, even in the case of the sample at 2%wt, suggesting that it can effectively act as lithium source in the cathode.

To assess the potential impact of LFP on cell performance under demanding conditions, the three different samples underwent cycling in half-cells at a consistent current density of 1C for both charging and discharging over 1000 cycles. It should be remembered that this type of testing turns out to be particularly stressful not only for the cathode but also for the liquid electrolyte used in this study, which has a fairly traditional composition with the addition of 5%$_{wt}$ of FEC.

Figure 6.24 showcases the discharge capacity comparison for the three types of

cathodes, with capacities normalized against the total active material mass of LNMO plus LFP. As shown in Figure 6.24 and further detailed in Table 6.3, the pure LNMO cathode demonstrates a higher initial specific capacity, corroborating the observations from prior rate capability evaluations. Nonetheless, as the cycling progresses, the LNMO cathode begins to show a significant decrease in capacity. Notably, after roughly 800 cycles, the blended cathode containing $2\%_{wt}$ LFP starts to outperform the pure LNMO in terms of capacity, and a similar trend is also observed for the $10\%_{wt}$ sample over 900 cycles.

Upon closer inspection of the capacity retention data for each cathodic composition (plotted in Figure 6.24 (b) and numerically summarized in Table 6.4), it is evident that after 800 cycles, the LNMO cathode undergoes a notable reduction in capacity retention, plummeting to approximately 70% by the 900^{th} cycle. Conversely, the cathodes that include LFP demonstrate consistently higher capacity retention, which constantly exceeds 80%. Remarkably, the LNMO+2% LFP composition maintains its capacity retention above 80% even after 1000 cycles, revealing its enhanced stability and reduced capacity loss over extensive cycling.

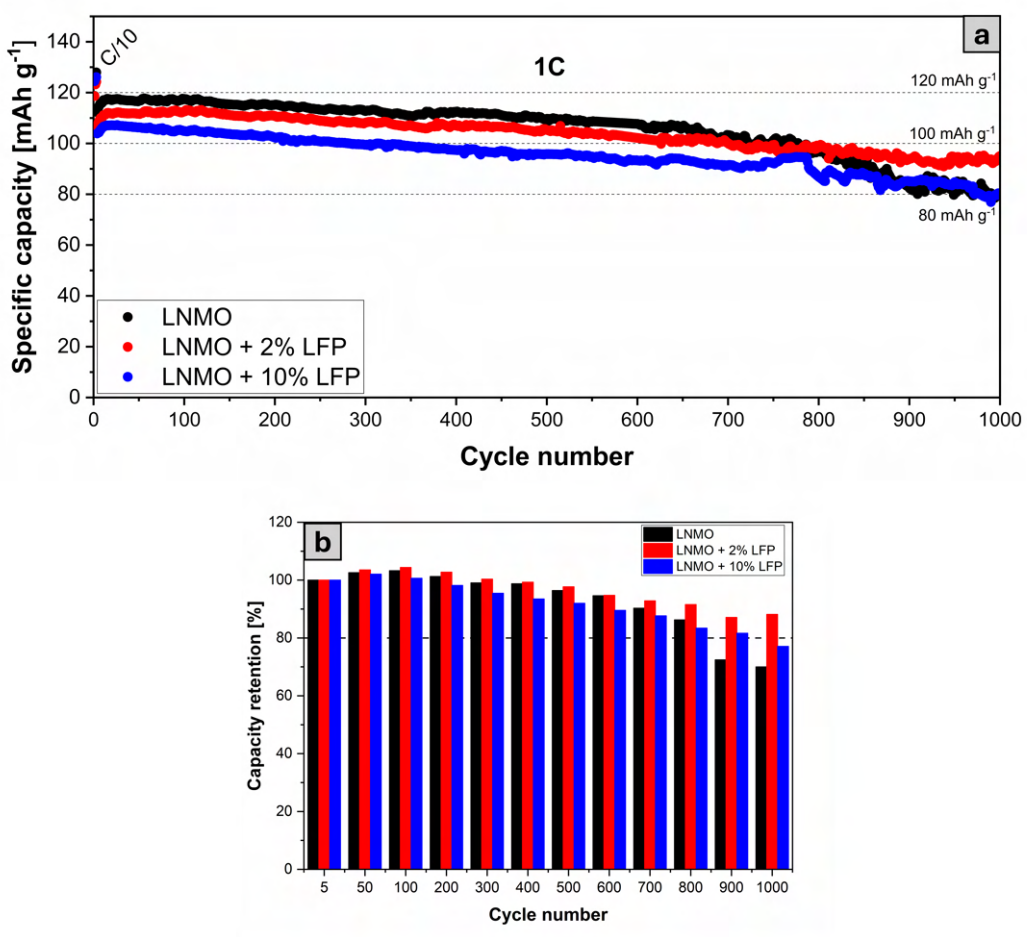

Fig. 6.24 Panel (a) compares the discharge capacities of the three different cathodes over 1000 cycles at the current of 1C, while panel (b) shows the capacity retention (calculated on the base of the 5^{th} cycle at 1C) of the three different samples over the cycling with a sampling of 100 cycles.

Table 6.3 The table summarizes the performance in terms of discharge capacity and coulombic efficiency of the three different cathodic compositions over the long cycling test performed at 1C for 1000 cycles.

Cycle number	**Discharge capacity, [mAh g^{-1}]**			**Coulombic Efficiency, [%]**		
	LNMO	**2%$_{wt}$LFP**	**10%$_{wt}$LFP**	**LNMO**	**2%$_{wt}$LFP**	**10%$_{wt}$LFP**
5^{th} (1C)	113.8	107.8	104.2	99.4	99.3	98.4
100^{th} (1C)	117.5	112.5	104.9	99.6	99.5	99.5
200^{th} (1C)	115.2	110.8	102.3	99.6	99.5	99.6
300^{th} (1C)	112.7	108.3	99.5	99.6	99.6	99.6
400^{th} (1C)	112.4	107.0	97.4	99.6	99.5	99.6
500^{th} (1C)	109.7	105.36	95.8	99.6	99.6	99.6
600^{th} (1C)	107.7	93.8	93.3	99.6	99.6	99.6
700^{th} (1C)	102.7	100.1	91.3	99.6	99.6	99.7
800^{th} (1C)	98.2	98.7	86.9	99.6	99.6	99.7
900^{th} (1C)	82.5	93.9	85.1	99.7	99.6	99.7
1000^{th} (1C)	79.7	95.1	80.3	99.7	99.6	99.7

Table 6.4 Discharge capacity retention values for the three samples over the long cycling (1000 cycles at 1C).

Cycle number	Discharge Capacity retention [%] vs. 5^{th} 1C		
	LNMO	**2%$_{wt}$LFP**	**10%$_{wt}$LFP**
5^{th} (1C)	102.6	103.5	102.1
100^{th} (1C)	103.6	104.4	100.6
200^{th} (1C)	101.3	102.7	98.2
300^{th} (1C)	99.1	100.3	95.5
400^{th} (1C)	98.7	99.3	93.5
500^{th} (1C)	96.4	97.7	92.0
600^{th} (1C)	94.6	94.8	89.5
700^{th} (1C)	90.3	92.8	87.6
800^{th} (1C)	86.3	91.6	83.5
900^{th} (1C)	72.4	87.1	81.6
1000^{th} (1C)	70.0	88.2	77.1

The progressive degradation that occurred in the cells tested with the long cycling protocol is more easily interpreted with the help of Figure 6.25, which shows, on its left side (panels a, b and c) the discharge/charge profiles of the three different cathode compositions for some selected cycles throughout the test, while on the right side (panels d, e and f) the differential curves (dQ/dV) extrapolated from the discharge/charge profiles at the 5^{th}, 500^{th} and 1000^{th} cycle are shown. In the dQ/dV profiles from the 5^{th} cycle, displayed in Figure 6.25 (d) for each electrode variant, a distinct peak in the 4-4.2 V range is observed across all samples, which is attributed to the $Mn^{3+/4+}$ redox transitions. Additionally, two peaks above 4.6 V, associated with the $Ni^{2+/4+}$ redox transitions, are evident for all the tested compositions. Notably, for the cathode with 10% LFP, an extra peak below 3.6 V, derivative from $Fe^{2+/3+}$ transitions, is distinctly visible. Over the course of the cycling test, the Fe peak vanishes, and there is a noticeable drift of both Mn and Ni peaks towards higher voltages. A closer inspection of the Ni peak shift, especially pronounced in the pure LNMO variant, shows that by the 1000^{th} cycle, the $Ni^{3+/4+}$ oxidation peak at 4.9 V disappears entirely, with a significantly reduced intensity for the reduction peak in the pure LNMO cathode. This phenomenon, as Howeling et al. [312] describe,

may result from reduced lithium intercalation into the spinel lattice, highlighting increased polarization and progressive degradation of the pure LNMO cathode over cycling, leading to significant capacity reduction.

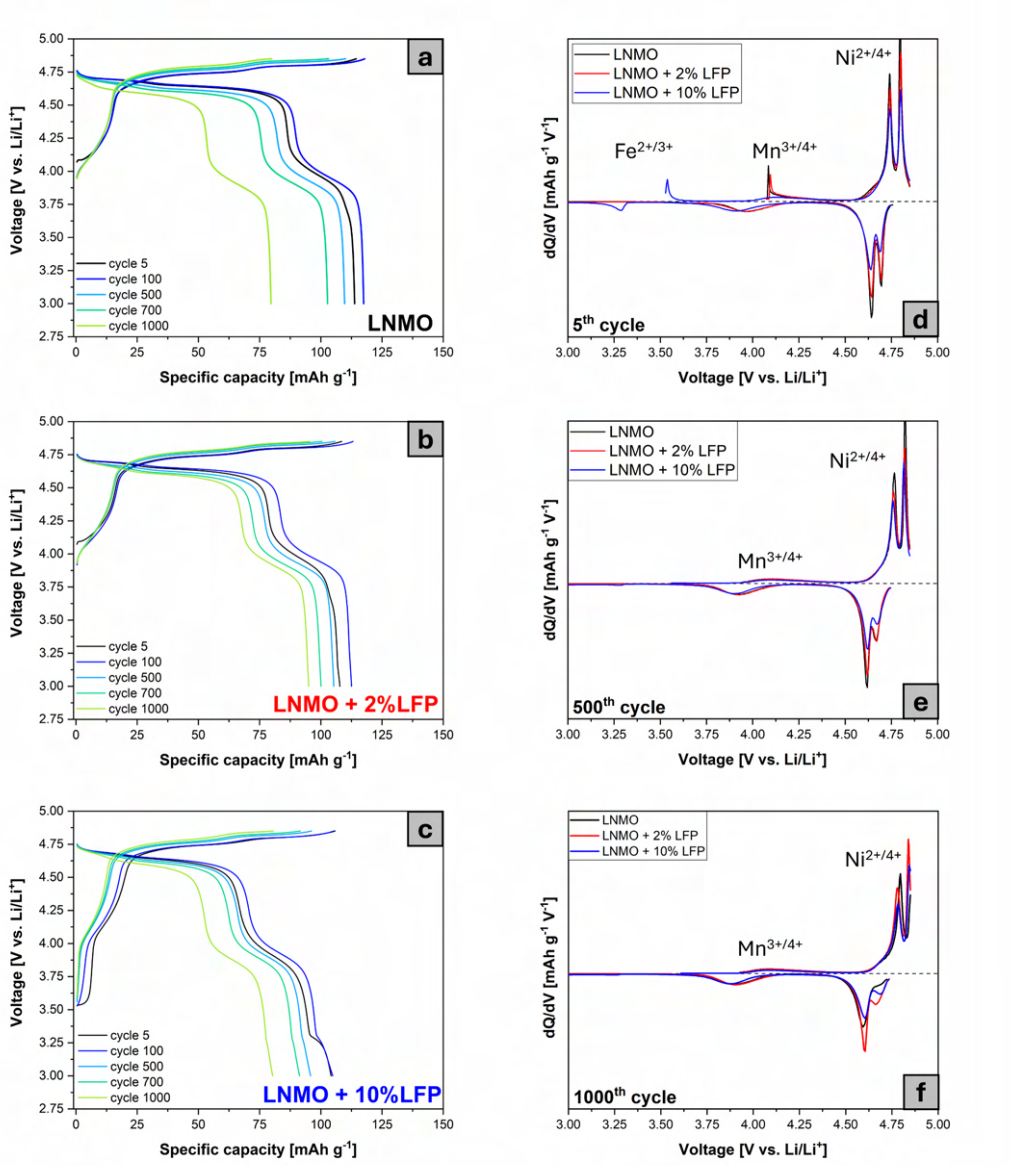

Fig. 6.25 Discharge and charge profiles of selected cycles for the three samples over the long cycling performed at 1C. Panel (a) shows the profiles of the pristine LNMO, while the profiles of LNMO+2%LFP and LNMO+10%LFP are shown in (b) and (c), respectively. The right part of the figure (panels, d, e , f) reports the dQ/dV profiles for the three samples of the 5^{th}, 500^{th} anf 10005^{th} cycles, respectively.

In order to better understand how the addition of different percentages of LFP to the pristine LNMO could affect the apparent diffusion coefficient of lithium ions and how this parameter varies as the state of charge of the battery varies, the Galvanostatic Intermittent Titration Technique (GITT) tests were carried out. This technique enabled the calculation of the apparent diffusion coefficients of Li^+ throughout the charge and discharge steps in a half-cell setup. The protocol for this test consisted of a current pulse at 0.1C lasting 10 minutes, followed by a relaxation step of 2 hours; the potential range in which the cells were tested was between 3 and 4.9 V.

In particular, Figure 6.26 (a-f) reveals that while the GITT profiles for the three samples are broadly comparable, both in charge (panels a,c and e) and discharge (panels b, d and f), distinct variations are evident at lower potentials.

In fact, by carefully observing the reported GITT curves, they can be divided into three distinct regions: one at low potential (below 4 V), one of intermediate transition (4 - 4.5 V) and one at high voltage (> 4.5 V). In particular, focusing on the first region, it can be noted how the pristine LNMO and LNMO+2%LFP are characterized by low overpotential values (ΔE), while the LNMO+10% LFP sample displays higher polarization values that seem to be related to a higher amount of LFP in the cathode composition. In the intermediate region, the three samples do not show substantial differences and are all characterized by a more marked ΔE, while the high potential zone turns out to be the one where ΔE is less evident, regardless of the considered sample.

The calculation of the apparent diffusion coefficient from the GITT was performed based on the equation reported below:

$$D_{Li^+} = \frac{4}{\pi}\left(\frac{IV_m}{Z_a F S}\right)\left(\frac{dE/d_x}{dE/d\sqrt{t}}\right)^2 \qquad t << \frac{l^2}{D_{Li^+}} \tag{6.3.1}$$

where "I" represents the current applied, "V_M" is the volume of the molecule, "Z_a" indicates the charge of the carrier, "F" stands for the Faraday constant, "S" denotes the electroactive surface area, and "E" is the voltage recorded over the duration "t" and composition "x".

An interesting feature that can be observed in the trend of the D_{Li^+} is the progressive shift to higher SOCs that its minimums undergo depending on the amount of LFP present in the blends (see Figure 6.26 c-f). This trend is in line with observations made by Rahim et al. [313], highlighting that the modest reduction in the Li^+ diffu-

sion coefficient correlates with the oxidation from Mn^{3+} to Mn^{4+} during the initial phase of lithium de-intercalation (at lower voltages) and with the oxidation from $Ni^{2+/3+}$ to $Ni^{3+/4+}$ at more advanced stages of lithium de-intercalation (at higher voltages).

The diffusion coefficients for the three cathode formulations exhibit comparable values that are in agreement with results obtained from cyclic voltammetry analysis, as well as with values reported in scientific literature, which are generally around the maximum value of 10^{-10} $cm^2 s^{-1}$. Moreover, a detailed examination of the diffusion coefficient comparisons for the samples (referenced in Figure 6.26 g-h) reveals that the blended samples with LFP exhibit slightly higher diffusion coefficients compared with pristine LNMO. This deviation of the D_{Li^+} for the blended cathodes becomes particularly noticeable for SOCs ranging from 20 to 40% and, to a lesser extent, for SOCs between 50 and 70%.

The observation of slightly higher diffusion coefficients in the blended samples strongly suggests that the presence of LFP exerts a significant influence, particularly at lower charge states. This indicates a potential interaction between the two materials, reflecting findings from cyclic voltammetry tests. Such an interaction might be triggered by the disparate redox potentials at which the two cathode materials become electrochemically active. Furthermore, the increased diffusion coefficient at lower voltages is directly associated with a higher oxidation state of manganese (Mn^{4+}), corroborating earlier report. [314] This aspect proves to be significant, as a higher oxidation state of manganese reduces the risk of dismutation and the subsequent formation of Mn^{2+}, along with the leaching of this species from the LNMO structure. [315] [316]

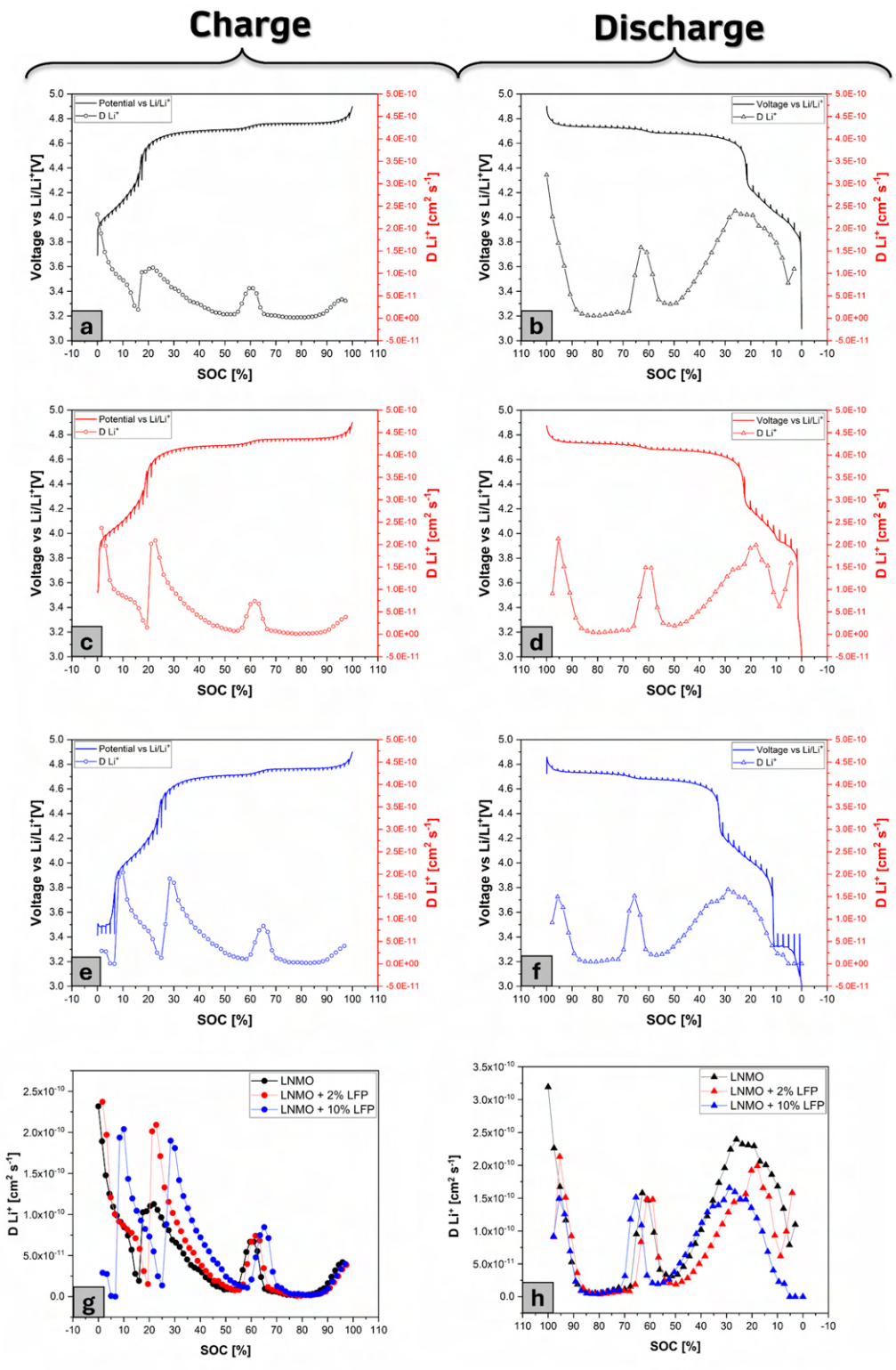

Fig. 6.26 GITT measurement profiles carried out both in charge and discharge, alongside the calculated Li^+ diffusion coefficient on the Y_2 axis. Panels (a), (c) and (e) report the charge GITT profiles for the charge of the pristine LNMO, LNMO+2%LFP and LNMO+10%LFP, while in (b) (d) and (f) the discharge profiles are shown. The comparison of the D_{Li^+} of the three samples over charge is plotted in (g), while in (h) the D_{Li^+} values are referred to the discharge step.

Alongside GITT measurements, EIS was also performed at different states of charge (10, 50, 75, and 100% within the potential range of 3.0 – 4.9 V) to investigate the changes in internal resistance across various cathodes. This EIS evaluation was carried out during the fourth cycle of charge, subsequent to three initial formation cycles at a C/10 rate.

The profiles of the charging curves during which the impedance tests were carried out are shown in Figure 6.27. The impedance measurement was preceded by a relaxation time of 1h to stabilize the potential; the regions of interest are highlighted by colored rectangles at different states of charge.

Figure 6.28 reveals that each Nyquist plot, regardless of the considered sample and the SOC, is characterized by three semicircles, followed by a diffusion line that moves from the high to the low-frequency areas. The impedance data have been analyzed with the ZView software, employing an equivalent circuit model (R1 + R2/CPE1 + R3/CPE2 + R4/CPE3 + W), as shown in Figure 6.28 (d). Delving deeper into details, the equivalent circuit model applied for fitting each Nyquist plot consists of an uncompensated resistance, R1, arranged in series with three R/CPE parallel configurations (where CPE denotes the constant phase element) and a Warburg element. The resistance encountered at high frequencies (R1) integrates various factors, including the ionic resistance of the separator and the electronic resistance associated with the external contacts of the electronic cell. The second resistance (R2), linked to the initial semicircle in the high-frequency domain (approximately 15000 Hz), is mainly due to the contact resistance encountered between the porous electrode and the current collector [41,42]. Generally, this resistance does not change significantly during the entire charging cycle. However, in the high-frequency area, another semicircle emerges, and the related resistance (R3) is ascribed to the resistance of the passivating surface layer on the particles. [43] Approaching the mid-frequency area, a distinct third semicircle emerges, illustrating a resistance (R4) that derives from both charge transfer and the resistance encountered in the pores at the electrode/electrolyte boundary. This part of the circuit precedes a Warburg diffusion component (W) detectable at reduced frequencies, which reflects the semi-infinite linear movement of Li^+ ions within the electrodes solid framework [40–45]. The Nyquist plot demonstrates that the semicircles corresponding to various processes are intertwined, thus challenging the differentiation of contributions from individual cathode materials. Specifically, the regions representing charge transfer and contact resistance for LNMO and LFP are indistinguishably overlapped, as it can be clearly

seen in the EIS spectra reported in Figure 6.28. However, it is also interesting to note that the R4 decreases as the SOC increases, in particular from 10% towards 50% and 75%, and this is a trend already reported in the literature [317] for materials that contain Mn, which oxidizes from 3+ to 4+, with a consequent reduction in charge transfer resistance. Moreover, the impedance spectra reveal that R4 maintains low values as it approaches the 4.7 V threshold, indicative of nickel oxidation reactions.

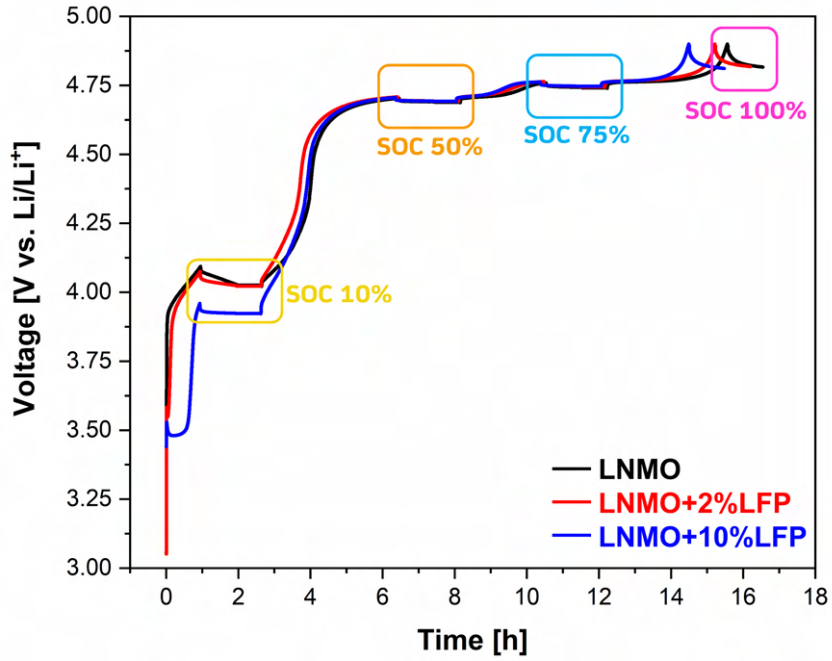

Fig. 6.27 Charge profiles during which the EIS measurements were carried out. The colored rectangles highlight the different SOC at which the charge was stopped and the EIS had been collected.

The resistance values extracted from the fitting process at various SOCs (10%, 50%, 75% and 100%) are listed in Table 6.5. As can be seen, a general characteristic is that the total resistance of the cathodes is higher at low SOCs, (i.e., when the cathode is rich in lithium) compared to higher charging stages. It can also be noted that at low SOCs, the presence of the LFP seems to lead to an increase in charge transfer resistance (R4) compared to the pristine LNMO sample. According to findings by Liebmann et al., [311], blending materials with distinct intercalation potentials typically results in elevated charge transfer resistance in comparison to single-material electrodes.

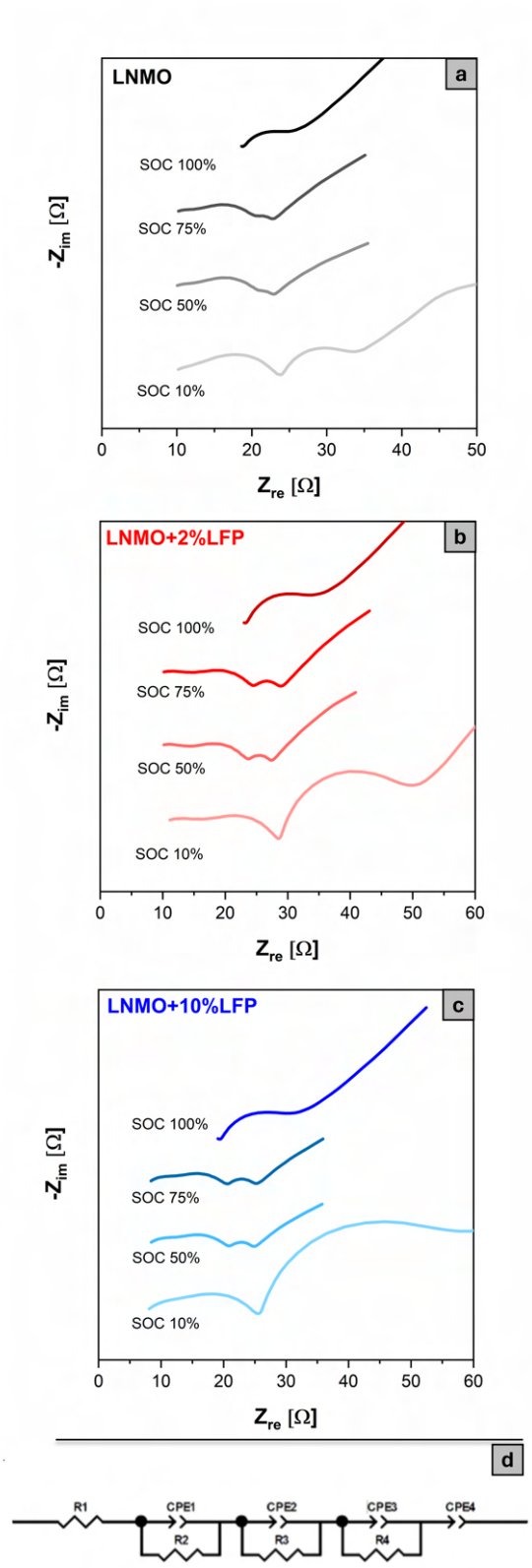

Fig. 6.28 (a) EIS spectra for pristine LNMO at different SOCs (b) EIS spectra for LNMO+2%LFP at different SOCs (c) EIS spectra for LNMO+10%LFP at different SOCs, (d) the equivalent circuit used to fit the EIS spectra

In summary, the impedance spectra consistently demonstrate that the LFP presence (even in low quantities) influences the cathode response at low SOC, indicating its effect at reduced potentials, while LNMO's influence becomes significantly more pronounced at elevated states of charge. When the state of charge reaches 100%, the overlapping contributions make it impossible to distinguish individual resistances, thus only the values of R1 and R4 can be found in Table 6.5. In this regard, for all the samples analyzed, R1 seems to increase more markedly as SOC increases, while the variation of R4 towards higher values is more limited.

Table 6.5 Detailed impedance values at various states of charge for cathode compositions: pure LNMO, LNMO blended with 2% LFP, and LNMO blended with 10% LFP.

SOC %	**Sample**	**R1** [Ω]	**R2** [Ω]	**R3** [Ω]	**R4** [Ω]
	LNMO	6.60	8.45	8.37	5.98
10	LNMO+2%LFP	5.06	12.55	10.98	17.21
	LNMO+10%LFP	6.17	7.78	11.38	26.21
	LNMO	6.71	8.66	7.8	0.87
50	LNMO+2%LFP	4.36	10.62	8.96	2.48
	LNMO+10%LFP	6.81	5.08	9.23	2.68
	LNMO	6.98	6.25	7.48	1.35
75	LNMO+2%LFP	4.09	11.76	8.98	2.97
	LNMO+10%LFP	6.76	5.16	8.96	3.22
	LNMO	17.98	-	-	6.56
100	LNMO+2%LFP	22.42	-	-	6.65
	LNMO+10%LFP	18.69	-	-	9.89

At this point in the discussion, it is appropriate to remember that the data presented so far were obtained in a half-cell configuration (i.e. with the cathode coupled to an anode made up of metallic lithium) while from this point forward in the chapter the data reported refer to complete cell (using graphite as anode material). This different pairing of electrodes has been studied for several reasons: firstly because graphite is commercially the most used anode material, secondly because the limitations of LNMO (capacity fading, Mn dissolution, and loss of active lithium) are more pronounced in full-cell, since lithium metal, acting as an infinite reserve of Li

ions, can partially mitigate these problems. Consequently, the effect of LFP in the cathode composition can also be very different in the two cell designs.
Given the fact that the reversible capacity of the full cell is based on the active mass of LNMO in the cathode, the areal capacity of the graphite negative electrode was calibrated to match the capacity of the positive electrode, aiming for an N/P ratio (anode capacity/cathode capacity) of about 1.00 to 1.1. In particular, the following data in full cell configuration were obtained with these N/P ratios: LNMO 1.07, LNMO+2%LFP 1.02 and LNMO+10%LFP 1.08. Moreover, to avoid excessive strain on the electrolyte, the cells were cycled in a voltage window of 3 to 4.75 V at room temperature.
The results of a galvanostatic cycling test consisting of five cycles at C/10 followed by 100 cycles at 1C on the three samples vs graphite anodes are shown in Figure 6.29. It can be seen how in the formation cycles (Figures 6.29 c and d) the cathodes with LFPs exhibit higher capacities both in terms of areal capacity, approximately 1.2 mAh cm^{-2} vs. the 1.05 mAh cm^{-2} of the pristine LNMO, and gravimetric capacity, 110.60 mAh g^{-1} vs 96.30 mAh g^{-1}. From the second cycle onwards, the two blended samples exhibit a Coulombic efficiency (CE) above 93%, in contrast to the LNMO sample which maintains a CE below 86%; however, by the completion of the forming cycles, all samples achieve a CE greater than 95%. In this regard, the increased Coulombic Efficiency detected in the formation step for the blended cathode suggests that the integration of LFP may effectively mitigate this irreversible behavior typical of LNMO-based cathodes.
Shifting the focus to the part of the test carried out at a higher current (1C), the capacity performances confirm the trend shown by the three samples during the formation cycles, with the blended cathodes outperforming the pristine LNMO. In more detail, the areal capacity of the blends is around 1.1mAh cm^{-2}, compared to about 0.9 mAh cm^{-2} for the pristine LNMO, while the gravimetric capacities show more varied values among the samples (see Figure 6.29 b) but are nonetheless greater for both blends.
In terms of capacity retention, which was calculated based on the value obtained at the first cycle carried out at 1C, both blended samples exhibit values above 80% at the end of the cycling test, while the LNMO presents values below this threshold.

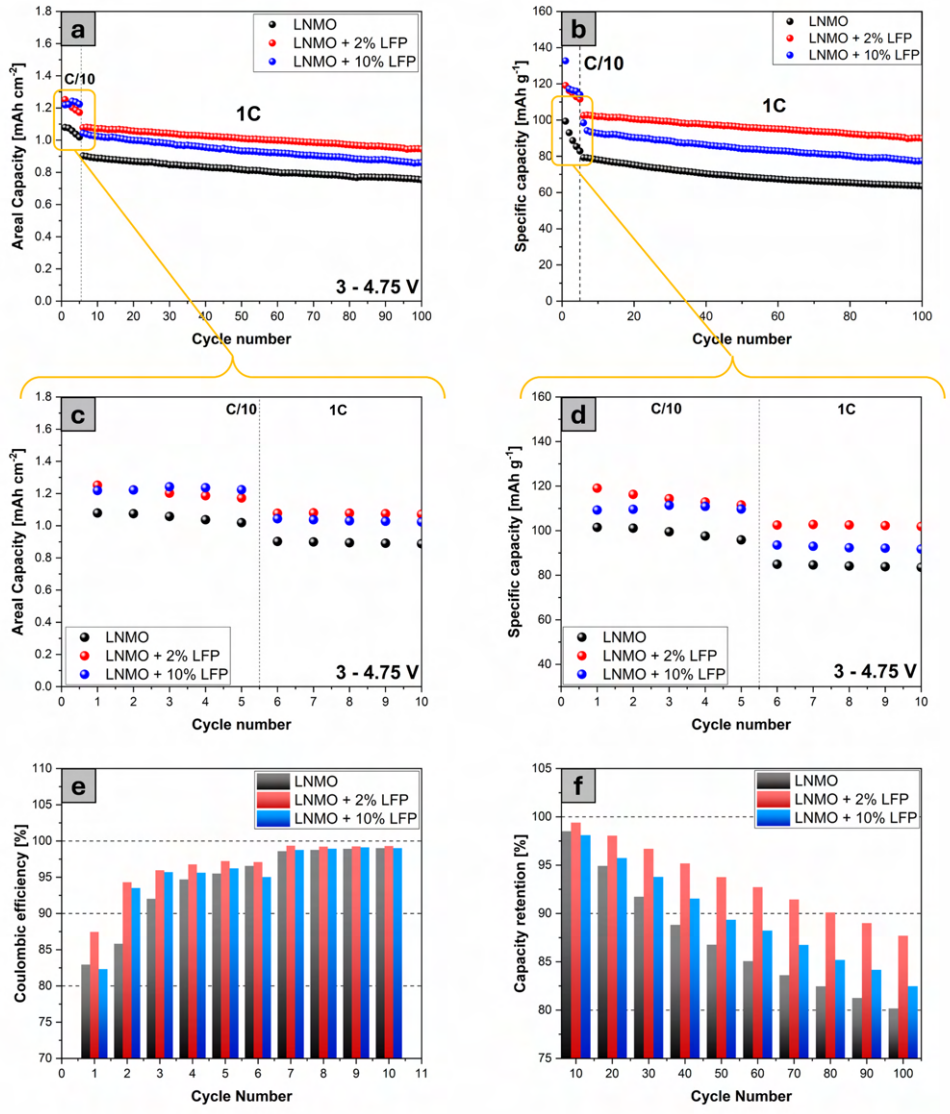

Fig. 6.29 The figure shows the electrochemical performance of the three cathodes coupled with a graphite-based anode; (a) areal capacity of the full-cells over cycling, (b) gravimetric capacity of the full-cells over cycling, panels (c) and (d) show a zoom of the formation cycles performed at 0.1C in terms of areal and gravimetric capacity, while in panel (e) and (f) are plotted the coulombic efficiency (CE) and capacity retention of the three samples over cycling, respectively.

In contrast to half-cells configuration, the cells coupled with graphite as anodic material present more complex differential capacity (dQ/dV) profiles, which were derived from their charge/discharge curves, as depicted in Figure 6.30. In particular,

all samples exhibit two significant peaks at 4.59 V and 4.68 V, indicative of the stepwise oxidation process of nickel (Ni^{2+} to Ni^{3+} and then to Ni^{4+}). Notably, the pure LNMO and the LNMO with the addition of 10% LFP display an extra peak at around 4.63 V, which progressively fades over subsequent cycles, as seen in Figure 6.30 (d) and (f). This additional peak in the dQ/dV profiles of full LNMO/graphite cells is presumably connected to electrolyte degradation, as Zou et al. [318] pointed out in earlier research. On the other hand, examining the dQ/dV profiles of the LNMO+2%LFP sample in panels (b) and (e) of Figure 6.30, it can be observed that they consist of two main, well-defined, and reproducible peaks across the five formation cycles analyzed, without the presence of the additional peak at 4.63 V shown by the other two samples.

Upon closer examination of the dQ/dV profiles at lower voltages (as shown in Figure 6.30 g, h, and i), a pronounced peak around 3.9 V is noticeable for all samples. This peak, which derives from the oxidation of manganese, shows a gradual shift with increasing cycles. Notably, in the case of the pure LNMO cathode, this peak becomes invisible after the first two cycles. It should be noted that the peak does not vanish but rather moves to considerably higher voltages (4.45 V), which is evident in the profiles from the third to the fifth cycle. On the other hand, in cathodes that incorporate LFP, the peak associated with manganese oxidation remains noticeable through several cycles, and a higher concentration of LFP in the cathode ($10\%_{wt}$) appears to be beneficial in counteracting the shift of the peak towards higher potentials, as can be seen in panel (i) of Figure 6.30. This observation suggests that the inclusion of LFP markedly reduces the polarization within the cell. Moreover, the distribution of LFP particles inside the cathode seems to play an important role, acting as a shield to prevent direct contact between LNMO particles and the electrolyte, thereby lessening the degradation of the latter.

In the testing protocol of the full-cell, a relaxation step of 30 minutes was incorporated between each cycle to enhance accuracy in determining the potential of the cells and to evaluate how effectively materials were utilized in a non-polarized state. Figure 6.31 illustrates the open circuit potential (OCP) for the three different samples after the rest step, reporting the OCP values at the 1^{st}, 5^{th}, 10^{th}, and 50^{th} cycles.

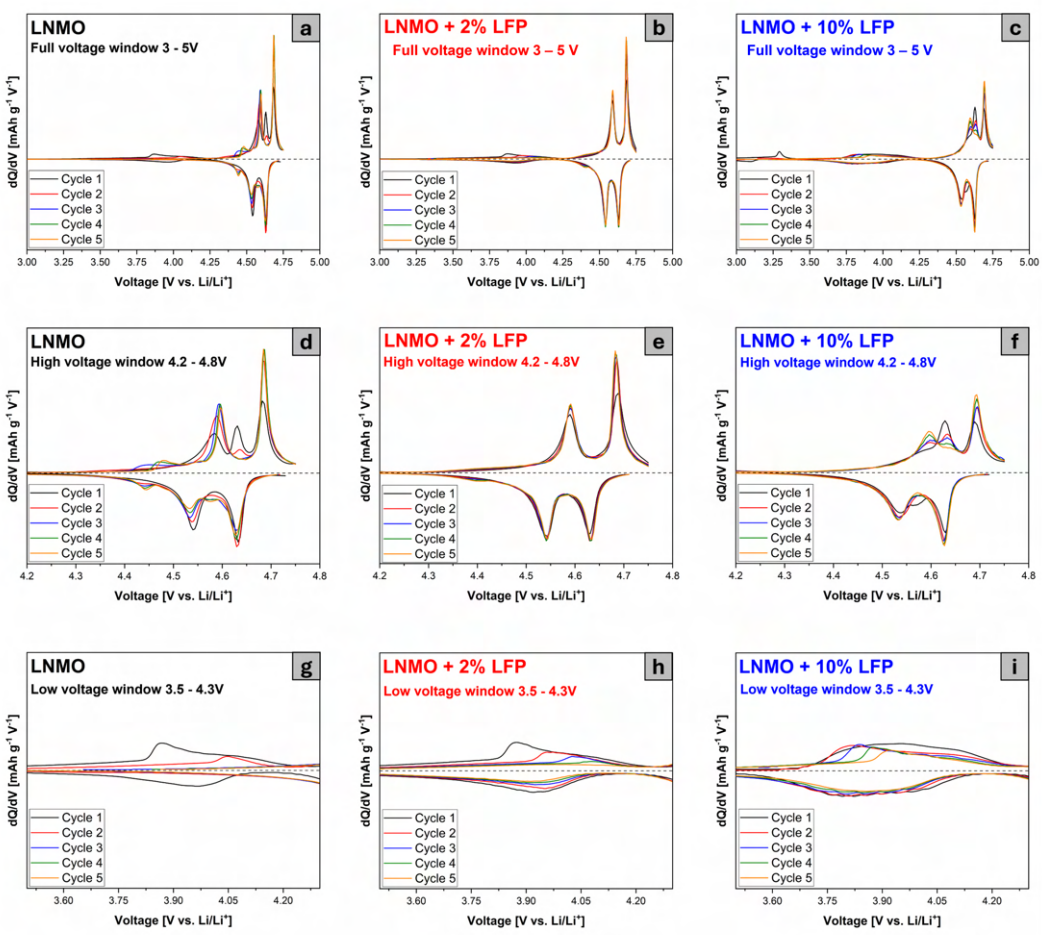

Fig. 6.30 Panels (a), (b), and (c) display the dQ/dV of the full-cells for the first five cycles conducted at 0.1C for pristine LNMO, LNMO+2%LFP, and LNMO+10%LFP, respectively. In panels (d), (e), and (f), enlargements of the same curves in the high potential zone 4.2 - 4.8 V are shown, where the electrochemical activity of Ni is concentrated. Finally, panels (g), (h), and (i) present the dQ/dV in the low potential zone 3.5 - 4.3 V, characterized by the activity of Mn.

Although the 30 minutes of relaxation may not allow every cell to achieve complete equilibrium (in fact the electrode potentials would relax further if allowed), it offers a pragmatic approach for approximating their equilibrium potential without significantly inducing calendar aging, as highlighted in the work of Klett et al. [319] In particular, starting from the second cycle onwards, the relaxation potential exceeds 3.5 V for the pure LNMO cell, whereas, for the two blended cathode samples, it stays below 3.2 V after the five cycles at 0.1C (see Figure 6.31 e). As the charge rate

increases to 1C, the relaxation potential for the blended samples maintains lower levels for the initial 50 cycles.

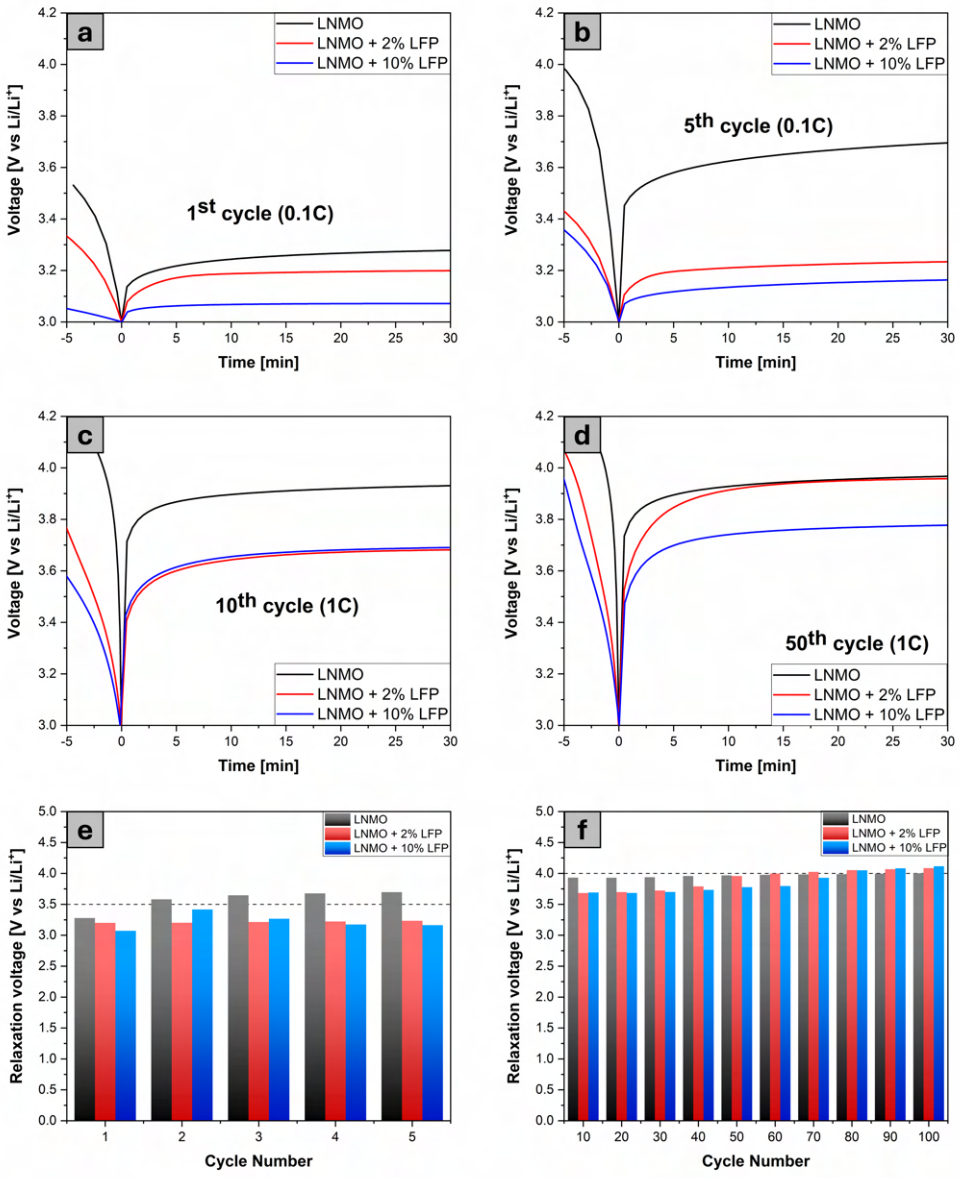

Fig. 6.31 Panels a, b, c and d show the relaxation potential profiles of the three different samples at the 1^{st}, 5^{th}, 10^{th} and 50^{th} cycle, respectively. In the two bottom panels are reported the OCP values after the relaxation step for the formation cycles (e) and during the 100 cycles at 1C (f).

Beyond this point, the sample containing $2\%_{wt}$ LFP exhibits a gradual increase in relaxation potential, eventually matching the value observed in the pristine LNMO cell. In contrast, the cell featuring the LNMO+10% LFP cathode takes around 80 cycles to reach the same relaxation potential value, as shown in Figure 6.31 (f). This phenomenon underscores the significant influence of LFP, which becomes more pronounced at lower C-rates and varies according to the amount of LFP introduced into the cathodic formulation. The relaxation potential incrementally rises throughout the cycling, indicating that lithium is being released from the LFP, effectively increasing the amount of cyclable lithium. This process appears to compensate for the continual depletion of electrochemically active lithium, likely due to persistent side reactions and the development of an unstable SEI layer.

To delve deeper into the impact of LFP on cathode performance, three-electrodes cells were assembled and tested using lithium as a reference electrode. The operational voltage of the cell was set from 3.0 to 4.75 V to closely examine the separate responses of the anode and cathode over five formation cycles at a C/10 rate. The possibility of observing the anode and cathode potentials individually can be very useful to undersand the possible causes of capacity fading during the cycling of full-cells, in which it is generally not possible to separate the contributions of the anode and cathode due to the cell design itself. Indeed, by defining a voltage range for a full-cell to operate, without separately monitoring each electrode, the voltage response observed by the potentiostat is the potential difference between the cathode and anode. This difference can change significantly depending on the state of charge of the cell. Therefore, although the overall cell potential may be within the established range, the potentials of the individual electrodes can be outside of this. For example, the cathode potential typically exceeds the upper threshold, going beyond 5V, while the anode potential can drop below 0 V, thus favoring lithium plating. [320–322]

The results of the galvanostatic cycling for five cycles at 0.1C of the three-electrodes full-cells are shown in Figure 6.32, which reports the full cycling test, and in Figure 6.33, where the first and fifth cycles are compared for the three samples. In particular, it can be seen that the voltage profiles for all the cathodes display the characteristic plateaus of Ni oxidation/reduction that were previously identified in half-cell studies. Additionally, for the blended cathodes, there is a noticeable plateau that corresponds to the redox reaction of iron. Simultaneously, the process of lithium being intercalated into and deintercalated from graphite takes place in several steps at potentials

below 0.2 V.
In more detail, by observing the charge and discharge profiles presented in Figure 6.33 and comparing them, it can be noted that the cells assembled with blended cathodes exhibit, during the cell's discharge process (and thus the de-lithiation of graphite), a lower increase in the anode potential (a phenomenon often referred to as "anode slippage"). Indeed, for the pristine LNMO sample, the anode potential at the end of the discharge step during the 5 formation cycles was always over 1 V, whereas in the case of LNMO+2%LFP, the anodic potential was around 0.5V at the end of the first cycle with a slight increase in the subsequent ones. In the case of the LNMO+10%LFP sample, this trend was even more pronounced, with the anodic potential consistently being below 0.5 V throughout the entire cell formation. This finding indicates that incorporating LFP with LNMO in the cathode composition can effectively mitigate the potential growth of the graphite anode, with notable implications for cycling stability.

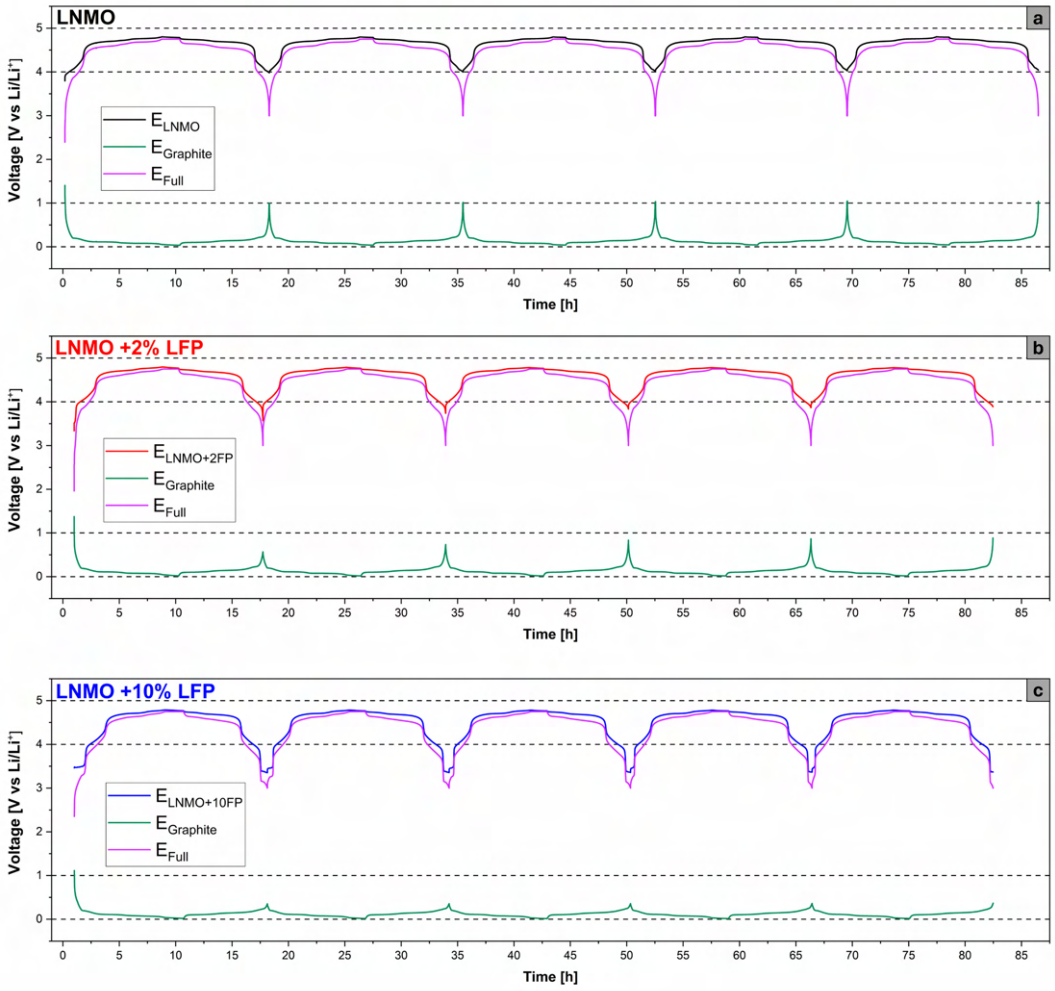

Fig. 6.32 Full-cell voltage profiles with the charging and discharging steps that are shown continuously vs time for (a) pristine LNMO vs graphite (b) LNMO+2%LFP vs graphite and (c) LNMO+10%LFP vs graphite.

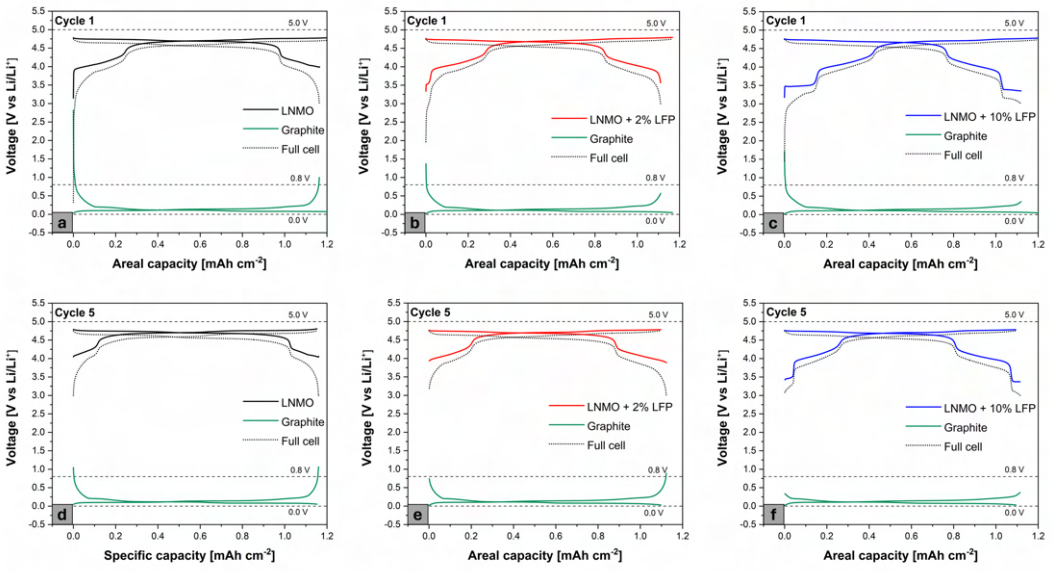

Fig. 6.33 The first cycle of the three-electrodes cells of each sample is shown in panels (a), (b) and (c) for the pristine LNMO, LNMO+2%LFP, and LNMO+10%LFP respectively. In the lower part of the figure, the fifth cycles for the three samples are shown in (d) for LNMO, (e) for LNMO+2%LFP, and (f) for LNMO+10%LFP.

Another interesting aspect that can be captured by this three-electrodea test is the cut-off value reached by the positive electrode at the end of the cell charging step. In particular, when examining the potential profile (see Figure 6.34) of the cathodes at the fifth cycle, it can be noticed that the pure LNMO cathode reaches a higher value for the upper cut-off voltage. Consequently, this causes the following CV step to be carried out at higher potentials compared to those observed for blended cathodes. It is reasonable to assume that this elevated cut-off value is not lowered in the subsequent cycles and might become more significant at higher C-rates, imposing significant stress on the electrolyte. Indeed, reaching and maintaining high potential values invariably leads to increased degradation of the electrolyte over the cycles, leading to a more pronounced capacity loss.

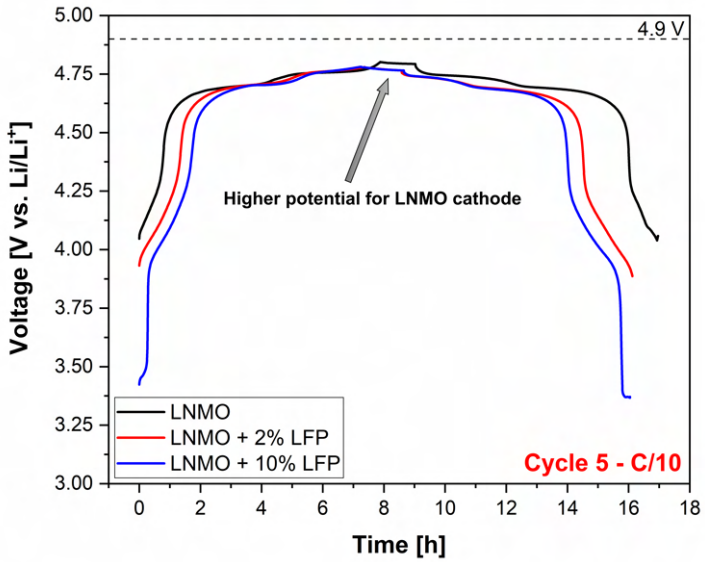

Fig. 6.34 Comparison of the charge profile of the fifth cycle for the three cathodes; the arrow highlights the higher potential reached by the LNMO cathode at the end of the charge and the subsequent constant voltage step.

In order to analyze in more depth the response of the three different positive electrodes in this type of cell configuration, the profiles of the charging curves of the first and fifth cycles (Figure 6.35 a and b) were used to derive the respective differential dV/dQ curves, which are shown in Figure 6.35 (d) and (c). In particular, the examination of the charge profiles of blended electrode cathodes in the initial cycle reveals that the oxidation reaction at lower potentials solely affects LFP. This reaction results in the liberation of an initial quantity of lithium ions from the cathode, which is consumed in the formation process of the SEI layer on the surface of the graphite anode. This stage is crucial for the stability and longevity of the battery. At high potentials, however, the LNMO undergoes de-lithiation, providing the lithium needed for the reversible charging and discharging process. It can therefore be seen how the two cathode components, although operating in two rather different potential windows, can work synergistically in the different charging stages of the cell. In the fifth cycle, there is a distinct upward shift in the cathodes potential (for all samples), clearly illustrated in Figure 6.35 (b). However, this trend is particularly marked in the case of the pure LNMO cathode. In fact, after five cycles, it consistently maintains a level above 4 V throughout both the charging and discharging processes, indicating a significant change in its electrochemical behavior. This highlights that LNMO

activity is confined to a higher voltage plateau near 4.75 V, and does not extend to lower voltages, thus bypassing the 4 V plateau, where Mn^{3+} to Mn^{4+} oxidation occurs. Furthermore, these findings highlight the fact that the cut-off potential of 3 V (i.e. the lower discharge limit after which the full-cell returns to charging), being calculated as the difference between the cathodic and anodic potential (and E_{we} - E_{ce}), is reached prematurely due to the growth of the graphite potential above 0.8V. This suggests that a fraction of the lithium fails to be efficiently de-intercalated from the graphite, resulting in its depletion during the renewal phase of the SEI layer. [312]

The differences in the electrochemical behavior between the pure LNMO cathode and the two blends are more prominently outlined through differential voltage analysis (DVA or dV/dQ), as depicted in the figures 6.35 (c) and (d). Particularly, in this form of galvanostatic cycling data analysis, peaks emerge in relation to the state of charge of the battery and each peak corresponds to transitions from one voltage plateau to another in the charging and discharging curves when the potential of the cell (or the cathode potential, in this case) is plotted against the state of charge. Indeed, the peaks observed in Figures 6.35 (c) and (d) are located at SOC values where, in Figures 6.35 (a) and (b), there are significant potential transitions.

Thus, DVA emerges as a valuable method to evaluate and compare the decay and degradation of the cell over cycling. In particular, by comparing the SOC positions of the peaks exhibited by the three cathodes at the first and fifth cycle, it can be observed that there is a shift of the peaks towards lower SOC levels; however, this displacement of the peaks is not uniform across the three samples. Indeed, for the pristine LNMO, it is clear that the shift of the peaks is much more pronounced (the peak at the beginning of charge SOC$\approx$0 is not visible) compared to the blended samples, with the LNMO+10%LFP sample showing the least potential variation of its peaks in dV/dQ curve.

One aspect worth focusing on involves the upper and lower potential cut-off values when operating in a full-cell configuration. Indeed, especially when working with high-voltage cathodes (such as in the case of LNMO), the electrolyte is subjected to significant stress, and a too high cut-off value can accelerate capacity fading. On the other hand, a cut-off potential that is too low would prevent utilizing the full reversible capacity of the cathode. In this sense, the value of 4.75 V, intended as the overall cell cut-off potential, has proven to be a good compromise. Similarly, the anode also has an ideal potential window within which it should always operate. Indeed, as Michalak

et al. [321] have highlighted, the SEI layer starts to deteriorate when the potential of graphite during discharge equals or exceeds 0.9 V. This breakdown of the SEI layer leads to the exposure of new reactive areas on the graphite anode, necessitating the use of additional lithium and electrolyte to form a new SEI layer. Concurrently, the cathode begins to produce detrimental oxidation by-products, further exacerbating anode degradation through an interactive mechanism between the electrodes, also known as "cross-talk". [320] This ongoing depletion of lithium and electrolyte incrementally raises the discharge potential for both LNMO and graphite electrodes with each cycle, speeding up their degradation [54] and contributing to an increase in the internal resistance of the cell. [323]

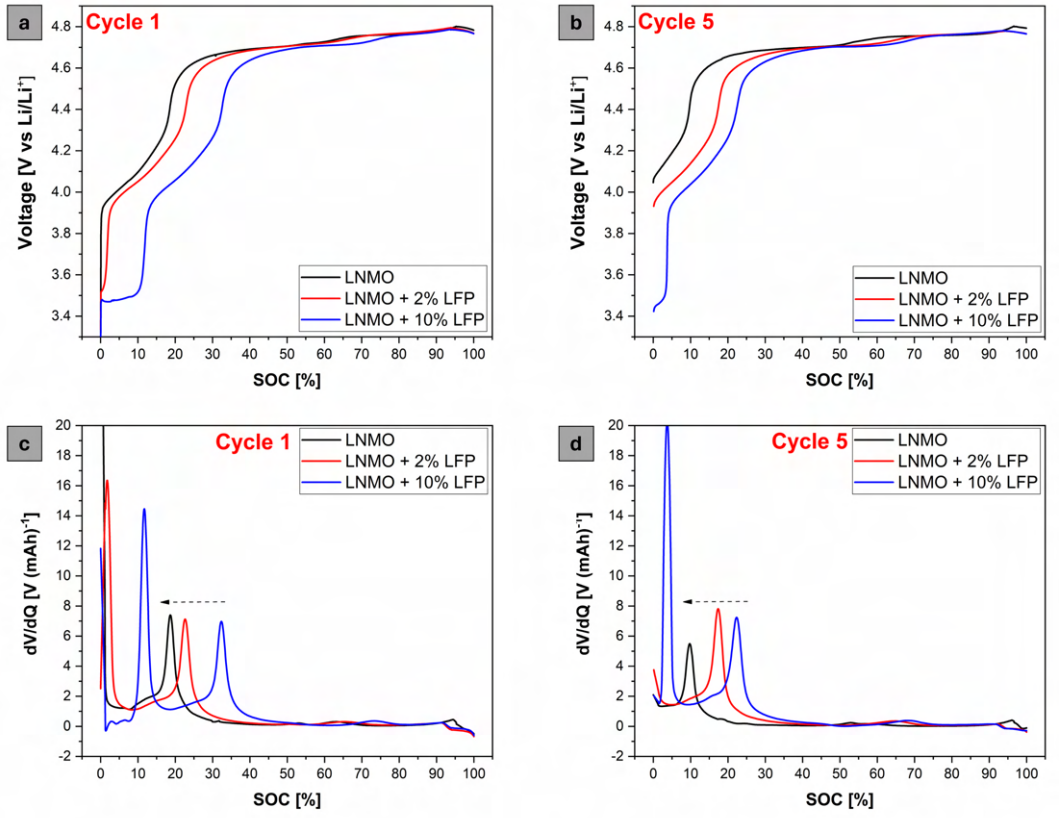

Fig. 6.35 (a) Comparison of the charge profile of the first cycle for the three cathodes (b) Comparison of the charge profile of the fifth cycle for the three cathodes; (c) Comparison of the dV/dQ curves of the first cycle for the three cathodes(d) Comparison of the dV/dQ curves of the fifth cycle for the three cathodes; the arrows highlight the shift of the peaks i nthe dV/dQ plots towards lower SOC.

The mitigation in the rise of discharge potentials of the graphite in cells with blended cathodes highlights the beneficial impact of LFP on SEI layer stabilization. In particular, the LFP addition seems to effectively diminish the consumption rates of lithium and electrolyte in the early stages of cycling and influences the cut-off potentials of the electrodes. This phenomenon could be largely due to the SEI formation occurring at potentials well under 4.5V vs Li/Li^+ , a range that steers clear of the formation zone for adverse secondary products stemming from parasitic oxidations at the cathode. [324] At the same time, the lithium initially supplied by the LFP proves to be beneficial for the overall cell operation since, in this way, the LNMO is able to recover more lithium during cycling, reducing the overall irreversibility of the system.

In conclusion, it can be said that RAM is an effective and scalable technique for generating blended active materials for Li-ion batteries. In the particular case of LNMO and LFP, the amount of LFP most homogeneously distributed through this process was found to be a low amount (about 2%). From an electrochemical point of view, the LFP appears to be reversibly active up to currents of 1C in half cells. Moreover, it has been noted that the impact of LFP is more significant at lower states of charge, affecting the diffusion coefficient of Li^+ in the electrode and, as a result, the performance of LNMO at reduced potentials (for example, 4.1 V). The most marked effect of LFP, however, appears to be on capacity retention in both half-cell and full-cell configurations with graphite as an anode. In this scenario, a reduced potential polarization of the cell was noted, attributed to LFP acting as a "lithium donor" and its impact on generating a stable SEI layer on graphite throughout the formation cycles.

Fascinatingly, the advantageous influence of LFP is most pronounced when used in minimal concentrations (such as $2\%_{wt}$), which boosts the capacity retention while not substantially affecting the total capacity of the system. Ultimately, the uniform distribution of particles in the electrode, together with the reduction in lithium inventory loss and electrolyte degradation, underscores the significance of achieving a compromise among mixing methodology, morphology, physicochemical properties, and ultimate electrochemical outcomes.

Chapter 7

Lithium Copper Manganese Oxide cathodes for Li-ion batteries

The last part of the thesis focuses on the synthesis and chemical-physical and electrochemical characterization of the high-voltage cathode material $LiCu_{0.4}Mn_{1.6}O_4$ (hereinafter referred to as LCMO) for Li-ion batteries. This work was the result of a collaboration with the research group of the Commissariat à l'énergie atomique (CEA)-LITEN in Grenoble, where a significant part of the research activities described below were carried out.

7.1 Pyshical-chemical and electrochemical properties of LCMO material

From a structural point of view, lithium copper manganese oxide (like LNMO) is derived from $LiMn_2O_4$ and therefore, like the latter, has a spinel structure. The idea of partially replacing Mn with other transition metals (Ni, Cr, Co, Cu, etc.) arises primarily from the need to improve the electrochemical stability, electronic conductivity and working potential of the material. Structurally, LCMO exhibits a certain degree of cation mixing between divalent Cu^{2+} ions and tetravalent Mn^{4+} ions, which occupy the 16*d* octahedral sites of the spinel structure. Theoretically, electroneutrality is achieved when all the manganese ions are tetravalent and the

copper ions are all divalent and distributed across the 16*d* sites. However, some ion exchange between copper and lithium could also occur in this material, both in the tetrahedral 8*a* sites because, as reported by Shannon et al. [325], tetrahedrally coordinated Cu^{2+} has a smaller ionic radius than Li^{+} (0.57 versus 0.59 Å), and in the octahedral 16*d* sites due to the small difference in ionic radii of only 0.03 Å. The typical spinel structure of LCMO along various crystallographic orientations is shown in Figure 7.1, thanks to which the different positions assumed by the Cu, Li, Mn, and O atoms in the crystal can be appreciated.

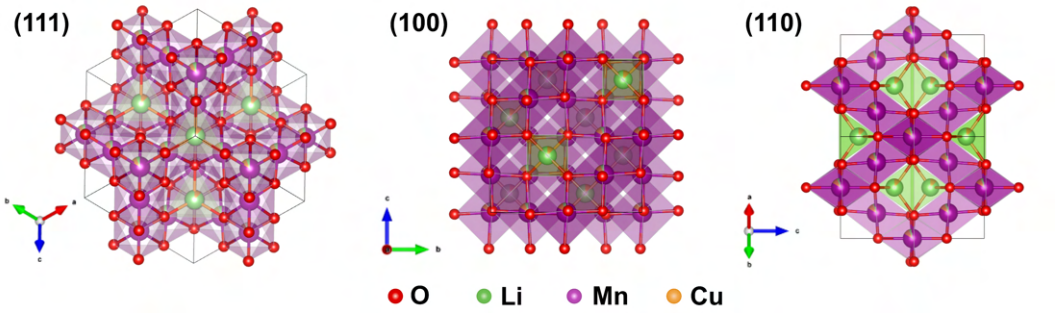

Fig. 7.1 Representation of the LCMO structure along the plane (111), (100) and (110). Oxygen atoms are reported in red, lithium atoms in green, manganese atoms in purple and copper atoms in dark orange.

LCMO was first synthesized and characterized by Eli et al. in 1998 [326] with different amounts of copper as a substitute for Mn ($LiCu_xMn_{2-x}O_4$ with $(0 < x < 0.5)$. As noted by Molenda et al. [327], the introduction of copper into the structure leads to an increase in electrical conductivity compared to the undoped spinel $LiMn_2O_4$; in particular with $x = 0.4$, the conductivity value was found to be increased by two orders of magnitude as Cu can participate in the electronic transport process. Moreover, Meng et al. [328] investigated how the substitution of Mn with different metallic ions (Cu, Ni, Cr, Fe, Ti) in the octahedral sites affects the diffusion activation barrier of Li ions. The results showed that this barrier remained essentially unchanged in the case of Ni and Fe, while it was significantly lowered by the presence of Cu.
From an electrochemical point of view, the samples synthesized by Eli exhibited a gradual decrease in overall capacity as the copper content increased (from about 119 mAh g^{-1} for x = 0.1 to about 71 mAh g^{-1} for $x = 0.5$). Specifically, observing the charge and discharge profiles of the various samples, Eli and his collaborators found that, as the content of Cu^{2+} increased, the capacity associated with the

plateau between 3.3 and 4.5 V (characteristic of $LiMn_2O_4$ and associated with the $Mn^{3+/4+}$ redox reaction) decreased, with the simultaneous appearance of an additional plateau around 4.9 V, which was instead attributed to the oxidation of $Cu^{2+/3+}$. The electrochemical behavior exhibited by the samples was thus consistent with their stoichiometry, since a greater quantity of copper resulted in a lower percentage of Mn^{3+} capable of reacting in the lower potential region.
The cation exchange between Cu and Mn in the octahedral sites also impacts the electrochemical performance.
In fact, a material with the composition $Li_{1.01}Cu_{0.32}Mn_{1.67}O_4$, rewritten in the typical notation of spinel materials as $(Li_{0.9}Cu_{0.1})_{8a}[Mn_{1.67}Cu_{0.22}Li_{0.11}]_{16d}O_4$, has a theoretical capacity of about 95 mAh g^{-1}, corresponding to the extraction of 0.65 moles of Li^+ and the complete oxidation of 0.33 mole fraction of Mn^{3+} to Mn^{4+} (in fact, the average oxidation number of Mn in this composition would be 3.8) and 0.32 mole fraction of Cu^{2+} to Cu^{3+}. A cathode with this capacity and an average discharge potential of about 4.4 V would therefore have a specific energy of about 350 Wh·Kg^{-1}.

7.2 Overlithiation of materials with spinel structure

It is well known that the spinel materials like $LiMn_2O_4$ and $LiNi_{0.5}Mn_{1.5}O_4$ can be electrochemically or chemically lithiated/delithiated in the compositional range $Li_xMn_2O_4$ $0 < x < 2.5$ in the potential window from 5 to 1.5V. In particular, for the overlithiated LNMO of formula $Li_2Ni_{0.5}Mn_{1.5}O_4$ the average oxidation state of Mn is 3.3^+, with Mn^{4+} ions still available until the composition $Li_{2.5}Ni_{0.5}Mn_{1.5}O_4$ is not reached. This further lithiation step, which occurs between 1.9 and 1.5V corresponds to approximately 75 mAh g^{-1}. Consequently, by extending the overall potential range between 5 and 1.5V, the LNMO is able to provide a notable energy density of approximately 1190 Wh kg^{-1}. [329]
Figure 7.2 shows a galvanostatic discharge curve of a cathode based on $LiNi_{0.5}Mn_{1.5}O_4$ chemistry. When this material is brought below 3V (i.e. when the number of moles of lithium exceeds 1), the Li^+ ions are arranged in the unoccupied octahedral sites 16*c* of the cubic structure, with a consequent reduction of the Mn^{4+} ions to Mn^{3+}. However, this further insertion of ions involves a structural modification of the cubic

material, which converts into a tetragonal spinel structure which is formed by vertex sharing between MnO_6 octahedrons and LiO_6 octahedrons, and face sharing between LiO_4 tetrahedrons and MnO_6 octahedrons, as shown on the right side of Figure 7.2. The transformation from a cubic to a tetragonal crystal structure leads to a 16% increase in the *c/a* ratio and a 6.5% expansion in unit-cell volume. This modification of the crystal structure is identified as the Jahn–Teller effect which is ascribed to the interactions or electrostatic repulsion among the non-bonding electrons in the *p* orbitals of the coordinating oxygen anions and the electrons in the *d* orbitals of the metal (M = Mn, Ni, Cu) cation at the center of the oxygen octahedrons. [330]

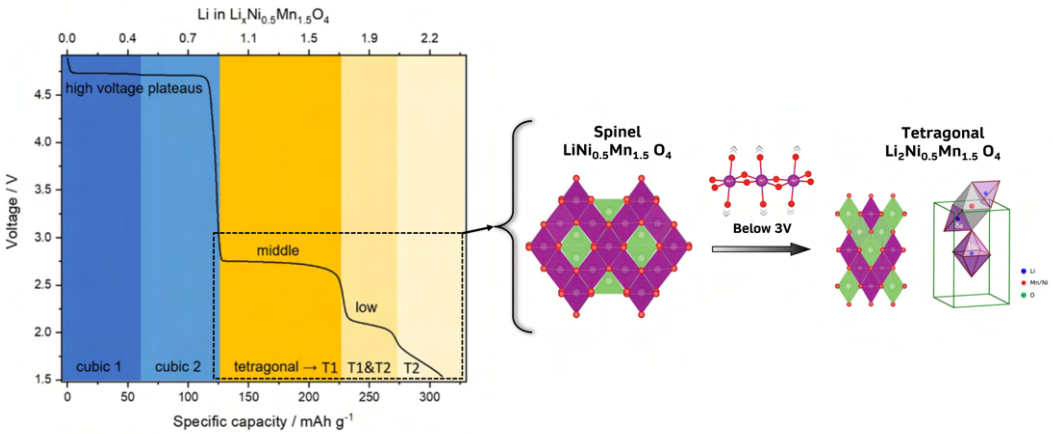

Fig. 7.2 On the left is a characteristic discharge curve of an LNMO in the potential range between 5 and 1.5V, on the right the structural changes of the spinel structure due to the Jahn-Teller distortion which occurs below 3V. Partially modified from [329]

The additional potential plateau at around 2.1 V during electrochemical lithiation is observed above 1.6 lithium per formula unit and has been reported for both ordered and disordered LNMO. However, manganese spinel (without Ni) does not show a similar behaviour, exhibiting a single plateau at around 2.8 V. Consequently, this peculiarity characterising LNMO has been the subject of various studies. [331] For example, Lee et al. [332] attributed the splitting of the plateau at 2.8 V to the formation of two different tetragonal phases (T1 and T2) and justified the overvoltage required to generate the T2 phase by a more difficult insertion of Li^+ ions into the octahedral sites 16*c*. Furthermore, according to this study, the occurrence of this second plateau appeared to be closely related to the degree of cationic ordering of the material, with the T2 phase (and hence the plateau at 2.1 V) predominating in

the case of a disordered spinel structure. More recently, Jobst et al. [329] applied different electrochemical techniques (GITT, EIS) to investigate this phenomenon, concluding that the plateau at 2.1 V is due to a different chemical composition between the core (poor in lithium) and the shell (rich in lithium) of the particles. These regions with different potentials (2.8 V and 1.51) react with each other at the interface and recombine, resulting in a region with a mixed potential of around 2.13 V.

In general, the utilisation of the low potential region of spinel materials is very attractive due to the associated higher specific energy, but difficult due to the strong structural changes that the material undergoes and which lead to a rapid drop in the capacity of the cell. However, it has been shown [324] [333] that the overliation ($x > 1$ $Li_xM_{0.5}Mn_{1.5}O_4$) of these materials can be very useful to compensate the irreversible capacity loss that occurs in the formation of full cells where graphite or graphite/silicon-based anodes require an additional amount of lithium to generate the SEI.

Therefore, in this section of the document, for the first time, we explored the possibility for chemically overlithiating the LCMO spinel material, examining its chemical and electrochemical behaviors in both half-cell and full-cell configurations.

7.3 Synthesis of $LiCu_{0.4}Mn_{1.6}O_4$ and overlithiated LCMO

The synthesis of the $LiCu_{0.4}Mn_{1.6}O_4$ and the lithium-rich material was carried out according to the scheme shown in Figure 7.3. This type of approach proves to be quite simple and can possibly be implemented on a larger scale. The starting materials, Li_2CO_3, $MnCO_3$, CuO and LiI were purchased from Sigma Aldrich without further modification. Typically, these precursors were mixed in stoichiometric ratios (with 5% excess Li_2CO_3 to compensate for loss during the calcination phase) in cyclohexane for a total time of 8 hours using a planetary mill (PM100, Retsh), which utilises Coriolis and centrifugal forces to rapidly accelerate the grinding balls and generate significant comminution forces. The result of this grinding process was a very homogeneous brownish slurry, which was dried in an oven at 60°C. In the next step, the dried powder was fired in air in a muffle in two successive stages, once at 600°C for 6 hours, followed by a further 6 hours at 900°C, at the end of which the

oven was allowed to cool naturally. The powders were then gradually sieved using the finest 50 μm mesh. At this point, the synthesis of the material referred to as $LiCu_{0.4}Mn_{1.6}O_4$ (LCMO) was complete. In order to obtain the lithium-rich spinel material, an additional step was necessary in which LCMO was mixed with LiI in a weight ratio of 1:3 in an agate mortar. The powder mixture was then placed in a quartz crucible in a Buchi B-585 sublimation oven. There, the temperature was raised to 200°C under vacuum for 2 hours, causing the LiI to decompose into Li and gaseous I_2, which was then condensed on a cooling finger present in the furnace. The synthesis is carried out according to the reaction:

$$LiCu_{0.4}Mn_{1.6}O_4 + LiI \rightarrow Li_2Cu_{0.4}Mn_{1.6}O_4 + 0.5I_{2(g)} \tag{7.3.1}$$

However, this equation assumes that all the lithium from the thermal decomposition of LiI can diffuse into the spinel material, without taking into account possible secondary reactions that the lithium could undergo (formation of LiOH and Li_2O reacting with moisture/oxygen), as well as possible loss of material during the sublimation process. At the end of the thermal process, the final product was washed several times with absolute ethanol, centrifuged and dried at 70°C under vacuum.

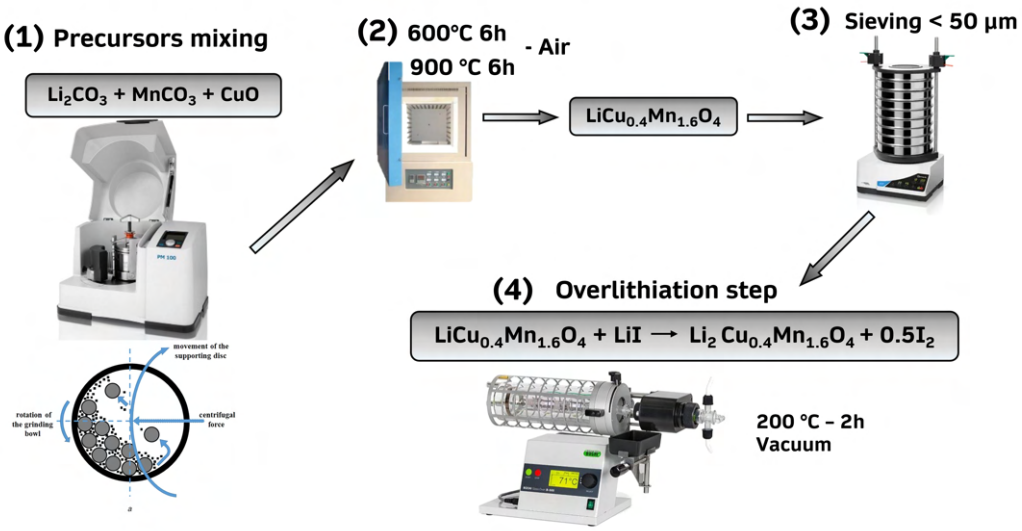

Fig. 7.3 Scheme of the synthesis procedure that was used to produce the $LiCu_{0.4}Mn_{1.6}O_4$ and the lithium rich spinel material.

7.4 Physical-chemical characterization of LCMO and overlithiated LRCMO

The physical-chemical methods used to characterize the two materials are reported in Appendix B.4. For simplicity, from this point forward, the samples will be referred to as LCMO for the pristine material of composition $LiCu_{0.4}Mn_{1.6}O_4$ and LRCMO for the material that underwent the chemical overlithiation process.
Figure 7.4 displays the outcomes of the ICP-OES analyses and particle size distribution for the two samples. Notably, the ICP results (Figure 7.4 a) corroborate the theoretical composition of the pristine material, specifically $Li_{0.99}Cu_{0.39}Mn_{1.61}O_4$. It is intriguing to observe that the sample subjected to chemical overlithiation exhibited a significant additional lithium content (approximately 0.85 mol), confirming the effectiveness of the LiI treatment. The ICP-OES results are briefly summarized in Table 7.1.

Table 7.1 Values of the concentration of the elements in LCMO and LRCMO samples from ICP and the correspective compositions.

Sample	**Element wt%**			**Calculated composition**
	Cu	**Mn**	**Li**	
LCMO	12.4 ± 0.1	45.8 ± 0.7	3.63 ± 0.07	$Li_{1.0}Cu_{0.38}Mn_{1.61}O_4$
LRCMO	12.5 ± 0.1	45.4 ± 0.6	6.39 ± 0.07	$Li_{1.76}Cu_{0.38}Mn_{1.6}O_4$

The granulometric analysis was conducted on both the untreated powders and after they had undergone one minute of ultrasonication in an ethanol-based suspension. As can be seen in Figure 7.4 (b), the LCMO sample overall presents three "families" of particles in terms of size, with a strong prevalence of particles around 5 μm, followed by a certain quantity of particles around 20 μm, and a small portion of nanoparticles. The effect of the ultrasonication step seems to be more effective on the latter, as the fraction of nanoparticles increases, while the rest of the distribution undergoes less marked changes. The LRCMO sample, on the other hand, is characterized by two main families of particles, with the more numerous and quantitatively significant around 4 μm, and the second, less defined around 200 nm. Also in this

case, ultrasonication (dark blue histogram in Figure 7.4 c) succeeded in breaking up larger particle agglomerates to significantly increase the fraction of nanoparticles present in the suspension.

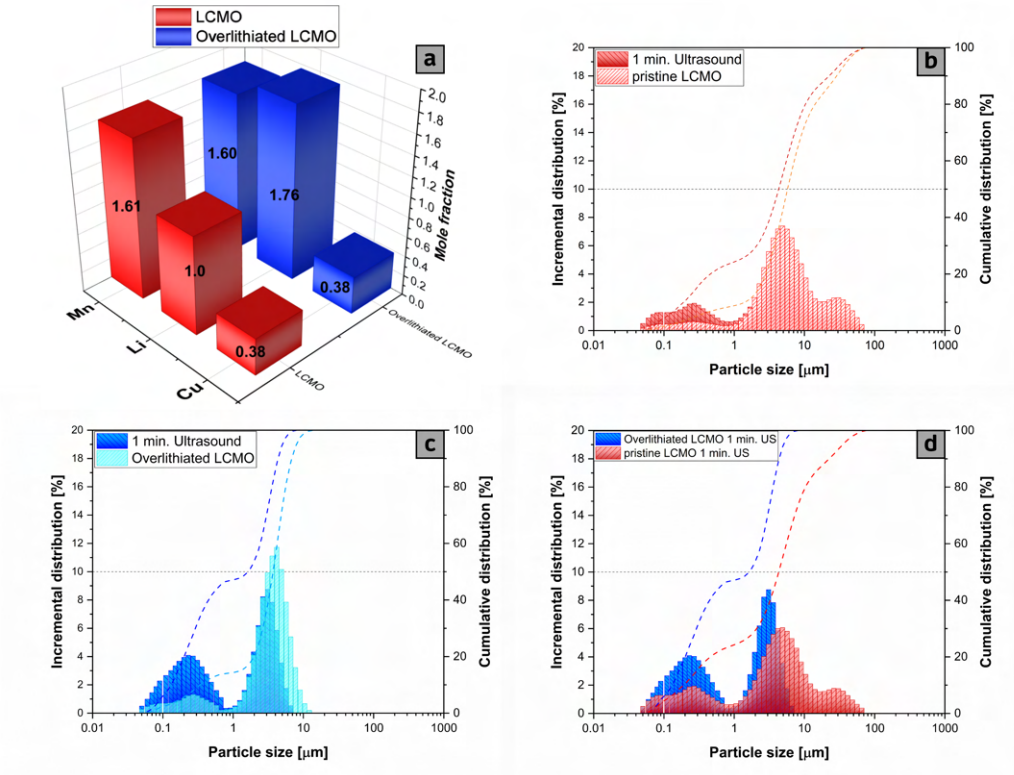

Fig. 7.4 (a) ICP-OES results for the LCMO and LRCMO (b) particle size distribution of the LCMO after sieving before and after 1 minute of ultrasonication (c) particle size distribution of LRCMO before and after 1 minute of ultrasonication (d) comparison of particle size distribution of the pristine LCMO and the LRCMO.

The comparison between the two sample distributions, depicted in Figure 7.4 (d), shows that the LRCMO generally exhibits smaller-sized particles and more narrowly distributed, highlighting how the overlithiation step evidently has an effect on this property of the material.
Figure 7.5 displays the results of the SEM analysis for the LCMO sample, which exhibits the typical spinel material morphology with predominantly octahedral particles and medium sizes consistent with the outcomes of the particle size analysis.

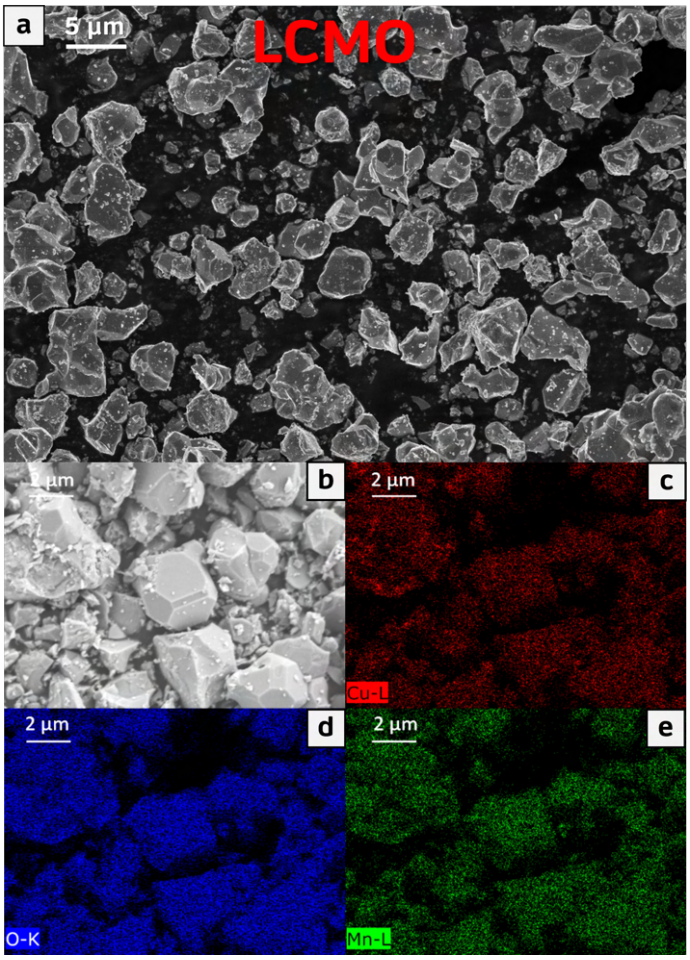

Fig. 7.5 (a) SEM micrograph of the LCMO sample, (b) area of the LCMO sample where the EDS mapping of Cu, O and Mn where performed, which are reported in panels (c), (d) and (e), respectively.

The EDS mappings carried out on the sample area shown in Figure 7.5 (b) demonstrate how the elements Cu, Mn, and O are homogeneously distributed throughout the particles of the LCMO, without areas of heightened concentration of any particular element.

Figure 7.6 presents the SEM analysis of the LRCMO sample, with corresponding EDS mappings in panels b, c, d, and e. Morphologically, there are no significant deviations from the pristine LCMO sample; however, clear fractures on the particle surfaces are noticeable.

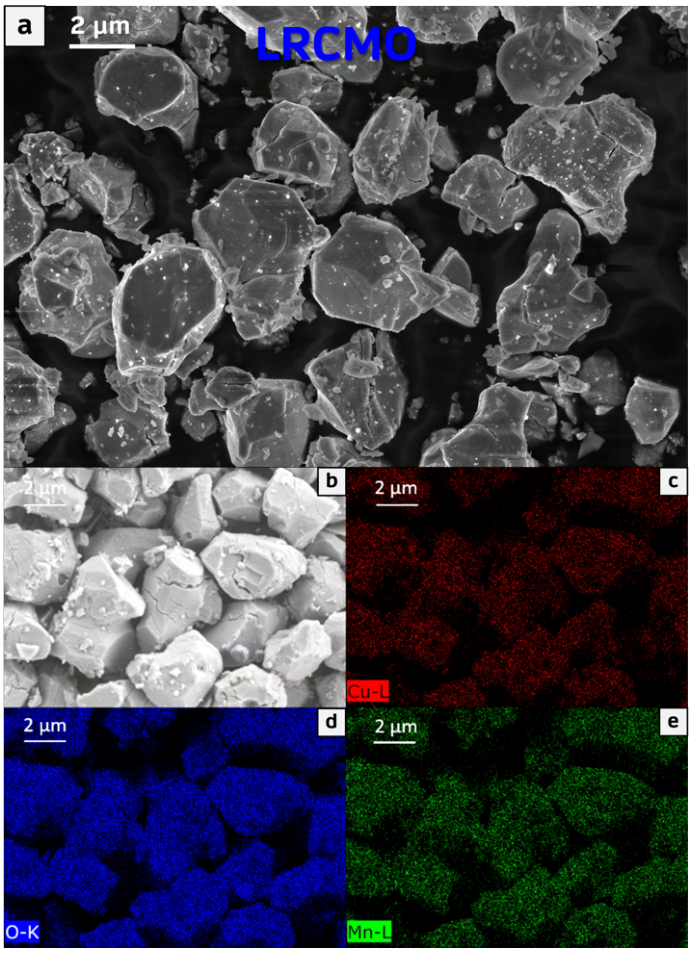

Fig. 7.6 (a) SEM micrograph of the LRCMO sample, (b) area of the LRCMO sample where the EDS mapping of Cu, O and Mn where performed, which are reported in panels (c), (d) and (e), respectively. Particle cracking is visible on the surface of the sample due to the additional insertion of Li ions.

These fractures are likely due to the mechanical stresses induced by the insertion of additional Li ions, resulting in a phase transition from cubic to tetragonal, which involves a significant volume change, as previously discussed in earlier sections. This phenomenon of particle cracking has also been noted in other studies where chemical overlithiation was achieved through a different method on the material $LiNi_{0.5}Mn_{1.5}O_4$. [334] [333]

Finally, X-ray diffraction was performed to identify the present phases and determine their structural properties. The XRD spectrum of the pristine LCMO sample, shown in the Figure 7.7, was analyzed following the Rietveld refinement procedure. Notably, the fitting of the diffractogram faithfully follows the experimental data

without evident discontinuities between the two (blue line at the bottom in the Figure 7.7). The quality of the refinement is assessed by the R_{wp} and χ^2 parameters, whose values are reported in Table 7.2 and are considered acceptable, although not optimal (a perfect fit would result in unitary values). Moreover, the XRD analysis also uncovered the presence of a second phase besides the cubic spinel one, which had not been identified in previous EDS analyses. The goodness of the fitting significantly improved by incorporating a monoclinic phase with the C2/m space group into the refinement, identified as Li_2MnO_3.

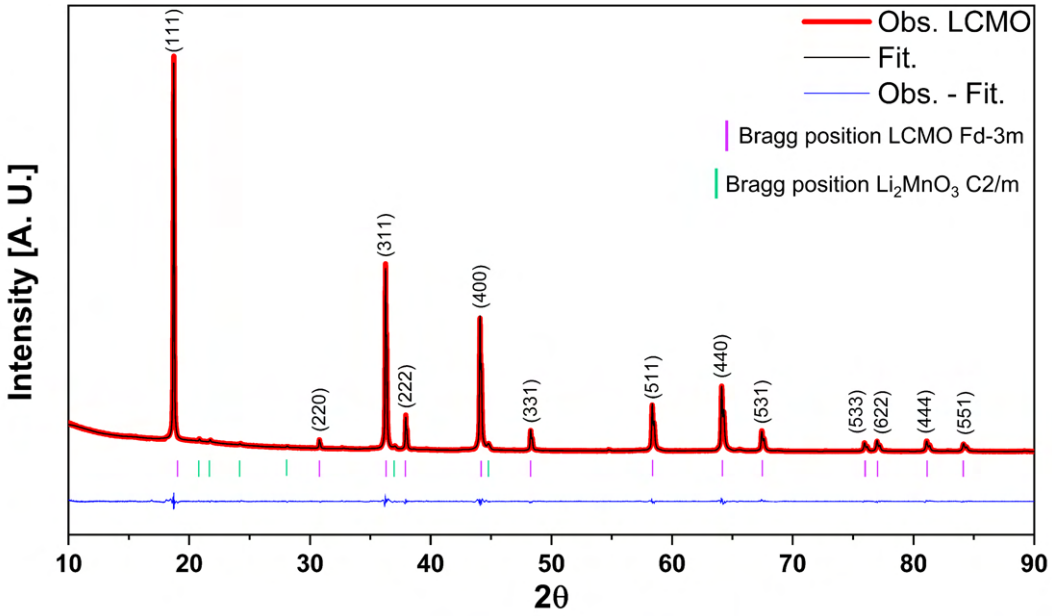

Fig. 7.7 Diffractogram of the LCMO sample with the experimental data in red, the profile used for fitting in black, and the difference between the two in blue. The measurement was carried out between 2θ values ranging from 10-110 with a step size of 0.0039°, collecting about $25{\cdot}10^3$ points.

The analysis results showed that the weight percentage of this impurity was approximately $4.85\%_{wt}$, with the remaining $95.15\%_{wt}$ consisting of the cubic phase $LiCu_{0.38}Mn_{1.61}O_4$. Another aspect highlighted by the refinement is the presence of a certain quantity of oxygen vacancies, a fact that aligns with the high temperatures used in the calcination step of the solid state reaction. Taking this into account, the composition of the material turns out to be $LiCu_{0.38}Mn_{1.61}O_{3.96}$. Since the synthesis process of LRCMO was carried out under vacuum, it was assumed that these O

vacancies are also retained in the Li-rich material. The parameters extracted from the refinement of the structure for the cubic phase of the LCMO sample are listed in Table 7.2. Notably, substituting Li atoms with Cu in the tetrahedral 8*a* sites significantly improved the fitting, especially in describing the intensity of the (220) peak. Therefore, it was assumed that the Li atoms displaced from the 8*a* sites could partially occupy the octahedral 16*d* sites.
Additionally, as reported in the literature by Ohzuku [335] and Yang et al. [336], the ratio of the integrated intensity of the peaks (400)/(311) is inversely proportional to the occupancy of the substituting metal ion in the 8*a* tetrahedral sites. For the LCMO sample, this ratio is about 0.813, a value that confirms the significant exchange between Cu and Li atoms in the 8*a* and 16*d* sites.

Table 7.2 List of crystallographic parameters extracted from the Rietveld refinement of the LCMO sample, which is found to consist of two phases, a cubic Fd-3*m* and a monoclinic C2/*m*, present at 95.15%$_{wt}$ and 4.85%$_{wt}$ respectively.

Crystal parameter	**Phase** $LiCu_{0.38}Mn_{1.61}O_4$	**Atom**	**Wyckoff notation**	**x**	**y**	**z**	**Site occupancy**
Crystal system	Cubic	Li (1)	8*a*	0.125	0.125	0.125	0.86(8)
Space group	Fd-3*m*	Cu (1)	8*a*	0.125	0.125	0.125	0.13(2)
a [Å]	8.208	Mn	16*d*	0.5	0.5	0.5	0.81
α	90	Cu (2)	16*d*	0.5	0.5	0.5	0.12(4)
Cell vol. [Å^3]	553.04	Li (2)	16*d*	0.5	0.5	0.5	0.065
2θ range	10-110	O	32*e*	0.265	0.265	0.265	0.98(9)
R_{wp}	7.23						
R_e	3.30						
χ^2	4.88						

The average size of the crystalline domains of the sample was then evaluated using the Scherrer equation:

$$D = \frac{K\lambda}{\beta \, cos\theta} \tag{7.4.1}$$

Where D is the mean size of the ordered (crystalline) domains, K is a dimensionless shape factor that has a typical value of about 0.9, which was assumed in this case. λ is the X-ray wavelenght and β is the line broadening at half the maximum intensity (FWHM), in radians while θ is the Bragg angle in radians.
Applying this equation to the LCMO sample and with the FWHM parameters extracted from the fitting, the average size of the crystallites is found to be about 90 nm, a value that is in line with those reported in the literature for materials with a spinel structure like LNMO. [336, 337]
The XRD analysis of the LRCMO sample is shown in Figure 7.8. Since the lithium-rich material is sensitive to air, the sample was prepared in a glove box, and its surface was protected with a Kapton film. As a result, a signal due to Kapton film could be detected at small 2θ angles (0–28°) in the diffraction patterns of the powders, which was then subtracted as part of the background. However, the quality of the experimental signal was not sufficient to conduct a refinement with values considered acceptable.
As can be seen, the diffractogram of LRCMO differs significantly from the typically cubic one of pristine LCMO. In particular, the addition of lithium leads to a structural change, made evident by the fact that the peaks exhibited by LRCMO are characteristic of a tetragonal structure with space group $I4_1/amd$ (identified by a light blue cross in Figure 7.8).

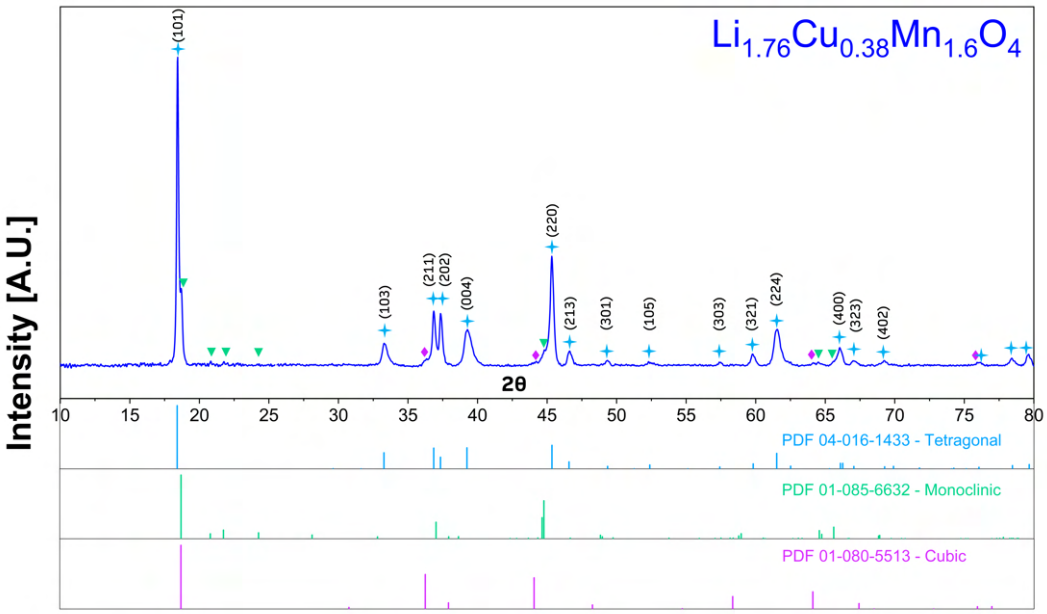

Fig. 7.8 Diffractogram of the LRCMO sample with chemical composition $Li_{1.76}Cu_{0.38}Mn_{1.6}O_4$. The material exhibits a complex structure with the coexistence of three different phases, with the tetragonal phase being largely predominant over the monoclinic and cubic ones. At the bottom, the characteristic peaks of the three phases and their corresponding Powder Diffraction Files are shown.

However, the spectrum still shows a small part of the signal coming from both the Li_2MnO_3 impurity and the original cubic structure, identified respectively by a green triangle and a purple diamond. These structural findings align with the literature on the overlithiation of spinel materials such as LNMO [338, 339], yet they have not been documented for a material with this specific chemical composition.

7.5 Electrochemical characterization of LCMO and overlithiated LRCMO

From the electrochemical perspective, the two materials were first tested in a half-cell configuration and subsequently in a full-cell configuration. Figure 7.9 shows the results of the first galvanostatic cycling test conducted against metallic lithium at a current of 0.1C in the extended potential range of 5.1 - 1.6 V vs Li/Li^+ . This test

was conducted to verify the possible influence of the chemical overlithiation process on the electrodes performance compared to the electrochemical one. In particular, by observing the profile of the first cycle of the two samples, reported in Figure 7.9 (a), it can be seen how LRCMO exhibits, during charging, two additional plateaus between 3 and 3.9 V compared to LCMO, with an associated capacity of about 115 $mAhg^{-1}$, which corresponds to the amount of Li inserted into the material during the chemical overlithiation process. The capacity provided by the two samples in the range between 3.9 and 5.1 V, however, is very similar and corresponds to the extraction of about 0.65 mol of Li, so that in both materials, there are still about 0.35 mol of unextracted Li at the end of the charging processes. In the discharge phase, the profiles are more similar to each other, however, a significant difference can be observed in the low voltage region (< 3V) which will be discussed later.
Furthermore, from the comparison of the charge/discharge capacities exhibited by the two samples, it can be observed how they are able to deliver practically the same capacity in the initial phase of the cycling, while as the cycles proceed, LRCMO exhibits a greater capacity retention, as also reported in the first lines of Table 7.3. This difference can be explained by observing the charge/discharge profiles and the coulombic efficiency values reported in Figure 7.9 (c), (d), and (e) respectively.

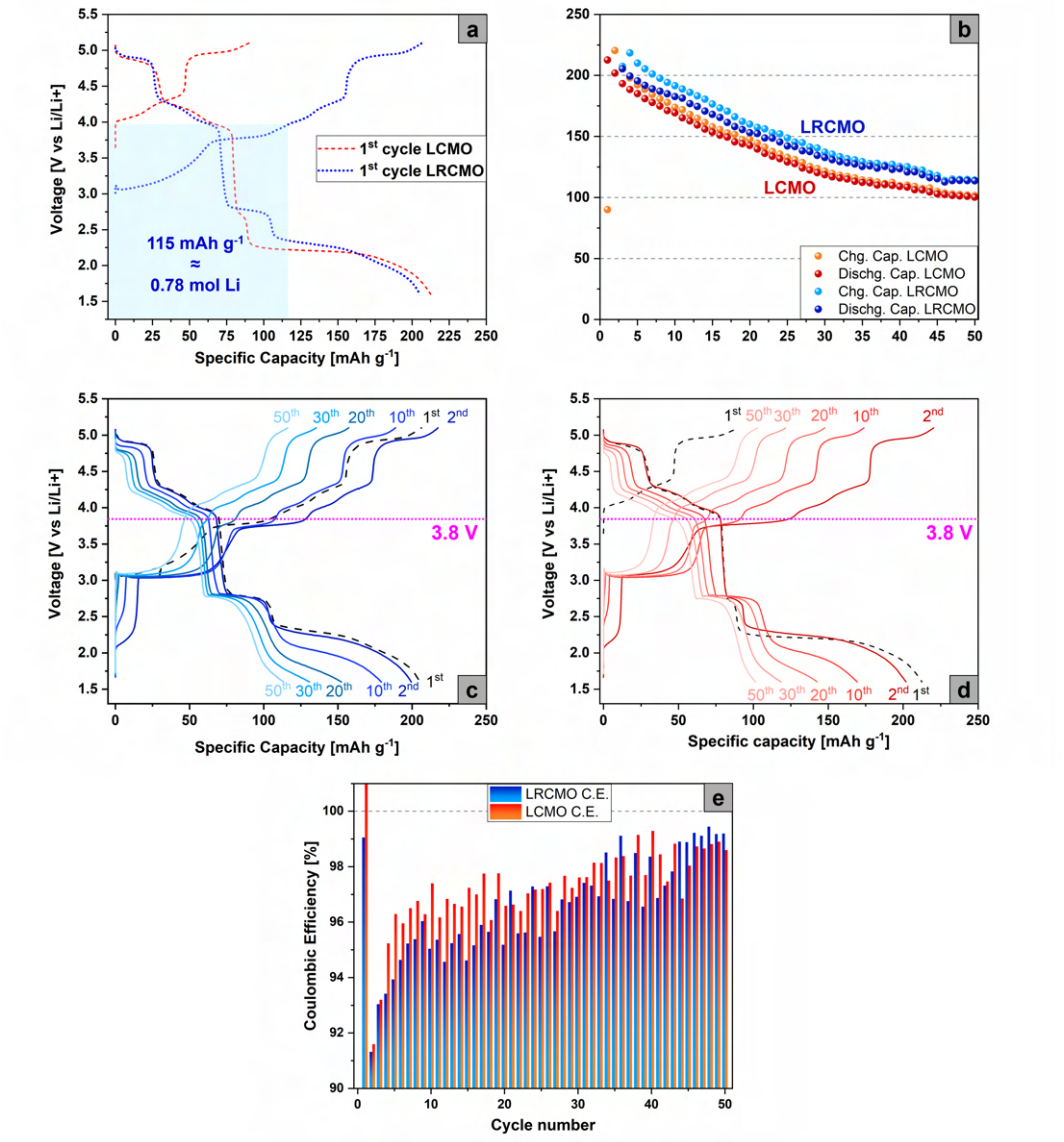

Fig. 7.9 (a) Charge/discharge profiles of the first cycle of LCMO and LRCMO based cathodes at current rate of C/10, (b) Specific capacity (charge and discharge) vs cycle number of the two samples, (c) Charge/discharge profile of the LRCMO at C/10, (d) Charge/discharge profile of the LCMO at C/10, (e) comparison of the coulombic efficiency over the cycle number for the two samples. The test was carried out with half-cell configuration.

In particular, it can be noted, as highlighted by the partial charge/discharge values in Table 7.3 and by their ratio in Table 7.4, that at the beginning of the cycling LCMO is able to deliver more capacity in the range 3.8 - 5.1 V and more efficiently (C.E.

of 82.6% vs 77.5%), a fact that is also reflected on the overall C.E., which turns out to be consistently higher for LCMO until about halfway through the cycling. However, as the cycles progress, the capacities and the C.E. of the two samples in this potential range align to the same values, with LRCMO even surpassing LCMO at the end of cycling. Moreover, when also considering the low voltage region (1.6 - 3.8V), it can be seen how LRCMO is able to provide more capacity from the initial phases and with D/C values (Table 7.4) much closer to the ideal (100%). Indeed, the data in Table 7.4 for this voltage region highlight how the insertion of Li is significantly easier compared to their extraction from the material, a fact that seems to be particularly true for LCMO.

Table 7.3 The table lists the charge and discharge capacity values for the LCMO and LRCMO samples during cycling at C/10 in the two potential ranges of interest (1.6 - 3.8V) and (3.8 - 5.1V) for the 2^{nd}, 25^{th} and 50^{th} cycles.

Electrochemical data	**Unit**	**Potential range**	**Cycle**	**Sample**	
				LCMO	**LRCMO**
Disch. cap. retention (vs 2^{nd})	[%]		25^{th}	63.9	71.3
Disch. cap. retention (vs 2^{nd})			50^{th}	49.6	56.9
Discharge Cap.	[mAh g^{-1}]	5.1 - 3.9 V	2^{nd}	78.2	67.9
Discharge Cap.		3.8 - 1.6 V		123.6	131.5
Charge Cap.		1.6 - 3.8 V		124.7	130.2
Charge Cap.		3.9 - 5.1 V		94.7	87.6
Discharge Cap.	[mAh g^{-1}]	5.1 - 3.9 V	25^{th}	56.7	55.2
Discharge Cap.		3.8 - 1.6 V		72.2	86.5
Charge Cap.		1.6 - 3.9 V		56.3	71.33
Charge Cap.		3.8 - 5.1 V		76.4	74.2
Discharge Cap.	[mAh g^{-1}]	5.1 - 3.9 V	50^{th}	45.7	48.7
Discharge Cap.		3.8 - 1.6 V		55.41	65.2
Charge Cap.		1.6 - 3.8 V		33.8	45.1
Charge Cap.		3.8 - 5.1 V		68.5	69.8

However, it is necessary to point out the significant loss of capacity exhibited by both samples at the end of cycling, with poor capacity retention values (49.6% and 56.9% for LCMO and LRCMO, respectively). Indeed, observing the charge/discharge curves, it becomes clear that in the region below 2.5V, the electrochemical processes are only partially reversible, with a clear and progressive reduction of the plateau at 2.2-2.1V. Moreover, the D/C ratio values reported in Table 7.4 for the region below 3.8V indicate a strong irreversibility of the processes and are likely made possible only by the presence of metallic lithium as an anode, which can act as a semi-infinite source of Li^+ ions.

Table 7.4 Discharge to charge capacity ratio (de facto, C.E.) of LCMO and LRCMO samples in the two potential ranges of interest (1.6 - 3.8V) and (3.8 - 5.1V) for the selected cycles during the test conducted at C/10.

Cycle	**Voltage range**	**Ratio D/C Capacity [%]**	
		LCMO	**LRCMO**
2^{nd}	5.1 - 3.8	82.6	77.5
	3.8 - 1.6	99.1	100
25^{th}	5.1 - 3.8	74.1	74.4
	3.8 - 1.6	128.4	121.1
50^{th}	5.1 - 3.8	66.7	69.8
	3.8 - 1.6	163.8	144.5

The analysis of the charge/discharge curves is facilitated by the use of differential dQ/dV curves shown in Figure 7.10 (a) and (b). Assuming a discharge process starting from 5.1V, a peak at about 4.9 V is encountered associated with the reduction of $Cu^{3+/2+}$, with Li^+ insertion into the tetrahedral 8*a* sites; moving forward, there is a double feature with peaks located at about 4.24 and 3.96 V, which are attributed to a two-step insertion of lithium into the tetrahedral 8*a* sites [237], resulting in the reduction of $Mn^{4+/3+}$. Below 3V, the insertion of Li^+ into the octahedral 16*c* sites begins, with a first peak at about 2.7V and a second at 2.2-2.1V, resulting in a distortion of the crystal lattice to a tetragonal structure. In this region, the two materials show differences, in fact, LCMO exhibits a peak at 2.7V much less marked compared to LRCMO from the first cycle up to about the 20^{th}, where the difference

levels off. The percentage of the capacity below 3.8V represented by these two peaks (plateau in Figure 7.9) is reported in Figure 7.10 (c) and (d). The reason for the presence of these two peaks/plateaus will be discussed with the GITT results, however, it appears clear that the prior chemical insertion of Li^+ ions makes this process easier in the initial phases of cycling, since a higher overpotential is required for LCMO to continue inserting Li^+ into the 16*c* sites. However, just as the plateau at 2.2 V exhibited a contraction over cycling, so does the corresponding peak in its intensity in the dQ/dV plot, confirming the only partial reversibility of the process.
Moving to the charging step, a small and poorly defined peak at about 2.1V is noted in both samples during the first cycle, while in subsequent ones it is no longer present. At 3V, a very intense peak can be seen which corresponds to the transition from tetragonal to cubic phase; both peaks are due to the extraction of Li^+ ions from the 16*c* sites. In particular, it can be observed how the peak at 3V turned out to be more intense and stable for LRCMO, showing that the process takes place more easily in the Li-rich material than in the pristine LCMO. These results are consistent with the higher capacity and C.E. values previously highlighted in the low voltage region for LRCMO, underscoring how chemical overlithiation proves to be beneficial for the material to adapt to the strong structural changes that it undergoes in this potential range.
Proceeding with the charging process, a peak is observed at about 3.8V, whose nature is not yet fully explained in the literature. However, Lee et al. [332] attributed this peak in LNMO to the completion of the transition from tetragonal to cubic. Finally, in the region above 3.8 V, the processes appear completely reversible, with the de-insertion of Li^+ from the tetrahedral 8*a* sites, resulting in the oxidation of $Mn^{3+/4+}$ around 4V (double peak) and of $Cu^{2+/3+}$ at about 4.95V.

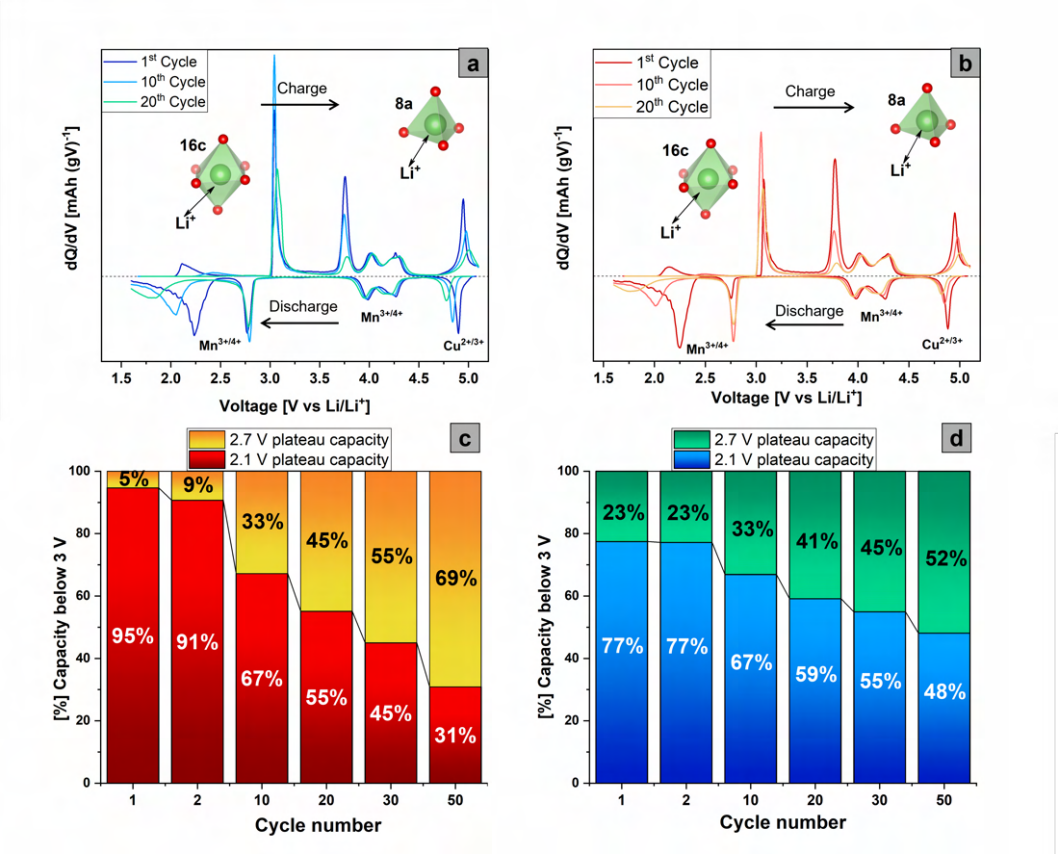

Fig. 7.10 dQ/dV plot derived from the charge/discharge curves performed at C/10 for (a) LCMO and (b) LRCMO, while in panels (c) and (d), the capacity percentages are presented, corresponding to the capacity attributed to the two plateaus at 2.7 and 2.1V compared to the total capacity exhibited by the two cathodes below 3.8V.

In order to have a clear idea of the structural changes that the material undergoes in a cycle within the extended potential range (1.6-5.1 V), *ex-situ* XRD measurements were performed on various LCMO cathodes (so the overlithiation is only electrochemical in this case) obtained by disassembling the cells in an Ar-filled glove box. The cathodes were then washed with DEC and protected with a Kapton film on the sample holder. The potentials at which the cells were stopped were selected based on points of interest in the respective charge-discharge curves. The obtained diffractograms are shown in Figure 7.11 (a), with the respective rhombohedral markers of different color representing the points of the equilibrium curve where the cell was stopped and disassembled. All the tested cathodes underwent an initial formation cycle and were disassembled during the second one

To better understand how the spectra vary with the state of charge of the cell, Figure

7.11 (b) reports the evolution of two diffraction peaks $(311)_c$ and $(400)_c$ (subscripts C and T indicate the cubic and tetragonal phases, respectively) in the range 2θ = 32-47°. Starting from the discharge process, the peaks of the cubic phase gradually shift towards lower 2θ values, without significant changes in the spectra up to 2.6 V. However, already in the spectrum at 2.6 V (orange one), the presence of the peak $(220)_t$ can be visibly noted, indicating that the transformation may begin just below 3 V. Bringing the spinel material below 2.5 V (red spectra collected at 2.05 V) makes the transformation from cubic to tetragonal more evident, with the $(311)_c$ peak being split into the $(103)_t$ and $(211)_t$ and the $(400)_c$ into the $(220)_t$. [237]

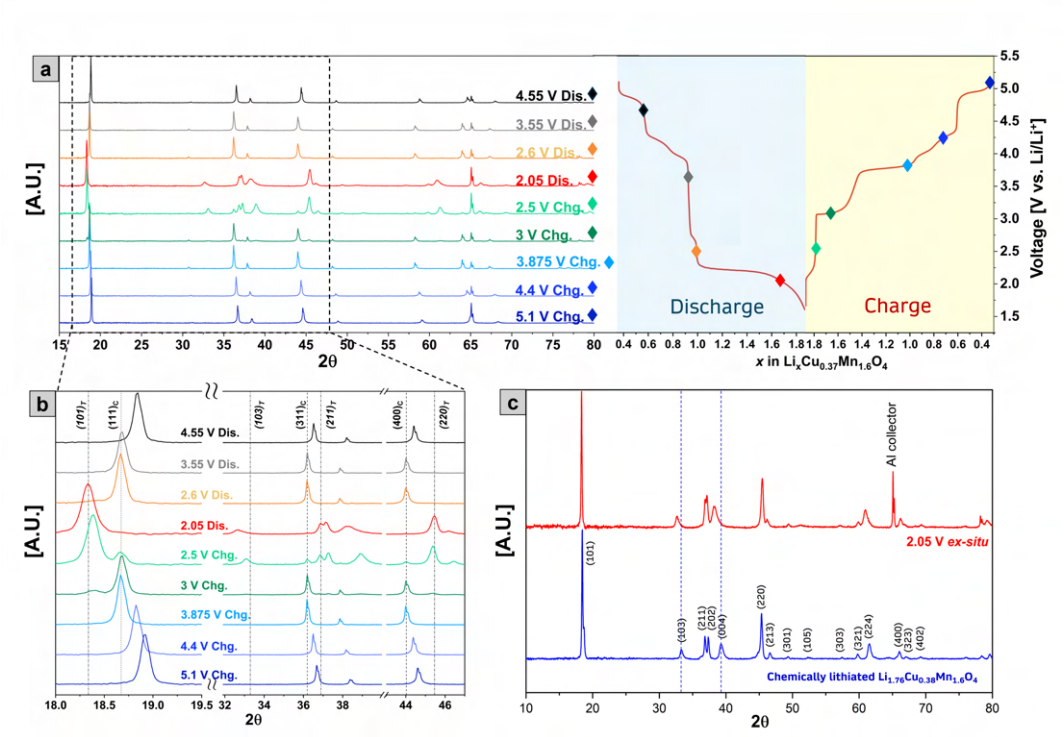

Fig. 7.11 In panel (a) are reported the *ex-situ* spectra of the cathodes that had been stopped at the desired potentials, which are identified on the charge/discharge curve in the right part of the figure by the coloured markers, and disassembled to get the XRD data (b) enlargement of the XRD spectra in the 2θ = 32-47° range (c) comparison of the XRD spectra of the cathode stopped at 2.05V x = 1.7 and the LRCMO obtained with chemical overlithiation with x = 1.76

Moving on to the charging process, it is interesting to note how the structure changes in the initial phases: in particular, it can be seen how at 2.5 V the tetragonal phase is still largely prevalent, with the cubic phase beginning to form and becoming

dominant already at 3 V. As can be seen, the disappearance of the tetragonal phase occurs between the spectra collected ath 3 and 3.875 V, thereby strengthening the hypothesis that the peak observed in the dQ/dV at 3.8 V could indeed be attributed to this phase transition in the material. In the final stages of the charging process, the peaks shift towards higher values of 2θ as the charge proceeds, a fact that is reported to be accompanied by a decrease in the lattice parameter and therefore a shrinkage of the crystal lattice. [340, 341]

For spinel-type materials, the evolution of the structure between 3-5 V during the charging phase is generally described in terms of the lithium mole content x. In particular, in the very early stages ($1 < x < 0.95$), the system displays characteristics of a solid solution (phase P1), then undergoes a first-order transition and moves to a system where first two and then subsequently three different cubic phases coexist (P1+P2+P3) in the range $0.71 < x < 0.25$. In this range, there is always one phase in clear minority compared to the other two (P3 and P1 at the beginning and end of charging, respectively). Below $x = 0.25$, the system returns to being biphasic (P2+P3) and ends the charge in a new solid solution for $x < 0.1$. [341] In the case of LCMO, and based on the *ex-situ* data collected here, it is not possible to propose an accurate model for the evolution of the material's structure (in-operando XRD could provide adequate sampling and resolution as SOC varies). However, the variation in the position of the $(311)_c$ peak is similar to that reported by Zhu [336] et al., making it plausible to hypothesize that LCMO also undergoes a first-order transition to a system that is first biphasic and then triphasic. It should be noted, however, that at the end of the charging step in LCMO, there are still 0.35 moles of Li, so the formation of the third phase (which should be virtually "lithium-free") could be strongly limited by this factor.

Finally, Figure 7.11 (c) shows the comparison between the XRD spectrum of the LRCMO obtained through chemical overlithiation with LiI (blue spectrum) and that of the electrode stopped at 2.05V (red), whose compositions should be very similar to each other ($x = 1.76$ and 1.7, respectively). It can be noted how the overall profile between the two samples is very similar, however, there are some differences such as the shift towards lower angles of the peaks (103) and (004) in the case of the electrode, which can be attributed to the different amount of lithium in the two structures. This comparison highlights the effectiveness of the treatment with LiI to achieve the overlithiation of the material.

The GITT technique was applied to the LRCMO sample in the extended potential range (1.6 - 5.1 V) with current pulses of 0.1C followed by a 2-hour relaxation step. Since high-voltage spinel materials undergo two-phase reactions during lithiation, GITT is able to provide only apparent diffusion coefficients, which implies the movement of Li^+ ions as well as the one of the interface between phases. [342] The results are shown in Figure 7.12 (a) and (b) for the discharge and charge process, respectively. Considering the discharge step, it can be noted that up to 3 V, the diffusion coefficient D_{Li^+} is around 10^{-14} m^2s^{-1}, and in this range, the difference between the voltage recorded at the end of the relaxation step (OCV, open-circuit voltage, depicted with a dashed yellow line in Figure 7.12) and the end of the current pulse (termed CCV, closed circuit voltage), which is a direct measure of the overpotential η, is minimal and indicative of low cell polarization. The transition zone between the high and low potential region at a SOC of about 70% (light green shaded area) shows a strong potential variation so that the cell could not reach an equilibrium condition to provide significant values of D_{Li^+}. In the zone below 3V, it can be observed how the CCV values faithfully trace the profiles of the galvanostatic discharge curves of Figure 7.9, highlighting the presence of two distinct plateaus at 2.7 and 2.1V, a fact that would suggest the occurrence of two different electrochemical reactions. On the contrary, the practically constant OCV values from 70% < SOC < 20% suggest that the material, with sufficient relaxation time, is capable of reaching equilibrium, and that the two plateaus of the CCV represent two distinct steps (requiring a different η) of the same Li^+ insertion phenomenon (namely, the metal species being reduced is always the same, in this case $Mn^{4+/3+}$). The trend of D_{Li^+} in this area reflects the difference between the CCV and OCV: for 70% < SOC < 55%, i.e., when the transition from cubic (C) to tetragonal (T) structure occurs, D_{Li^+} undergoes a drastic reduction (four orders of magnitude). This strong reduction seems to be particularly pronounced during the transition between the CCV plateau from 2.7 to 2.1 V, a fact also observed by Jobst et al. [329]. Subsequently, D_{Li^+} shows a gradual increase that can be explained by the fact that in the progressively formed Li-rich structure, the octahedral 16*c* sites are characterized by energy comparable to those of 8*a* in the spinel structure. Indeed, the values of D_{Li^+} for SOC = 15% are of the same order of magnitude as those of the high voltage region, before undergoing a decrease likely linked to an excessive occupation of the 16*c* sites with consequent reduced mobility for the Li^+ ions.

During the charging process, as illustrated in Figure 7.12 (b), a noticeable discrep-

ancy between the CCV and OCV persists up to approximately 4 V/SOC ≈ 55%. In particular, D_{Li^+} significantly decreases up to SOC ≈ 25% (3V), coinciding with the transition from T to C. However, it is also noticeable how the extent of η increases considerably at SOC ≈ 30% (3.7 V) up to SOC ≈ 50% (3.85 V), indicating a marked polarization of the cell. This observation is consistent with the data from *ex-situ* XRD measurements performed at 3 and 3.875 V during charging, which showed that the transition from T to C was only completed at voltages higher than 3.875 V. Consequently, it seems logical to associate the peak of overpotential exhibited by the material during the charging phase between SOC 30% and 50% (3.7 - 3.85 V) with the completion of the structural transition and with the peak exhibited by the dQ/dV curves in the same potential range. It should be noted that in this range of SOC, the cell struggled to reach equilibrium during the relaxation step, and this is reflected in the values of D_{Li^+} (which progressively increases) and η (which decreases). A longer relaxation time could indeed reveal constant OCV values (about 2.9 V, as in the region 5% < SOC < 30%) with consequent stabilization of both D_{Li^+} and η. However, even with these parameters, the GITT measurement was able to provide valuable information on the electrochemical behavior of the materials in the low voltage region; moreover, these parameters allow the measurement not to be excessively prolonged in terms of time.

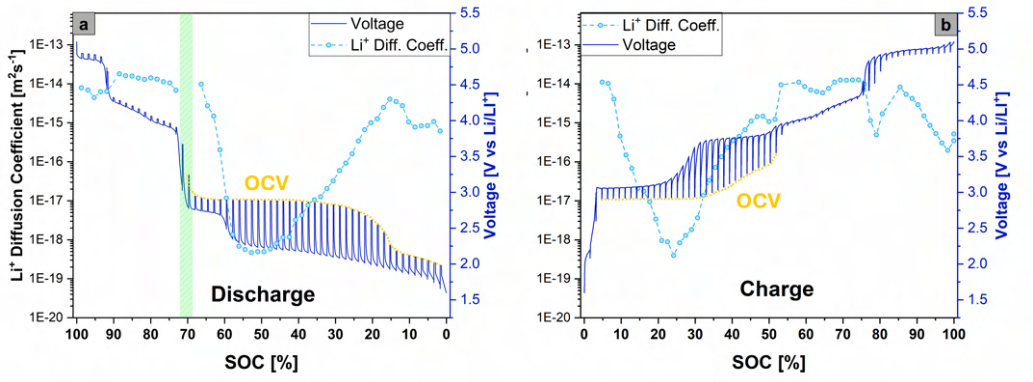

Fig. 7.12 GITT test carried out on the LRCMO based cathode between 1.6 - 5.1 V with 10 min of applied current 0.1C and 2h rest (a) discharge process, (b) charge process. The figure reports both the voltage vs SOC of the cell and the values of D_{Li^+} in function of the SOC.

Recently, Jobst et al. [329] and Dose et al.[339] have thoroughly investigated the nature of the two plateaus in the low-voltage region exhibited by LNMO. Con-

sequently, since the LCMO analyzed here shows the same type of structure and electrochemical behavior, and based on the results just described, this work assumes a similar model. In particular, it can be better understood with the aid of Figure 7.13. The basic assumption is that the insertion of Li^+ ions below 3 V involves a core-shell type reaction mechanism of the LCMO crystallites beyond a certain degree of lithiation. More specifically, it is possible to hypothesize that a certain concentration gradient begins to develop at 2.8V (where the GITT discharge curve shows a first increase in overpotential) between the core of the crystallites (which remains cubic with Li = 1) and the outer part, which becomes lithium-enriched (1 < Li < 2) and converts to a tetragonal structure. Therefore, during the later stages of discharge, lithium needs to penetrate this Li-enriched layer. The presence of this blocking shell thus leads to the formation of a super-lithiated phase in the outermost part (namely $Li_{2.5}Cu_{0.4}Mn_{1.6}O_4$) which has an equilibrium potential of about 1.5 V vs Li/Li^+ , rather than a lithiation of the LCMO core. During the GITT relaxation step, the two reactions shown in Figure 7.13 occur, where the super-lithiated material reacts cathodically while the core reacts anodically, both transforming into $Li_2Cu_{0.4}Mn_{1.6}O_4$ and bringing the system to the OCV of 2.78 V. The mixed potential generated by the juxtaposition of these two phases turns out to be about 2.13 V [329], in line with the value of the CCV plateau for SOC > 55%.

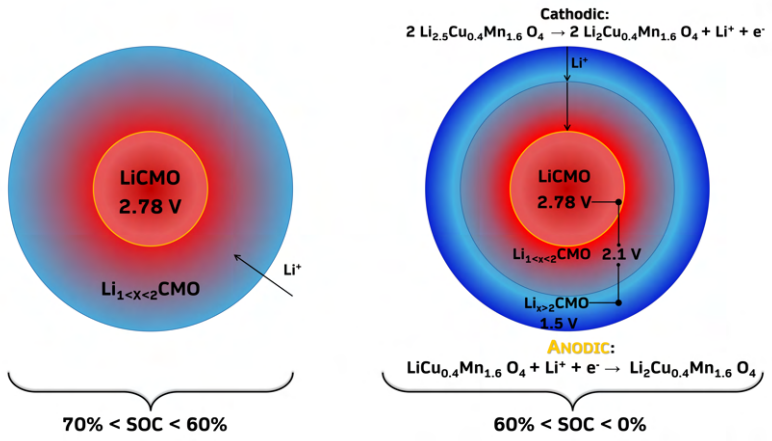

Fig. 7.13 Scheme of the proposed lithiation process in a single crystallite of LCMO, including the simultaneous anodic and cathodic reactions that occur during lithiation in the low voltage region (for 60% < SOC < 70% on the left and for 60% < SOC < 0% on the right).

To better study the phenomena that occur during the charge/discharge processes of the material, various electrochemical impedance tests were conducted during the cycling of a half-cell in a coin-cell configuration. This test was preceded by a formation step involving three cycles at 0.1C in the potential range of 1.6 - 5.1 V vs Li/Li^+ . As in the case of GITT, the material used for this test was solely LRCMO. Figure 7.14 shows the charge/discharge profiles and the points where the impedance spectra were recorded.

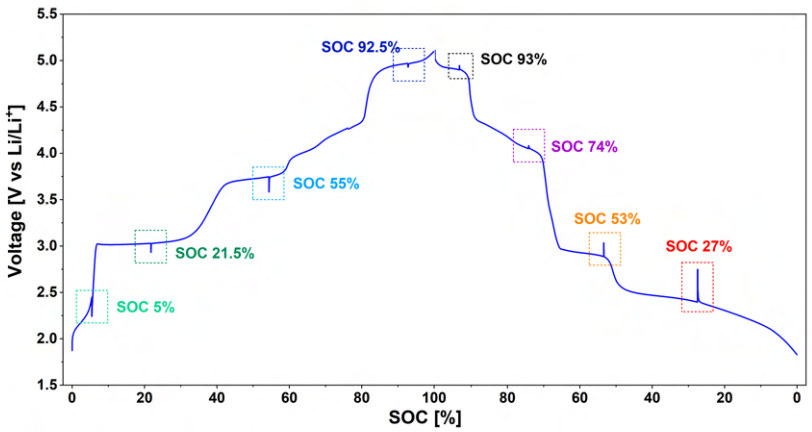

Fig. 7.14 The charge/discharge profile of the LRCMO in half cell between 1.6 - 5.1 V with colored squares thath highlight the points where the EIS was performed.

The spectra obtained during the charging step were reported in Figure 7.15 (a), while those collected during the discharge were shown in Figure 7.15 (c). Figures 7.15 (b) and (d) displayed the same graphs enlarged for better readability. All collected impedances were fitted using a simplified equivalent circuit consisting of an initial resistance followed by three RC elements and possibly a constant phase element (CPE). More specifically, the high-frequency resistance (R_s) accounted for the ionic resistance of the separator/electrolyte and the external electronic contacts of the cell and was approximately constant throughout the entire charging/discharging process (about 10 Ohm). The resistance R1 represented the impedance due to the contact between the current collector and active material and was also quite stable over the course of cycling (7-10 Ohm); the contribution of this resistance was particularly evident at high frequencies in the spectra at low SOC in the early stages of charging (panel b of Figure 7.15). At medium frequencies (935 Hz), the resistance R2 was

associated with the passivating layer of the LCMO particles and their electronic conductivity. Finally, the low-frequency region (5-0.1 Hz) was characterized by a resistance (R3) that could be linked to charge transfer and pore resistance at the electrode/electrolyte interface.

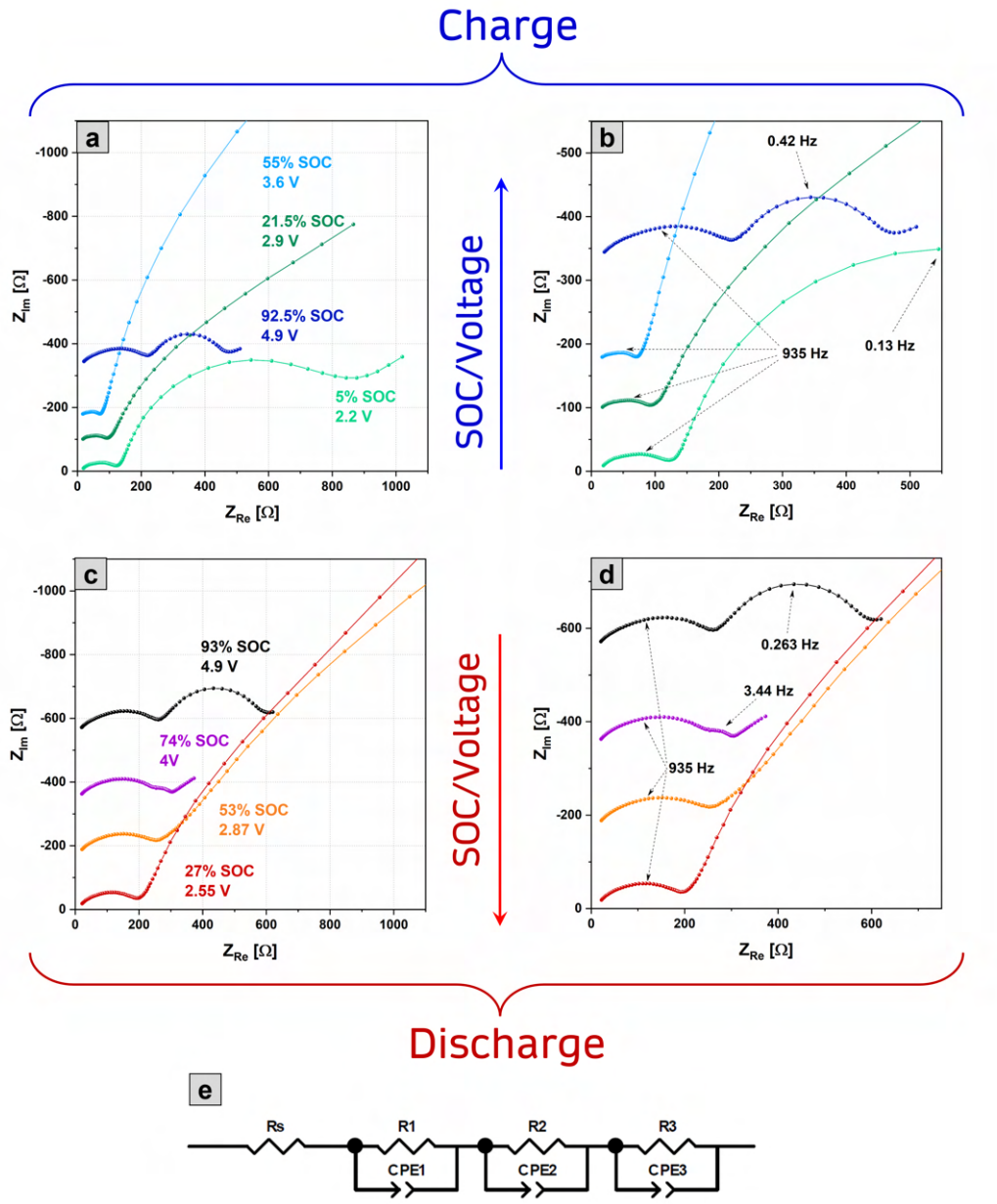

Fig. 7.15 EIS spectra at different SOC of the LRCMO sample. (a) EIS spectra collected during the charge process, (b) magnification of panel (a) for better readability. (c) EIS spectra collected during the charge process, (d) magnification of panel (c) for better readability. In (e) is reported the equivalent circuit used to fit the EIS spectra.

This was eventually followed by a Warburg diffusion element (W) at lower frequencies, which indicated the semi-infinite linear diffusion of Li^+ ions within the

solid electrode. The fitting results were summarized in Table 7.5 for the charging phase and in Table 7.6 for the discharge step.
Analyzing the impedances during the charging process, it was noticeable how R2 decreased until a SOC of 55% (3.6 V). This decrease was in line with other results reported in the literature [343, 344] since, as delithiation proceeded, the electronic conductivity of the spinel materials increased due to the mixed valence state of $Mn^{3+/4+}$. At the end of the charging process (SOC 92.5%, 4.9 V), the increase in R2 could be attributed to the complete oxidation to Mn^{4+} and the increased resistance of the CEI at high voltage. The trend of the resistance associated with charge-transfer (R3) was different: it increased considerably from SOC 5% to SOC 55%, then decreased at the end of charging (SOC 92.5%). In particular, at low SOC (that is, when the material is still over-lithiated), the extraction of Li^+ ions results in a shift of the interface between delithiated material and still Li-rich material towards the interior of the crystallites, leading to an increase in the resistance associated with charge transfer. The fact that the maximum value of R3 was identified at approximately the same voltage (3.6 V) at which the GITT test showed the minimum values of DLi^+ and the maximum value of overpotential corroborated this hypothesis. At the end of the charging phase, R3 presented a significantly lower value, indicative of the fact that delithiation occurred more homogeneously at these potentials compared to low SOC. Moving to the discharge process, it was notable that the impedance recorded at 4.9 V (SOC 93%) was very similar to the last of the charge, although with slightly different values of R2 and R3. It was significant to note that the minimum value of R3 was found at a SOC of 74% (corresponding to the maximum of D_{Li^+} highlighted by the GITT and minimum overvoltage values). The values of R2 during the discharge process were less variable compared to the charging process, thus showing how the contribution of the passivating layer formed at high voltage during charging was predominant at these frequencies.

Table 7.5 Fitted impedance values based on Figure 7.15 at different SOC, for the LRCMO material during the charge step.

Charge				
SOC [%]	**R1** [Ohm]	**R2** [Ohm]	**R3** [Ohm]	χ^2
5	9.3	111.5	570.4	$7.32 \cdot 10^{-5}$
21.5	9.5	80.4	1796	$1.57 \cdot 10^{-4}$
55	7.0	60.4	4575	$3.98 \cdot 10^{-4}$
92.5	11.6	214.6	240.4	$8.9 \cdot 10^{-5}$

Table 7.6 Fitted impedance values based on Figure 7.15 at different SOC, for the LRCMO material during the discharge step.

Discharge				
SOC [%]	**R1** [Ohm]	**R2** [Ohm]	**R3** [Ohm]	χ^2
93.5	9.5	264.8	324.9	$8.27 \cdot 10^{-5}$
75	9.5	254.1	25.4	$1.57 \cdot 10^{-4}$
55	10.4	249.2	6883	$1.45 \cdot 10^{-4}$
25	10.5	185.1	3852	$1.1 \cdot 10^{-4}$

The characterization of the two materials in half-cell setups was completed by performing a long cycling test at a current of 1C for 500 cycles for both LRCMO and LCMO within the restricted potential range of 3-5.1 V vs Li/Li^+ , which is of greater interest as it is also used in the full cell configuration. The results of the cycling test are shown in Figure 7.16. It can be observed that for both samples, the Coulombic Efficiency (C.E.) increases over the course of cycling, moving from 97.0% to 98.8% for LRCMO and from 97.4% to 99.0% for LCMO (the values reported refer to the first and the 500^{th} cycle at 1C). Additionally, it is noted that in the case of LRCMO, the cathode exhibits a practically linear reduction in capacity throughout the cycling process (about 0.079% of discharge capacity per cycle), with a capacity retention at the end of the test of 60.8%. On the other hand, LCMO shows a more marked capacity reduction in the initial cycles (particularly at the 4^{th} cycle when switching

from the three formation cycles conducted at 0.1C to the 1C current), then displays a recovery up to the 200^{th} cycle and subsequently loses capacity slowly until the end of the test (loss of about 0.053% per cycle), with a final capacity retention of 74.5% relative to the first cycle at 0.1C.

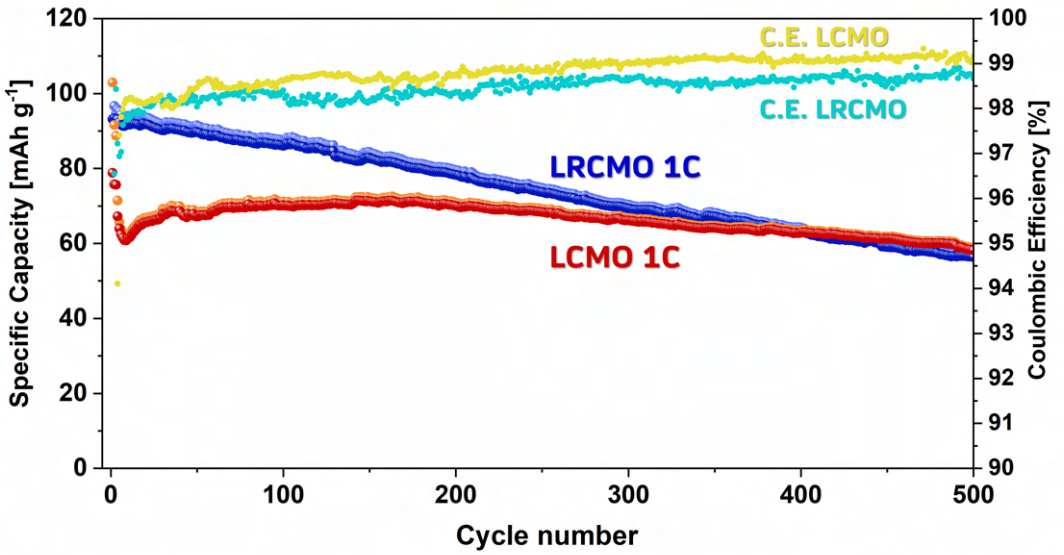

Fig. 7.16 Long cycling at 1C for 500 cycles for LRCMO and LCMO at 1C in the potential range 3-5.1 V vs Li/Li^+ . The coulombic efficiency is reported on the right y-axis in aqua green and cyan for LRCMO and LCMO, respectively.

This trend highlights how chemical overlithiation can indeed act as a boost of available lithium (thereby providing greater capacity, at least up to the 400^{th} cycle where both LRCMO and LCMO exhibit a capacity of about 63 mAh g^{-1}), but at the same time damage the structure of the material and thus cause a higher loss of capacity per cycle.

The charge and discharge profiles of the cycling tests for LRCMO and LCMO are presented in Figure 7.17 (a) and (b), respectively. Notably, the profiles of LRCMO exhibit a gradual shift towards lower capacities, whereas this trend is less pronounced for LCMO.

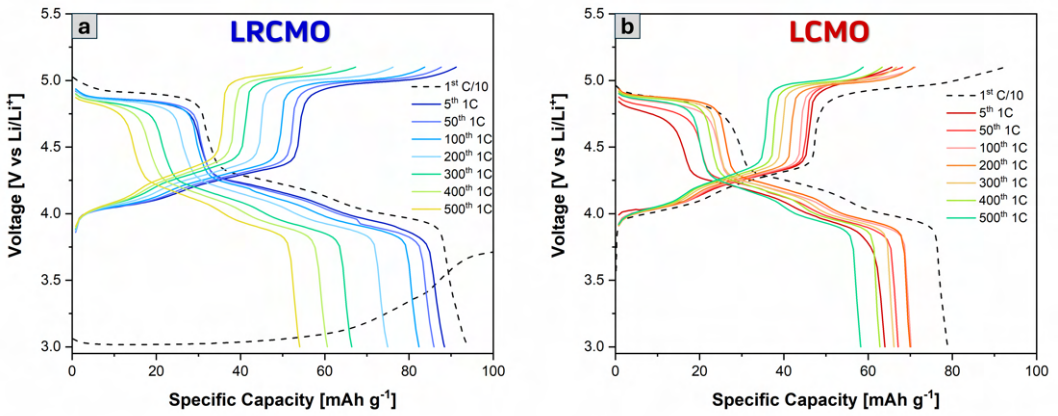

Fig. 7.17 Charge and discharge voltage profiles over the cycling test performed at 1C for (a) LRCMO and (b) LCMO.

Finally, the two materials were tested in a full-cell configuration, using commercial graphite as anode material. Using graphite instead of lithium has two main consequences: a greater loss of capacity in the first few cycles due to the formation of the SEI on the surface of the graphite particles (generally quantifiable in the range of 7-10% in the first cycle) and the lack of a semi-infinite lithium reserve as in the case of an anode of metallic lithium. In fact, in a full cell, all the lithium comes from the cathode structure, so any irreversible lithium consumption translates into a loss of cell capacity. Consequently, the approach of using a lithium-rich material aims to compensate for this initial loss thanks to the "reserve" of lithium stored in the cathode.
In this case, the N/P ratio was slightly increased to about 1.3 due to the difference in theoretical capacity of the two materials within the 3 - 5 V potential window (95 mAh g^{-1} for LCMO and 372 mAh g^{-1} for graphite), which would have led to the production of excessively light anodes by maintaining an N/P ratio of 1.1. This ratio has, however, been previously used in the literature for the production of full-cells based on LNMO-graphite [334, 345].

The three-electrodes setup used for the cell configuration enabled separate monitoring of the cathode and anode equilibrium curve evolution. The testing procedures were differentiated for the two different samples and are reported in Table 7.7 and 7.8 for LCMO and LRCMO, respectively. In particular, the main difference concerns the formation phase performed at 0.1C: for LCMO the cut-off limits are mixed ($E_{WE\text{-}CE}$

and E_{CE}), while for LRCMO the formation is based on the typical cycling potential window of graphite (the limit on $E_{WE\text{-}CE}$ is purely for safety and never reached). This difference is made possible by the overlithiation of the material and aims to promote the formation of a stable SEI and mitigate the loss of irreversible capacity that occurs during the first cycles. A similar protocol was used by Betz et al. [334]

Table 7.7 Testing protocol for the LCMO-graphite three-electrode cell.

LCMO	**Formation 0.1 C** Cut off condition	**Cycling 0.3 C** Cut off condition
Discharge	$E_{WE\text{-}CE} < 3$ V $E_{CE} > 0.8$ V	$E_{WE\text{-}CE} < 3$ V $E_{CE} > 1.2$ V
Rest	10 minutes	15 minutes
Charge	$E_{WE\text{-}CE} > 4.9$ V $E_{CE} < 0.01$ V	$E_{WE} > 4.95$ V -
C.V.	-	20 minutes

Table 7.8 Testing protocol for the LRCMO-graphite three-electrode cell.

LRCMO	**Formation 0.1 C** Cut off condition	**Cycling 0.3 C** Cut off condition
Discharge	- $E_{CE} > 0.8$ V	$E_{WE\text{-}CE} < 3$ V $E_{CE} > 1.2$ V
Rest	10 minutes	15 minutes
Charge	$E_{WE\text{-}CE} > 4.9$ V $E_{CE} < 0.01$ V	$E_{WE} > 4.95$ V -
C.V.	-	20 minutes

The cycling results for LCMO and LRCMO are shown in Figure 7.18 (a) and (b), respectively, whereas Figure 7.19, shows some of the more significant cycles enlarged for better readability. In particular, it can be noted that during the formation phase, LCMO always reached the condition of $E_{WE\text{-}CE} = 4.9$ V during cell charging, while the exit condition of the discharge step was the one set on the graphite ($E_{CE} = 0.8$ V). Therefore, it can be observed that, as the cycles progress, the potential of the graphite at the End of Charge (EOC) increased, as did the potential of the cathode at the end of the discharge. This leads to a progressive narrowing of the potential window in which the two electrodes operate (electrode slippage) [322], with a consequent significant reduction of the active material utilization and capacity fade. Particularly, observing Figure 7.19 (a), which shows the last formation cycle of LCMO, it is noticeable how a substantial part of the plateau associated with the $Mn^{3+/4+}$ redox was cut out from the cycling, as well as the last stage of intercalation of the graphite.

The formation phase of the LRCMO is quite different: since the cathode was overlithiated, it could provide all the capacity necessary for the SEI formation to the graphite without the anode potential curve being cut during the formation cycles. In this phase, the potential window in which the cathode operated varied significantly from cycle to cycle due to the increased capacity from the additional lithium in the structure and the absence of cutoff constraints related to $E_{WE\text{-}CE}$. In particular, the window in which the cathode operated was lower (between approximately 2.3 and 4.4 V) in the first six cycles compared to the typical window (3 - 5.1 V), which is reached in the last formation cycle, as shown in Figure 7.19 (b). The variation in the window is likely due to the limited reversibility of the reactions that occur at low potential for the cathode, as already reported in the study of half-cells.

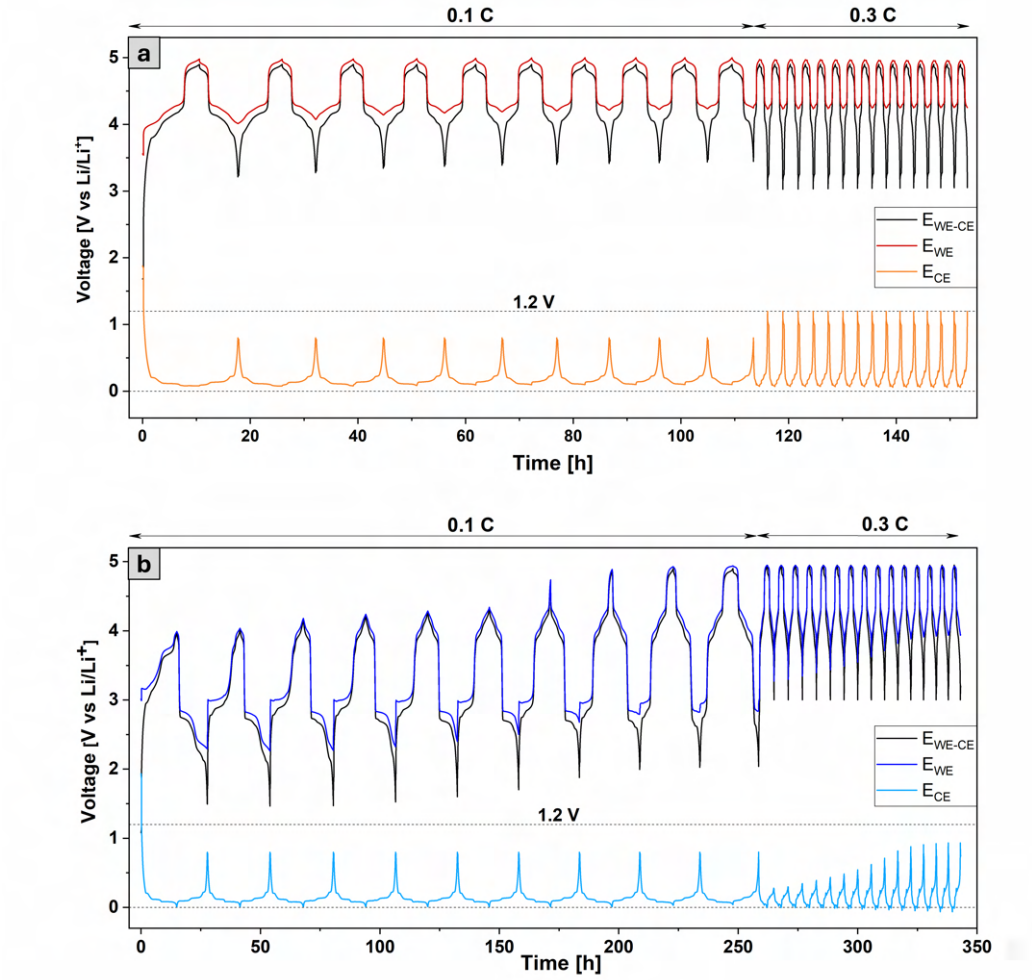

Fig. 7.18 (a) Cycling of LCMO in a three-electrode cell, the cathode equilibrium curve is shown in red E_{WE}, the anode in orange E_{CE}, and the overall cell potential curve is reported in black EWE-CE; (b) cycling of LRCMO in a three-electrode cell. The blue curve shows the cathode potential E_{WE}, the light blue curve the anode potential E_{CE}, and the black curve represents the overall cell potential E_{WE-CE}. The third electrode is a reference lithium ring.

As a result, in Figure 7.19 (b), which shows the last formation cycle at 0.1C for the LRCMO, it can be noted that both the cathode and anode equilibrium curves were complete (E_{CE} reaches a potential of 0.01 V at the end of the charge while E_{CE} reaches 2.83 V at the end of discharge, EOD), in contrast to those of the LCMO reported in Figure 7.19.

In the subsequent cycling carried out at a current of 0.3C, the testing protocols were standardized for the two samples; moreover, a constant voltage (C.V.) step lasting

20 minutes was introduced at the end of the charge step (E_{WE} = 4.95 V), in order to ensure the completion of the cell charge with low currents. Additionally, the potential limit for the anode was extended to 1.2 V for the discharge phase and it was removed during the charge phase. As can be seen in Figure 7.18 and in Figures 7.19 (c) and (d), the potential profiles of the anode and cathode in the case of LCMO show a trend very similar to that already shown in the last cycle at 0.1C. However, in this case, the EOC of the graphite reaches 1.2 V from the first cycle at 0.3C, and without the imposed limit, it would have exceeded that, since the cathode equilibrium curve was still in the middle of the $Mn^{3+/4+}$ redox plateau. The uncontrolled increase in Ece can be problematic for the stability of the SEI, which can then crack and lead to further lithium consumption during its reformation in the subsequent phase of graphite intercalation. Consequently, as cycling continues, a smaller portion of the low-voltage region of the cathode is utilized — meaning less lithium returns to the cathode at the end of discharge due to its immobilization in the graphite SEI. At the same time, a smaller fraction of graphite capacity is utilized, with higher voltage plateaus (100 mV) accounting for a larger share of the capacity. [322, 346] Another interesting feature that can be observed from Figure 7.19 (e) is that at the transition between the $Mn^{3+/4+}$ redox plateau and the $Cu^{2+/3+}$ plateau, there is a corresponding spike in the anode equilibrium curve. Specifically, during the charging step, this spike is negative, while in the discharge phase, it appears as a positive peak. This demonstrates how the potentials of the anode and cathode can influence each other during cycling, an aspect not observable in two-electrodes measurements.
Regarding the LRCMO, it can be seen that switching to a current of 0.3C (see Figure 7.19 d) results in much less electrode slippage compared with LCMO, since both typical cathode plateaus are clearly visible and complete in both charging and discharging, and the values of EOC (0.01 V) and EOD (0.29 V) reached by the graphite indicate a better utilization of the active material. However, it should also be noted that at the end of the cycling (Figure 7.19 f), the LRCMO shows a problem of lithium plating on the anode side, since the cathodic voltage jump during charging translates into a minimum potential on the anodic curve, with the graphite reaching negative potentials.

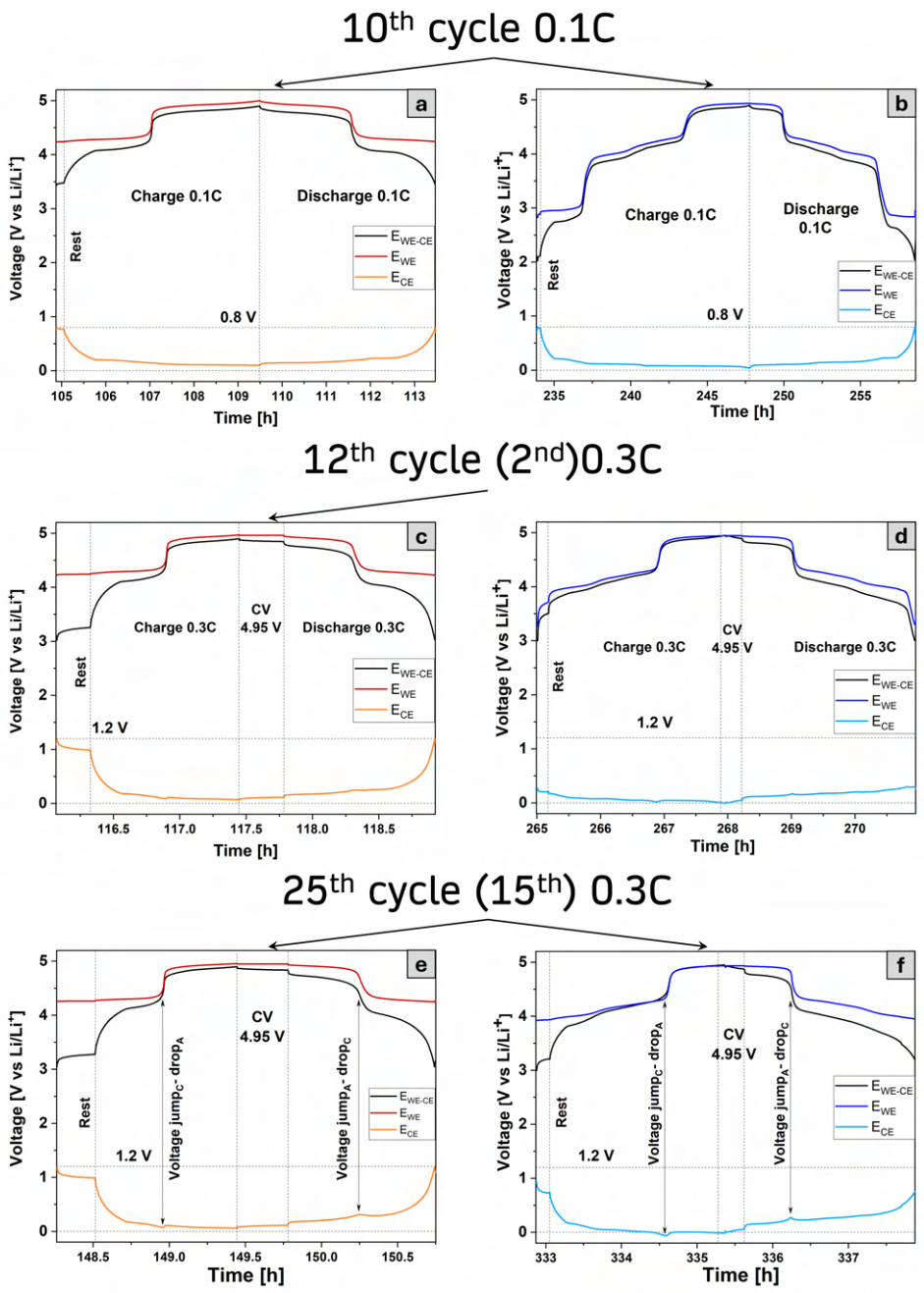

Fig. 7.19 Panels (a) and (b) show the last formation cycle at a current of 0.1C for LCMO and LRCMO, respectively. Panels (c) and (d) represent the second cycle performed at 0.3C for LCMO and LRCMO, while in (c) and (d) the last cycle (15^{th} at 0.3C) of the test is reported. The arrows in panela /e) and (f) indicate the voltage jump/drop on the cathode and anod equilibrium potenzial curve in correspondace of the transition between the $Mn^{3+/4+}$ and $Cu^{2+/3+}$ plateau.

To better analyze the phenomenon of electrode slippage, differential voltage analysis (DVA, dV/dQ) was used for the two samples on significant cycles depicted in Figure 7.19. The results are displayed in Figure 7.20 (a) and (b) for the charging and discharging of LCMO, and in Figures (c) and (d) for the charging and discharging of LRCMO. Features attributable to cathodic reactions are marked with a green diamond, while various transition phases from one graphite phase to another are indicated with a red cross [347]. The constant voltage (C.V.) step applied at the end of the charge is not considered because the resulting dV/dQ would be zero. DVA was applied on the overall cell equilibrium curve $E_{WE\text{-}CE}$ and normalized to the cell capacity.

Starting with LCMO, it can be observed that the peak related to the transition between the $Mn^{3+/4+}$ and $Cu^{2+/3+}$ plateaus shifts to lower capacities, indicating slippage (as the separation of peaks in the DVA corresponds to the charge/discharge plateaus in the potential curves). Similarly, in the discharge phase (Figure 7.20 b), it is notable how the cathodic peak progressively shifts toward lower capacities during cycling. It is also interesting to note that in the initial phases of charging, the present peak is attributable to the sudden decrease in graphite potential during the transition from S4 to S3.

In the case of LRCMO, the DVA curves from the tenth formation cycle are quite different, as there is still a plateau at about 2.8 V in the charge/discharge curves, which is reflected in the peak at about 0.1 mAh cm^{-2} in the charge phase and about 0.275 mAh cm^{-2} in the discharge phase. The presence of this plateau thus causes the shift charge capacity values of the transition peak from $Mn^{3+/4+}$ to $Cu^{2+/3+}$, which is visible at about 0.3 mAh cm^{-2} in Figure 7.20 (c). Nevertheless, it is noteworthy how the shift of the cathodic peak from the 12^{th} to the 25^{th} cycle at 0.3C in the charging phase is smaller compared to that exhibited by LCMO. Moreover, in the discharge phase, it can be seen how the first cathodic peak moves towards higher capacities from the last formation cycle (black curve) to the second performed at 0.3C (blue curve). This is likely due to the CV step included in the cycling at higher current and the expansion of the potential window to 4.95 E_{WE}. At the end of the cycling (light blue curve), the peak is practically overlapped compared to the one exhibited at the last formation cycle, a sign of the good reversibility of the reaction in this region. Analyzing the initial charging zone, it can be noted that in the last cycle at 0.1C, the shoulder present at about 0.03 mAh cm^{-2} is due to both cathodic (transition from the 2.8 V plateau to the 4 V plateau) and anodic contributions, whereas in the second

cycle at 0.3C (blue curve), the DVA exhibits a much less pronounced feature. This is due to the fact that in this phase of the cycling, the EOD values of graphite are very low (about 0.29 V), so there are no strong voltage variations in this region. At the end of the cycling, the presence of a shoulder is noted again, due to the voltage reduction from S4 to S3. Similarly, in the final part of the discharge (Figure 7.20 d), it can be seen that for the last cycle at 0.1C and the second at 0.3C, there is a peak attributable to the reduction of the cathodic potential, while in the last cycle at 0.3C the peak (only partially visible) is instead due to the rise of the anodic potential. Overall, the DVA curves illustrate how the approach of over-lithiation of the cathode helps to mitigate the phenomenon of electrode slippage.

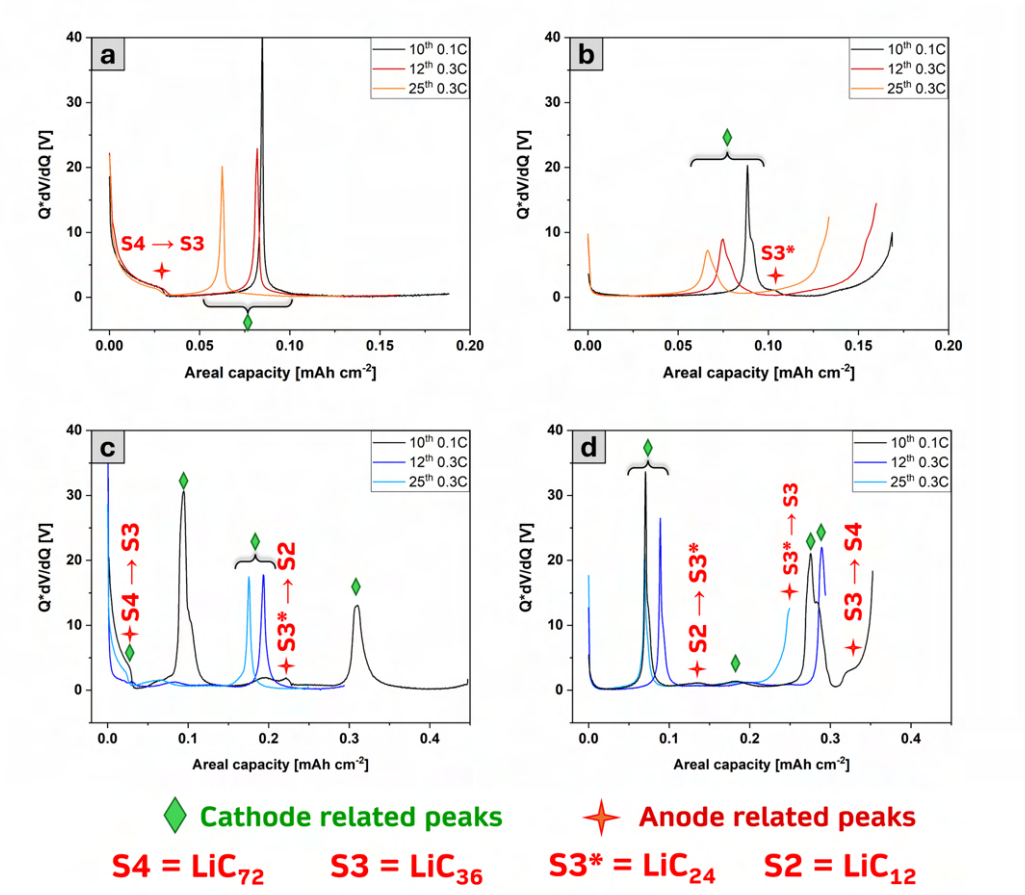

Fig. 7.20 (a) DVA of the charge step of the LCMO sample for the three selected cycles, (b) DVA of the same cycles for the discharge phase of LCMO; (c) DVA curves for the charge step of the LRCMO sample and (d) DVA curves for the LRCMO sample in the discharge step. The DVA were obtained from the overall equilibrium curve potential, $E_{WE\text{-}CE}$.

The performance, in terms of areal capacity and coulombic efficiency, of the two samples during cycling in a three-electrode cell, are reported in Figures 7.21 (a) and (b). It can be observed that the LCMO exhibits a lower capacity throughout the cycling process, with a considerable loss of capacity already during the formation phase at 0.1C, due to the electrode slippage previously described. The capacity, as well as the coulombic efficiency, appear to be more stable during the cycles conducted at 0.3C, where the capacity is largely provided by the electrochemical activity of $Cu^{2+/3+}$.

On the other hand, the LRCMO exhibits higher capacity and better coulombic efficiency from the beginning, although in the last cycles of formation, the latter

experiences a significant decrease. This is attributable to the progressive variation of the potential window across different cycles; in particular, it takes a few cycles before the electrochemical activity of $Cu^{2+/3+}$ can achieve a more acceptable levels of coulombic efficiency. The superior capacity of the LRCMO is also maintained in the cycles performed at 0.3C, while the coulombic efficiency (C.E.) levels are comparable to those of the LCMO, as shown in Figure 7.21 (b).

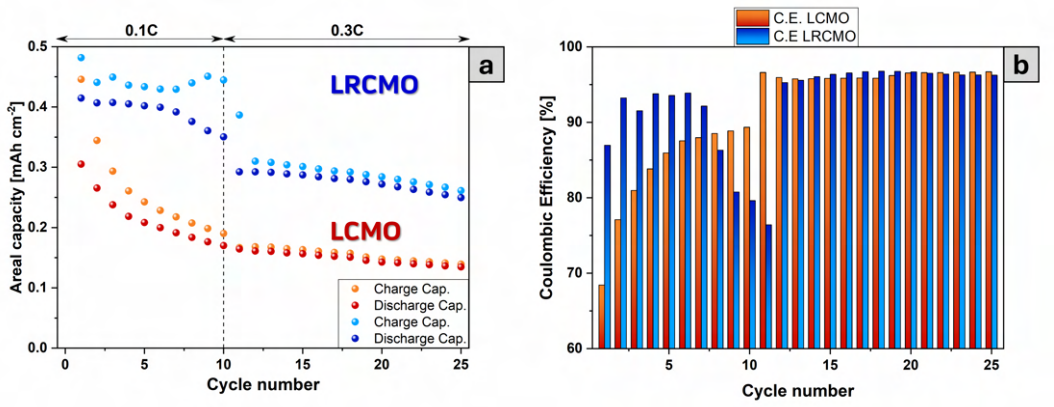

Fig. 7.21 (a) Areal capacity comparison between LCMO and LRCMO (b) coulombic efficiency comparison between LCMO and LRCMO for the cyling in three electrode cell configuration.

Chapter 8

Concluding remarks

This Ph.D. research focused on the synthesis of new cathode materials for Li-ion and post Li-ion batteries (Li-S batteries), and their comprehensive characterization from both physicochemical and electrochemical perspectives.
The initiative to investigate cathode materials for two types of batteries with different chemistries stemmed from the state of art of research and the expected prospects. Li-S batteries, with their high specific capacity and superior environmental sustainability compared to Li-ion batteries, emerge as potential alternatives to Li-ion batteries in the near future. Consequently, the first part of this work dealt with the development of cathode materials for Li-S batteries. For High Entropy Oxides (HEO), the approach aimed to limit the shuttling of LiPSs, one of the main degradation mechanisms in Li-S batteries, by adopting a "double layer" strategy. This involved applying a second layer of material (in this case, HEO) capable of physicochemically interacting with LiPSs over the first carbon-sulfur layer. This second layer served as a barrier against the diffusion of LiPSs towards the anode, and if the material exhibited catalytic activity towards LiPSs, it re-enabled their participation in the conversion reaction. The study investigated two different formulations of the double layer based on HEO (80% and 90%) and compared them to a carbon-sulfur based standard cathode. Physicochemical and electrochemical characterizations revealed that HEO improved the performance of the double-layer cathodes, which demonstrated better rate capability (520 mAh g^{-1} vs. 100 mAh g^{-1} at 1C) and capacity retention (55.31% vs. 49.341% after 250 cycles at 0.2C) compared to the standard cathode.
The second cathode material developed for Li-S applications was a composite based

on reduced graphene oxide and zinc sulfide nanoparticles (rGO/ZnS). Used as a carbon matrix to be infiltrated by sulfur through melt infusion, this method differed from the approach used with the HEO. The synthesis process included a microwave-assisted hydrothermal step, significantly reducing the time required compared to traditional autoclave hydrothermal synthesis. This process involved the reduction of GO and its doping with N and S, as well as the formation of ZnS nanoparticles. The combination of rGO and ZnS nanoparticles was chosen to exploit the synergistic effect of the two materials such as the good conductivity and interaction with LiPSs (thanks to S and N doping) of rGO and the catalytic activity of ZnS particles towards LiPSs. Physicochemical and electrochemical characterizations were carried out to assess the influence of the nanoparticles on cathode operation, comparing the doped rGO material with and without ZnS nanoparticles. The catalytic activity of these materials towards LiPSs was tested through various analyses (UV-Vis of a LiPSs solution in contact with the two materials, symmetrical CV, and Tafel plot). The rGO/ZnS sample showed better capacity retention after 750 cycles at 0.5C compared to the S-N doped rGO (48.2% vs 32.5%) and better performance at higher C-rates (613 vs. 547 mAh cm^{-2} at 1C). Additionally, the rGO/ZnS sample demonstrated superior efficiency in using active material, achieving better conversion of polysulfides and exhibiting reduced cell polarization.

The latter part of the thesis focused on developing high-voltage cathode materials for Li-ion batteries. This part of the research was closer to potential immediate future applications of the developed materials. Moreover, the importance of limiting the use of critical raw materials is currently a key factor in battery research, seeking to make the battery production chain more sustainable from an environmental point of view. In this sense, the study of a new high-voltage cathode based on blending two Co-free materials like LNMO and LFP was conducted in the frame of the European project HYDRA (Horizon 2020). The blending technique employed was Resonant Acoustic Mixing (RAM), which can achieve high efficiency in terms of homogeneity and treatment time, performed by the partner ICSI. The materials obtained were characterized by XRD, BET, and SEM, and used to produce cathodes with a mass loading of about 10 mg/cm^{-2}. The work delved into the electrochemical characterization of the blended cathodes compared to pristine LNMO using techniques such as GITT, and EIS at different states of charge, and cycling in a three-electrode cell. The results indicated that LFP stabilized the cathode potential at low states of charge, reducing cell polarization in both half-cell and full-cell configurations, and acted

electrochemically to donate lithium up to currents of 1C. The most promising results were obtained in full-cell configurations, where blended cathodes exhibited superior areal capacity compared to pristine LNMO (approximately 1.1 mAh cm^{-2} vs. 0.9), and better coulombic efficiency and capacity retention (87.5% and 82.5% for the two blends vs. 80% for pristine LNMO) at the end of 100 cycles.

Finally, the last part of the work was advanced through collaboration with the Commissariat à l'énergie Atomique (CEA) in Grenoble, where a high-voltage material for Li-ion batteries was synthesized. This material, featuring the same spinel structure as LNMO, was achieved by substituting Ni with Cu (composition $LiCu_{0.4}Mn_{1.6}O_4$), enhancing the operational potential up to about 4.95 V due to the electrochemical activity of copper. Additionally, the material was chemically overlithiated to increase the stored lithium quantity in the cathode structure to counteract the active material losses in initial formation cycles in full-cell configurations. The two materials, LCMO and LRCMO, were characterized structurally and morphologically, then tested in half-cell and three-electrode cell configurations against graphite. Techniques such as GITT, EIS at various SOC, and ex-situ XRD were applied to investigate the electrochemical behavior of the material, particularly focusing on the potential window between 1.6 - 3 V, a range previously unexplored for this material. From a performance standpoint, LCMO and LRCMO exhibited similar results in half-cell configurations (60 mAh g^{-2} over 500 cycles at 1C), with LRCMO showing a higher capacity in the initial cycling phase but lower capacity retention (60.8% vs. 74.5%). When paired with graphite anodes, LRCMO outperformed the LCMO in terms of capacity retention and coulombic efficiency.

In conclusion, this Ph.D. project was dedicated to synthesizing and assessing various cathode materials for two different types of batteries: it focused on high-voltage materials for Li-ion batteries to improve a well-established and commercially viable technology, and it explored materials for the yet-to-be-commercialized Li-S batteries. Moving forward, several strategies could extend the research of this work, such as altering the structure of Li-S materials by incorporating defects and/or functional groups to enhance interaction with LiPSs. For Li-ion batteries, additional combinations of cathode materials with similar operational potentials (like LMFP/LNMO) could be explored and analyzed using the same methodology applied here, while chemical over-lithiation might be employed on other cathode materials (such as LNMO, NMC) to complement high-energy anodes in the graphite/silicon system.

References

[1] M. Fichtner, K. Edstrom, E. Ayerbe, M. Berecibar, A. Bhowmik, I. E. Castelli, S. Clark, R. Dominko, M. Erakca, A. A. Franco, et al., *Advanced Energy Materials* **2022**, *12*, 2102904.

[2] H. Zhang, X. He, Z. Chen, Y. Yang, H. Xu, L. Wang, X. He, *Advanced Energy Materials* **2022**, *12*, 2202022.

[3] K. Jia, J. Ma, J. Wang, Z. Liang, G. Ji, Z. Piao, R. Gao, Y. Zhu, Z. Zhuang, G. Zhou, et al., *Advanced Materials* **2023**, *35*, 2208034.

[4] D. Yang, Y. Zhou, H. Geng, C. Liu, B. Lu, X. Rui, Q. Yan, *Coordination Chemistry Reviews* **2020**, *424*, 213521.

[5] M. Wang, Z. Bai, T. Yang, C. Nie, X. Xu, Y. Wang, J. Yang, S. Dou, N. Wang, *Advanced Energy Materials* **2022**, *12*, 2201585.

[6] A. Suryatna, I. Raya, L. Thangavelu, F. R. Alhachami, M. M. Kadhim, U. S. Altimari, Z. H. Mahmoud, Y. F. Mustafa, E. Kianfar, *Journal of Chemistry* **2022**, *2022*, 1–32.

[7] J. Janek, W. G. Zeier, *Nature Energy* **2023**, *8*, 230–240.

[8] D. Bresser, K. Hosoi, D. Howell, H. Li, H. Zeisel, K. Amine, S. Passerini, *Journal of Power Sources* **2018**, *382*, 176–178.

[9] M. Winter, R. J. Brodd, *Chemical reviews* **2004**, *104*, 4245–4270.

[10] M. V. Reddy, A. Mauger, C. M. Julien, A. Paolella, K. Zaghib, *Materials* **2020**, *13*, 1884.

[11] B. Scrosati, *Journal of solid state electrochemistry* **2011**, *15*, 1623–1630.

[12] J. Tarascon, M. Armand, *Nature* **2001**, *414*, 359–367.

[13] E. Moyassari, T. Roth, S. Kucher, C.-C. Chang, S.-C. Hou, F. B. Spingler, A. Jossen, *Journal of The Electrochemical Society* **2022**, *169*, 010504.

[14] K. Mizushima, P. Jones, P. Wiseman, J. B. Goodenough, *Materials Research Bulletin* **1980**, *15*, 783–789.

[15] M. X. Tran, P. Smyrek, J. Park, W. Pfleging, J. K. Lee, *Nanomaterials* **2022**, *12*, 3897.

[16] H. Zhao, W.-Y. A. Lam, L. Sheng, L. Wang, P. Bai, Y. Yang, D. Ren, H. Xu, X. He, *Advanced Energy Materials* **2022**, *12*, 2103894.

[17] X. Tang, S. Lv, K. Jiang, G. Zhou, X. Liu, *Journal of Power Sources* **2022**, *542*, 231792.

[18] J. Amici, C. A. Calderon, D. Versaci, G. Luque, D. Barraco, E. Leiva, C. Francia, S. Bodoardo, *Electrochimica Acta* **2022**, *404*, 139772.

[19] X. Yuan, H. Liu, J. Zhang, *Lithium-ion batteries: advanced materials and technologies*, CRC press, **2011**.

[20] C. Li, Z. Xi, D. Guo, X. Chen, L. Yin, *Small* **2018**, *14*, 1701986.

[21] M. S. Whittingham, *Science* **1976**, *192*, 1126–1127.

[22] A. Yoshino, *Nature Energy* **2021**, *6*, 449–449.

[23] S. A. Arote, *Lithium-ion and Lithium–Sulfur Batteries: Fundamentals to performance*, IOP Publishing, **2022**.

[24] A. Kor nyushchenko, A. H. Jayatissa in *Applications of Nanocomposites*, CRC Press, **2022**, pp. 90–121.

[25] J. B. Goodenough, Y. Kim, *Chemistry of materials* **2010**, *22*, 587–603.

[26] H. Zhang, R. Lu, C. Zhu, Y. Zhao, *International Journal of u-and e-Service Science and Technology* **2014**, *7*, 301–310.

[27] R. Rotas, P. Iliadis, N. Nikolopoulos, A. Tomboulides, E. Kosmatopoulos, *Energies* **2022**, *15*, 3688.

[28] J.-H. Jung, S. Ahmed, *Journal of Power Electronics* **2010**, *10*, 739–748.

[29] P. Selinis, F. Farmakis, *Journal of The Electrochemical Society* **2022**, *169*, 010526.

[30] H. Cheng, J. G. Shapter, Y. Li, G. Gao, *Journal of Energy Chemistry* **2021**, *57*, 451–468.

[31] R. A. Huggins, *Advanced Batteries: Materials Science Aspects* **2009**, 339–373.

[32] X.-B. Cheng, R. Zhang, C.-Z. Zhao, Q. Zhang, *Chemical reviews* **2017**, *117*, 10403–10473.

[33] C. Du, Z. Zhao, H. Liu, F. Song, L. Chen, Y. Cheng, Z. Guo, *The Chemical Record* **2023**, *23*, e202300004.

[34] S. Li, K. Wang, G. Zhang, S. Li, Y. Xu, X. Zhang, X. Zhang, S. Zheng, X. Sun, Y. Ma, *Advanced Functional Materials* **2022**, *32*, 2200796.

[35] A. D. Jara, A. Betemariam, G. Woldetinsae, J. Y. Kim, *International Journal of Mining Science and Technology* **2019**, *29*, 671–689.

[36] Y.-G. Guo, J.-S. Hu, L.-J. Wan, *Advanced Materials* **2008**, *20*, 4384–4384.

[37] Q. Cheng, R. Yuge, K. Nakahara, N. Tamura, S. Miyamoto, *Journal of Power Sources* **2015**, *284*, 258–263.

[38] T.-H. Kim, E. K. Jeon, Y. Ko, B. Y. Jang, B.-S. Kim, H.-K. Song, *Journal of Materials Chemistry A* **2014**, *2*, 7600–7605.

[39] F.-S. Li, Y.-S. Wu, J. Chou, M. Winter, N.-L. Wu, *Advanced materials* **2015**, *27*, 130–137.

[40] D. Y. Rhee, J. Kim, J. Moon, M.-S. Park, *Journal of Alloys and Compounds* **2020**, *843*, 156042.

[41] H. Hou, X. Qiu, W. Wei, Y. Zhang, X. Ji, *Advanced energy materials* **2017**, *7*, 1602898.

[42] T.-F. Yi, S.-Y. Yang, Y. Xie, *Journal of Materials Chemistry A* **2015**, *3*, 5750–5777.

[43] J. T. Warner, *Lithium-ion battery chemistries: a primer*, Elsevier, **2019**.

[44] X. H. Liu, L. Zhong, S. Huang, S. X. Mao, T. Zhu, J. Y. Huang, *ACS nano* **2012**, *6*, 1522–1531.

[45] B. Wang, J. Ryu, S. Choi, X. Zhang, D. Pribat, X. Li, L. Zhi, S. Park, R. S. Ruoff, *ACS nano* **2019**, *13*, 2307–2315.

[46] Z. Li, M. Du, X. Guo, D. Zhang, Q. Wang, H. Sun, B. Wang, Y. A. Wu, *Chemical Engineering Journal* **2023**, 145294.

[47] X.-Y. Yu, L. Yu, X. W. Lou, *Advanced Energy Materials* **2016**, *6*, 1501333.

[48] Y. Lu, L. Yu, X. W. D. Lou, *Chem* **2018**, *4*, 972–996.

[49] J. Cabana, L. Monconduit, D. Larcher, M. R. Palacin, *Advanced materials* **2010**, *22*, E170–E192.

[50] G. Chen, L. Yan, H. Luo, S. Guo, *Advanced Materials* **2016**, *28*, 7580–7602.

[51] K. Zhang, X. Han, Z. Hu, X. Zhang, Z. Tao, J. Chen, *Chemical Society Reviews* **2015**, *44*, 699–728.

[52] H. B. Wu, G. Zhang, L. Yu, X. W. D. Lou, *Nanoscale Horizons* **2016**, *1*, 27–40.

[53] L. Cong, H. Xie, J. Li, *Advanced Energy Materials* **2017**, *7*, 1601906.

[54] H. Cheng, J. G. Shapter, Y. Li, G. Gao, *Journal of Energy Chemistry* **2021**, *57*, 451–468.

[55] S. Li, K. Wang, G. Zhang, S. Li, Y. Xu, X. Zhang, X. Zhang, S. Zheng, X. Sun, Y. Ma, *Advanced Functional Materials* **2022**, *32*, 2200796.

[56] L. Zhang, S. Ji, L. Yu, X. Xu, J. Liu, *RSC advances* **2017**, *7*, 24004–24010.

[57] W. Lee, S. Muhammad, C. Sergey, H. Lee, J. Yoon, Y.-M. Kang, W.-S. Yoon, *Angewandte Chemie International Edition* **2020**, *59*, 2578–2605.

[58] N. Nitta, F. Wu, J. T. Lee, G. Yushin, *Materials today* **2015**, *18*, 252–264.

[59] H. Sun, K. Zhao, *The Journal of Physical Chemistry C* **2017**, *121*, 6002–6010.

[60] H. Sun, K. Zhao, *The Journal of Physical Chemistry C* **2017**, *121*, 6002–6010.

[61] R. M. Salgado, F. Danzi, J. E. Oliveira, A. El-Azab, P. P. Camanho, M. H. Braga, *Molecules* **2021**, *26*, 3188.

[62] J. Kim, H. Cho, H. Y. Jeong, H. Ma, J. Lee, J. Hwang, M. Park, J. Cho, *Advanced Energy Materials* **2017**, *7*, 1602559.

[63] Z. Ahaliabadeh, X. Kong, E. Fedorovskaya, T. Kallio, *Journal of Power Sources* **2022**, *540*, 231633.

[64] H.-J. Noh, S. Youn, C. S. Yoon, Y.-K. Sun, *Journal of power sources* **2013**, *233*, 121–130.

[65] R. Chen, T. Zhao, X. Zhang, L. Li, F. Wu, *Nanoscale horizons* **2016**, *1*, 423–444.

[66] S. Kim, W. Cho, X. Zhang, Y. Oshima, J. W. Choi, *Nature communications* **2016**, *7*, 13598.

[67] S. Wan, W. Ma, Y. Xiao, S. Chen, *Batteries & Supercaps* **2022**, *5*, e202200368.

[68] Y.-K. Liu, C.-Z. Zhao, J. Du, X.-Q. Zhang, A.-B. Chen, Q. Zhang, *Small* **2023**, *19*, 2205315.

[69] L. Hu, Z. Zhang, K. Amine, *Electrochemistry communications* **2013**, *35*, 76–79.

[70] L. Suo, W. Xue, M. Gobet, S. G. Greenbaum, C. Wang, Y. Chen, W. Yang, Y. Li, J. Li, *Proceedings of the National Academy of Sciences* **2018**, *115*, 1156–1161.

[71] X. Fan, X. Ji, L. Chen, J. Chen, T. Deng, F. Han, J. Yue, N. Piao, R. Wang, X. Zhou, et al., *Nature Energy* **2019**, *4*, 882–890.

[72] J. Kalhoff, G. G. Eshetu, D. Bresser, S. Passerini, *ChemSusChem* **2015**, *8*, 2154–2175.

[73] G. Xu, X. Shangguan, S. Dong, X. Zhou, G. Cui, *Angewandte Chemie International Edition* **2020**, *59*, 3400–3415.

[74] T. Doi, R. Masuhara, M. Hashinokuchi, Y. Shimizu, M. Inaba, *Electrochimica Acta* **2016**, *209*, 219–224.

[75] W. Wang, J. Zhang, Q. Yang, S. Wang, W. Wang, B. Li, *ACS applied materials & interfaces* **2020**, *12*, 22901–22909.

[76] Z. Song, F. Chen, M. Martinez-Ibañez, W. Feng, M. Forsyth, Z. Zhou, M. Armand, H. Zhang, *Nature Communications* **2023**, *14*, 4884.

[77] S. Rana, R. C. Thakur, H. S. Dosanjh, *Solid State Ionics* **2023**, *400*, 116340.

[78] V. A. Nguyen, C. Kuss, *Journal of the Electrochemical Society* **2020**, *167*, 065501.

[79] H.-w. Jiang, Y. Yang, Y.-m. Nie, Z.-f. Su, Y.-f. Long, Y.-x. Wen, J. Su, *RSC advances* **2022**, *12*, 5997–6006.

[80] J. He, C. Das, F. Yang, J. Maibach, *Electrochimica acta* **2022**, *411*, 140038.

[81] A. Oishi, R. Tatara, E. Togo, H. Inoue, S. Yasuno, S. Komaba, *ACS Applied Materials & Interfaces* **2022**, *14*, 51808–51818.

[82] V. A. Nguyen, C. Kuss, *Journal of the Electrochemical Society* **2020**, *167*, 065501.

[83] P. Arora, *Chem. Rev* **2004**, *104*, 4419.

[84] R. Demir-Cakan, *Li-s Batteries: The Challenges Chemistry Materials And Future Perspectives* **2017**, 1.

[85] E. Cha, M. Patel, S. Bhoyate, V. Prasad, W. Choi, *Nanoscale Horizons* **2020**, *5*, 808–831.

[86] M. Wild, G. J. Offer, *Lithium-sulfur batteries*, John Wiley & Sons, **2019**.

[87] D. Parra, M. Swierczynski, D. I. Stroe, S. A. Norman, A. Abdon, J. Worlitschek, T. O'Doherty, L. Rodrigues, M. Gillott, X. Zhang, et al., *Renewable and Sustainable Energy Reviews* **2017**, *79*, 730–749.

[88] P. Kumta, A. F. Hepp, M. K. Datta, O. I. Velikokhatnyi, *Lithium-sulfur batteries: Advances in high-energy density batteries*, Elsevier, **2022**.

[89] Y. Yang, G. Zheng, S. Misra, J. Nelson, M. F. Toney, Y. Cui, *Journal of the American Chemical Society* **2012**, *134*, 15387–15394.

[90] M. Barghamadi, A. S. Best, A. I. Bhatt, A. F. Hollenkamp, M. Musameh, R. J. Rees, T. Ruther, *Energy & environmental science* **2014**, *7*, 3902–3920.

[91] S. Waluś, C. Barchasz, R. Bouchet, J.-C. Leprêtre, J.-F. Colin, J.-F. Martin, E. Elkaım, C. Baehtz, F. Alloin, *Advanced Energy Materials* **2015**, *5*, 1500165.

[92] Y. Huang, L. Lin, C. Zhang, L. Liu, Y. Li, Z. Qiao, J. Lin, Q. Wei, L. Wang, Q. Xie, et al., *Advanced Science* **2022**, *9*, 2106004.

[93] B.-W. Zhang, B. Sun, P. Fu, F. Liu, C. Zhu, B.-M. Xu, Y. Pan, C. Chen, *Membranes* **2022**, *12*, 790.

[94] H. Li, Y. Li, L. Zhang, *SusMat* **2022**, *2*, 34–64.

[95] A. Jozwiuk, B. B. Berkes, T. Weiß, H. Sommer, J. Janek, T. Brezesinski, *Energy & Environmental Science* **2016**, *9*, 2603–2608.

[96] N. Shen, H. Sun, B. Li, B. Xi, X. An, J. Li, S. Xiong, *Chemistry–A European Journal* **2023**, *29*, e202203031.

[97] Z.-C. Lv, P.-F. Wang, J.-C. Wang, S.-H. Tian, T.-F. Yi, *Journal of Industrial and Engineering Chemistry* **2023**.

[98] X. Yang, X. Li, K. Adair, H. Zhang, X. Sun, *Electrochemical Energy Reviews* **2018**, *1*, 239–293.

[99] U. Zubair et al., **2019**.

[100] X.-F. Yu, B. He, W.-C. Li, T. Wu, X.-R. Chen, A.-H. Lu, *Journal of Materials Chemistry A* **2022**, *10*, 12168–12176.

[101] M. Zhang, B. Chen, M. Wu, *Acta Physico-Chimica Sinica* **2022**, *38*, 2101001–.

[102] F. Sultanov, A. Mentbayeva, S. Kalybekkyzy, A. Zhaisanova, S.-T. Myung, Z. Bakenov, *Carbon* **2023**, *201*, 679–702.

[103] A. I. Kamisan, T. I. T. Kudin, A. S. Kamisan, A. F. C. Omar, M. F. M. Taib, O. H. Hassan, M. Z. A. Yahya, et al., *International Journal of Hydrogen Energy* **2022**, *47*, 8630–8657.

[104] W. Hooch Antink, Y. Choi, K.-d. Seong, J. M. Kim, Y. Piao, *Advanced Materials Interfaces* **2018**, *5*, 1701212.

[105] L. Borchardt, M. Oschatz, S. Kaskel, *Chemistry–A European Journal* **2016**, *22*, 7324–7351.

[106] P. Wang, B. Xi, M. Huang, W. Chen, J. Feng, S. Xiong, *Advanced Energy Materials* **2021**, *11*, 2002893.

[107] S. Evers, T. Yim, L. F. Nazar, *The Journal of Physical Chemistry C* **2012**, *116*, 19653–19658.

[108] J. Li, B. Ding, G. Xu, L. Hou, X. Zhang, C. Yuan, *Nanoscale* **2013**, *5*, 5743–5746.

[109] X. Z. Ma, B. Jin, H. Y. Wang, J. Z. Hou, X. B. Zhong, H. H. Wang, P. M. Xin, *Journal of Electroanalytical Chemistry* **2015**, *736*, 127–131.

[110] Q. Li, Z. Zhang, K. Zhang, L. Xu, J. Fang, Y. Lai, J. Li, *Journal of solid state electrochemistry* **2013**, *17*, 2959–2965.

[111] K. Xie, K. Zhang, Y. Han, K. Yuan, Q. Song, J.-g. Wang, C. Shen, X. Liu, B. Wei, *Electrochimica Acta* **2016**, *210*, 415–421.

[112] Z. Wei Seh, W. Li, J. J. Cha, G. Zheng, Y. Yang, M. T. McDowell, P.-C. Hsu, Y. Cui, *Nature communications* **2013**, *4*, 1331.

[113] Q. Pang, D. Kundu, M. Cuisinier, L. Nazar, *Nature communications* **2014**, *5*, 4759.

[114] U. Zubair, J. Amici, C. Francia, D. McNulty, S. Bodoardo, C. O'Dwyer, *ChemSusChem* **2018**, *11*, 1838–1848.

[115] G. Zhou, H. Tian, Y. Jin, X. Tao, B. Liu, R. Zhang, Z. W. Seh, D. Zhuo, Y. Liu, J. Sun, et al., *Proceedings of the National Academy of Sciences* **2017**, *114*, 840–845.

[116] X. Liang, C. Y. Kwok, F. Lodi-Marzano, Q. Pang, M. Cuisinier, H. Huang, C. J. Hart, D. Houtarde, K. Kaup, H. Sommer, et al., *Advanced Energy Materials* **2016**, *6*, 1501636.

[117] U. Zubair, K. Jori, J. E. Thomas, J. Amici, C. Francia, S. Bodoardo, *Journal of Power Sources* **2023**, *580*, 233457.

[118] X. Li, C. Shao, X. Wang, J. Wang, G. Liu, W. Yu, X. Dong, J. Wang, *Chemical Engineering Journal* **2022**, *446*, 137267.

[119] Y. Xing, M. Zhang, J. Guo, X. Fang, H. Cui, X. Hu, X. Cao, *Journal of Solid State Chemistry* **2022**, *316*, 123642.

[120] F.-J. Liu, W.-L. Luo, Z. Zhang, J. Yu, J.-X. Cai, Z.-Y. Yang, *Chemical Engineering Journal* **2023**, *456*, 140948.

[121] Z. Yuan, H.-J. Peng, T.-Z. Hou, J.-Q. Huang, C.-M. Chen, D.-W. Wang, X.-B. Cheng, F. Wei, Q. Zhang, *Nano letters* **2016**, *16*, 519–527.

[122] Q. Pang, D. Kundu, L. F. Nazar, *Materials Horizons* **2016**, *3*, 130–136.

[123] Z. W. Seh, J. H. Yu, W. Li, P.-C. Hsu, H. Wang, Y. Sun, H. Yao, Q. Zhang, Y. Cui, *Nature communications* **2014**, *5*, 5017.

[124] C. Y. Zhang, C. Zhang, J. L. Pan, G. W. Sun, Z. Shi, C. Li, X. Chang, G. Z. Sun, J. Y. Zhou, A. Cabot, *eScience* **2022**, *2*, 405–415.

[125] D. Versaci, I. Canale, S. Goswami, J. Amici, C. Francia, E. Fortunato, R. Martins, L. Pereira, S. Bodoardo, *Journal of Power Sources* **2022**, *521*, 230945.

[126] C. Wei, Y. Han, H. Liu, R. Gan, Q. Li, Y. Wang, P. Hu, C. Ma, J. Shi, *Carbon* **2021**, *184*, 1–11.

[127] Z. Jin, T. Lin, H. Jia, B. Liu, Q. Zhang, L. Chen, L. Zhang, L. Li, Z. Su, C. Wang, *Nanoscale* **2020**, *12*, 16201–16207.

[128] J. Liu, S. Xiao, L. Chang, L. Lai, R. Wu, Y. Xiang, X. Liu, J. S. Chen, *Journal of Energy Chemistry* **2021**, *56*, 343–352.

[129] Z. Shen, X. Jin, J. Tian, M. Li, Y. Yuan, S. Zhang, S. Fang, X. Fan, W. Xu, H. Lu, et al., *Nature Catalysis* **2022**, *5*, 555–563.

[130] H. Li, L. Sun, Y. Zhao, T. Tan, Y. Zhang, *Applied Surface Science* **2019**, *466*, 309–319.

[131] T. Li, X. Bai, U. Gulzar, Y.-J. Bai, C. Capiglia, W. Deng, X. Zhou, Z. Liu, Z. Feng, R. Proietti Zaccaria, *Advanced Functional Materials* **2019**, *29*, 1901730.

[132] S. S. Zhang, *Journal of Power Sources* **2013**, *231*, 153–162.

[133] N. Angulakshmi, A. M. Stephan, *Frontiers in Energy Research* **2015**, *3*, 17.

[134] S. Xiong, K. Xie, Y. Diao, X. Hong, *Electrochimica Acta* **2012**, *83*, 78–86.

[135] C. Wang, K. Su, W. Wan, H. Guo, H. Zhou, J. Chen, X. Zhang, Y. Huang, *Journal of Materials Chemistry A* **2014**, *2*, 5018–5023.

[136] X. Liang, C. Hart, Q. Pang, A. Garsuch, T. Weiss, L. F. Nazar, *Nature communications* **2015**, *6*, 5682.

[137] X. Li, Y. Lu, Z. Hou, W. Zhang, Y. Zhu, Y. Qian, J. Liang, Y. Qian, *ACS applied materials & interfaces* **2016**, *8*, 19550–19557.

[138] X. Liang, Y. Rangom, C. Y. Kwok, Q. Pang, L. F. Nazar, *Advanced Materials* **2017**, *29*, 1603040.

[139] U. Zubair, S. Bianco, J. Amici, C. Francia, S. Bodoardo, *Journal of Power Sources* **2020**, *461*, 228144.

[140] Y. Zhong, X. Xu, Y. Liu, W. Wang, Z. Shao, *Polyhedron* **2018**, *155*, 464–484.

[141] G. Li, X. Wang, M. H. Seo, M. Li, L. Ma, Y. Yuan, T. Wu, A. Yu, S. Wang, J. Lu, et al., *Nature communications* **2018**, *9*, 705.

[142] W. Chen, T. Lei, T. Qian, W. Lv, W. He, C. Wu, X. Liu, J. Liu, B. Chen, C. Yan, et al., *Advanced Energy Materials* **2018**, *8*, 1702889.

[143] D. Chen, K. Wen, W. Lv, Z. Wei, W. He, *physica status solidi (RRL)–Rapid Research Letters* **2018**, *12*, 1800249.

[144] T. Li, X. Bai, U. Gulzar, Y.-J. Bai, C. Capiglia, W. Deng, X. Zhou, Z. Liu, Z. Feng, R. Proietti Zaccaria, *Advanced Functional Materials* **2019**, *29*, 1901730.

[145] P.-K. Huang, J.-W. Yeh, T.-T. Shun, S.-K. Chen, *Advanced Engineering Materials* **2004**, *6*, 74–78.

[146] J.-W. Yeh, S.-K. Chen, S.-J. Lin, J.-Y. Gan, T.-S. Chin, T.-T. Shun, C.-H. Tsau, S.-Y. Chang, *Advanced engineering materials* **2004**, *6*, 299–303.

[147] M. C. Gao, J.-W. Yeh, P. K. Liaw, Y. Zhang, *High-entropy alloys: fundamentals and applications*, Springer, **2016**.

[148] C. M. Rost, E. Sachet, T. Borman, A. Moballegh, E. C. Dickey, D. Hou, J. L. Jones, S. Curtarolo, J.-P. Maria, *Nature communications* **2015**, *6*, 8485.

[149] A. Iqbal, Z. A. Ghazi, A. M. Khattak, A. Ahmad, *Journal of Solid State Chemistry* **2017**, *256*, 189–195.

[150] Y. Zheng, Y. Yi, M. Fan, H. Liu, X. Li, R. Zhang, M. Li, Z.-A. Qiao, *Energy Storage Materials* **2019**, *23*, 678–683.

[151] L. Tian, Z. Zhang, S. Liu, G. Li, X. Gao, *Energy & Environmental Materials* **2022**, *5*, 645–654.

[152] M. Kheradmandfard, S. F. Kashani-Bozorg, A. H. Noori-Alfesharaki, A. Z. Kharazi, M. Kheradmandfard, N. Abutalebi, *Materials Science and Engineering: C* **2018**, *92*, 236–244.

[153] M. Kheradmandfard, H. Minouei, N. Tsvetkov, A. K. Vayghan, S. F. Kashani-Bozorg, G. Kim, S. I. Hong, D.-E. Kim, *Materials Chemistry and Physics* **2021**, *262*, 124265.

[154] M. J. Collins Jr, *Future medicinal chemistry* **2010**, *2*, 151–155.

[155] Y. Li, W. Yang, *Journal of Membrane Science* **2008**, *316*, 3–17.

[156] A. De la Hoz, A. Diaz-Ortiz, A. Moreno, *Chemical Society Reviews* **2005**, *34*, 164–178.

[157] C. O. Kappe, *Angewandte Chemie International Edition* **2004**, *43*, 6250–6284.

[158] M. Baghbanzadeh, L. Carbone, P. D. Cozzoli, C. O. Kappe, *Angewandte Chemie International Edition* **2011**, *50*, 11312–11359.

[159] W. C. Conner, G. A. Tompsett, *The Journal of Physical Chemistry B* **2008**, *112*, 2110–2118.

[160] A. Mao, H.-Z. Xiang, Z.-G. Zhang, K. Kuramoto, H. Yu, S. Ran, *Journal of Magnetism and Magnetic Materials* **2019**, *484*, 245–252.

[161] D. Berardan, A. Meena, S. Franger, C. Herrero, N. Dragoe, *Journal of Alloys and Compounds* **2017**, *704*, 693–700.

[162] M. Biesuz, L. Spiridigliozzi, G. Dell'Agli, M. Bortolotti, V. M. Sglavo, *Journal of materials science* **2018**, *53*, 8074–8085.

[163] M. S. Lal, R. Sundara, *ACS applied materials & interfaces* **2019**, *11*, 30846–30857.

[164] Y. Zheng, Y. Yi, M. Fan, H. Liu, X. Li, R. Zhang, M. Li, Z.-A. Qiao, *Energy Storage Materials* **2019**, *23*, 678–683.

[165] S. Evers, T. Yim, L. F. Nazar, *The Journal of Physical Chemistry C* **2012**, *116*, 19653–19658.

[166] M. Biesuz, L. Spiridigliozzi, G. Dell'Agli, M. Bortolotti, V. M. Sglavo, *Journal of materials science* **2018**, *53*, 8074–8085.

[167] X. Zhao, J. Wang, X. Sun, K. Wei, W. Wang, A. Wang, Y. Huang, Y. Guan, *Journal of The Electrochemical Society* **2021**, *168*, 040506.

[168] C. Barchasz, F. Molton, C. Duboc, J.-C. Leprêtre, S. Patoux, F. Alloin, *Analytical chemistry* **2012**, *84*, 3973–3980.

[169] Y. Wang, X. Guo, C. Chen, Y. Wang, Q. Li, Z. Wu, B. Zhong, Y. Chen, *Electrochimica Acta* **2020**, *354*, 136704.

[170] M. Kheradmandfard, H. Minouei, N. Tsvetkov, A. K. Vayghan, S. F. Kashani-Bozorg, G. Kim, S. I. Hong, D.-E. Kim, *Materials Chemistry and Physics* **2021**, *262*, 124265.

[171] R. Ponraj, A. G. Kannan, J. H. Ahn, D.-W. Kim, *ACS applied materials & interfaces* **2016**, *8*, 4000–4006.

[172] N. J. Usharani, R. Shringi, H. Sanghavi, S. Subramanian, S. Bhattacharya, *Dalton Transactions* **2020**, *49*, 7123–7132.

[173] Z. Yuan, H.-J. Peng, T.-Z. Hou, J.-Q. Huang, C.-M. Chen, D.-W. Wang, X.-B. Cheng, F. Wei, Q. Zhang, *Nano letters* **2016**, *16*, 519–527.

[174] Y.-T. Liu, D.-D. Han, L. Wang, G.-R. Li, S. Liu, X.-P. Gao, *Advanced Energy Materials* **2019**, *9*, 1803477.

[175] X. Tao, J. Wang, C. Liu, H. Wang, H. Yao, G. Zheng, Z. W. Seh, Q. Cai, W. Li, G. Zhou, et al., *Nature communications* **2016**, *7*, 11203.

[176] A. Sarkar, Q. Wang, A. Schiele, M. R. Chellali, S. S. Bhattacharya, D. Wang, T. Brezesinski, H. Hahn, L. Velasco, B. Breitung, *Advanced Materials* **2019**, *31*, 1806236.

[177] Y.-S. Su, Y. Fu, T. Cochell, A. Manthiram, *Nature communications* **2013**, *4*, 2985.

[178] Y.-C. Lin, Y.-H. Wu, J.-M. Ting, S.-H. Chung, *Energy & Fuels* **2023**.

[179] R. Colombo, D. Versaci, J. Amici, F. Bella, M. L. Para, N. Garino, M. Laurenti, S. Bodoardo, C. Francia, *Nanomaterials* **2023**, *13*, 2149.

[180] R. Thangavel, A. G. Kannan, R. Ponraj, K. Kaliyappan, W.-S. Yoon, D.-W. Kim, Y.-S. Lee, *Nanomaterials* **2020**, *10*, 1220.

[181] B. Wei, C. Shang, X. Pan, Z. Chen, L. Shui, X. Wang, G. Zhou, *Nanomaterials* **2019**, *9*, 1724.

[182] H.-J. Kang, G. A. R. Bari, T.-G. Lee, T. T. Khan, J.-W. Park, H. J. Hwang, S. Y. Cho, Y.-S. Jun, *Nanomaterials* **2020**, *10*, 2012.

[183] J. Castillo, A. Santiago, X. Judez, J. A. Coca-Clemente, A. Saenz de Buruaga, J. L. Gomez-Urbano, J. A. Gonzalez-Marcos, M. Armand, C. Li, D. Carriazo, *ACS Applied Energy Materials* **2023**, *6*, 3579–3589.

[184] B. Wang, T. Li, X. Qian, L. Jin, S. Yao, X. Shen, S. Qin, *Journal of Solid State Electrochemistry* **2021**, *25*, 1579–1590.

[185] Z. Cao, Y. Wang, J. Guo, J. Jia, Z. Zhang, Y. Cui, Y. Yin, M. Yang, S. Yang, *Carbon* **2023**, *204*, 102–111.

[186] X.-Y. Yu, L. Yu, X. W. Lou, *Advanced Energy Materials* **2016**, *6*, 1501333.

[187] H. Lu, Q. Guo, Q. Fan, L. Xue, X. Lu, F. Zan, H. Xia, *Journal of Alloys and Compounds* **2021**, *870*, 159341.

[188] G. Zhou, H. Tian, Y. Jin, X. Tao, B. Liu, R. Zhang, Z. W. Seh, D. Zhuo, Y. Liu, J. Sun, et al., *Proceedings of the National Academy of Sciences* **2017**, *114*, 840–845.

[189] W. Sun, Y. Li, S. Liu, Q. Guo, Y. Zhu, X. Hong, C. Zheng, K. Xie, *Nano Research* **2020**, *13*, 2143–2148.

[190] W. Zhang, D. Hong, Z. Su, S. Yi, L. Tian, B. Niu, Y. Zhang, D. Long, *Energy Storage Materials* **2022**, *53*, 404–414.

[191] R. Liu, W. Tao, Y. Du, C. Wu, H. Ye, M. Fan, S. Chen, G. Chen, J. Mao, S. Xin, et al., *ACS Applied Energy Materials* **2022**, *5*, 12408–12414.

[192] R. Razaq, D. Sun, J. Wang, Y. Xin, G. Abbas, J. Zhang, Q. Li, T. Huang, Z. Zhang, Y. Huang, *Journal of Power Sources* **2019**, *414*, 453–459.

[193] S. Kumar, A. Garg, A. Chowdhuri, *Materials Research Express* **2019**, *6*, 085620.

[194] X. Wang, J. Wang, D. Wang, S. Dou, Z. Ma, J. Wu, L. Tao, A. Shen, C. Ouyang, Q. Liu, et al., *Chemical communications* **2014**, *50*, 4839–4842.

[195] K. Satheesh, R. Jayavel, *Materials Letters* **2013**, *113*, 5–8.

[196] J. Yan, X. Fang, L. Zhang, Y. Bando, U. K. Gautam, B. Dierre, T. Sekiguchi, D. Golberg, *Nano Letters* **2008**, *8*, 2794–2799.

[197] D. Jiang, L. Cao, W. Liu, G. Su, H. Qu, Y. Sun, B. Dong, *Nanoscale research letters* **2009**, *4*, 78–83.

[198] D. Versaci, M. Cozzarin, J. Amici, C. Francia, E. P. Leiva, A. Visintin, S. Bodoardo, *Applied Materials Today* **2021**, *25*, 101169.

[199] C.-Y. Fan, H.-Y. Yuan, H.-H. Li, H.-F. Wang, W.-L. Li, H.-Z. Sun, X.-L. Wu, J.-P. Zhang, *ACS applied materials & interfaces* **2016**, *8*, 16108–16115.

[200] J.-W. Park, H. J. Hwang, H.-J. Kang, G. A. R. Bari, T.-G. Lee, B.-H. An, S. Y. Cho, Y.-S. Jun, *Nanomaterials* **2021**, *11*, 408.

[201] A. M. Golsheikh, N. Huang, H. Lim, R. Zakaria, *Rsc Advances* **2014**, *4*, 36401–36411.

[202] M. Thommes, K. Kaneko, A. V. Neimark, J. P. Olivier, F. Rodriguez-Reinoso, J. Rouquerol, K. S. Sing, *Pure and applied chemistry* **2015**, *87*, 1051–1069.

[203] L. Shen, L. Zhang, K. Wang, L. Miao, Q. Lan, K. Jiang, H. Lu, M. Li, Y. Li, B. Shen, et al., *RSC advances* **2018**, *8*, 17209–17217.

[204] N. Dengo, A. F. De Fazio, M. Weiss, R. Marschall, P. Dolcet, M. Fanetti, S. Gross, *Inorganic Chemistry* **2018**, *57*, 13104–13114.

[205] J. Song, T. Xu, M. L. Gordin, P. Zhu, D. Lv, Y.-B. Jiang, Y. Chen, Y. Duan, D. Wang, *Advanced functional materials* **2014**, *24*, 1243–1250.

[206] H.-J. Peng, T.-Z. Hou, Q. Zhang, J.-Q. Huang, X.-B. Cheng, M.-Q. Guo, Z. Yuan, L.-Y. He, F. Wei, *Advanced Materials Interfaces* **2014**, *1*, 1400227.

[207] H. Lin, L. Yang, X. Jiang, G. Li, T. Zhang, Q. Yao, G. W. Zheng, J. Y. Lee, *Energy & Environmental Science* **2017**, *10*, 1476–1486.

[208] G. JIN, H. HE, J. WU, M. ZHANG, Y. LI, Y. LIU, *Journal of Inorganic Materials* **2021**, *36*.

[209] Y. Li, H. Wang, L. Xie, Y. Liang, G. Hong, H. Dai, *Journal of the American Chemical Society* **2011**, *133*, 7296–7299.

[210] Q. Pang, C. Y. Kwok, D. Kundu, X. Liang, L. F. Nazar, *Joule* **2019**, *3*, 136–148.

[211] J.-L. Yang, S.-X. Zhao, Y.-M. Lu, X.-T. Zeng, W. Lv, G.-Z. Cao, *Journal of Materials Chemistry A* **2020**, *8*, 231–241.

[212] F. Y. Fan, W. C. Carter, Y.-M. Chiang, *Advanced Materials* **2015**, *27*, 5203–5209.

[213] Z. Li, Y. Zhou, Y. Wang, Y.-C. Lu, *Advanced Energy Materials* **2019**, *9*, 1802207.

[214] J.-L. Yang, D.-Q. Cai, X.-G. Hao, L. Huang, Q. Lin, X.-T. Zeng, S.-X. Zhao, W. Lv, *ACS nano* **2021**, *15*, 11491–11500.

[215] Z. Han, S. Zhao, J. Xiao, X. Zhong, J. Sheng, W. Lv, Q. Zhang, G. Zhou, H.-M. Cheng, *Advanced Materials* **2021**, *33*, 2105947.

[216] W. Yao, W. Zheng, J. Xu, C. Tian, K. Han, W. Sun, S. Xiao, *ACS nano* **2021**, *15*, 7114–7130.

[217] Z. Yuan, H.-J. Peng, T.-Z. Hou, J.-Q. Huang, C.-M. Chen, D.-W. Wang, X.-B. Cheng, F. Wei, Q. Zhang, *Nano letters* **2016**, *16*, 519–527.

[218] Y. Gorlin, M. U. Patel, A. Freiberg, Q. He, M. Piana, M. Tromp, H. A. Gasteiger, *Journal of The Electrochemical Society* **2016**, *163*, A930.

[219] D. Di Lecce, R. Brescia, A. Scarpellini, M. Prato, J. Hassoun, *ChemSusChem* **2016**, *9*, 223–230.

[220] L. Carbone, T. Coneglian, M. Gobet, S. Munoz, M. Devany, S. Greenbaum, J. Hassoun, *Journal of Power Sources* **2018**, *377*, 26–35.

[221] C. Heubner, T. Liebmann, M. Schneider, A. Michaelis, *Electrochimica Acta* **2018**, *269*, 745–760.

[222] W. Lee, S. Muhammad, C. Sergey, H. Lee, J. Yoon, Y.-M. Kang, W.-S. Yoon, *Angewandte Chemie International Edition* **2020**, *59*, 2578–2605.

[223] Y. Zhang, Q. Liang, C. Huang, P. Gao, H. Shu, X. Zhang, X. Yang, L. Liu, X. Wang, *Journal of Solid State Electrochemistry* **2018**, *22*, 1995–2002.

[224] V. Ragupathi, S. Krishnaswamy, S. Raman, P. Panigrahi, J. Lee, G. S. Nagarajan, *Applied Surface Science* **2018**, *449*, 421–425.

[225] G. Liang, V. K. Peterson, K. W. See, Z. Guo, W. K. Pang, *Journal of Materials Chemistry A* **2020**, *8*, 15373–15398.

[226] Y. Xue, L.-L. Zheng, J. Wang, J.-G. Zhou, F.-D. Yu, G.-J. Zhou, Z.-B. Wang, *ACS Applied Energy Materials* **2019**, *2*, 2982–2989.

[227] N. Voronina, Y.-K. Sun, S.-T. Myung, *ACS Energy Letters*.

[228] H. Wang, W.-D. Zhang, L.-Y. Zhu, M.-C. Chen, *Solid State Ionics* **2007**, *178*, 131–136.

[229] K. Zaghib, M. Trudeau, A. Guerfi, J. Trottier, A. Mauger, R. Veillette, C. Julien, *Journal of Power Sources* **2012**, *204*, 177–181.

[230] E.-S. Lee, A. Huq, H.-Y. Chang, A. Manthiram, *Chemistry of Materials* **2012**, *24*, 600–612.

[231] J. Xiang, J. Tu, L. Zhang, X. Wang, Y. Zhou, Y. Qiao, Y. Lu, *Journal of Power Sources* **2010**, *195*, 8331–8335.

[232] T.-F. Yi, Y.-M. Li, X.-Y. Li, J.-J. Pan, Q. Zhang, Y.-R. Zhu, *Science Bulletin* **2017**, *62*, 1004–1010.

[233] D. Liu, J. Trottier, P. Charest, J. Frechette, A. Guerfi, A. Mauger, C. Julien, K. Zaghib, *Journal of Power Sources* **2012**, *204*, 127–132.

[234] F. Vasquez, N. Rosero-Navarro, A. Miura, Y. Goto, K. Tadanaga, J. Calderon, *Electrochimica Acta* **2023**, *437*, 141544.

[235] M. Fehse, N. Etxebarria, L. Otaegui, M. Cabello, S. Martin-Fuentes, M. A. Cabanero, I. Monterrubio, C. F. Elkjaer, O. Fabelo, N. A. Enkubari, et al., *Chemistry of Materials* **2022**, *34*, 6529–6540.

[236] L. Wang, H. Li, X. Huang, E. Baudrin, *Solid State Ionics* **2011**, *193*, 32–38.

[237] M. M. Thackeray, *Progress in Solid State Chemistry* **1997**, *25*, 1–71.

[238] X. Ma, B. Kang, G. Ceder, *Journal of The Electrochemical Society* **2010**, *157*, A925.

[239] M. Fehse, N. Etxebarria, L. Otaegui, M. Cabello, S. Martin-Fuentes, M. A. Cabanero, I. Monterrubio, C. F. Elkjaer, O. Fabelo, N. A. Enkubari, et al., *Chemistry of Materials* **2022**, *34*, 6529–6540.

[240] R. Amin, I. Belharouk, *Journal of Power Sources* **2017**, *348*, 311–317.

[241] D. Liu, W. Zhu, J. Trottier, C. Gagnon, F. Barray, A. Guerfi, A. Mauger, H. Groult, C. Julien, J. Goodenough, et al., *Rsc Advances* **2014**, *4*, 154–167.

[242] G. Liang, V. K. Peterson, K. W. See, Z. Guo, W. K. Pang, *Journal of Materials Chemistry A* **2020**, *8*, 15373–15398.

[243] D. Aurbach, B. Markovsky, A. Shechter, Y. Ein-Eli, H. Cohen, *Journal of the Electrochemical Society* **1996**, *143*, 3809.

[244] L. Yang, B. Ravdel, B. L. Lucht, *Electrochemical and Solid-State Letters* **2010**, *13*, A95.

[245] N. P. Pieczonka, Z. Liu, P. Lu, K. L. Olson, J. Moote, B. R. Powell, J.-H. Kim, *The Journal of Physical Chemistry C* **2013**, *117*, 15947–15957.

[246] R. Qiao, Y. Wang, P. Olalde-Velasco, H. Li, Y.-S. Hu, W. Yang, *Journal of Power Sources* **2015**, *273*, 1120–1126.

[247] H. Sun, A. Hu, S. Spence, C. Kuai, D. Hou, L. Mu, J. Liu, L. Li, C. Sun, S. Sainio, et al., *Advanced Functional Materials* **2022**, *32*, 2112279.

[248] N.-S. Choi, J.-T. Yeon, Y.-W. Lee, J.-G. Han, K. T. Lee, S.-S. Kim, *Solid State Ionics* **2012**, *219*, 41–48.

[249] Z. Zou, H. Xu, H. Zhang, Y. Tang, G. Cui, *ACS Applied Materials & Interfaces* **2020**, *12*, 21368–21385.

[250] N.-S. Choi, J.-T. Yeon, Y.-W. Lee, J.-G. Han, K. T. Lee, S.-S. Kim, *Solid State Ionics* **2012**, *219*, 41–48.

[251] L. Xing, O. Borodin, G. D. Smith, W. Li, *The Journal of Physical Chemistry A* **2011**, *115*, 13896–13905.

[252] O. Borodin, T. Jow, *ECS Transactions* **2011**, *33*, 77.

[253] K. Xu, *Chemical reviews* **2004**, *104*, 4303–4418.

[254] M. Metzger, C. Marino, J. Sicklinger, D. Haering, H. A. Gasteiger, *Journal of The Electrochemical Society* **2015**, *162*, A1123.

[255] K. Leung, *The Journal of Physical Chemistry C* **2012**, *116*, 9852–9861.

[256] R. Sahore, D. C. O'Hanlon, A. Tornheim, C.-W. Lee, J. C. Garcia, H. Iddir, M. Balasubramanian, I. Bloom, *Journal of The Electrochemical Society* **2020**, *167*, 020513.

[257] S. Martha, B. Markovsky, J. Grinblat, Y. Gofer, O. Haik, E. Zinigrad, D. Aurbach, T. Drezen, D. Wang, G. Deghenghi, et al., *Journal of the Electrochemical Society* **2009**, *156*, A541.

[258] Y. Yu, P. Karayaylali, Y. Katayama, L. Giordano, M. Gauthier, F. Maglia, R. Jung, I. Lund, Y. Shao-Horn, *The Journal of Physical Chemistry C* **2018**, *122*, 27368–27382.

[259] J. L. Tebbe, T. F. Fuerst, C. B. Musgrave, *ACS Applied Materials & Interfaces* **2016**, *8*, 26664–26674.

[260] L. Yang, B. Ravdel, B. L. Lucht, *Electrochemical and Solid-State Letters* **2010**, *13*, A95.

[261] M. He, L. Boulet-Roblin, P. Borel, C. Tessier, P. Novak, C. Villevieille, E. J. Berg, *Journal of The Electrochemical Society* **2015**, *163*, A83.

[262] M. Moshkovich, M. Cojocaru, H. Gottlieb, D. Aurbach, *Journal of Electroanalytical Chemistry* **2001**, *497*, 84–96.

[263] Y. Cai, S.-Z. Huang, F.-S. She, J. Liu, R.-L. Zhang, Z.-H. Huang, F.-Y. Wang, H.-E. Wang, *RSC Advances* **2016**, *6*, 2785–2792.

[264] X. Zhu, X. Li, Y. Zhu, S. Jin, Y. Wang, Y. Qian, *Journal of Power Sources* **2014**, *261*, 93–100.

[265] H. Liu, G. Liang, C. Gao, S. Bi, Q. Chen, Y. Xie, S. Fan, L. Cao, W. K. Pang, Z. Guo, *Nano Energy* **2019**, *66*, 104100.

[266] W. Sun, Y. Li, K. Xie, S. Luo, G. Bai, X. Tan, C. Zheng, *Nano Energy* **2018**, *54*, 175–183.

[267] B. Hai, A. K. Shukla, H. Duncan, G. Chen, *Journal of Materials Chemistry A* **2013**, *1*, 759–769.

[268] K. R. Chemelewski, D. W. Shin, W. Li, A. Manthiram, *Journal of Materials Chemistry A* **2013**, *1*, 3347–3354.

[269] S. H. Oh, K. Y. Chung, S. H. Jeon, C. S. Kim, W. I. Cho, B. W. Cho, *Journal of Alloys and Compounds* **2009**, *469*, 244–250.

[270] J.-J. Shiu, W. K. Pang, S.-h. Wu, *Journal of power sources* **2013**, *244*, 35–42.

[271] T. Yang, N. Zhang, Y. Lang, K. Sun, *Electrochimica Acta* **2011**, *56*, 4058–4064.

[272] N.-S. Choi, K. H. Yew, K. Y. Lee, M. Sung, H. Kim, S.-S. Kim, *Journal of Power Sources* **2006**, *161*, 1254–1259.

[273] J. Xia, M. Nie, J. Burns, A. Xiao, W. Lamanna, J. Dahn, *Journal of Power Sources* **2016**, *307*, 340–350.

[274] C.-H. Yim, J. Tam, H. Soboleski, Y. Abu-Lebdeh, *Journal of The Electrochemical Society* **2017**, *164*, A1002.

[275] Y. Yamada, A. Yamada, *Journal of The Electrochemical Society* **2015**, *162*, A2406.

[276] D. W. McOwen, D. M. Seo, O. Borodin, J. Vatamanu, P. D. Boyle, W. A. Henderson, *Energy & Environmental Science* **2014**, *7*, 416–426.

[277] X. Fan, C. Wang, *Chemical Society Reviews* **2021**, *50*, 10486–10566.

[278] M. Armand, F. Endres, D. R. MacFarlane, H. Ohno, B. Scrosati, *Nature materials* **2009**, *8*, 621–629.

[279] E. T. Fox, J. E. Weaver, W. A. Henderson, *The Journal of Physical Chemistry C* **2012**, *116*, 5270–5274.

[280] H. Matsumoto, N. Terasawa, T. Umecky, S. Tsuzuki, H. Sakaebe, K. Asaka, K. Tatsumi, *Chemistry letters* **2008**, *37*, 1020–1021.

[281] A. L. Michan, B. S. Parimalam, M. Leskes, R. N. Kerber, T. Yoon, C. P. Grey, B. L. Lucht, *Chemistry of Materials* **2016**, *28*, 8149–8159.

[282] R. Petibon, E. Henry, J. Burns, N. Sinha, J. Dahn, *Journal of The Electrochemical Society* **2013**, *161*, A66.

[283] X. Zuo, J. Wu, M. Zhao, C. Wang, J. Liu, J. Nan, *Ionics* **2016**, *22*, 201–208.

[284] J. Im, J. Lee, M.-H. Ryou, Y. M. Lee, K. Y. Cho, *Journal of The Electrochemical Society* **2017**, *164*, A6381.

[285] K. Kim, Y. Kim, S. Park, H. J. Yang, S. J. Park, K. Shin, J.-J. Woo, S. Kim, S. Y. Hong, N.-S. Choi, *Journal of Power Sources* **2018**, *396*, 276–287.

[286] M. Xu, L. Zhou, Y. Dong, U. Tottempudi, J. Demeaux, A. Garsuch, B. L. Lucht, *ECS Electrochemistry Letters* **2015**, *4*, A83.

[287] Q. Yu, Z. Chen, L. Xing, D. Chen, H. Rong, Q. Liu, W. Li, *Electrochimica Acta* **2015**, *176*, 919–925.

[288] M. Hadouchi, T. Koketsu, Z. Hu, J. Ma, *Battery energy* **2022**, *1*, 20210010.

[289] J.-M. Tarascon, M. Armand, *nature* **2001**, *414*, 359–367.

[290] D. Morgan, A. Van der Ven, G. Ceder, *Electrochemical and solid-state letters* **2003**, *7*, A30.

[291] M. S. Islam, D. J. Driscoll, C. A. Fisher, P. R. Slater, *Chemistry of Materials* **2005**, *17*, 5085–5092.

[292] T. Maxisch, F. Zhou, G. Ceder, *Physical review B* **2006**, *73*, 104301.

[293] C. Delacourt, C. Wurm, L. Laffont, J.-B. Leriche, C. Masquelier, *Solid State Ionics* **2006**, *177*, 333–341.

[294] P. P. Prosini, *Journal of the Electrochemical Society* **2005**, *152*, A1925.

[295] T. Zhang, X. Liu, P. He, R. Peng, M. Wang, M. Han, H. Zhou, et al., *Journal of power sources* **2013**, *233*, 299–303.

[296] V. Srinivasan, J. Newman, *Electrochemical and solid-state letters* **2006**, *9*, A110.

[297] C. Delmas, M. Maccario, L. Croguennec, F. Le Cras, F. Weill, *Nature materials* **2008**, *7*, 665–671.

[298] G. Kobayashi, S.-i. Nishimura, M.-S. Park, R. Kanno, M. Yashima, T. Ida, A. Yamada, *Advanced Functional Materials* **2009**, *19*, 395–403.

[299] P. Gibot, M. Casas-Cabanas, L. Laffont, S. Levasseur, P. Carlach, S. Hamelet, J.-M. Tarascon, C. Masquelier, *Nature materials* **2008**, *7*, 741–747.

[300] P. Bai, D. A. Cogswell, M. Z. Bazant, *Nano letters* **2011**, *11*, 4890–4896.

[301] H. Liu, F. C. Strobridge, O. J. Borkiewicz, K. M. Wiaderek, K. W. Chapman, P. J. Chupas, C. P. Grey, *Science* **2014**, *344*, 1252817.

[302] M. Hadouchi, T. Koketsu, Z. Hu, J. Ma, *Battery energy* **2022**, *1*, 20210010.

[303] L. Laffont, C. Delacourt, P. Gibot, M. Y. Wu, P. Kooyman, C. Masquelier, J. M. Tarascon, *Chemistry of materials* **2006**, *18*, 5520–5529.

[304] J. Hu, W. Huang, L. Yang, F. Pan, *Nanoscale* **2020**, *12*, 15036–15044.

[305] J. Wang, X. Sun, *Energy & Environmental Science* **2012**, *5*, 5163–5185.

[306] P. S. Herle, B. Ellis, N. Coombs, L. Nazar, *Nature materials* **2004**, *3*, 147–152.

[307] Z. Mao, M. Farkhondeh, M. Pritzker, M. Fowler, Z. Chen, *Journal of The Electrochemical Society* **2016**, *164*, A39.

[308] H. Zheng, J. Li, X. Song, G. Liu, V. S. Battaglia, *Electrochimica Acta* **2012**, *71*, 258–265.

[309] Z. Fang, X.-L. Zhang, X.-Y. Hou, W.-L. Huang, L.-B. Li, *Rare Metals* **2022**, *41*, 2268–2279.

[310] Y. Li, J. Guo, Y. Chen, S. Deng, J. Zhu, G. Cao, T. Lei, J. Zhang, S. Wang, S. Chang, *Ionics* **2020**, *26*, 1681–1693.

[311] T. Liebmann, C. Heubner, C. Lammel, M. Schneider, A. Michaelis, *ChemElectroChem* **2019**, *6*, 5728–5734.

[312] A. Howeling, S. Glatthaar, D. Notzel, J. R. Binder, *Journal of Power Sources* **2015**, *274*, 1267–1275.

[313] A. S. A. Rahim, M. Z. Kufian, A. K. M. Arof, Z. Osman, *Journal of Electrochemical Science and Technology* **2022**, *13*, 128–137.

[314] Y.-s. Jiang, G. Sun, F.-d. Yu, L.-f. Que, L. Deng, X.-h. Meng, Z.-b. Wang, *Ionics* **2020**, *26*, 151–161.

[315] G. Lim, D. Shin, K. H. Chae, M. K. Cho, C. Kim, S. S. Sohn, M. Lee, J. Hong, *Advanced Energy Materials* **2022**, *12*, 2202049.

[316] J. C. Hestenes, J. T. Sadowski, R. May, L. E. Marbella, *ACS Materials Au* **2022**, *3*, 88–101.

[317] H. Duncan, Y. Abu-Lebdeh, I. J. Davidson, *Journal of the Electrochemical Society* **2010**, *157*, A528.

[318] F. Zou, H. C. Nallan, A. Dolocan, Q. Xie, J. Li, B. M. Coffey, J. G. Ekerdt, A. Manthiram, *Energy Storage Materials* **2021**, *43*, 499–508.

[319] M. Klett, J. A. Gilbert, S. E. Trask, B. J. Polzin, A. N. Jansen, D. W. Dees, D. P. Abraham, *Journal of The Electrochemical Society* **2016**, *163*, A875.

[320] M. D. Levi, V. Dargel, Y. Shilina, V. Borgel, D. Aurbach, I. C. Halalay, *Journal of Power Sources* **2015**, *278*, 599–607.

[321] B. Michalak, B. B. Berkes, H. Sommer, T. Brezesinski, J. Janek, *The Journal of Physical Chemistry C* **2017**, *121*, 211–216.

[322] W. M. Dose, C. Xu, C. P. Grey, M. F. De Volder, *Cell Reports Physical Science* **2020**, *1*.

[323] S. Krueger, R. Kloepsch, J. Li, S. Nowak, S. Passerini, M. Winter, *Journal of the Electrochemical Society* **2013**, *160*, A542.

[324] G. Gabrielli, M. Marinaro, M. Mancini, P. Axmann, M. Wohlfahrt-Mehrens, *Journal of Power Sources* **2017**, *351*, 35–44.

[325] R. Shannon, *Revised effective ionic radii and systematic studies of interatomic distances in halides and chalcogenides* **1976**, *32*, 751–767.

[326] S. Mukerjee, J. T. Vaughey, *J. Electrochem. Soc* **1998**, *145*.

[327] J. Molenda, J. Marzec, K. Swierczek, W. Ojczyk, M. Ziemnicki, M. Molenda, M. Drozdek, R. Dziembaj, *Solid State Ionics* **2004**, *171*, 215–227.

[328] M.-C. Yang, B. Xu, J.-H. Cheng, C.-J. Pan, B.-J. Hwang, Y. S. Meng, *Chemistry of Materials* **2011**, *23*, 2832–2841.

[329] N. M. Jobst, M. Mancini, M. Holzle, M. Wohlfahrt-Mehrens, P. Axmann, *Journal of The Electrochemical Society* **2023**, *170*, 020513.

[330] C. Liu, Z. G. Neale, G. Cao, *Materials Today* **2016**, *19*, 109–123.

[331] K. Ariyoshi, Y. Iwakoshi, N. Nakayama, T. Ohzuku, *Journal of The Electrochemical Society* **2004**, *151*, A296.

[332] E.-S. Lee, K.-W. Nam, E. Hu, A. Manthiram, *Chemistry of Materials* **2012**, *24*, 3610–3620.

[333] Y. Tan, R. Wang, X. Liu, J. Du, W. Wang, R. Zhan, S. Tu, K. Cheng, Z. Chen, Z. Huang, et al., *Energy Storage Materials* **2023**, *63*, 102962.

[334] J. Betz, L. Nowak, M. Winter, T. Placke, R. Schmuch, *Journal of The Electrochemical Society* **2019**, *166*, A3531–A3538.

[335] T. Ohzuku, K. Ariyoshi, S. Takeda, Y. Sakai, *Electrochimica Acta* **2001**, *46*, 2327–2336.

[336] E. Zhao, L. Wei, Y. Guo, Y. Xu, W. Yan, D. Sun, Y. Jin, *Journal of Alloys and Compounds* **2017**, *695*, 3393–3401.

[337] T. Kozawa, *Journal of power sources* **2019**, *419*, 52–57.

[338] M. Mancini, G. Gabrielli, P. Axmann, M. Wohlfahrt-Mehrens, *Journal of The Electrochemical Society* **2016**, *164*, A6229.

[339] W. M. Dose, J. Blauwkamp, M. J. Piernas-Munoz, I. Bloom, X. Rui, R. F. Klie, P. Senguttuvan, C. S. Johnson, *ACS Applied Energy Materials* **2019**, *2*, 5019–5028.

[340] W. Zhu, D. Liu, J. Trottier, C. Gagnon, A. Mauger, C. Julien, K. Zaghib, *Journal of power sources* **2013**, *242*, 236–243.

[341] K. Saravanan, A. Jarry, R. Kostecki, G. Chen, *Scientific Reports* **2015**, *5*, 8027.

[342] Y. Zhu, C. Wang, *The Journal of Physical Chemistry C* **2010**, *114*, 2830–2841.

[343] S. A. J. Al-Hail, M. R. Amin, R. K. Petla, U. Nisar, R. Essehli, S. Ahzi, I. Belharouak, *ACS Applied Energy Materials* **2020**, *3*, 6400–6407.

[344] R. Amin, I. Belharouk, *Journal of Power Sources* **2017**, *348*, 311–317.

[345] M. Y. Abeywardana, N. Laszczynski, M. Kuenzel, D. Bresser, S. Passerini, B. Lucht, et al., *International Journal of Electrochemistry* **2019**, *2019*.

[346] S. J. An, J. Li, C. Daniel, D. Mohanty, S. Nagpure, D. L. Wood III, *Carbon* **2016**, *105*, 52–76.

[347] D. Allart, M. Montaru, H. Gualous, *Journal of The Electrochemical Society* **2018**, *165*, A380–A387.

Appendix A

List of abbreviations

AQ - Anthraquinone
ASSB - All solid state batteries
BET - Brunauer–Emmett–Teller
BGM - Bulk Metallic Glass
C.V. - Constant Voltage
C.E. - Coulombic Efficiency
CMC - Carboxymethyl Cellulose
CNT - Carbon Nanotube
CRM - Critical Raw Materials
CV - Cyclic Voltammetry
DEC - Diethyl Carbonate
DFT - Density Functional Theory
DIOX - 1,3-Dioxolane
DME - 1,2-Dimethoxyethane
DMC - Dimethyl Carbonate
DVA - Differential Voltage Analysis
EC - Ethylene Carbonate
EDX - Energy Dispersive X-ray Spectroscopy
EIS - Electrochemical Impedance Spectroscopy
EOD - End of Discharge
EOC - End of Charge
ESW - Electrochemical Stability Window
EV - Electric Vehicle

FEC - Fluorinated Ethylene Carbonate
FESEM - Field Emission Scanning Electron Microscopy
FS - Polysulfides
GPE - Gel-Polymer Electrolytes
GITT - Galvanostatic Intermittent Titration Technique
HEA - High Entropy Alloy
HEO - High Entropy Oxides
HOMO – highest occupied molecular orbital
ICE - Initial Coulombic Efficiency
ICP-OES - Inductively Coupled Plasma Optical Emission Spectrometry
IEA - International Energy Agency
ILs - Ionic Liquids
IPCEI - Important Projects of Common European Interest
IRENA - International Renewable Energy Agency KB - Ketjenblack
LCMO - Lithium Copper Manganese Oxide
LCO - Lithium Cobalt Oxide
LIB - Lithium-Ion Battery
LiBOB - Lithium Bis(oxalate)borate
LiDFOB - Lithium Difluoro(oxalate)borate
LiPSs - Lithium Polysulfides
LiTFSI - Lithium Bis(trifluoromethanesulfonyl)imide
LNMO - Lithium Nickel Manganese Oxide
LRCMO - Lithium-Rich Copper Manganese Oxide
LUMO - lower un-occupied molecular orbital
LTO - Lithium Titanate Oxide
MOF - Metal Organic Framework
NCA - Lithium Nickel Cobalt Aluminum Oxide
NMC - Nickel-Manganese-Cobalt Oxide
NMP - N-Methyl-2-pyrrolidone
OCV - Open-circuit Voltage
ODH - Oxygen Dumbell Hopping
PANI - Polyaniline
PC - Propylene Carbonate
PDF - Portable Document Format
PE - Polyethylene

PEI - Polyethylenimine
PES - Prop-1-ene-1,3-sultone
PPy - Polypyrrole
PP - Polypropylene
PVdF - Poly(vinylidene difluoride)
PVDF - Polyvinylidene Fluoride
RRF - Recovery and Resilience Facility
rGO - Reduced Graphene Oxide
rGO-ZnS - Reduced Graphene Oxide and Zinc Sulfide
SEM - Scanning Electron Microscopy
SEI - Solid Electrolyte Interphase
SOC - State of Charge
SPE - Solid-Polymer Electrolytes
SBR - Styrene-Butadiene
TEM – Transmission electron microscopy
TGA -Thermogravimetric analysis
XPS – X-ray photoelectron spectroscopy
XRD – X-ray powder diffraction

Appendix B

Physical-chemical and electrochemical characterization - Conditions

B.1 Chapter 4 - High entropy Oxides in Li-S batteries

Physical-Chemical characterization: X-ray diffraction (XRD) analysis was carried out by a PANalytical X'Pert (Cu K_α radiation) diffractometer. Data were collected with a 2D solid-state detector (PIXcel) from 10 to 90 (2θ) with a step size of 0.026 (2θ) and a wavelength of 1.54187 Å. Field emission scanning electron microscopy (FESEM) analysis was carried out by Zeiss SUPRA^{TM} 40 with Gemini column and Schottky field emission tip (tungsten at 1800 K). Acquisitions were made at acceleration voltage of 3 kV and working distance between 2.1 and 8.5 mm, with magnification up to 1000 kX. Transmission electron microscopy (TEM) analysis was performed by High-Resolution JEOL 300 kV. The Brunauer–Emmett–Teller (BET) specific surface area (SSA) was determined by nitrogen physisorption at 77 K using a Micrometrics ASAP 2020 instrument. The specific surface area was calculated with the BET model in the relative pressure range of 0.07–0.30 by assuming 0.162 nm^2/molecule as the molecular area of nitrogen. X-Ray PhotoLectron Spectroscopy (XPS) Measurements Were Carried Out use a Phi Model 5000 Electron Spectrometer Equipped with an Aluminum Anade (1486 eV) Monochromatic Source, with a power of 25.0 W and High-resolution Scan with 11.75 eV Pass Energy. The instrument

typically operates at pressures below $5\times10^{\breve{}8}$ mbar.

Electrochemical methods: The electrochemical performances were investigated by galvanostatic discharge/charge cycling (GC) using an Arbin LBT-21084 battery tester at room temperature. GC tests were carried out in the potential range of 1.8–2.6 V versus Li/Li^+ at different current regimes. The C-rate was calculated with respect to the theoretical capacity of sulfur (1672 mAh g^{-1}). For cyclic voltammetry (CV), the electrode potential was reversibly scanned from 1.7 to 2.8 V versus Li/Li^+ at different scan rates using a Biologic 092-11/2e potentiostat/galvanostat. Electrochemical impedance spectroscopy (EIS) was performed in coin cells to analyze the time-dependent processes that occur on the standard (STD) and modified cathodes (HEO80 and HEO90), the responses were recorded before and after eight CV cycles. The impedance was measured at OCV from 10^5 to $5\cdot 10^{-3}$ Hz, with a 10 mV amplitude perturbation.

B.2 Chapter 5 - rGO/ZnS in Li-S batteries

Physical-Chemical characterization: The physical-chemical characterization of the materials was carried out using the same equipment and tests already mentioned in section section B.1, except for the Thermogravimetric analysis which was performed on a TG 209 F Tarsus (Netzsch, Selb, Germany) instrument by heating the samples at 10 °C min^{-1} from room temperature to 800 °C and 1000 °C in air and nitrogen to evaluate the sulfur content inside the composite material and to the UV-vis absorption spectra which were detected by a UV–vis spectrophotometer (Hitachi U-5100 Spectrophotometer, Tokyo, Japan) within the spectral range of 300–550 nm.

Electrode preparation: The cathodes were prepared using the solvent tape casting method. Active materials, namely SN-rGO/S_8 and SN-rGO/ZnS/S_8, were utilized, along with Ketjenblack as a conductive carbon additive, and a polymeric binder (PVdF, 8 wt.% in N-methyl-2-pyrrolidinone solution). The electrode composition was set at a ratio of 80:10:10 wt.% for (SN-rGO/S_8:KjB:PVdF) or (SN-rGO/ZnS/S_8:KjB:PVdF) in all preparations. These components were mixed and gently ball-milled to achieve a uniform slurry, which was then mechanically applied onto an aluminum current collector using the doctor blade technique. The blade was adjusted to deposit a 200 μm layer at a speed of 10 mm s^{-1} using an automatic film

applicator (Sheen-AB4120). After the slurry deposition, the coated aluminum foil was dried at 50 °C in ambient air. Subsequently, 1.76 cm^2 disks were cut out and vacuum-dried at 40 °C in a Büchi Glass Oven B-585 for 4 hours. The dried disks were then transferred to an Argon-filled dry glove-box (MBraun Labstar, H_2O, and O_2 content $\leq$ 1 ppm) for cell assembly. The loading of active material (referred to as S_8) on both SN-rGO/S_8 and SN-rGO/ZnS/S_8 based cathodes ranged between 1 and 1.3 mg cm^{-2}.

For the electrodes used in catalytic tests (Tafel, symmetrical cyclic voltammetry, and Li_2S deposition), a slurry of 80:10:10 wt% (SN-rGO:KjB:PVdF), (SN-rGO/ZnS:KjB:PVdF), and 90:10 wt% (KjB:PVdF) was cast on carbon paper (CB, GDL 39BB SGL Carbon, Wiesbaden, Germany) with a thickness of 200 μm. Importantly, these prepared electrodes did not contain any sulfur. The procedure for cutting and drying was identical to that used for the cathodes.

Electrochemical methods: Symmetric cells of Li_2S_8 were assembled within an argon-filled glove box to analyze the kinetic behavior of SN-rGO/S_8 and SN-rGO/ZnS/S_8 materials. Specifically, two identical electrodes were integrated into a CR2032 coin cell with a PP polymeric membrane (Celgard 2500, 25 μm thickness) serving as a separator. A catholyte solution of 50 μL 1,2-dimethoxyethane (DME) and 1,3-dioxolane (DIOX) 1:1 (v/v) with Li_2S_8 0.125 M was employed. The symmetrical cyclic voltammetry (CV) test was also conducted using a blank solution of 1,2-dimethoxyethane (DME) and 1,3-dioxolane (DIOX) 1:1 (v/v). Tafel and Li_2S precipitation tests were carried out on CR2032 coin cells comprising carbon fiber electrodes of SN-rGO, SN-rGO/ZnS, and KjB against a lithium disk. Linear sweep voltammetry at 0.005 mVs^{-1} from the open circuit voltage of the cell to $\pm$30 mV was performed after an hour of rest. For the Tafel test, 50 μL of 1,2-dimethoxyethane (DME) and 1,3-dioxolane (DIOX) 1:1 (v/v) Li_2S_8 6.25 mM solution was used as catholyte, while for the Li_2S precipitation test, the concentration of Li_2S_8 was 25 mM.

To assess the electrochemical properties of SN-rGO/S_8 and SN-rGO/ZnS/S_8 materials, electrodes based on these materials were assembled in CR2032 coin-type cells with a lithium disk as the counter electrode and Celgard 2500 as a separator. The electrolyte comprised a solution of 1,2-dimethoxyethane (DME) and 1,3-dioxolane (DIOX) 1:1 (v/v) with 1.0 M lithium bis(trifluoromethanesulfonyl)imide ($CF_3SO_2NLiSO_2CF_3$), LiTFSI) and 0.25 M lithium nitrate ($LiNO_3$, 99.9%). The amount of electrolyte was determined based on the sulfur content in each cath-

ode, maintaining a consistent ratio of 10–11 μL of electrolyte per mg of sulfur. The cycling performances of the cathodes were evaluated through galvanostatic discharge-charge cycling (GC) using an Arbin LBT-21084 battery tester at room temperature. Galvanostatic discharge-charge tests were conducted in the potential range of 1.85–2.6 V vs. Li/Li^+ at different current rates, with C-rate calculated based on the theoretical capacity of sulfur (1675 mAh g^{-1}). Cyclic voltammetry (CV) was performed in the potential range between 1.7 and 2.8 V vs. Li/Li^+ at 0.05, 0.1 mVs^{-1} and between 1.7 and 3.0 V vs. Li/Li^+ at 0.2, 0.3, 0.4, and 0.5 mVs^{-1}. CV tests at different scan rates aimed to evaluate the diffusion coefficient of Li^+ in the electrode using the Randles-Sevcik equation:

$$i_p = (2.687 \times 10^5) n^{\frac{3}{2}} A C_{Li^+} D^{\frac{1}{2}} \tag{B.2.1}$$

Where the constant term 2.687x10^5 has the unit of [C· mol^{-1}· $V^{-\frac{1}{2}}$], n is the number of electrons transferred in a redox cycle, A is the electrode surface area [cm^2], C_{Li^+} is the concentration of Li^+ inside the cathodic material [mol· cm^{-3}] and D is the lithium-ion diffusion coefficient [cm^2· s^{-1}]. Electrochemical Impedance Spectroscopy tests (EIS) were performed with Bio-Logic®VSP-3e multichannel potentiostat equipped with impedance modules. The spectra were recorded in the frequency range of 100 kHz to 10 mHz, with an excitation potential of 5 mV and 10 points per decade. The EIS spectra were collected at the end of the anodic scan (2.8 V vs Li/Li^+ for the scan rate performed at 0.05 and 0.1 mVs^{-1}, and 3.0 V vs Li/Li^+ for the 0.2, 0.3, 0.4 and 0.5 mVs^{-1}), after 30 min of rest, at each different scan rate that was performed.

B.3 Chapter 6 - LNMO/LFP blended cathodes

Electrodes preparation: Electrodes were fabricated using the solvent tape casting technique. The cathode slurry was obtained by mixing 90 wt.% of active material (pure or blended), 5 wt.% of conducting Carbon Black (TIMCAL C-NERGYTM Super C65, ImerysCarb.) and 5 wt.% of binder poly(vinylidene fluoride) (PVdF - HSV900) solution, (10 wt.% in N-methyl pyrrolidone - NMP). Following the complete dissolution of the binder, carbon black and the active component were added to

the mixture which was uniformly blended with a ball mill at 30 Hz for 15 minutes. The resulting slurries were spread onto carbon-coated aluminum foil (supplied by ARMOR Group, with thicknesses of 19.8 μm and a carbon layer of 1.1 μm) using a doctor blade set to achieve a layer thickness of 300 μm, and an automated film applicator (Sheen 1133N) at a speed of 50 mm per second.

Following the solvent evaporation at 50 °C for an hour, electrode discs were punched out to sizes of 0.785 and 1.766 cm^2, and then vacuum dried at 120 °C for four hours in a Büchi Glass Oven B-585. They were subsequently placed in an argon-filled dry glove box (MBraun Labstar, with H_2O and O_2 levels below 1 ppm) in preparation for assembling into half-cells and full-cells. The dried LNMO and blended-based electrodes had a mass loading ranging from 10.5 to 11.5 mg cm^2.

Electrochemical methods: Cyclic voltammetry tests using a three-electrodes Swagelok-type T-cell were performed at room temperature, employing lithium disks as both counter and reference electrodes, within a voltage range of 3 – 4.9 V at the scan rate of 0.1 mV s^{-1} and at increasing rates (i.e. 0.1, 0.2, 0.3, 0.4 and 0.5 mV s^{-1}).

The cycling performances (rate capability and capacity retention test), in half and full configuration, were investigated by assembling 2032-type coin cells, using lithium disks (∅ 16 mm, 0.6 mm-thick, Tobmachine) or graphite anode (∅ 14 mm PE16, Elkem) as counter and reference electrode, respectively. All galvanostatic charge-discharge cycling tests were carried out using an Arbin BT-2000 battery tester at room temperature, in the potential range of 3 – 4.9 V vs. Li/Li^+ for half-cell configuration and 3 – 4.75 V for full-cell configuration. The charge/discharge rates were based on the LNMO theoretical specific capacity of 147 mAh g^{-1}.

The galvanostatic intermittent titration technique (GITT) was utilized on half-cells to examine overpotentials and changes in the lithium-ion diffusion coefficient across various states of charge. This involved initial formation cycles at a 0.1C rate, followed by GITT cycles with a 10-minute current pulse at 0.1C and a 2-hour relaxation period.

Potentiostatic electrochemical impedance spectroscopy (PEIS) measurements were taken using a VMP-3 Biologic multichannel potentiostat to assess internal cell (in half-cell configuration, i.e. using lithium metal as anode) resistance at various SOC, applying a 10 mV amplitude across a frequency spectrum from 500 kHz to 50 mHz. Cycling performance in a three-electrode setup was also evaluated using a PAT-Cell (EL Cell) and a VMP-3 Biologic potentiostat, with graphite and a lithium ring as the

counter and reference electrodes, respectively. This configuration helped isolate and analyze the charge-discharge behaviors of the anode and cathode separately.
All electrochemical experiments were conducted at a standard room temperature of 25 °C, using an electrolyte composed of 1.0 M $LiPF_6$ in a 1:1 volume mix of ethylene carbonate (EC) and diethyl carbonate (DEC), with an added 5% fluoroethylene carbonate (FEC) from Solvionic, absorbed into a glass fiber separator (Whatman GF/A; 0.63 mm thickness).

B.4 Chapter 7 - LCMO and LRCMO materials

Physical-Chemical characterization : The chemical and physical properties of the synthesized materials were investigated using SEM, XRD, and particle size distribution analysis in the laboratories of CEA-Liten. Scanning electron microscopy and energy-dispersive X-ray spectroscopy were performed using a Zeiss brand MEB LEO 1530 Gemini microscope. X-ray diffraction (XRD) analyses were conducted on a BRUKER AXS D8 diffractometer, utilizing a Cu Kα (λ = 1.5406 Å) anticathode. The sample was scanned in the range of 10 – 80° with a step size of 0.02° and 10 - 110° with a step size of 0.00396° for a more precise measurement used to refine the structure of the $LiCu_{0.4}Mn_{1.6}O_4$ sample. The XRD measurements on the dissasembled electrodes and the overlithiated sample, which is sensitive to air, were performed by protecting them with a Kapton film applied in Argon filled glove box. As a result, a signal due to Kapton film could be detected at small 2θ angles (0–28°) in the diffraction patterns of these samples, which was then subtracted as part of the background. However, the quality of the experimental signal was not sufficient to conduct a refinement with values considered acceptable. Particle size distribution was determined using a Mastersizer granulometer series from Malvern Instrument. The chemical analysis is performed by using ICP-OES (Agilent Technologies 700 Series ICP-OES).

Appendix C

List of publications and contribution

Publications

Colombo, R., Garino, N., Versaci, D. et al. Designing a double-coated cathode with high entropy oxides by microwave-assisted hydrothermal synthesis for highly stable Li–S batteries. J Mater Sci 57, 15690–15704 (2022). https://doi.org/10.1007/s10853-022-07625-7

Colombo, R., Versaci, D., Amici, J., Bella, F., Para, M.L., Garino, N., Laurenti, M., Bodoardo, S. and Francia, C., 2023. Reduced graphene oxide embedded with ZnS nanoparticles as catalytic cathodic material for Li-S batteries. Nanomaterials, 13(14), p.2149. https:doi.org/10.3390/nano13142149

Contributions - Oral/poster presentations

Giornate dell'Elettrochimica Italiana (GEI) 11-15 Settembre 2022, Orvieto
Poster: "Microwave synthesis of rGO/ZnS nanocomposite as cathodic material for Li-S batteries"

72 nd Annual Meeting of the International Society of Electrochemistry 29-3 September 2021, Jeju
Poster: "A double-layered sulfur cathode exploiting the effect of high entropy oxides synthesized by microwave irradiation for excellent performances of lithium-sulfur batteries"
Poster: "Innovative hybrid high voltage electrodes based on LMNO/LFP materials

for lithium-ion batteries"

Swiss Battery Days 2022, 29-31 Agosto 2022, Zurich
Oral presentation: "Hybrid designs/architectures for cathode material for Li-Ion batteries"

Second Italian Workshop on Energy Storage (IWES 2023), Bressanone
Oral presentation: "Hybrid designs/architectures for cathode material for Li-Ion batteries"

74^{th} Annual Meeting of the International Society of Electrochemistry 3-9 September 2023, Lion Oral presentation: "Reduced Graphene Oxide Embedded with ZnS Nanoparticles as Catalytic Cathodic Material for Li-S Batteries"

SEABAT 2^{nd} ACADEMIC EVENT, 14-15 june 2023
Poster: "Lithium Copper Manganese Oxide (LCMO) as cathodic material for the next generation of Co-free Li-Ion batteries"